UNIVERSIDAD POLITÉCNICA DE MADRID
Escuela Técnica Superior de Ingeniería Aeronáutica y del Espacio

Retaining Exact Blade Counts in Turbomachinery Scale-Resolving Simulations Using the Time-Inclined Method

T E S I S D O C T O R A L

Presentada para optar al título de Doctor por:

Miguel Montiel Ruiz
Máster en Ingeniería Aeronáutica

Madrid, 2024


UNIVERSIDAD POLITÉCNICA DE MADRID
Escuela Técnica Superior de Ingeniería Aeronáutica y del Espacio

Doctorado en Ingenieria Aeroespacial

Retaining Exact Blade Counts in Turbomachinery Scale-Resolving Simulations Using the Time-Inclined Method

T E S I S D O C T O R A L

Presentada para optar al título de Doctor por:

Miguel Montiel Ruiz
Máster en Ingeniería Aeronáutica

Bajo la dirección de:
Dr. Roque Corral García

Madrid, 2024

Título: Retaining Exact Blade Counts in Turbomachinery Scale-Resolving Simulations Using the Time-Inclined Method

Autor: Miguel Montiel Ruiz

Programa de Doctorado: Ingenieria Aeroespacial

Dirección de Tesis:

Dr. Roque Corral García, Catedrático en el Departamento de Mecánica de Fluidos y Propulsión Aeroespacial, Universidad Politécnica de Madrid (Director)

Revisores Externos:

Tribunal de Tesis:

Fecha de Defensa de Tesis:

Esta tesis ha sido financiada por el proyecto TASTE: TECNOLOGÍAS AERODINÁMICAS PARA TURBOFANES ENGRANADOS (RTC2019-007194-4), del Ministerio de Ciencia e Innovación y la Agencia Estatal de Investigación (programa RETOS-Colaboración)

A mi abuela, Puri

Acknowledgements

Firstly, I would like to thank my PhD. supervisor, Roque Corral, to whom I am very grateful for sharing his knowledge and experience.

I would also like to thank ITP Aero for supporting this work. In particular, I am specially grateful to Fernando Gisbert, a foundational pillar for this project.

On such note, I would like to thank the Head of the Simulation Department, Pedro de la Calzada, for his support, as well as Jesús Contreras for reviewing part of this work and providing helpful technical advice. Jaime Quintanal deserves an special mention, not only for his technical support, but also for his company and his friendship.

Likewise, mentions are due to Adrián Sotillo, Javier Crespo and Jesús Pueblas, whose input throughout these last years has helped me immensely, and deserve their due recognition.

Additionally, I would like to acknowledge the help and advice I have received from many peers in the Simulation Department, who have also made me feel very welcomed, such as José María Chaquet, Juan Manuel Gallardo, Óscar Bermejo and Óscar Pérez.

I also greatly appreciate the financial support I received for this work, which was funded by the Ministerio de Ciencia e Innovación under grant RTC2019-007194-4 (TASTE) from RETOS-Colaboración program, and I am thankful to Carlos Martel for providing me the opportunity to be a part of the project.

On a more personal level, I am grateful to have shared these years with awesome research colleagues. In particular, I would like to thank Michele Greco, Ricardo Blázquez, Yago Blando, David Romera, Álvaro Saiz and Marc Bolinches. The support from Marc Bolinches is greatly acknowledged, as he helped me get to speed when I first arrived to the research group and was an essential part of the foundations of this work.

Last, but definitely not least, I deeply acknowledge the love and support from my partner, Irene, and my mother, Yolanda. Thank you.

Abstract

Scale-Resolving Simulations (SRSs) of turbulent flows in turbomachinery are becoming increasingly common at the industry level for reduced computational domains and moderate Reynolds numbers. The full annular domains are reduced to a single passage computational domain, and the solution is assumed to be spatially periodic in each passage. However, the unsteady character of turbomachinery stages and non-integer pitch ratios prevent the imposition of spatial periodicity in the passages.

Several methodologies have been developed to account for arbitrary blade counts in reduced computational domains for Unsteady Reynolds-Averaged Navier-Stokes (URANS) simulations. Nevertheless, the stochastic nature of turbulent flows impedes the direct imposition of temporal periodicity to the flow, on which most time-marching methodologies rely. Thus, the blade count is commonly approximated to the nearest integer in SRSs, so that spatial periodicity can be imposed in a single passage.

The Time-Inclined (TI) method is a domain-reducing approach successfully used for URANS in the past. It is easily implemented in time-marching solvers but, more importantly, it does not directly impose any temporal periodicity to the flow. Additionally, it has been shown not to degrade the convergence rate to a quasi-periodic state, contrary to other approaches. Nevertheless, it still has not been explored as an alternative to the single-passage approximation for SRSs.

Thus, the goal of this thesis is to evaluate the suitability of the TI method for retaining the exact blade count in SRSs. To that end, several objectives of incremental complexity, which form the structure of the present work, have been formulated.

The usual TI formulation for the Navier-Stokes (NS) equations excludes some of the diffusive terms. Providing insight into such a potential source of errors is one of the main objectives of the present thesis, since it has never been thoroughly analysed and might be relevant for SRSs. Hence, Chapter 3 includes a novel analysis on the truncation of the inclined NS equations.

Chapter 4 verifies the implementation of the TI method into the high-order baseline solver via simulations of two-dimensional linear cascades of flat plates and of T106 Low-Pressure

Turbine (LPT) airfoils. The cascades are subjected to upstream perturbations that are only spatially periodic in a multi-passage domain, motivating the use of the TI method.

Figures of merit from multi-passage and TI inviscid simulations are nearly identical, proving the correct implementation of the method. Meanwhile, viscous simulations allow fulfilling the second objective of this work: to validate the theoretical analysis of the viscous TI approximation. As predicted, the truncated terms become relevant for regions of high Strouhal numbers. Due to their viscous origin, their impact is most noticeable for low Reynolds number flows.

In Chapter 5, the results from 3D simulations of the T106 LPT linear cascade with incoming wakes are reported. The pitch ratio between the wakes and the cascade is not an integer, and the TI method is used to reduce the problem to a single-passage computational domain. Three-way comparisons have been generated between the solutions of the multi-passage domain, the single-passage time-inclined solution and the single-passage solution approximating the pitch ratio of the problem to the nearest integer.

Thus, Chapter 5 is concerned with the third main objective of the present thesis: to assess the accuracy and performance of the TI method in a 3D problem of industrial interest. The results indicate that the TI method, retaining the exact blade count, produces very accurate predictions for turbulence-resolving simulations. Moreover, it outperforms the standard single-passage methodology in most of the variables of interest and is equivalent in the rest.

The results of the turbulent flows in Chapter 5 are complemented by virtual experiments of canonical turbulence problems in Chapter 6, which features the numerical solution of a transitional problem and the simulation of turbulent boundary layers in periodic channels. Although some differences are found for the mixing process at the smallest scales, Chapter 6 shows how the TI method can be used for accurate simulations of turbulent flows, the fourth and last objective of this work.

Keywords: Turbomachinery, Time-Inclined Method, Numerical Modeling, Rotor/Stator Simulations, Turbine, Scale-Resolving Simulations, Turbulent Flows, Computational Fluid Dynamics, Large Eddy Simulations, Direct Numerical Simulations.

Resumen

El uso de simulaciones de resolución de escalas (SRSs) está cada vez más extendido en entornos industriales. Las geometrías anulares suelen ser reducidas a un solo pasaje en el que se asume que la solución es periódica en dirección acimutal. Sin embargo, el carácter no-estacionario del problema y el hecho de que los números de álabes de rotor y estátor no suelen ser divisibles impiden imponer dicha periodicidad en un solo pasaje.

Varias metodologías han sido desarrolladas para simular configuraciones arbitrarias de una etapa en dominios reducidos mediante la resolución de las ecuaciones no-estacionarias de Navier-Stokes promediadas por Reynolds, o URANS. No obstante, la naturaleza estocástica de los flujos turbulentos resueltos en SRSs impide establecer una periodicidad temporal en los pasajes, esencial para la formulación de la mayoría de dichas metodologías. Por ese motivo, en SRSs es común aproximar los números de álabes de las filas de modo que sean divisibles, permitiendo imponer condiciones de periodicidad en muy pocos pasajes.

El método "Time-Inclined" (TI) es una técnica de reducción de dominio computacional que ha sido usada con éxito para URANS. Una de sus características más relevantes es que no impone de forma directa la periodicidad temporal del flujo. Además, al contrario que otros métodos, no muestra una degradación de la convergencia a soluciones cuasi-periódicas. Sin embargo, su uso no está extendido para SRSs. Por tanto, el propósito de esta tesis es evaluar la idoneidad del método TI para retener el número exacto de álabes en simulaciones SRS.

La formulación usual del método TI para las ecuaciones de Navier-Stokes (NS) excluye algunos de los términos difusivos. Un primer objetivo de este trabajo es cuantificar el impacto de dicho truncamiento en la precisión del método, y evaluar si puede suponer una fuente de error relevante en SRSs de turbomaquinaria. El análisis teórico de los términos truncados se encuentra en el Capítulo 3, en el que se introduce el método TI y se describen otras posibles limitaciones del mismo.

En el Capítulo 4 se verifica la implementación del TI en el código del resolvedor base. El proceso se ha llevado a cabo mediante simulaciones 2D de cascadas lineales de placas planas y de perfiles T106 de turbina de baja presión (LPT). Las cascadas están sometidas a perturbaciones aguas arriba que solo son periódicas en un dominio multi-pasaje, motivando el uso del TI para reducirlo a un único pasaje.

Los resultados del análisis multi-pasaje y del TI para simulaciones no viscosas son prácticamente idénticos, lo que indica la correcta implementación del método. Los resultados de las simulaciones viscosas permiten completar el segundo objetivo de esta tesis: validar el análisis teórico sobre la aproximación de las ecuaciones de NS "inclinadas". Tal y como predice la teoría, los términos truncados son relevantes en regiones de altos números de Strouhal y, dada su proveniencia viscosa, su impacto es apreciable a bajos números de Reynolds.

En el Capítulo 5 se presentan los resultados de simulaciones 3D de una cascada lineal de perfiles T106 aguas abajo de estelas provenientes de una fila anterior. El número de estelas no es divisible por el de álabes, por lo que el método TI se utiliza para reducir a uno el número de pasajes que se deben incluir en el dominio computacional. Se han generado comparaciones triples entre las soluciones multi-pasaje, TI, y una solución al problema aproximado que modifica el número de estelas para obtener periodicidad en un solo pasaje sin recurrir al TI.

Por lo tanto, el Capítulo 5 se centra en el tercer objetivo de la tesis: estudiar la precisión y el desempeño del método TI en simulaciones 3D de interés industrial. Los resultados indican que el TI, reteniendo la geometría original del problema, es capaz de alcanzar soluciones muy precisas en estas simulaciones con flujos turbulentos. De hecho, se obtienen mejores resultados que con la metodología aproximada de un solo pasaje en la mayoría de las variables de interés, y resultados de calidad semejante en el resto.

El Capítulo 6 incluye la resolución numérica de problemas canónicos de flujos turbulentos como la solución numérica de un problema de flujo en transición (el vórtice de Taylor-Green) y la de capas límite turbulentas en canales periódicos. A pesar de que se encuentran diferencias apreciables en el proceso de mezclado para las escalas más pequeñas, los resultados indican que el TI puede reproducir fielmente flujos turbulentos, lo que conforma el cuarto y último objetivo de esta tesis.

Palabras clave: Turbomaquinaria, Time-Inclined, Métodos Numéricos, Simulaciones Rotor/Estátor, Turbina, Flujos Turbulentos, Dinámica de Fluidos Computacional, Simulación Numérica Directa.

Contents

List of Figures xviii
List of Tables xix
Nomenclature xxv

1 Introduction **1**
1.1 Background and Motivation 2
1.1.1 Challenges of LPT Aerodynamic Simulations 4
1.1.2 Numerical Methods for High-Fidelity Simulations 7
1.1.3 High-Fidelity Simulations of LPTs 10
1.1.4 Scale-Resolving Simulations in Aeroacoustics 16
1.1.5 Methods for Stator/Rotor Interaction 18
1.2 Objectives and Outline 27
1.3 Original Contributions 30

2 Baseline Solver Description **33**
2.1 Spatial Discretisation 34
2.1.1 The FR Method for One-Dimensional Conservation Laws 34
2.1.2 The Lifting Collocation Penalty Method 37
2.1.3 The Navier-Stokes Equations 41
2.2 Flux Splitting 43
2.3 Boundary Conditions 45
2.3.1 The 3D Navier-Stokes Characteristics Boundary Conditions 46
2.4 The Mortar Method for Non-Conformal Grids 52
2.4.1 Method Description 53
2.4.2 Algorithm for Rotor/Stator Simulations 56
2.5 Temporal Integration 60

3 The Time-Inclined Method **63**
3.1 Time-Inclined Method Formulation 65
3.2 Limitations of the Time-Inclined Method 70
3.2.1 Inclination of the Computational Planes 70
3.2.2 Time-Step Size 73

3.2.3 Multi-Stage Analysis . . . 74
3.3 The Viscous Problem . . . 75
3.3.1 Analysis of the Viscous Approximation . . . 77
3.4 The Rotor/Stator Problem . . . 79
3.5 The Time-Inclined Method in SRS . . . 82
3.6 Implementation Into a High-Order Solver . . . 85
3.6.1 Effect on the Boundary Conditions Formulation . . . 85

4 Two-Dimensional Verification of the Time-Inclined Method 89
4.1 Flat-Plate Cascades . . . 90
4.1.1 Verification of the Time-Inclined Implementation . . . 90
4.1.2 Viscous Cases . . . 95
4.2 T106A Low-Pressure Turbine Linear Cascade . . . 110
4.2.1 Case Description . . . 110
4.2.2 Verification Results . . . 112
4.2.3 Viscous Results . . . 114
4.3 Computational Cost Considerations . . . 120

5 Three-Dimensional Scale-Resolving Simulations 125
5.1 Upstream Perturbation Modelling . . . 126
5.2 Cases Description . . . 129
5.3 Results . . . 135
5.4 Summary and Conclusions . . . 153

6 Turbulent Flow Test Cases 155
6.1 Taylor-Green Vortex . . . 155
6.2 Turbulent Channel Flow . . . 159
6.2.1 Case A: $Re_\tau = 180$ . . . 161
6.2.2 Case B: $Re_\tau = 870$ . . . 167
6.3 Closing Remarks . . . 169

7 Conclusions 171
7.1 Summary and Main Takeaways . . . 171
7.2 Future Work . . . 175

Bibliography 177

List of Figures

1.1 Sketch of the interface scaling in the Profile Transformation Approach for a single-passage simulation. 22

1.2 Schematic of the block-wise spectral reconstruction of the 1^{st} harmonic in a domain consisting of six blocks. Solid diamonds: Data used to reconstruct the solution on the boundaries. Empty diamonds: Interpolated data outside of the computational domain. Circles: Computational node. Extracted from Corral et al. [70] 25

2.1 Entropy isolines of vortices crossing the sliding plane in a two-dimensional rotor/stator simulation showing high-order elements in red with their interior points in black (a). Sketch of the definition of mortars Ξ_1 and Ξ_2 from element Ω (b). 53

2.2 Sketch of the interpolation process of the solution from an element face, Ω, to one side of the adjacent mortars, Ξ_1 and Ξ_2. 55

2.3 Sketch of a rotor/stator interface showing the correspondence between numbered elements at each side. 58

2.4 Static temperature isolines and field in a two-dimensional rotor/stator simulation of T106 profiles over a 6^{th}-order mesh. General view of the computational domain (a) and close-up of the non-conformal sliding plane interface (b). 60

3.1 Nomenclature and illustration of a stator/rotor problem with unequal pitches. 66

3.2 Representation of the computational domain for a problem of unequal pitches, where the solid circles (●) represent nodes storing the solution. Computational domain for Erdos' method (a) and time-inclined computational plane (b). 67

3.3 Characteristics of the Euler equations and regions of permissible inclination of the computational planes, λ. 71

3.4 Rotor/stator interface diagram. 81

4.1 Schematic of the flat-plate cascade with inlet perturbations in the physical (left) and time-inclined (right) planes. 91

4.2 Close-up view of the plate's mesh showing elements without their interior points for the inviscid case (a) and detail of the leading edge mesh with 4^{th} order elements (in red) and interior points (in black) (b). 92
4.3 Time-averaged static pressure along the passage at $y = y_{plate^+}$, on the plate's top side. The flat plate is included for reference. 93
4.4 Modulus of the first harmonic of the unsteady pressure on the plate's lower surface for the inviscid case. 94
4.5 Modulus of the first harmonic of the unsteady pressure for the multi-passage (left) and time-inclined (right) inviscid simulations. 94
4.6 Modulus of the second (a) and third (b) harmonics of the unsteady pressure on the plate's lower surface for the inviscid case. 95
4.7 Modulus of the first harmonic of the unsteady pressure for the multi-passage (a) and time-inclined (b) low-resolution simulations of the cascade of flat plates with $Re_c = 1.1 \times 10^5$. 96
4.8 Distribution of the 1^{st} harmonic of the unsteady pressure on the flat plate's lower side for the $Re_c = 1.1 \times 10^5$ case. Comparison between the multi-passage solution with the time-inclined method (a) and with the approximate single-passage simulation (b). 97
4.9 Physics of the viscous flow past a cascade of flat plates at high Reynolds numbers sketched by a snapshot of the entropy. 98
4.10 Flat plate's mesh showing elements without their interior points for the high-resolution case (a) and detail of the leading edge mesh showing the flow separation and vortex shedding (b). 99
4.11 Time-averaged (a) and 1^{st} harmonic of the static pressure (b) along the passage mid-line for the $Re_c = 1.1 \times 10^5$ case. 100
4.12 Distribution of the 1^{st} harmonic of the unsteady pressure on the flat plate's lower side for the $Re_c = 1.1 \times 10^5$ and fine mesh case. Comparison between the multi-passage solution with the time-inclined method (a) and with the approximate single-passage simulation (b). 101
4.13 Modulus of the second (a) and third (b) harmonic of the unsteady pressure on the plate's lower surface for the $Re_c = 1.1 \times 10^5$ case. 102
4.15 Stream-wise evolution of the dimensionless time-averaged total pressure profiles in the flat plate wake at $Re = 1.1 \times 10^5$. 102
4.14 Profiles of the time-averaged velocity (top) and root mean squared fluctuations of the unsteady velocity (bottom) at several axial stations of the flat plate boundary layer for the $Re_c = 1.1 \times 10^5$ case. 103
4.16 Isolines over a snapshot of the stream-wise velocity v_x in the flat-plate passage for a viscous flow of $Re_c = 1.1 \times 10^4$. 104

4.17 Time average (a) and 1^{st} harmonic of the static pressure (b) along the passage mid-line for the $Re_c = 1.1 \times 10^5$ case. 105
4.18 Distribution of the 1^{st} harmonic of the unsteady pressure on the flat plate's lower side for the $Re_c = 1.1 \times 10^4$ case. Comparison between the multi-passage solution with the time-inclined method (a) and with the approximate single-passage simulation (b). 106
4.19 Modulus of the second (a) and third (b) harmonics of the unsteady pressure on the plate's lower surface for the $Re_c = 1.1 \times 10^4$ case. 106
4.20 Stream-wise evolution of the dimensionless time-averaged total pressure profiles in the flat plate wake at $Re = 1.1 \times 10^4$. 107
4.21 Close-up of a snapshot of the entropy isolines for $Re = 1.1 \times 10^4$ in the flat-plates wakes, where $\widetilde{x} = x - x_{TE}$. Top: Time Inclined. Bottom: Multi-Passage 108
4.22 Profiles of the time-averaged velocity (top) and root mean squared fluctuations of the unsteady velocity (bottom) at several axial stations of the flat plate boundary layer for the $Re_c = 1.1 \times 10^4$ case. 109
4.23 Stream-wise evolution of the total pressure loss for the flat-plate cascade at $Re = 1.1 \times 10^4$. 110
4.24 Schematic of the T106A cascade with inlet perturbations. 111
4.25 Second-order mesh detail of the T106A airfoil. 111
4.26 Grid sensitivity analysis for the static pressure on the T106A airfoil at $Re_c = 1.1 \times 10^5$. 112
4.27 First harmonic of the unsteady pressure about an inviscid T106A linear cascade. Comparison of the multi-passage solution to the time-inclined (a) and single-passage (b) methodologies. 113
4.28 Modulus of the first harmonic of the unsteady pressure for the inviscid T106A cascade. Reference (left), time-inclined (centre) and approximate pitch ratio (right) simulations. 114
4.29 Snapshot of the of the entropy field of the T106A airfoil cascade with the location of boundary layer measuring stations **a**, **b** and **c**. 115
4.30 Real part of the 1^{st} harmonic of the entropy about the T106A airfoil at $Re_c = 1.1 \times 10^5$. 115
4.31 Comparison of the mean isentropic Mach number distribution about the T106A cascade between the multi-passage analysis and the time-inclined method. 116
4.32 First harmonic of the unsteady pressure about the T106A linear cascade. Comparison of the multi-passage solution to the time-inclined (a) and single-passage (b) methodologies. 116

4.33 Boundary layer profiles of the time-averaged velocity (top) and the first harmonic of the unsteady velocity in the wall-tangential direction (bottom) at the three measuring stations for the T106A cascade. 117

4.34 Pitch-wise distribution of the time-averaged total pressure in the T106A wake. 118

4.35 Pitch-wise distribution of the time-averaged total pressure in the T106A wake. 119

4.36 Pitch-wise distribution of exit angle (a), velocity (b) and Reynolds stress tensor component $\overline{u'v'}$ (c) on the viscous T106A cascade case at $(x - x_{TE}) / c_x = 30\%$. 119

4.37 Convergence history of a flat plate cascade as a function of the number of inlet perturbation periods and through-flow times ($t_r = c/V_{2,is}$). 123

5.1 Snapshot of the unsteady entropy for 2d (top) and 3d (bottom) simulations of the T106 cascade with incoming sinusoidal perturbations (a), immersed boundary bars as wake generators (b) & (d) and wake-like perturbations at the inlet section (c) & (e). 128

5.2 Iso-surfaces of Q-criterion coloured by the Mach number with the entropy field in the background for the time-inclined simulations of the T106 cascade with immersed boundary bars (a). Iso-surfaces of Q-criterion coloured by the entropy with the static pressure field in the background in the aft of the airfoil (b). 130

5.3 Sketch of the MP and TI computational domains with the location of the upstream immersed bar cascade (green), inflow (red) and exit (blue) measuring stations. 131

5.4 Time-inclined snapshot of the unsteady pressure for the case with immersed bars (the computational domain is extended an additional pitch for clarity). 132

5.5 Phase-locked average of the total pressure for the multi-passage or reference case with inlet perturbations. 132

5.6 Total pressure distributions imposed at the inlet boundary for the multi-passage and time-inclined simulations. 133

5.7 General view of the mesh for the case with inlet perturbations. 133

5.8 Mesh detail of the trailing edge region with 6^{th}order elements (in red) and interior points (in black). 134

5.9 Radially and time-averaged isentropic Mach number distribution along the blade surface for the cases with immersed bars (a) and inlet perturbations (b) 135

5.10 Axial evolution of the pitch-wise and time-averaged inflow angle (in red) and total pressure (in blue) for the cases with immersed bars (a) and inlet perturbations (b) 136

5.11 Radially and time-averaged skin friction coefficient along the blade surface for the cases with immersed bars (a) and inlet perturbations (b) 137

5.12 Evolution of the turbulence intensity upstream of the T106 cascade in the cases with immersed bars (a) and with inlet perturbations (b). 138

5.13 Comparison between the multi-passage and time-inclined velocity perturbations spectra for the immersed bar (a) and inlet perturbations (b) cases. . 139

5.14 Distribution of the flow angle at the exit station for the cases with immersed bars (a) and inlet perturbations (b) referenced to the averaged exit angle of the respective MP simulation 141

5.15 Axial evolution of the pitch-wise and time-averaged total pressure distributions for the cases with immersed bars (top) and inlet perturbations (bottom) 142

5.16 Distribution of $-\overline{u'v'}$ at the exit station for the cases with immersed bars (a) and inlet perturbations (b) 143

5.17 Axial evolution of the cascade losses ω for the cases with immersed bars (a) and inlet perturbations (b). 144

5.18 Modulus of the first harmonic of the unsteady pressure for the cases with the immersed bars cascade. Multi-passage (a), time-inclined (b) and approximate pitch ratio (c) simulations. 145

5.19 First, (a) and (b), and second, (c) and (d), harmonic of the unsteady pressure along the blade surface for the case with immersed bars (top) and with inlet perturbations (bottom). 146

5.20 Snapshot of the swirl angle, α_s, for the time-inclined case with immersed bars, and location of the measuring stations in the boundary layer. 148

5.21 Time-averaged velocity modulus profiles (top) and RMS of the velocity fluctuations profiles (bottom) at different stations of the boundary layer for the case with immersed bars. 149

5.22 Time-averaged velocity modulus profiles (top) and RMS of the velocity fluctuations profiles (bottom) at different stations of the boundary layer for the case with inlet perturbations. 150

5.23 Profiles of the modulus of the 1^{st} harmonic of the velocity parallel to the wall at different stations of the boundary layer for the case with immersed bars (top) and with inlet perturbations (bottom). 152

6.1 Initial condition of the Taylor-Green Vortex problem: Mach number field (a) and z-component of the vorticity (b). 156
6.2 Evolution of the total kinetic energy (a) and enstrophy (b) for the baseline and time-inclined simulations of the TGV. 157
6.3 Vorticity modulus field in the baseline (left) and time-inclined (right) TGV simulations after 40 characteristic times. 159
6.4 Schematic of the turbulent channel computational domain. 160
6.5 Snapshot of the Mach number field for a turbulent channel cases with $Re_\tau = 180$ (top) and $Re_\tau = 870$ (bottom). 160
6.6 Time- and span-wise averaged velocity profile in wall units for the $Re_\tau = 180$ case. Comparison between the baseline and wall-normal time-inclined simulations and DNS in [140]. 162
6.7 Profiles of the root-mean-squared velocity fluctuations in wall units for the $Re_\tau = 180$ case. Comparison between the baseline and wall-normal time-inclined simulations and DNS in [140]. 163
6.8 Comparisons of the averaged velocity profiles for the $Re_\tau = 180$ case between the baseline and time-inclined simulations. Results for the x-inclined time-inclined simulation (a) and for the z-inclined time-inclined simulation. 164
6.9 Comparisons of the profiles of velocity fluctuations for the $Re_\tau = 180$ case between the baseline and x-inclined time-inclined simulations. 165
6.10 Comparisons of the profiles of velocity fluctuations for the $Re_\tau = 180$ case between the baseline and z-inclined time-inclined simulations. 166
6.11 Time- and span-wise averaged velocity profile in wall units for the $Re_\tau = 870$ case. Comparison between the baseline and time-inclined simulations and DNS in [146] for a turbulent channel with $Re_\tau = 950$. 167
6.12 Profiles of the root-mean-squared velocity fluctuations in wall units for the $Re_\tau = 870$ case. Comparison between the baseline and time-inclined simulations and DNS in [146] for a turbulent channel with $Re_\tau = 950$. . . . 168

List of Tables

4.1 Main parameters of the 2D T106 cascades 114

5.1 Main parameters of the simulations. 131
5.2 Number of nodes in the computational domains, in millions. 134

6.1 Mesh details for the turbulent channel flow simulations. 161

Nomenclature

Abbreviations

BC	Boundary Conditions
BL	Boundary Layer
CFD	Computational Fluid Dynamics
CFL	Courant–Friedrichs–Lewy
CPR	Collocation Procedure via Reconstruction
DES	Detached Eddy Simulation
DG	Discontinuous Galerkin
DNS	Direct Numerical Simulation
DOF	Degrees Of Freedom
FR	Flux Reconstruction
GPU	Graphics Processing Unit
HO	High–Order
HPC	High Performance Computing
HPT	High–Pressure Turbine
ILES	Implicit Large Eddy Simulation
KH	Kelvin–Helmholtz
LCP	Lifting Collocation Penalty
LE	Leading Edge

LES	Large Eddy Simulation
LODI	Locally One–Dimensional Inviscid
LPT	Low–Pressure Turbine
MP	Multi–Passage
NGV	Nozzle Guide Vane
OGV	Outlet Guide Vane
PTA	Profile Transformation Approach
RANS	Reynolds–Averaged Navier-Stokes
RDT	Rapid Distortion Theory
RK	Runge–Kutta
RMS	Root Mean Square
SBLI	Shock Boundary Layer Interaction
SD	Spectral Difference
SGS	SubGrid–Scale
SP	Solution Points; Single Passage
SRS	Scale–Resolving Simulations
TE	Trailing Edge
TGV	Taylor–Green Vortex
TI	Time–Inclined
TRL	Technology Readiness Level
TS	Tollmien–Schlichting; Tyler-Sofrin
UHBR	Ultra–High By–pass Ratio
URANS	Unsteady Reynolds–Averaged Navier–Stokes
ZDES	Zonal–Detached Large Eddy Simulation

Greek Symbols

α	Flow Angle
δ	Boundary Layer Thickness
ϵ	Standard Element Computational Coordinate
γ	Correction Flux
κ	Thermal Conductivity
λ	Inclination Parameter
μ	Dynamic Viscosity
Ω	Rotor Angular Velocity; Element Volume;
ω	Angular Frequency; Cascade Losses;
Φ	Flow Coefficient
ρ	Density
σ	Stress Tensor Components
τ	Inclined Time; Shear Stress

Roman Symbols

ΔT	Time Lag
Δt	Time-Step Size
a	Speed of Sound
c	Airfoil Chord
c_f	Friction Coefficient
c_x	Airfoil Axial Chord
f	Frequency; Blade-Passing Frequency
F_{red}	Reduced Frequency
L	Lagrange Polynomial

M	Mach Number
P	Blade Pitch
p	Static Pressure
Re	Reynolds Number
St	Strouhal Number
T	Temperature; Period
t	Time
V	Velocity Modulus; Rotor Velocity
x, y, z	Cartesian Coordinates
$\mathbf{F}, \mathbf{G}, \mathbf{H}$	Viscous Fluxes in the x, y and z direction
$\mathbf{f}, \mathbf{g}, \mathbf{h}$	Convective fluxes in the x, y and z direction
$\mathbf{Q}$	Inclined Variables
$\mathbf{S}$	Source Term
$\mathbf{U}$	Vector of Conservative Variables

Sub- and Super-scripts

$\bar{\square}$	Time-Averaged
$\square_1$	Inflow Measuring Station
$\square_2$	Exit Measuring Station
$\square_i s$	Isentropic
$\square_r$	Rotor
$\square_s$	Stator
$\square_t$	Total or Stagnation Conditions
$\square_{\text{rms}}$	Root Mean Square Value
$\square^C$	Continuous

$\square^D$	Disontinuous
$\square^I$	Interface
$\square'$	Inclined Coordinate

1 Introduction

Contents

1.1 Background and Motivation **2**

1.2 Objectives and Outline **27**

1.3 Original Contributions **30**

As the title suggests, the premise of the present thesis is the necessity to carry out very accurate numerical simulations of turbomachinery stages. For such virtual experiments, the computational cost of simulating the whole annular domain is enormous and, therefore, the simulations are carried out in smaller annular sections or single passages of linear cascades. Dissimilar blade counts in the rotor and stator rows prevent the application of periodicity conditions in the boundaries of the sector or passage. Then, the common practice is to alter the geometry to fit into the reduced domain. However, such a strategy to circumvent the problem of retaining the exact blade counts with low computational costs defeats the holistic and model-free nature of very high-fidelity simulations.

The physical phenomena that take place in turbomachinery flow is very complex, it may justify the use of very accurate numerical experiments. Such phenomena are briefly described after a providing some background on the topic.

The numerical schemes and modelling approaches for Scale-Resolving Simulations (SRS) are broadly discussed next, since Chapter 2 provides a detailed description of the numerical solver used to carry out this work. In short, High-Order (HO) numerical schemes are typically used for SRS, which aim to resolve most–if not all–of the scales of the turbulent flows in turbomachinery.

Afterwards, a literature review of relevant high-fidelity simulations featuring the aforementioned numerical schemes and physical phenomena is presented. The objective is to provide a background for the state-of-the-art Low-Pressure Turbine (LPT) aerodynamic performance prediction and a brief assessment of scale-resolving simulations for aeroacoustics.

To complete the background and state-of-the-art exposition, the most common methodologies used to deal with dissimilar blade counts in less physically accurate simulations are

described, which puts into context the rationale behind the choice of the method used in this thesis.

Lastly, a list of original contributions follows the description of the objectives and the outline of this thesis, concluding the chapter.

1.1 Background and Motivation

In the aerospace industry, one of the main figures of merit in most –if not all– of engineering designs is weight. This, of course, is also the case for aero-engines, where a great effort is put into lowering the weight of the components while increasing their performance. The increase in efficiency of engine components is translated into higher sustainability, which is a fundamental goal of the industry and a commitment to protecting the environment. Such targets are reflected in the policies and goals set by international organisations such as the European Commission's Flightpath 2050 [1] or the United States Aviation Climate Plan [2].

The growing urgency for more sustainable aviation has become increasingly present in society in recent years. However, the effort to improve the efficiency of aero-engines has been linked to the development of air transport since its early days. Moreover, most of the components of aircraft engines have efficiencies above ninety percent, which makes improvements harder and harder to achieve.

The international policies towards reducing fuel consumption have driven the industry to adapt to increasing engine bypass ratios. For the Low-Pressure Turbine (LPT) in direct-drive engines, this is translated into a higher power demand to drive larger fans. Turbines can contribute up to a third of the total weight of the engine. To alleviate this, modern LPTs are designed with fewer blade counts which result in the high-lift and ultra-high-lift approaches to turbine blade design.

The increase in lift is achieved through high deceleration zones on the suction side, which, in turn, elevates the risk of encountering large separation bubbles and complex transition mechanisms. Such boundary layer interactions can increase the losses and decrease the overall efficiency of the engine cycle, as well as elevate the risk of unexpected behaviour at off-design conditions. Moreover, the efficiency of the LPT is of great importance due to its impact on the efficiency of the overall engine: a 1% increase in polytropic efficiency may improve fuel consumption close to 1% [3].

To make things worse, the impact on the turbine performance of engineering decisions such as reducing the number of stages, blade counts and axial gap size between rows is challenging to predict. The presence of very complex phenomena characterises turbomachinery

flow. Engineers cannot solely rely on extensive experimental campaigns to assess the viability or aptness of new designs at multiple operating points and conditions, especially in the earliest phases of design. Therefore, the interest in computational tools to obtain insight into the physical phenomena in such complex machines may not come as a surprise. The ever-growing power and affordability of computing hardware have popularised simulations of increasing levels of fidelity to overcome the constraints of experimentation. The accuracy and physical fidelity of the simulations are of paramount importance since they translate into increased reliability in their predictive capabilities at off-design conditions, which can complement the data gathered in experimental campaigns.

Thus, high-fidelity virtual experiments are becoming progressively popular at the industry level [4–11], and have been shown to be able to compete with low Technology Readiness Level (TRL) experiments [4, 5]. Albeit there are some limitations, such as the size of the computational domain, numerical simulations of complex three-dimensional flow are nowadays relatively affordable for moderate Reynolds numbers, which are characteristic of LPTs. For steady circumferentially uniform inflow simulations of a single row of blades, a sector containing one blade may suffice as an adequate computational domain since the geometry allows the imposition of periodicity conditions in the boundaries of the sector.

However, turbine stages are inherently unsteady due to the relative movement of rotors and stators. Moreover, each stage typically consists of different numbers of blades per row, and the rotor/stator pitch ratio is, in most cases, a non-reducible fraction by design. The issue, therefore, is that the periodicity conditions cannot be imposed in a small sector or a single passage in linear cascades. This aggravates the matter of the minimum periodic computational domain size in the virtual experiment containing the rotor and stator.

The common practice for scale-resolving simulations is to simulate an approximation of the actual geometry. This strategy–which typically reduces the computational domain in each row to a single passage–can enable very accurate simulations that would be otherwise unfeasible at the industrial level. However, it is problematic if we bear in mind that the goal of the simulations is to maintain high fidelity and representativeness of the physical phenomena down to the smallest resolved scales, because the largest scales are grossly captured due to the direct alteration of the geometry. Additionally, the rougher the approximation to the actual geometry, the larger the misprediction. Thus, the common practice in current SRS cannot be relied upon for the intended use of such high-fidelity virtual experiments, especially for turbine or compressor stages of arbitrary pitch ratio.

Even though there are methods that deal with this precise challenge, only some of them are suitable for high-fidelity simulations, as will be discussed later. This thesis focuses on one of such methods: the Time-Inclined (TI) method.

The TI method is the principal topic of this thesis (it is presented in detail in Chapter

3) and can allow for accurate simulations of arbitrary blade counts in computational domains of reduced size. However, it is not free of flaws. In fact, the errors intrinsic to the TI methodology for viscous flows had not been investigated in the context of high-fidelity simulations before this work. Hence, no information was available in the literature regarding its suitability. However, the absence of alternative methods that may be conceptually applicable to high-fidelity simulations makes very interesting to answer the question of how accurate the TI method is in comparison with a direct simulation of the sector-periodic domain. Furthermore, there is an apparent lack of data and literature comparing the time-inclined method to the procedure of approximating the pitch ratio to the nearest integer (while also altering the geometry). This thesis intends to answer such questions.

1.1.1 Challenges of LPT Aerodynamic Simulations

The simulation of turbomachinery flows entails numerous difficulties. There are physical phenomena that play important roles in the loss generation of LPTs that need to be captured. Accurate simulations of complex unsteady three-dimensional flows enable greater predictive capabilities and provide insight into the impact of current design trends in LPT performance.

Current trends in turbomachinery show a reduction on the blade counts, which results in the high- and ultra-high-lift blade designs. To counter potential efficiency losses due to high blade loadings, the rotational speeds are increased as well, resulting in stronger blade-to-blade and row-to-row interactions.

Deterministic unsteadiness caused by the relative motion between the rotor and stator rows coexists with the stochastic phenomena of turbulent flow. Reynolds-Averaged Navier-Stokes (RANS) and Unsteady RANS (URANS) methods assume a separation between the slow deterministic scales and the fast turbulent scales (also known as spectral gap). However, the typical turbomachinery rotational speeds result in the overlap of the two spectra, which harms the predictive capabilities of RANS simulations [12].

The large aspect ratios of LPT blades cause the profile losses to be the largest contributor to LPT efficiency loss (even above 60%) [13], since secondary flows occupy a small fraction of the span. Moreover, throughout the operation of LPTs, the Reynolds number may vary from the low hundred thousands or below at high-altitude cruise up to a few hundred thousands at take-off [14]. LPT performance is very sensitive to the so-called Reynolds lapse and can be especially concerning at the lowest Reynolds numbers. Boundary Layer (BL) development, separation, transition and reattachment have an enormous impact on the overall efficiency of the turbine but are sensitive to the Reynolds number and the

unsteady disturbances environment into which the BLs are immersed. Unfortunately, RANS/URANS methodologies are unable to accurately predict such processes due to the challenges in the derivation of a model that can account for all the complexities in this kind of flow, though they can be calibrated for this type of problems [15].

Until recently, engineers relied solely on steady-state simulations for turbomachinery design. Almost every LPT in operation has been design through steady-state simulations [16]. However, such systems are unsteady–most evidently due to the relative motion between the rotor and the stator rows–and that unsteadiness affects integral flow parameters. Hodson et al. [17] described such influence using turbines and compressors as examples, where a time-varying static pressure was found to induce changes in the stagnation enthalpy and stagnation pressure.

Deterministic unsteadiness comes from three sources in LPTs. First, the potential interaction between rotor and stator rows generates unsteady fluctuations due to the rotor and stator rows moving relatively to each other and experiencing the non-uniform fields of the adjacent row in their respective frame of reference. This potential influence is purely inviscid–that is why it is called "potential"– and decays exponentially only for low Mach number low-frequency cut-off interactions. However, the pressure fluctuations due to potential effects become relevant in transonic conditions. Secondly, preceding wakes are convected downstream to interact with the adjacent row. The relative movement between stators and rotors causes the wakes to be "chopped" and can be modelled as negative jets that impinge on the blade surfaces [18]. These negative jets cause fluctuations that distort surface velocity and pressure, affecting the boundary layers and the transition mechanisms at the suction and pressure sides while they are transported through the blade passage. Thirdly, for transonic and supersonic turbines, Shock Boundary Layer Interaction (SBLI) gives rise to complex BL dynamics that alter transition paths and can lead to separation.

Coull and Hodson [19] summarise the fundamental paths by which transition occurs in turbomachinery boundary layers:

- Natural or Tollmien-Schlichting (TS) transition can occur in low free-stream disturbance environments. Two-dimensional linear oscillations (TS waves) in laminar boundary layers take place if the critical momentum Reynolds number is exceeded. The amplitude of the oscillation slowly increases up to a point when span-wise non-linear interactions occur, develop, and grow in size. Eventually, they burst into turbulent spots evolving and merging to form a continuous turbulent boundary layer. However, natural transition is not likely in the high-level disturbance environment found in turbines.
- Bypass transition takes its name from the circumvention of the formation of TS wave processes to generate turbulent spots. In this transition mode, long wavelengths of

free-stream turbulence, filtered by the so-called "shear sheltering" [20], can act as the disturbances that give rise to stream-wise perturbations that further intensify until they break down, forming turbulent spots. The characteristic length at which this phenomenon takes place is also shorter, which promotes an earlier transition of the boundary layer than natural transition.

- Laminar boundary layers that separate may experience rapid transition to turbulence within the separated region. Kelvin-Helmholtz (KH) instabilities contribute to the roll-up of the separated shear layer into coherent vortices. Free-stream turbulence and/or passing wakes can act as secondary instabilities that distort the vortices and initiate a break-down process [6, 19, 21]. The KH instability can also add up to intrinsic instabilities of the boundary layer and produce transition, although both paths can lead to turbulence by themselves. The resulting separated-flow transition mode can originate a separation bubble, since the separated layer can reattach after the transition.

The unsteady environment of LPT flow strongly influences the transition mechanisms in the BL. For example, Coull and Hodson [19] noted how incoming wakes generate structures called "Klebanoff streaks" close to the leading edges that promote an early (bypass) transition onset.

In 1997, a comprehensive study consisting of experimental [22, 23] and numerical [24] analyses were published by Halstead et al. to study unsteady boundary layer development in turbines and compressors. The authors conducted multiple experiments for compressors and turbines at several operation points along steady state and unsteady simulations to describe the boundary layers and assess the capabilities of the state-of-the-art codes available at that time.

The turbulent spots that originate in the BL then propagate and form different regions in the flow field. These turbulent spots intercept laminar regions as they propagate downstream. The laminar-like calmed regions that form after the spot feature elevated shear stress, which makes the boundary layers more resistant to separation. The boundary layers in this region are more stable, which helps to suppress the development of further instabilities.

In LPTs, incoming wakes from preceding rows are convected through the passage, and two different laminar to turbulent boundary layer transition paths arise. The wake-induced path is related to the areas directly influenced as the wake passes, characterised by high disturbance levels contributing to bypass transition processes. The path between wakes is influenced by the lower levels of disturbances, and any of the three previously described mechanisms could be present, although Halstad et al. [23] only documented the presence of bypass and separated-flow transition. Moreover, the calmed region that forms after

turbulent strips in the wake-induced path substantially impacts delaying transition and suppressing instabilities, as previously mentioned. It is also important to note that the paths differ in the position at which the transition to turbulence is achieved. As described in [23], when the Reynolds number decreases, the disturbance environment becomes less able to destabilise the laminar boundary layers, and consequently, the transition onset in the wake-induced path moves further downstream. The calmed regions may prevent separation in the path between wakes, which in turn might generate a transitional boundary layer instead of a fully turbulent one. In any case, as the wakes travel through the passage, the aforementioned mechanisms take place in the different regions of the suction side, generating an intermittent behaviour that needs to be captured by the numerical tools to predict the overall performance of the turbine accurately.

Experimental campaigns can yield crucial information to increase the knowledge about the complex phenomena described so far. However, the demanding environment in a real engine at operating conditions (temperature, pressure, rotational speeds, turbulence level, etc.) makes the experiments very troublesome and expensive, and the quality or amount of information that can be obtained is not always enough to derive conclusions that may result in improvements in engine performance. Such experiments require manufacturing large parts of the engine, if not the whole engine, contributing to their elevated monetary cost and the time it takes to set up and carry out the testing campaigns.

It is clear that RANS analyses fall short when it comes to accurately account for most of the aforementioned phenomena and their intricate interactions [6]. Reynolds numbers in LPTs may allow for high-fidelity simulations, but the cost of SRS is still very high. Nevertheless, such numerical experiments enable researchers and designers to gain understanding of the physics involved in these flows. In addition, high-fidelity simulations produce vast amounts of data that may be used to calibrate in-house turbulence models, which are fed to RANS/URANS and other numerical tools of low turnaround times which are commonly used in the design cycles.

1.1.2 Numerical Methods for High-Fidelity Simulations

Computational Fluid Dynamics Methodologies

Computational power has rapidly increased, and Computational Fluid Dynamics (CFD) has followed along. Faster, larger and more detailed simulations have been made available as information technology, computer science and microelectronics have developed and matured. The relative affordability of hardware has also increased if we bear in mind that household personal computers can perform some of the simulations carried out daily

in the aerodynamic departments of aerospace companies. Consequently, it is understandable that as High-Performance Computing (HPC) capabilities increase and become more affordable, scale-resolving simulations will expand to applications where greater accuracy and fidelity is most needed. Moreover, the availability of efficient scale-resolving simulations will generate a vast amount of data, which can be used to improve the predictive capabilities of lower-order methodologies.

Up to this day, the use of RANS simulations has contributed to an impactful trend of large cost savings by reducing the number of expensive rig and wind tunnel tests, and severely shortening redesign time. However, in recent years, such a trend has plateaued due to the challenges and shortcomings of turbulence modelling in RANS and URANS.

The temporal averaging of the Navier-Stokes equations in RANS modelling removes the requirement of resolving most turbulent time and length scales. The catch, is that the equations require closure for the Reynolds stresses in the time-averaged equations, for which extensive formulations exist. At the other end of the fidelity/complexity spectrum, Direct Numerical Simulations (DNS) aim to resolve the smallest turbulence scales by directly integrating the governing differential equations on fine meshes.

Large Eddy Simulations (LES) only model the effects of the finest scales on the resolved ones, for which a dissipation term is introduced in the governing equations. If the effect of such small scales is included explicitly, the term is called a SubGrid-Scale model (SGS). Otherwise, the simulations are named ILES, which stands for Implicit LES, where dissipation for the under-resolved scales comes from the numerical scheme itself. The latter approach is used for the simulations carried out in the present thesis.

A hybrid approach between the spatial averaging of the finest scales and the space and time-averaging from RANS such as Detached Eddy Simulations (DES) have been lately proposed to exploit the accuracy of LES for the largest scales in the free stream and the cost reduction of RANS in near-wall regions. Nevertheless, these mixed approaches are not free of challenges that limit their application for aerodynamic performance predictions, but can be very effective for other purposes such as broadband noise simulations [25, 26].

Laskowski et al. [27] published a comprehensive study of the future challenges of CFD in turbomachinery, focusing on high-fidelity simulations for aero-thermal analyses. They concluded that low-order models and RANS/URANS will continue to be the workhorse for the design of turbomachinery components. As previously discussed, boundary layers in turbomachinery flow experience intermittent laminar to turbulent transition through different mechanisms. Accurate predictions of the transition points and the unsteady physical phenomena involved are mainly achieved with DNS and, to some extent, with sufficiently resolved LES. A clear benefit from such simulations is the capacity to show the processes that take place, potentially revealing how to tackle specific problems whose

cause would be hidden in standard RANS/URANS simulations. A clear disadvantage is the considerable turnaround time that prevents LES from replacing RANS in design cycles. Such approaches are fast, computationally affordable, and allow for the inclusion of complex geometries. Much literature exists on turbomachinery flow simulations that feature such methods, and virtually all fluid solver suites (either commercial, company's in-house or open source codes) are based on RANS modelling. Nevertheless, the accuracy of such methods is highly dependent on the aptness of the Reynolds stress closures that model turbulent flow to predict its effects on the time-averaged solution. Moreover, URANS simulations struggle when there is no spectral gap, and the large-scale periodic unsteadiness can no longer be captured and must be time-averaged.

Numerical Schemes

Since Chapter 2 is dedicated to describing the numerical scheme used in the CFD solver in the present thesis, what follows only aims to briefly provide the necessary context for the numerical tools used in SRS.

Regarding the numerical schemes used for SRS, high-order methods have gained much popularity. Generally speaking, numerical schemes have different dispersion and diffusion properties depending on the wavelength of the scale being resolved. Such properties rapidly deteriorate in classical second-order methods as the wavelength decreases. To avoid stringent grid size requirements, HO methods use discretisations that have more suitable properties for the same or even less computational cost. These schemes reduce the number of points that are required to resolve each wavelength correctly.

Complex geometries in turbomachinery internal flow justify using compact unstructured meshes. A good example is the Flux Reconstruction (FR) [28] family of schemes. Variants of this scheme are implemented in the baseline solver High-Order Mu^2s^2T, which is used to carry out the simulations in the present thesis.

Such methods are characterised by large amounts of operations per degree of freedom (which grow as polynomial order increases). They mainly require information from the nodes of the element they belong to. This is beneficial for Graphics Processing Unit (GPU) architectures, which excel in the speed at which they carry out operations but generally suffer from memory write/read operations. The baseline solver HO Mu^2s^2T can run on multiple GPUs to leverage this property of FR schemes in GPU architectures.

From a numerical point of view, HO methods and SRS are not free of limitations. For once, the lack of accurate non-linear non-reflecting boundary conditions in SRS can discourage using SRS in certain applications. HO methods suffer from robustness issues and can be outperformed by second-order schemes if the solver has no special considerations for

discontinuities. Mesh generation can also be a source of errors and uncertainties if high-order elements on the surface and internal nodes fail to capture the subject's geometry adequately.

Concerning the motivation of the present work, Laskowski et al. [27] concluded that effort should be focused, among other fronts, on the "development and demonstration of robust high-order unstructured algorithms for scale resolved CFD" as well as on the development of "... boundary conditions for variants of LES to handle non-integral airfoil counts". The TI method has the potential to overcome the latter difficulty, which is what motivates this work.

1.1.3 High-Fidelity Simulations of LPTs

Scale-resolving simulations can be used to improve the understanding of unsteady features involved in the flow through a blade passage of a low-pressure turbine. High-fidelity virtual experiments can provide insight into the complex flow features of turbine rows and stages, which can contribute to enhancements in their design and ultimately increase their aerodynamic performance. Moreover, virtual experiments generate a vast amount of data that can be used to calibrate the turbulence models that are usually fed into design tools. Lower-order steady-state simulations, which still constitute the primary numerical tool in the design process, are highly dependent on the calibration of such models [15] and can therefore benefit from high-fidelity simulations.

Stadtmüller and Fottner [29, 30] performed an extensive test program on a large-scale linear LPT cascade of what constituted by that time highly loaded T106 profiles (though this is not the case for present standards). The data sets were obtained at the Universität der Bundeswehr München in a high-speed cascade wind tunnel with the intention of investigating the influence of wake passing on the development of boundary layers and, consequently, in loss generation. In addition, the results were made available as the authors intended the test to serve as a code validation case. Indeed, such data sets have been used by other authors [6].

Michelassi et al. [6] performed the DNS, LES, and URANS simulations of one of the cases of Stadtmüller [29]. Among the two configurations with available experimental data, they chose the case which featured an integral blade–wake pitch ratio of 2. The decision was made in order to avoid incorporating several blade passages in the computational domain and reduce the computational cost, which would have been much greater for the non-integral blade–wake pitch ratio. The results show that the wake dynamics and the details of the flow patterns in the suction side are partially lost in the URANS case, for which the boundary layer suffers an earlier transition to turbulence than the DNS and LES. Nonetheless, the price for such accuracy is steep, as the number of processors and

computational time required for such fidelity is several orders of magnitude higher than for URANS simulations.

Wu and Durbin [31] also performed DNS of the T106 blade at $Re = 1.48 \times 10^5$ with incoming wakes, and the same case was reproduced by Michelassi et al. [32] with a LES approach. Even though the results showed an overall agreement of both approaches, especially for the pressure side, characterised by the lesser effects of impinging wakes in the laminar boundary layer, the complex mechanisms for transition at the suction side were not fully reproduced by the LES experiment. Thus, the transition point was miscalculated by a non-negligible amount. The study's conclusions suggest that LES might require finer grids at the wall to be able to predict transition physics and turbulent features accurately.

Sandberg et al. [7] also showed the importance of high-fidelity simulations in their unsteady simulations of the T106 blade at $Re = 6 \times 10^4$. The authors showcased their high-performance compressible Navier-Stokes solver with several DNS that could be achieved within a day, arguing that parameter sweeps are becoming affordable to study the non-trivial influence of unsteady effects such as wakes and inlet disturbances and turbulence levels. The tests also revealed the sensitivity of wake loss to turbulence intensity artificially imposed at the inflow, which only matched the experimental data when the inlet disturbance level was exactly replicated, highlighting the necessity of measuring and imposing the precise disturbance characteristics in the experiments and numerical simulations, respectively.

Michelassi et al. [8] carried out multiple DNS of the T106 linear cascade with different combinations of Reynolds number, reduced frequency and background turbulence. The results show losses to be highly affected by various phenomena and are not proportional to the reduced frequency. Wake distortion remains dominant in loss generation when wakes remain discrete. However, in the cases with the highest reduced frequency, the incoming wakes merge, and their influence is similar to that of the highest turbulence level inflow and no moving bars. The size of the separation bubble, which is related to profile loss generation, varies across the parameter sweep. The boundary layers become fully attached for the highest Reynolds number cases with incoming wakes. However, for the lowest Reynolds number cases, the bubble is large when there are no incoming wakes (i.e. no moving bars) but decreases with increasing inflow turbulence level. The behaviour is not monotonous with the increment of the reduced frequency from the bars: at first, the size of the bubble shrinks until the separation is fully suppressed; as the F_{red} increases, wakes are subjected to more mixing and decay before reaching the leading edges of the blades and their stabilising effect decreases as well, resulting in the growth of the separation bubble.

Cui et al. [33] used several high-fidelity LES to investigate different flow phenomena in three separate regions: the suction side, pressure side and endwalls. The subject of their simulations was the T106A linear cascade with passing bars, which was tested at the Whittle Laboratory of the University of Cambridge. The base for the analysis carried out were some of the experiments performed by Opoka et al. [34], which consisted of three different Reynolds numbers of 0.9×10^5, 1.6×10^5 and 2.1×10^5 and two levels of inflow turbulence (0.5% and 4%). The pitch ratio between the bars and the cascade in the experiments was the unity, which allows for periodic boundary conditions to be imposed in a single passage computational domain. There was good agreement with the experimental data in [33], where the authors also present a detailed exposition of the flow features in each of the aforementioned three regions. For the suction side, where a small bubble was only present at low inflow turbulence conditions, they captured the effect of inflow turbulence in the dominant transition mechanism. In the pressure surface, elongated vortices attributed to the Taylor-Görtler instability and/or large straining of the incoming wakes were observed for low inflow turbulence cases. However, higher levels of background turbulence prevented their formation. The importance of accurately predicting the state of the incoming boundary layer on the endwall flow was also shown, although such effects are out of the scope of the background and motivation for this thesis.

Bolinches et al. [4, 5] also performed LES to study Reynolds number effects on LPT performance, comparing the numerical results to experimental data obtained at the Fluid Dynamics Laboratory of the Universidad Politécnica de Madrid. The test subject was a low-speed, high-lift linear cascade designed by ITP Aero. They studied the relationship between the non-dimensional total pressure losses with the Reynolds number, which is not linear due to the change in the predominant loss generation mechanisms at play [4]. For higher Reynolds number operating points, the thin boundary layer approximation holds and allows the prediction of a loss scaling proportionality of $\sim Re^{-1/2}$, as opposed to the lower Reynolds cases where the laminar separation bubble thickness has a size comparable to that of the profile thickness. The losses are then inversely proportional to the Reynolds number, and the physical phenomena involving bubble dynamics, length and thickness must be properly reproduced to achieve an accurate loss prediction. In addition to the numerical investigation, the results were compared to experimental data, even including the Root Mean Squared values of the fluctuations, showing a good agreement in the prediction not only of integral quantities but also of the turbulence details. Moreover, the trend of the losses with varying Reynolds numbers was also well captured.

The phenomena by which losses increase as the Reynolds number decreases is known as Reynolds lapse and was also investigated by means of RANS in [35] for highly loaded low-pressure turbine airfoils. Lyall et al. encountered inaccuracies attributed to the

transition model in their Reynolds lapse study for aft-loaded profiles, which also highlights the relevance of high-fidelity simulations due to the difficulty of predicting losses at low Reynolds numbers in LPTs.

Bolinches et al. [5] extended their analysis in [4] to the effects of incoming wakes from upstream moving bars. The authors compared the experimental data to LES of the linear cascade at $Re \times 10^{-3} = [50, 100, 200]$ and $F_{red} = [0.5, 1]$. For the purpose of providing background to the present thesis, it is worth noting that the actual ratio of the bar pitch to the cascade pitch was not exactly reproduced in the simulations. The experimental setup produced a pitch ratio of 1.07, which would have required a computational domain immensely large. Such size would have been translated into an unfeasible task due to the disproportionate cost of the simulations. The computational domain was limited to a single passage, and therefore, the bar pitch and speed was adjusted so that the pitch ratio was unity and the reduced frequency matched that of the experiments. The flow parameter was also inevitably altered, but the results agreed well, within the experimental measurement uncertainty, with the actual tests. In their work, the authors found that losses increased with the reduced frequency. However, it was found that for the lowest Reynolds number case the presence of wakes reduced the size of the laminar separation bubble as compared to the steady inflow test. Such an effect contributed to a decrease in momentum loss and therefore, overall loss generation. As the F_{red} increased, so did the number of wakes –which remained fairly discrete– present in the passage conducting to higher passage losses. Moreover, the boundary layers were subjected to earlier separation and transition which also gave rise to higher profile losses due to more extensive turbulent boundary layers.

Most of the studies mentioned above are focused on the impact of the reduced frequency, but the flow coefficient, Φ, is also a key parameter in the design of LPTs and has a non-trivial effect on losses. Michelassi et al. [9] investigated the combined effect of the flow coefficient and the reduced frequency, carrying out high-fidelity simulations of a LPT linear cascade with upstream moving bars. In a linear cascade, the flow coefficient is defined as the ratio between the axial velocity and the bar tangential speed. The pair F_{red} and Φ define the route that wakes follow while travelling through the cascade passages. In their path, wakes suffer from dilation or distortion which contributes to the overall generated losses, and thus, the combined effect of both variables should be accounted for.

In their work, Michelassi et al. [9] chose the T106A [29] as the subject to the incoming wakes from the moving bars. They performed simulations with a computational domain consisting of a single passage of such cascade. The authors noted that the variations of Φ in a real LPT come through changes in the axial flow velocity along the span height since the rotor rotational speed is fixed due to the fan speed requirements. The fluctuation

of the axial velocity involves a change in the turning angle, which, in turn, requires a profile redesign. To avoid contaminating the study of the losses with the influence of different profiles, they decided to carry out the tests maintaining the characteristics of the blade intact and only varying the bar speed and spacing. The inlet flow angle – imposed upstream of the moving bars– also suffered variations to keep the rest of the operating conditions constant. Nevertheless, the influence of such variations on profile losses for the application range in their study was investigated and deemed negligible.

The conclusions of the design space investigation, composed of eight different LES with a unique pair of F_{red} and Φ, were that the loss generation is greatly affected by both variables: for lower flow parameter values, losses were reduced in the pressure side region; for high reduced frequencies and low flow parameters, wake strength decreased as wakes suffered from greater turbulent diffusion until they reached the downstream leading edges. Additionally, wake-to-wake interaction produces higher levels of turbulence upstream of the leading edge and reduces the wake strength at the leading edges. This contrasts with the cases where stronger wakes have more discrete effects and are distorted in the passage, increasing the so-called distortion losses. However, as noted by the authors, increasing the wake-to-wake interaction through higher reduced frequencies and lower flow parameters might involve additional problems outside of the scope of their study such as higher end-wall losses and larger (heavier) blades. Moreover, weaker wakes might harm the stability of the boundary layer, making it more susceptible to the effects of adverse pressure gradients and, consequently, increasing profile losses. This study showcases the importance of high-fidelity methods that can accurately account for wake interaction and decay, which is a weak point for lower-order methods.

The conclusions of the work of Pichler et al. [10] on the influence of axial gap size on losses align with the results of [9], where combinations of F_{red} and Φ that produced strong discrete wakes that entered the blade passage significantly contributed to loss generation due to the so-called wake distortion losses. Pichler et al. found that doubling the axial gap size had no effect on rotor profile losses, even when the weaker wakes had a lesser effect on reducing the suction side separation. The conclusion is, then, that if the suction side separation is small and closed, the benefit of discrete wakes to keep the boundary layer more attached is negligible regarding profile loss reduction. In contrast, the smaller gap size produced stronger wakes at the leading edges that did not merge with the suction side boundary layer for their case. Therefore, the wakes are distorted as they travel through the passage, increasing the production of turbulent kinetic energy on its path. The authors introduced the concept of "wake maturity" as the difference between the mixed-out losses and the mass-averaged losses along the axial distance from the upstream trailing edge to the downstream leading edge. As previously stated, the

profile losses remained unchanged for the tested axial gap sizes; they found a correlation between the wake maturity and the blade mixed-out losses, which agrees with the concept of an increase of the distortion losses due to the less mixed-out wakes reaching the leading edge in the small gap configuration.

Hammer et al. [36] performed several LES of the T106A linear cascade with incoming wakes generated by passing bars. Their work focused on the influence of inaccurate incoming wake modelling by moving bars on the loss mechanisms of the cascade. After their experimental work, Halstead et al. [23] concluded that wakes with higher TKE were related to extensive and strong calmed regions, eliminating the tendency for flow separation and delaying transition onset. Thus, Hammer et al. [36] were concerned with the representativeness of the wakes generated by upstream bars in terms of intensity and width. To study such an effect, they conducted three different tests comparing the influence in loss generation of wakes generated from non-rotating, clockwise and counter-clockwise rotating bars. The rotation of the bars generates lift owing to the Magnus effect, which is sought after to generate a wake that better resembles one coming from an airfoil in the preceding row. The counter-clockwise rotating bars, which would better approximate the actual incoming inflow, generated significantly weaker wakes, leading to lower maximum and overall losses despite of a larger and longer-lasting separation bubble, which was almost completely suppressed for the clockwise rotating case.

So far, it is clear that the unsteady flow in LPTs and its impact on loss generation is very intricate and difficult to predict. Several studies featuring high-fidelity simulations of high-lift LPT blades have been reviewed to emphasise the benefit and utility of such virtual experiments but also to allude to the uncertainties still prevalent in LPT flow simulations. Undoubtedly, SRS are essential to understand and to account for the involved mechanisms that drive loss generation and can complement experimental campaigns. Nonetheless, the preceding review also exhibits some limitations, most of which are driven by computational cost considerations.

Although this thesis is not focused on scale-resolving simulations in aeroacoustics, they are starting to gain popularity. In contrast with SRS for aerodynamic performance prediction, high-fidelity aeroacoustic analyses require capturing the propagation of small scales throughout the whole computational domain. Consequently, grid requirements become more stringent and add to any aerodynamics-oriented SRS's already high computational cost. To make things worse, the flows of interest feature higher Reynolds numbers. As one may expect from the previous review, high-fidelity rotor-stator simulations are often performed approximating the real geometry to enable the imposition of periodic boundary conditions in a single passage. Although the impact of retaining the exact blade count in broadband noise prediction might not be large, it clearly affects tonal noise prediction and

contradicts the idea behind performing such expensive and detailed simulations. The TI method can provide an accurate tonal spectrum which may justify its use for aeroacoustic SRS.

1.1.4 Scale-Resolving Simulations in Aeroacoustics

In recent years, scale-resolving simulations have also increased in popularity for fan and jet noise noise prediction. Similarly to the aerodynamic studies reviewed so far, the application of high-fidelity simulations to aeroacoustics is heavily restricted by the Reynolds numbers pertaining to the flows of interest. The lower Reynolds numbers that can be found in LPTs contribute to the feasibility of SRS but, as previously stated, the computational domains are restricted to a single passage. Even for single stage simulations, if the blade counts are dissimilar the pitch ratio must be approximated, which directly alters the acoustics of the virtual experiment and dissuades from performing SRS for aeroacoustics in the first place.

The literature review conducted so far aims to achieve more accurate predictions of the aerodynamic performance of LPTs with high-lift airfoils, which are representative of the flow characteristics present in current turbomachinery designs. As previously noted, contemporary LPT designs involve fewer stages and fewer blade counts per stage. As described by Hultgren [37], fewer blade counts and the resultant higher blade loadings "produce stronger wakes and potentially increased tone intensities, less stage solidity, which reduces the attenuation of noise from earlier stages" and a reduction on the frequencies of the tones, whose harmonics may fall into more annoying frequency bands. Moreover, designs that entail smaller stage gaps and smaller spacing between the last-stage rotor and turbine-exit struts decrease the decay and mixing of wakes, giving rise to stronger cut-on modes.

Future Ultra-High By-pass Ratio (UHBR) designs will follow such trends for their turbines, for which overall noise contribution is expected to increase. In UHBR, larger fan diameters and shorter and thinner nacelles will contribute to increase the overall noise level from the fan stage [38]. Fan noise sources are, mainly, fan tip leakage flow noise, turbulence interaction noise, and airfoil self-noise (for a broader review, the reader is referred to [39]). At approach conditions–one of the three certification operation conditions along cutback and take-off–turbulent flow originated in the fan wakes interacts with the Outlet Guiding Vane (OGV), resulting in the main contribution to fan broadband noise. Therefore, SRS of fan/OGV geometries are receiving increasing attention and as a consequence, several works aiming at tackling this specific problem have been recently published.

A thorough literature review of broadband noise prediction can be found in [40] and [41], which include relevant applications of scale-resolving simulations in the context of

fan/OGV interaction noise. What follows is intended to show some of the state-of-the-art high-fidelity simulations for broadband noise prediction from fan/OGV interaction. Most of the following costly simulations resort to approximations of the test subject geometry. This is a consequence of the lack of a methodology for retaining the exact blade count in reduced computational domains for SRS, which also motivates the research of the present thesis.

Arroyo et al. [42] performed LES to simulate noise generated by the fan/OGV pressure fluctuations and to assess its relationship with the turbulent wakes impinging in the OGV. As stated by the authors, "a precise description of the state of turbulence reaching the stator vanes leading edge is mandatory, which strongly justified the LES". The number of guide vanes was modified to deal with the dissimilar blade count between rotor and stator and reduce the computational domain. The test subject was the scale-model simplified NASA SDT turbofan at approach conditions, for which experimental data and a RANS simulation were available. The results showed good agreement between the experiments and both simulations (LES and RANS). However, there were apparent differences in the flow features predicted for the leading edges and tips of the rotor blades. Moreover, the vast amount of data obtained through the unsteady high-fidelity simulation allows an improvement of the prediction through lower-order acoustic codes.

The same goal is shared by Polacsek et al. in [26], who also performed acoustic analyses of the ACAT1 fan stage. In their work, they used a hybrid RANS/LES approach to gather data that was later fed to acoustic codes to compare their results with experimental data. The numerical solver, based on a Zonal-Detached Eddy Simulation (ZDES) strategy, was used to perform the simulation on a single-passage computational domain. Since the ratio between the number of blades and vanes was 20/44, and to obtain a smaller periodic sector, the number of vanes was adjusted to 40. The blade solidity in the modified case is kept unaltered by increasing the vane chord. Lewis et al. [43], who performed LES on the same fan stage, followed the same procedure to reduce the computational domain and the associated cost of the simulations. Nevertheless, the results from the ZDES and LES-informed computational aeroacoustic codes are promising.

The impact of periodicity conditions imposed on the azimuthal boundaries of reduced computational domains has not been extensively investigated. Recently, Al-Am et al. [44] compared the full-annulus LES of the ECL5 fan stage with a smaller periodic sector, for which the number of vanes was modified to allow the imposition of boundary conditions in a sector containing a single rotor blade and two vanes. Although techniques such as maintaining solidity can help ensure that the stage performance is similar to the actual geometry, the authors remark that some impact on noise emissions is expected, mostly attributed to rotor-stator interaction noise. They also note that periodicity in the azi-

muthal boundaries imposes a correlation that may contribute to an "over-prediction of the correlation levels, mainly at low to mid frequencies".

The objections to such high-fidelity simulations also include the lack of accurate, non-linear, non-reflecting boundary conditions required to achieve high accuracy for the small perturbations that must be captured in broadband noise prediction. Additionally, the relative movement between rotor and stator meshes requires special attention since spurious noise sources might originate due to numerical errors in the sliding mesh treatment. Nevertheless, high-fidelity simulations can contribute to accurate descriptions of the flow field for which lower-order methods are unsuited.

Al-Am et al. [45] investigated airfoil self-noise conducting LES of the ECL5 fan stage at approach conditions. At this operating point, the flow may separate close to the leading edges of the rotor, leading to the formation of recirculation bubbles that are followed by a transition to turbulence and reattachment of the boundary layer. Albeit for approximate geometries (to allow for azimuthal periodicity to be imposed in smaller sectors), DNS and LES can be used to deal with the description of such complex mechanisms, from which additional noise sources may originate. Al-Am et al. identified high-frequency peaks associated with the recirculating bubble, from which interaction tones with the vanes were also found. An accurate description of the physics in such operating conditions in early design phases might help prevent or mitigate the effects of such noise sources.

Even though the use of scale-resolving simulations for broadband noise prediction might still be deterred by their immense cost in the near future, there have been successful applications for which such an approach was justified. In most studies, computational domains contain the smallest periodic sector available, and when such size is unaffordable, the blade count is modified and the resulting domain is scaled. The resulting smaller periodic sectors can therefore be simulated, but altering the actual geometry of the test subject contradicts the idea behind performing such "model-less", detailed and expensive simulations.

Furthermore, with altered blade counts, tonal noise predictions will be inaccurate by definition, while accurate calculations for that goal can be achieved using other methodologies, such as URANS, that are several orders of magnitude cheaper than SRS. Thus, high-fidelity simulations in aeroacoustics can benefit from retaining the exact blade counts which would enable simulations on smaller computational domains.

1.1.5 Methods for Stator/Rotor Interaction

In turbomachinery, power is either injected or extracted by forcing the flow to turn across rotating rows of airfoils, or rotors, and static rows, or stators. A key feature of the

geometry of such rows is that the airfoil passages that compose them are identical.

Such a pattern is the cause of the predictability of some features of the unsteady flow in a rotor/stator stage. The spatial periodicity of the problem is achieved in the $360^{\underline{o}}$ annulus, but simulations spanning such a large domain entail a computational effort that is, in general, out of reach for most designers seeking short turnaround times.

Thus, so far, turbomachinery blades have been designed by using single-passage steady flow methods. The steep increase in computing power along the past decades has motivated the use of unsteady methodologies, but their benefits may still not offset their higher costs and much slower speeds. Although feasible [46,47], modelling unsteady aerodynamic effects using full-annulus transient simulations is very computationally expensive. This is due to the size of the computational domains but also because of the necessity of simulating long computational times, spanning several engine revolutions, to achieve accurate results. In this context, the requirement for developing efficient methods is called for, and the motivation for the development of domain-reducing methods is underpinned.

Rotor/stator interaction methods aim to reduce the size of the computational domain to a single or few blade passages while retaining an accurate representation of the true transient flow field. A large range of methodologies, such as the time-inclined method, have been developed over the last decades by numerous researchers. To provide context to the present work, some of such methodologies are introduced below, divided into two categories: frequency-domain and time-domain methods. Nevertheless, the interested reader is directed to the extensive review by He [48].

1.1.5.1 Frequency-Domain Methods

Linear Frequency-Domain Method

Linear frequency-domain methods assume that the unsteadiness of the flow is periodic and small compared to the steady-state flow:

$$\begin{cases} \mathbf{U}(\mathbf{x},t) = \overline{\mathbf{U}}(\mathbf{x}) + \mathbf{U}'(\mathbf{x},t) \\ \mathbf{U}'(\mathbf{x},t) << \overline{\mathbf{U}}(\mathbf{x}) \end{cases} \tag{1.1}$$

Under such assumptions, the governing equations can be linearised around the steady state. Therefore, the first step to solve the unsteady solution is to obtain the mean flow from a steady-state simulation.

Since the unsteady part of the solution, i.e. the small perturbations, are assumed to be

periodic, they can be expressed as a sum of Fourier components:

$$\mathbf{U}'(\mathbf{x},t) = \sum_n \mathbf{U}'_n(\mathbf{x}) e^{I\omega_n t} \tag{1.2}$$

Injecting this formulation into the linearised equations allows the removal of the time dependency, and the unsteady perturbations at each frequency can be solved independently.

For flows that do not exhibit highly non-linear phenomena, linear frequency-domain methods can provide accurate solutions in the realm of RANS simulations. A good example, part of the ITP Aero's CFD suite of solvers, is the time-linearised solver $Mu^2s^2T - L$, which has been validated for flutter calculations [49, 50] and for turbine tonal noise prediction [51–53].

A major drawback of these solvers is that non-linear interactions are neglected and the frequencies that compose the unsteady flow must be known beforehand. These limitations are severe if the flow is driven by flow instabilities, of which their fundamental frequencies are part of the solution.

Non-Linear Harmonic Method

Ning and He [54] developed a non-linear frequency-domain methodology, which was based on the linear harmonic method and in which the steady-state part of the solution is instead substituted by the time-averaged solution of the problem. In this approach, non-linearities are intended to be captured by the extra terms that appear in the time-averaged governing equations.

Thus, in the non-linear harmonic method, there are several sets of governing equations that are coupled. The uncoupled steady state simulation in the linear harmonic method is substituted by the time-averaged equations, which feature the aforementioned extra terms that require evaluation through the unsteady part of the solution. Therefore, the linearised equations for each perturbation, which in turn depend on the time-averaged solution, must also be solved. Such coupling require the systems of equations to be integrated simultaneously, which can be achieved by marching both equations in pseudo-time.

In this manner, the non-linear harmonic method is able to retain the non-linear interactions between the mean flow and some perturbations, but still neglects the non-linear interactions between different perturbations.

Harmonic Balance Method

In the harmonic balance approach of Hall [55], the equations are evaluated at $2N + 1$ equally spaced time instants in a whole period of the fundamental harmonic, where N is the number of harmonics that are included in the unsteady part of the solution. Such an approach is followed instead of simply substituting the flow variables by their Fourier approximations in the non-linear governing equations, which would also lead to $2N + 1$ balance equations.

Thus, owing to such evaluations, the non-linear time-domain problem is made time-independent. The $2N + 1$ steady-state problems that stem from such procedure can then be solved, after which the harmonics that compose the solution are obtained from the $2N + 1$ phases. To solve the steady-state problems, the solutions at all the time levels are advanced simultaneously in a pseudo-time marching scheme until convergence is found.

Evidently, the harmonic balance formulation of Hall is based on the assumption of flow periodicity, which is also used to generate the periodic boundary conditions in a single-passage computational domain. For example, the conservation variable ρ is expressed as:

$$\rho(\mathbf{x}, t) = \sum_n R_n(\mathbf{x}) e^{I\omega nt} \tag{1.3}$$

which allows imposing the lagged periodic boundary condition

$$\rho(x, y + P, z, t) = \rho(x, y, z, t + \Delta T) \tag{1.4}$$

where P is the blade pitch and ΔT is the time lag associated with the interblade phase lag. By substitution, and then dividing by $e^{I\omega nt}$, one arrives at:

$$\sum_n R_n(x, y + P, z) = \sum_n R_n(x, y, z) e^{I\omega n\Delta T} \tag{1.5}$$

Another advantage of the harmonic balance method of Hall is that the treatment of the turbulence models is straightforward. Turbulence models can become troublesome in frequency-domain methods, while Hall's harmonic balance avoids the linearisation of the non-linear models, and the turbulence transport equations can be solved as any other fluid transport equation. However, the computational time scales with the number of Fourier terms retained in the solution. Moreover, some potentially important non-linear interactions between different frequencies or perturbations and the time-averaged flow might still be neglected.

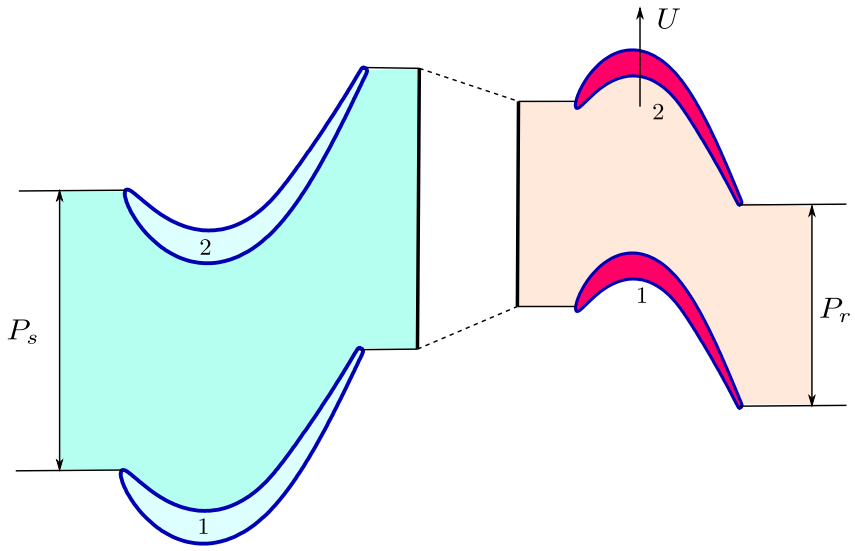

Figure 1.1: Sketch of the interface scaling in the Profile Transformation Approach for a single-passage simulation.

1.1.5.2 Time-Domain Methods

Profile Transformation Approach

The Profile Transformation Approach (PTA) is a fairly simple method in which the flow is scaled at the sliding plane interface between two rows of unequal pitches, as sketched in Fig. 1.1. Such process is performed in order to communicate the computational domains, which can then consist of a single passage per row and in which direct spatial periodicity conditions are imposed.

The PTA is not to be confused with methods involving the scaling of the geometry [56,57]. In such methodologies the geometry of the rows is modified in order to obtain matching computational domains, allowing the imposition of spatial periodicity in the boundaries of the domain, and a "direct" communication of the rows through a conformal sliding plane interface. However, the geometry transformation of the airfoils not only might result time-consuming in a design environment, but also changes the performance of the turbomachine.

The profile transformation approach is an extension of the mixing plane approach [58], and has been implemented in commercial solvers. It has been used in the past in the context of URANS simulations [59,60]. However, the flow homothety of the method modifies not only the blade passing frequency but other aspects of the flow, such as the mean total pressure losses of the incoming flow.

Recently, Gout et al. [61] have assessed this method for scale resolving simulations. The simplicity of the method is very appealing for SRSs, but some of the results are worrisome.

Firstly, the transformation at the sliding plane gives rise to artificial vortical and acoustic waves, which is shown in [61] through the convection of an Euler vortex across several transformed sliding planes.

Secondly, the authors compare the solution from a multi-passage periodic High-Pressure Turbine (HPT) configuration consisting of 2 Nozzle Guide Vanes (NGV) and 5 rotating blades, to the PTA solution computed in a reduced computational domain of a single NGV passage and 2 rotor passages. The authors choose this configuration instead of a single-passage approach for each row in order to reduce the PTA angle ratio, since it is directly related to the errors of the approach. The results, however, show a difference in the computation of exit angles of up to $1.4^{\underline{o}}$.

Phase-Shifted Boundary Conditions Methods

The pioneering work of Erdos et al. [62] firstly addressed rotor/stator interaction problems of arbitrary blade counts in a single passage. To that end, the solution was assumed to be temporally and spatially periodic. They proposed storing the solution at the periodic boundaries of the reduced domain at earlier times. Then, to impose the lagged periodic conditions in one of such boundaries, the appropriate information was retrieved from the stored solution at the opposite boundary. For example, for the upper periodic line ($\square_u$), Erdos et al. retrieved information on the lower periodic line ($\square_l$) at an earlier time, $t - \Delta T$:

$$\mathbf{U}(\mathbf{x} = \mathbf{x}_u, t) = \mathbf{U}(\mathbf{x} = \mathbf{x}_l = \mathbf{x}_u - P, t - \Delta T) \tag{1.6}$$

This approach allowed marching in time the non-linear governing equations in a single-passage domain, but required quite an amount of storage. The Fourier "shape correction" method of He [63] reduced the amount of storage by approximating the temporal variation of the flow variables by discrete Fourier series for both periodic lines.

During the solution process, the Fourier harmonics at both boundaries are obtained and updated after a full period of the disturbance has elapsed. To impose the phase-shifted boundary conditions, the obtained temporal "shapes" at each periodic line are appropriately shifted to correct the flow variables at the opposite periodic line.

Further improvements led to the development of the generalised shape correction method, firstly introduced for vibrating airfoils [64], which allowed including multiple disturbances with unrelated frequencies. One of its key features is that the updating process for the Fourier coefficients does not require long integration periods to carry out such calculations, which stemmed from the necessity that all the unrelated disturbances *beat* in such an integration time. In this method, the updating process is performed for each disturbance by removing the contributions of the rest of the disturbances from the solution, obtaining its harmonic coefficients after a single period of such disturbance.

The shape correction method was extended to reduce the amount of storage and successfully applied to rotor/stator interaction problems [65,66], while Gerolymos et al. [67] combined the spatial and temporal periodicity assumption to derive a similar set of boundary conditions. A few years later, the formulation of the method was extended for multistage analyses [68] and, in spite of being conceived in the $90's$, the method began to gain popularity among commercial solvers [69] not so long ago.

However, the difficult treatment of the temporal signals in a complex spectrum, and the large memory requirements due to the size and resolution of the computational domains, make the use of phase-shifted boundary conditions far from ideal in the context of SRSs. The stringent time-step sizes and high-order discretisations make these matters worse than for URANS, and the use of some degree of data compression might be unavoidable if this approach is to be applied to SRSs.

Moreover, the convergence rate of such a domain-reducing methodology is typically slow and the method itself its not robust. The errors associated to the convergence to a quasi-periodic state usually persist in time owing to their information being stored for several periods in the reconstruction of the boundary conditions.

Techniques such as the dual-passage method may prove very effective to accelerate convergence. However, it doubles the computational cost associated to the size of the computational domain, thereby hindering a strong point of the phase-lagged method: it no longer allows the reduction of an arbitrary blade count problem to a single passage domain.

Block-Spectral Methods

So far, all aforementioned Fourier formulations involved temporal Fourier harmonic modelling for unsteady axisymmetric flows. Nevertheless, spatial Fourier modelling may also be leveraged to reduce computational resources, owing to the the circumferential periodicity of turbomachinery flow.

A truncated spatial Fourier series can be employed to obtain an approximate description of the flow in the full-annulus. The samples involved in such computation, or blocks, are a few blade passages in which the flow equations are simultaneously solved. However, the discretisation of the governing equations entails a dependency on information from neighbouring passages. Since neighbouring passages are not included in the computational domain, the block-spectral method computes the coefficients of the truncated spatial Fourier series and uses them to reconstruct the solution in the neighbouring nodes to the boundaries of the retained passages.

The process is exemplified for a one-dimensional problem in Figure 1.2 from Corral et al. [70], where only three blocks (blocks 1, 3 and 5) are included in the computational domain. It can be observed how the solution of the right-hand side neighbour to the

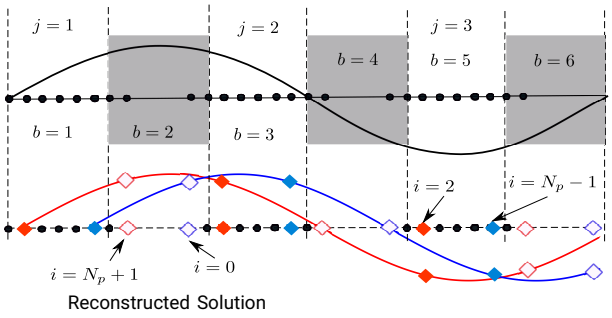

Figure 1.2: Schematic of the block-wise spectral reconstruction of the 1^{st} harmonic in a domain consisting of six blocks. Solid diamonds: Data used to reconstruct the solution on the boundaries. Empty diamonds: Interpolated data outside of the computational domain. Circles: Computational node. Extracted from Corral et al. [70]

boundary node in block 1, denoted as node $i = N_p + 1$ and depicted by a empty red diamond, is obtained from the reconstruction of the first spatial harmonic. Such node could be denoted as node $i = 2$ in their respective block, block 2. Thus, the information needed to compute the harmonic resides in the homologous nodes to node $i = N_p + 1$ of block 1 in the retained blocks, which are nodes $i = 2$ in their respective blocks, and depicted by solid red diamonds in blocks 1, 3 and 5. The process to compute the Fourier coefficients and reconstruct the signal at the opposite boundary is analogous, and drawn in blue.

The use of spatial Fourier methods for the computation of non-linear flows in turbomachinery was first proposed by He [71] in his study of a steady 2D interaction between a fan OGV and a Pylon. Simplified unsteady cases with two-dimensional [71] or axisymmetric [72] configurations undergoing long-wavelength unsteady perturbations were also expanded in spatial Fourier series. A high level of agreement between the spectral method and the full-annulus computation was achieved with significant computational savings. Afterwards, He applied the same idea to film cooling configurations [73], dimples [74], and lined acoustic intakes [75].

Recently, Romera and Corral [76] verified the block-spectral method (which they indistinctively refer to as passage-spectral method) for rotating stall and forced response cases in an isolated fan-stage, comparing the solution to a full-annulus simulation. In addition, Romera and Corral [77] modified the method in order to efficiently deal with a single spatial harmonic, and demonstrated its use in a study of non-linear fan stability under inlet distortion conditions.

Moreover, Corral et al. [70] demonstrated that the block-spectral method is able to accurately capture three different families of spatial harmonics:

- Firstly, M fundamental harmonics with wave-number $k = m \leq M$ are clearly captured, since they are explicitly retained in the formulation through the choice of including $2M + 1$ blocks in the simulation.
- Secondly, the so-called embedded harmonics are also retained, since they are defined by being self-contained in each block. For a block discretised by N_P points in the circumferential direction, $N = (N_P - 1)/2$ embedded harmonics can be captured.
- Finally, $2MN$ scattered harmonics are natively retained in the block-spectral formulation. This is of special importance for the application of the block-spectral method to rotor/stator interaction problems, since turbomachinery configurations exhibit the so-called Tyler–Sofrin modes [78]. These modes are the scattered modes originating from the interaction between rotor blades and stator vanes, and can result in long-wavelength modes. The block-spectral method can natively retain them using the appropriate number of blocks in its formulation.

However, the utility of the method is hindered for SRSs, since the simulation of a common single stage configuration would require a minimum of six passages in the computational domain, whereas a time-domain alternative such as the shape correction method would require four (assuming the use of a dual-passage methodology in both rows to mitigate potential convergence problems). Furthermore, the time-inclined method, which will be described next and may exhibit no degradation of the convergence rate, would only require two. However, due to its inherent limitations, which are thoroughly discussed in Chapter 3, the required amount of passages in the worst-case scenario for a common single stage configuration could amount to five.

The Time-Inclined Method

In 1988, Giles [79] introduced the time-inclined computational planes, stemming from a coordinate transformation from the physical to a computational set of coordinates, $(\mathbf{x}, t) \rightarrow (\mathbf{x}', \tau)$, which enabled the imposition of direct spatial periodicity in a single-passage[1] computational domain

$$\mathbf{U}(x', y', z', \tau) = \mathbf{U}(x', y' + P_r, z', \tau), \tag{1.7}$$

instead of the lagged boundary conditions

$$\mathbf{U}(x, y, z, t) = \mathbf{U}(x, y + P_r, z, t + \Delta T) \tag{1.8}$$

[1] In reality, not every problem can be solved in a single-passage time-inclined computational domain. However, common configurations for turbomachinery stages and operation points can be either reduced to a single or a few passages per row, as thoroughly described in Chapter 3.

The advantage of solving the problem in a reduced computational domain comes at the price of solving the transformed set of governing equations, for which a new set of variables are conserved. Nevertheless, the resulting form of the transformed Euler equations is very convenient, since the formulation of the fluxes remains unchanged. For such inviscid flows, Giles derived simple algebraic relations between the transformed conservation variables and the physical conservation variables. As a result, Giles obtained a very efficient method for inviscid rotor/stator interaction problems. Although the transformation of the Navier-Stokes equations is a bit more troublesome, the TI method has been successfully used in the context of URANS simulations [80–87].

The TI method has been chosen as the subject of the present SRS suitability study. Firstly, it seems a strong candidate for SRSs since it falls under the non-linear time-domain category of methods, while it does not directly impose any temporal periodicity of the flow. Consequently, it does not require to *a priori* know the spectral content of the unsteady flow.

Moreover, the convergence rate of the TI method, although it has not been thoroughly analysed, has been shown to be better than phase-lagged boundary conditions methods [82]. Despite its success for URANS simulations, there is a clear lack of literature surrounding its use for SRS, which also might be related to the absence of studies about its capabilities and limitations. Chapter 3 describes, in detail, the formulation of the time-inclined computational planes for the Euler and Navier-Stokes equations, and includes a novel analysis of the potential sources of error in the most common formulation for viscous flows.

A clear limitation of the TI method is that it is formulated for a pitch ratio. Since rows in multi-stage turbomachines are intentionally designed not to have the same number of blades, the TI method can only be formulated for a single stage, generally speaking. Nevertheless, this limitation has been circumvented for URANS simulations [84, 85, 87], as discussed in Chapter 3. Moreover, multi-stage scale-resolving simulations of arbitrary blade counts might not represent a short term concern at this moment.

1.2 Objectives and Outline

Current trends in the industry advocate for an increase in LES to understand the complexities present in turbomachinery flow. However, the computational cost associated with these kind of virtual experiments is still too large to allow for a simulation of the complete annular geometry of a turbine or compressor row and, evidently, the cost is even higher for a single stage.

For that reason, compromise is found today in the form of simulations of single passages

of linear cascades. However, because pitch ratios are rarely a small integer number, reducing the computational domain to a single passage is generally impossible without some treatment of the periodic boundary conditions or the sliding plane interface. To tackle this problem, existing methodologies rely on the imposition of the flow periodicity. This strategy contradicts the philosophy behind performing LES or quasi-DNS, which is to avoid modelling, at least of the largest scales. Thus, the problem at hand resides in the need for an appropriate methodology to perform virtual experiments of arbitrary pitch ratios in LES and DNS.

Although known for over thirty years, the time-inclined method of Giles [88, 89] has not been extensively applied to tackle the problem of pitch ratio disparity. Proof of this is the small amount of published works using such strategy (in general, but specially true for high-fidelity studies) and the lack of implementations of this method into many industrial fluid flow solvers, with few exceptions [82].

The time-inclined method, contrary to more widespread methods such as the harmonic balance or the shape correction methods, does not directly impose a temporal periodicity, which makes it a good candidate for the solution of the aforementioned problem. Nevertheless, the lack of information regarding the errors that are made while applying time-inclination to the Navier-Stokes equations, even for URANS, may have deterred practitioners and researchers from implementing and employing this method and thus, very little has been published about it in comparison to the aforementioned alternative methods.

The present work aims to assess the suitability of the time-inclined method for retaining the exact blade count in high-fidelity simulations of turbines and compressors. This task can be divided into several objectives of incremental complexity:

- Analyse the transformed Navier-Stokes equations, to investigate the errors that arise from the truncation of some complex diffusive terms, to identify potential sources of inaccuracy in the simulation of turbulent flows. Study the limitations of the TI method that may hinder its application to SRSs.
- Verify the implementation and conduct two-dimensional simulations to compare the directly periodic domain (i.e. multi-passage) solution with the time-inclined and single-passage methodologies. This milestone is set in order to analyse simple and relatively inexpensive test cases and observe the performance of the time-inclined method, which includes the study of the convergence rate to a quasi-periodic solution and the total speed-up factor with respect to the multi-passage solution.
- Evaluate the influence of time-inclination in the resolution of turbulent flow, due to its relevance for LES and DNS.

- Assess the accuracy and performance of the time-inclined method in a three-dimensional problem of industrial interest by comparing the solution of the directly periodic domain to a time-inclined solution, and contrast these results with those obtained through the most common methodology currently used by designers and researchers.

To fulfil the aforementioned objectives, this thesis is organised in the following manner:

Chapter 1 introduced the problem of retaining the exact blade count in high-fidelity turbomachinery simulations. This first chapter describes an overview of the physical phenomena that take place in turbine and compressor flow which justifies the interest in affordable wall-resolved LES and DNS.

Chapter 2 describes the industrial high-order code used for turbomachinery LES and quasi-DNS, which is has been chosen for the implementation of the time-inclined method. The spatial discretizations for the Euler and Navier-Stokes equations are overviewed. Additionally, the formulation of the boundary conditions and detailed information about the implementation of the baseline solver can be found in this chapter.

Chapter 3 presents the time-inclined method for the Euler and Navier-Stokes equations. The advantages and limitations of this method are described. Moreover, a novel theoretical analysis of the errors of the method for viscous simulations is provided.

Chapter 4 has a twofold objective: firstly, verifying the implementation of the time-inclined method into the baseline solver. Since the method is exact for inviscid flow, the goal is to prove that the baseline solver produces identical solutions when calculations of the multi-passage domain and with time-inclined method (in a reduced computational domain) are conducted. The second objective of Chapter 4 is to assess (and confirm) the theoretical analysis carried out in the previous chapter about the errors of time inclination for viscous flow.

Chapter 5 is devoted to assessing the suitability of the time-inclined method for ILES/quasi-DNS of three-dimensional linear cascades of turbines and compressors in an industrial context. The purpose is to compare the current methodology of approximating the pitch ratio to time inclination and to the solution of the directly periodic (multi-passage) domain. The solutions obtained through these methodologies are presented and compared.

Chapter 6 contains a short study of the capabilities of time inclination to solve the turbulent spectrum in ILES accurately. The canonical turbulent channel flow and the transitional Taylor-Green vortex problems are chosen for such objective. These virtual experiments aim to isolate, as much as possible, other potential sources of error that may be present in more complex cases. The goal is to address, in simpler contexts, whether or

not the time-inclined formulation and the truncated inclined equations for viscous flows can accurately reproduce such transitional flows and turbulent boundary layers.

Chapter 7 summarises the work that has been carried out, its main takeaways, and provides recommendations for future works.

1.3 Original Contributions

The main original contributions of this thesis can be summarised as follows:

1. The time-inclined method has been implemented for the first time into a state-of-the-art high-order solver for turbomachinery simulations. Several test cases of academic and industrial relevance have been studied. The simulations have led to interesting results that have been and are in the process of being published, providing literature on the previously non-existent topic of time-inclination in high-fidelity simulations of turbomachinery.
2. The effects of the truncated terms in the inclined Navier-Stokes equations have been studied from a theoretical and a numerical standpoint, which has provided insight into the ability of time-inclined simulations to accurately capture complex flow phenomena and proved the usefulness of this approximation for most flows of interest in turbomachinery.
3. The capabilities and limitations of the time-inclined method for wall-resolved LES and DNS are illustrated for the first time in test cases of academic and industrial relevance. This thesis shows how time-inclination allows for accurate resolution of laminar and turbulent boundary layers, resolving a more accurate spectrum of scales than the single-passage approach and providing better accuracy in the prediction of losses.
4. Comparisons between the directly periodic domain simulation (i.e. following the full-annulus or multi-passage approach), the time-inclined method and single-passage approximations have been performed for a realistic engineering problem. Turbulence-resolving aeroacoustic analyses often use the single-passage approximation strategy, which cannot provide accurate predictions for tonal noise and hinders the holistic approach of SRS. This work demonstrates for the first time (for SRS) that the TI method can provide accurate predictions for the acoustic field since it retains the exact blade count, while also outperforming the single-passage methodology in

aerodynamic analyses. It constitutes an original study of the viability of the time-inclined method for industrial applications where high-fidelity full-annulus simulations are prohibitively expensive and single-passage approaches, although conceptually flawed, are commonly used.

5. The convergence rate of time-inclination in high-order simulations has also been compared for the first time to that of multi-passage approaches, and it was shown no degradation of the convergence time to a quasi-periodic solution while reducing the total computational time and the required resources to perform the simulation. This is important since it constitutes a vital performance metric and is often omitted in publications that introduce or compare new methodologies.

2 Baseline Solver Description

Contents

2.1 Spatial Discretisation **34**

2.2 Flux Splitting **43**

2.3 Boundary Conditions **45**

2.4 The Mortar Method for Non-Conformal Grids **52**

2.5 Temporal Integration **60**

To overcome the limitations of RANS methodologies for accurately capturing complex fluid phenomena in turbomachinery flow, CFD practitioners have turn to LES and DNS. Even though RANS simulations continue to be –and will be in the near future– the standard workhorse of aerodynamic design for turbomachinery, the growth in computational power and its affordability have popularised the use of LES at the industrial level. Generally speaking, LES and DNS reduce or eliminate turbulence modelling but, in turn, the computational cost of the simulations is severely increased with respect to RANS approaches.

In the context of LES and DNS, high-order methods (i.e. those whose solution error is proportional to the mesh size to the power of three or higher) can outperform the standard second-order discretisations widely spread in RANS solvers. The lower dispersion and diffusion properties of high-order spatial discretisations [90, 91] are leveraged to reduce the computational cost of scale-resolving simulations. In turn, lower-order discretisations require more solution points per resolved wave-length, which is a severe disadvantage since we intend to resolve small scales in the rich spectrum of LES and DNS.

Thus, the baseline code into which the time-inclined method has been implemented consists of a high-order Flux Reconstruction (FR) Navier-Stokes solver for unstructured grids. The solver, which is part of ITP Aero's in-house CFD solver suite, Mu^2s^2T, has been thoroughly described, validated, and benchmarked in the past [4, 5, 92–95].

The scope of the present chapter is to provide the numerical setup for the work that is presented in the following chapters, which includes: the spatial discretisation of the

governing equations with a flux-splitting strategy to minimise aliasing errors and increase stability, the explicit temporal integration scheme, the formulation for the Boundary Conditions (BC), and a mortar method to deal with non-conformal meshes at the sliding plane of rotor/stator simulations.

2.1 Spatial Discretisation

As previously mentioned, the spatial discretisation of the governing equations in the baseline solver belongs to the so-called Flux Reconstruction family of schemes. High-order numerical methods of the FR family offer low numerical dissipation and dispersion properties, and thus, they are well-suited for the simulation of vortical structures and turbulent flows. Moreover, the FR approaches are, generally speaking, robust, efficient and simple to implement.

Vincent et al. [96] showed that the formulation of existing high-order linearly stable numerical schemes such as the nodal Discontinuous Galerkin (DG), the Spectral Difference (SD) scheme and the original FR scheme of Huynh, could be recovered from a generalised formulation of the FR method by choosing the appropriate correction functions.

The formulations of the actual implementations of the solver's FR schemes are included below for completeness sake, along with the governing equations for the simulations carried out in this work. In particular, the solver recovers the nodal DG scheme: quadrilateral and hexahedral elements that mesh the computational domain are discretised following Huynh's scheme. Triangular, prismatic, tetrahedral and pyramidal elements are discretised following the Lifting Collocation Penalty (LCP) approach, also referred to as the Collocation Procedure via Reconstruction (CPR), which is also equivalent to the nodal DG formulation [97].

2.1.1 The FR Method for One-Dimensional Conservation Laws

To introduce the FR scheme, let us consider the solution of one-dimensional conservation laws such as

$$\frac{\partial \mathbf{U}}{\partial t} + \frac{\partial \mathbf{f}}{\partial x} = 0 \tag{2.1}$$

The integration domain $x \in \Omega \equiv [0, L]$ is discretized into N_e elements, with the ith element defined by $V_i = [x_i, x_{i+1}]$. For each element i we define $p + 1$ Solution Points (SPs), which constitute the degrees of freedom at which the state vector $\mathbf{U}$ is evaluated.

For each element we define a local coordinate, $\xi = [-1, 1]$, such that the physical coordinate of any solution point, x_j, can be related to its local coordinate, ξ_j, from

$$x_j = x_i + \frac{\triangle x_i}{2} \left(\xi_j + 1\right), \tag{2.2}$$

where $\Delta x_i = x_{i+1} - x_i$. In such a local or computational reference frame, all the elements share the same coordinates for each of their $p+1$ SPs, regardless of their actual physical coordinates. In other words, the jth SPs of element i and of element $i+1$ are represented by the same local coordinate ξ_j, even though $x_j^i = x_i + \frac{\triangle x_i}{2}(\xi_j + 1) \neq x_{i+1} + \frac{\triangle x_{i+1}}{2}(\xi_j + 1) = x_j^{i+1}$. The particular distribution of SPs in the local coordinate system corresponds to the distribution of $p+1$ Gauss-Lobatto points.

The state vector $\mathbf{U}$ within each element can be approximated using a basis of Lagrange polynomials as:

$$\mathbf{U}(\xi, t) \simeq \mathbf{U}_i^h(\xi, t) = \sum_{j=1}^{p+1} \mathbf{U}_{i,j}^h(t) L_j(\xi) \tag{2.3}$$

where $\mathbf{U}_{i,j}^h$ is the approximated solution at SP j of element i, and $L_j(x)$ is the Lagrange polynomial which values 1 at $\xi = \xi_j$, and 0 elsewhere:

$$L_j(\xi) = \prod_{k=1, k\neq j}^{p+1} \frac{\xi - \xi_k}{\xi_j - \xi_k} \tag{2.4}$$

The flux, $\mathbf{f}(\mathbf{U}^h)$, is defined analogously to the solution $\mathbf{U}^h$:

$$\mathbf{f}(\mathbf{U}^h) \simeq \mathbf{f}_i^D(\xi, t) = \sum_{j=1}^{p+1} \mathbf{f}_{i,j}^D(\mathbf{U}_{i,j}^h) L_j(\xi) \tag{2.5}$$

In general, the solution and the fluxes are discontinuous across element interfaces, hence the super-index D in Equation 2.5. However, since we require the scheme to be conservative, the flux must be reconstructed in such a way that the reconstructed flux $\mathbf{f}^C$:

- is of degree $p+1$, where p is the degree of $\mathbf{U}^h$, so that the spatial derivative of the reconstructed flux is of the same polynomial degree as the solution.
- is close to $\mathbf{f}^D$, such that the correction function approximates the function 0, minimising $\left\|\mathbf{f}^C(\xi) - \mathbf{f}^D(\xi)\right\|$.
- takes the value of the interface fluxes at the boundaries of the element.

Therefore, the corrected flux is of the form

$$\mathbf{f}_i^C(\xi) = \mathbf{f}_i^D(\xi) + \gamma_i(\xi) \tag{2.6}$$

and $\gamma_i(\xi)$ is the correction flux function defined as:

$$\gamma_i(\xi) = [\mathbf{f}_L^I - \mathbf{f}^D(\xi = -1)] g_L(\xi) + [\mathbf{f}_R^I - \mathbf{f}^D(\xi = 1)] g_R(\xi) \tag{2.7}$$

where $\mathbf{f}_L^I$ and $\mathbf{f}_R^I$ are the *left* and *right* interface fluxes, corresponding to the SPs at $\xi = -1$ and $\xi = 1$, respectively. Analogously, $g_L(\xi)$ and $g_R(\xi)$are the *left* and *right* correction functions. In order to compute the common fluxes at each side of the interface, $\mathbf{f}_L^I$ and $\mathbf{f}_R^I$, we resort to the approximate Riemann solver of Roe [98].

The correction functions can be chosen to obtain different stability and accuracy properties of the final scheme [28]. Generally speaking, improvements on the accuracy of the scheme lead to a more restrictive Courant–Friedrichs–Lewy (CFL) condition to ensure stability, leading to smaller time-step sizes in the temporal integration of the governing equations.

To recover the nodal-based discontinuous Galerkin formulation, one may choose the left Radau polynomial as the right correction function, $g_R(\xi)$, and the right Radau polynomial as the left correction function, $g_L(\xi)$:

$$\begin{array}{c} g_L(\xi) = \frac{(-1)^p}{2}\left(P_p - P_{p+1}\right) \\ g_R(\xi) = \frac{1}{2}\left(P_p + P_{p+1}\right) \end{array}, \tag{2.8}$$

where P_p is the Legendre polynomial of degree p, which can be obtained, for example, using Rodrigues' formula:

$$P_p(\xi) = \frac{1}{2^p p!}\frac{d^p}{d\xi^p}\left[(\xi^2 - 1)^p\right] \tag{2.9}$$

Finally, a discrete form of Eq. 2.1 can be achieved by obtaining the derivatives of the Lagrange polynomials conforming the discontinuous flux and of the correction functions, which is done in the standard element frames bearing in mind the chain rule:

$$\frac{\partial \mathbf{U}}{\partial t} + \frac{\mathrm{d}\xi}{\mathrm{d}x}\left\{\sum_{j=1}^{p+1}\mathbf{f}(\mathbf{U}_{ij}^h)\frac{\mathrm{d}L_j}{\mathrm{d}\xi}(\xi) + [\mathbf{f}_L^I - \mathbf{f}^D(\xi=-1)]\frac{\mathrm{d}g_L}{\mathrm{d}\xi}(\xi) + [\mathbf{f}_R^I - \mathbf{f}^D(\xi=1)]\frac{\mathrm{d}g_R}{\mathrm{d}\xi}(\xi)\right\} = 0, \tag{2.10}$$

Equation 2.10 can then be advanced in time as described later in the present chapter.

Extension to Multiple Dimensions

The method can be extended to quadrilateral and hexahedral elements, allowing the discretisation of two- and three-dimensional domains via the construction of tensor product bases.

A two-dimensional conservation law

$$\frac{\partial \mathbf{U}}{\partial t} + \nabla \cdot (\mathbf{f}, \mathbf{g}) = \frac{\partial \mathbf{U}}{\partial t} + \frac{\partial \mathbf{f}}{\partial x} + \frac{\partial \mathbf{g}}{\partial y} = 0, \tag{2.11}$$

can be cast in the standard element frame $(\xi, \eta) = [-1, 1] \times [-1, 1]$ as

$$|J|\frac{\partial \mathbf{U}}{\partial t} + \frac{\partial \tilde{\mathbf{f}}(\mathbf{U})}{\partial \xi} + \frac{\partial \tilde{\mathbf{g}}(\mathbf{U})}{\partial \eta} = 0, \tag{2.12}$$

where $|J|$ is the determinant of the Jacobian matrix defining the coordinate transformation $(x, y) \iff (\xi, \eta)$

$$\mathbf{J} = \begin{bmatrix} \frac{\partial x}{\partial \xi} & \frac{\partial x}{\partial \eta} \\ \frac{\partial y}{\partial \xi} & \frac{\partial y}{\partial \eta} \end{bmatrix} \tag{2.13}$$

and the fluxes $\tilde{\mathbf{f}}(\mathbf{U})$ and $\tilde{\mathbf{g}}(\mathbf{U})$ read

$$\begin{aligned} \tilde{\mathbf{f}}(\mathbf{U}) &= |J| \left(\frac{\partial \xi}{\partial x}\mathbf{f} + \frac{\partial \xi}{\partial y}\mathbf{g} \right) \\ \tilde{\mathbf{g}}(\mathbf{U}) &= |J| \left(\frac{\partial \eta}{\partial x}\mathbf{f} + \frac{\partial \eta}{\partial y}\mathbf{g} \right) \end{aligned} \tag{2.14}$$

The solution and discontinuous fluxes take the form

$$\mathbf{U}(\xi, t) \simeq \mathbf{U}_i^h(\xi, \eta, t) = \sum_{j=1}^{p+1} \sum_{k=1}^{p+1} \mathbf{U}_{i,jk}^h(t) L_j(\xi) L_k(\eta) \tag{2.15}$$

and

$$\mathbf{f}(\mathbf{U}^h) \simeq \mathbf{f}_i^D(\xi, \eta, t) = \sum_{j=1}^{p+1} \sum_{k=1}^{p+1} \mathbf{f}_{i,jk}^D(\mathbf{U}_{i,jk}^h) L_j(\xi) L_k(\eta) \tag{2.16}$$

The definition of the correction function is analogous to the one-dimensional case (see Equation 2.7):

$$\begin{aligned} \gamma_i(\xi, \eta) = [\tilde{\mathbf{f}}_L^I - \tilde{\mathbf{f}}^D(\xi = -1, \eta)] g_L(\xi) + [\tilde{\mathbf{f}}_R^I - \tilde{\mathbf{f}}^D(\xi = 1, \eta)] g_R(\xi) + \\ + [\tilde{\mathbf{g}}_D^I - \tilde{\mathbf{g}}^D(\xi, \eta = -1)] g_L(\eta) + [\tilde{\mathbf{g}}_U^I - \tilde{\mathbf{g}}^D(\xi, \eta = 1)] g_R(\eta) \end{aligned}, \tag{2.17}$$

where the subscripts D and U denote "down" and "upper" sides of the standard quadrilateral element, respectively.

Finally, we obtain the governing equations discretised in the standard quadrilateral element:

$$\begin{aligned} |J| \frac{\partial \mathbf{U}}{\partial t} + \sum_{j=0}^{p+1} \sum_{k=0}^{p+1} \tilde{\mathbf{f}}_{jk}^D \frac{dL_j(\xi)}{d\xi} L_k(\eta) + \sum_{m=0}^{p+1} \sum_{n=0}^{p+1} \tilde{\mathbf{g}}_{jk}^D L_j(\xi) \frac{dL_k(\eta)}{d\eta} + \\ + [\tilde{\mathbf{f}}_L^I - \tilde{\mathbf{f}}^D(\xi = -1, \eta)] \frac{\mathrm{d}g_L}{\mathrm{d}\xi}(\xi) + [\tilde{\mathbf{f}}_R^I - \tilde{\mathbf{f}}^D(\xi = 1, \eta)] \frac{\mathrm{d}g_R}{\mathrm{d}\xi}(\xi) + \\ + [\tilde{\mathbf{g}}_D^I - \tilde{\mathbf{g}}^D(\xi, \eta = -1)] \frac{\mathrm{d}g_L}{\mathrm{d}\eta}(\eta) + [\tilde{\mathbf{g}}_U^I - \tilde{\mathbf{g}}^D(\xi, \eta = 1)] \frac{\mathrm{d}g_R}{\mathrm{d}\eta}(\eta) = 0 \end{aligned} \tag{2.18}$$

2.1.2 The Lifting Collocation Penalty Method

The lifting collocation penalty method, which is also referred to as the correction procedure via reconstruction, is a scheme originally proposed by Wang and Gao [97] to extend the FR approach for triangular, prismatic and tetrahedral elements. The LCP scheme, as part of the FR family, can be obtained from the FR formulation by selecting the appropriate correction functions.

Let us assume we are discretising a two-dimensional domain into N_e non-overlapping triangular elements. A scalar hyperbolic conservation law

$$\frac{\partial U}{\partial t} + \nabla \cdot \mathbf{F}(U) = 0, \tag{2.19}$$

where $\mathbf{F} = \begin{bmatrix} F^x & F^y \end{bmatrix}^T$ is the flux vector, can be cast in a weighted residual form on each element V_i as

$$\int_{V_i} \left(\frac{\partial U}{\partial t} + \nabla \cdot \mathbf{F} \right) W dV = \int_{V_i} \frac{\partial U}{\partial t} W dV + \int_{\partial V_i} W \mathbf{F} \cdot \mathbf{n} dS - \int_{V_i} \nabla W \cdot \mathbf{F} dV = 0 \tag{2.20}$$

The solution in each triangular element is approximated by a Lagrange basis of polynomials of degree p on N_p solution points:

$$U_i \simeq U_i^h = \sum_{j=1}^{N_p} U_{i,j}^h(t) L_j(\mathbf{x}_{i,j}) \tag{2.21}$$

Using such approximation, the continuity of the solution between elements is not enforced. Therefore, a common approximate Riemann flux, $\widetilde{F}^n(U_i^h, U_{i+}^h, \mathbf{n})$, is used as the normal flux across the element interfaces in the second term of the right-hand side of Eq. 2.20:

$$\int_{\partial V_i} W \mathbf{F} \cdot \mathbf{n} dS = \int_{\partial V_i} W \widetilde{F}^n(U_i^h, U_{i+}^h, \mathbf{n}) dS, \tag{2.22}$$

where U_{i+}^h refers to the approximate solution in the neighbouring element at the interface ∂V_i of element i.

The third term of the right-hand side of Eq. 2.20 can be integrated by parts, leading to:

$$-\int_{V_i} \nabla W \cdot \mathbf{F} dV = \int_{V_i} W \nabla \cdot \mathbf{F} dV - \int_{\partial V_i} W F^n(U_i^h) dS, \tag{2.23}$$

where $F^n(U_i^h)$ is the normal component of the fluxes computed within element i at the boundary ∂V_i.

Then, Equation 2.20 reads, for each triangular element i:

$$\int_{V_i} \frac{\partial U_i^h}{\partial t} W dV + \int_{V_i} W \nabla \cdot \mathbf{F} dV + \int_{\partial V_i} W \left[\widetilde{F}^n(U_i^h, U_{i+}^h, \mathbf{n}) - F^n(U_i^h) \right] dS = 0 \tag{2.24}$$

In the LCP approach, the third term in Equation 2.24 is viewed as the penalty term, since it penalises the differences between the Riemann flux and the discontinuous normal flux.

Such term is replaced by a correction field δ_i by means of a so-called 'lifting operator':

$$\int_{V_i} W\delta_i dV = \int_{\partial V_i} W\left[\widetilde{F}^n(U_i^h, U_{i+}^h, \mathbf{n}) - F^n(U_i^h)\right] dS \tag{2.25}$$

Bearing in mind that the test space is selected such that a unique solution exists for Eq. 2.24, we can reduce the residual formulation into a differential form:

$$\begin{aligned}\int_{V_i} \frac{\partial U_i^h}{\partial t} W dV + \int_{V_i} W\nabla\cdot\mathbf{F} dV + \int_{V_i} W\delta_i dV = \int_{V_i}\left[\frac{\partial U_i^h}{\partial t} + \nabla\cdot\mathbf{F} + \delta_i\right] W dV = \\ = \frac{\partial U_i^h}{\partial t} + \nabla\cdot\mathbf{F} + \delta_i = 0\end{aligned} \tag{2.26}$$

The correction field can also be described with the same polynomial basis of the solution U, since it must belong to the space of polynomials of degree p or less. Therefore,

$$\delta_i = \sum_{j=1}^{N_p} \delta_{i,j} L_j(\mathbf{x}_{i,j}) \tag{2.27}$$

where $\delta_{i,j}$ is the evaluation of the correction field at the solution point j of element i.

Finally, the formulation for the solution point j of element i reads:

$$\frac{\partial U_{i,j}^h}{\partial t} + \nabla\cdot\mathbf{F}(U_{i,j}^h) + \delta_{i,j} = 0 \tag{2.28}$$

To recover the DG scheme, the weighting function W, which must belong to the space of polynomials of degree p or less, is set to belong to the Lagrange polynomial basis that approximates the solution U_i. Then, if we also introduce the definition of the correction field in Eq. 2.27 into Eq. 2.25, we can obtain a system of equations that allows us to determine $\delta_{i,j}$:

$$\int_{V_i} L_k \sum_{j=1}^{N_p} \delta_{i,j} L_j dV = \int_{\partial V_i} L_k \left[\widetilde{F}\right]_{i,j} dS \qquad k = 1, ..., p+1 \tag{2.29}$$

The right-hand side of Equation 2.29 can also be expressed in terms of the normal flux differences in each of the solution points l at the faces f of the element. Thus, the integral over the boundary of element V_i reads:

$$\int_{\partial V_i} L_k \left[\widetilde{F}\right]_{i,j} dS = \sum_{f\in\delta V_i} \int_f L_k \sum_{l}^{p+1} L_l \left[\widetilde{F}\right]_{f,l} dS \tag{2.30}$$

and we can re-cast the system of equations that leads to $\delta_{i,j}$ as:

$$\int_{V_i} L_k \sum_{j=1}^{N_p} \delta_{i,j} L_j dV = \sum_{f \in \delta V_i} \int_f L_k \sum_{l}^{p+1} L_l \left[\widetilde{F}\right]_{f,l} dS \qquad k = 1, ..., p+1 \tag{2.31}$$

At this point, it is worth noting that the governing equations are solved in a computational reference frame for each element, as described for the FR scheme in Section 2.1.1. In such a computational frame, any 'physical' triangle in the mesh is transformed into the standard (straight-faced) right triangle. Therefore, $\delta_{i,j}$ can be computed in terms of the normal flux jumps at the element faces and in terms of **constant lifting coefficients**, $\alpha_{j,f,l}$, which only need to be pre-computed once, since they are independent of the geometry and solution:

$$\delta_{i,j} = \frac{1}{|V_i|} \sum_{f \in \delta V_i} \sum_{l}^{p+1} \alpha_{j,f,l} \left[\widetilde{F}\right]_{f,l} S_f \tag{2.32}$$

To conclude, we obtain the hyperbolic conservation law for a solution point j of element i in the LCP formulation:

$$\frac{\partial U^{\xi}_{i,j}}{\partial t} + \nabla^{\xi} \cdot \mathbf{F}^{\xi}(U^{\xi}_{i,j}) + \frac{1}{\left|V^{\xi}_i\right|} \sum_{f \in \delta V_i} \sum_{l}^{p+1} \alpha_{j,f,l} \left[\widetilde{F}\right]^{\xi}_{f,l} S^{\xi}_f = 0, \tag{2.33}$$

where

$$\begin{aligned} U^{\xi}_{i,j} &= |J|\, U^{h}_{i,j} \\ \nabla^{\xi} &= \left(\tfrac{\partial}{\partial \xi}, \tfrac{\partial}{\partial \eta}\right) \\ \mathbf{F}^{\xi}(U^{\xi}_{i,j}) &= (F_{\xi}, F_{\eta}) \\ F^{\xi} &= |J|\, (\xi_x F^x + \xi_y F^y) \\ F^{\eta} &= |J|\, (\eta_x F^x + \eta_y F^y) \end{aligned} \tag{2.34}$$

and J is the Jacobian of the transformation from the triangular element in the mesh to the standard computational element. The distribution of solution points within the standard computational triangle corresponds to that of Warburton [99].

The LCP procedure is also followed for tetrahedra and pyramids, where the SPs distributions in the local coordinate system correspond to those of Hesthaven and Warburton [100] and Chan and Warburton [101], respectively.

2.1.3 The Navier-Stokes Equations

The Navier-Stokes equations can be written in conservative form as:

$$\frac{\partial \mathbf{U}}{\partial t} + \frac{\partial \mathbf{f}}{\partial x} + \frac{\partial \mathbf{g}}{\partial y} + \frac{\partial \mathbf{h}}{\partial z} = \frac{\partial \mathbf{F}}{\partial x} + \frac{\partial \mathbf{G}}{\partial y} + \frac{\partial \mathbf{H}}{\partial z} + \mathbf{S}, \tag{2.35}$$

where $\mathbf{U} = \begin{bmatrix} \rho & \rho u & \rho v & \rho w & \rho E \end{bmatrix}^T$ is the vector of conservative variables,

$$[\mathbf{f} \quad \mathbf{g} \quad \mathbf{h}] = \begin{bmatrix} \rho u & \rho v & \rho w \\ \rho u^2 + p & \rho uv & \rho uw \\ \rho uv & \rho v^2 + p & \rho vw \\ \rho uw & \rho vw & \rho w^2 + p \\ u\left(\rho E + p\right) & v\left(\rho E + p\right) & w\left(\rho E + p\right) \end{bmatrix}, \tag{2.36}$$

are the inviscid fluxes, S is a source term, and the viscous fluxes $[\mathbf{F} \quad \mathbf{G} \quad \mathbf{H}]$ are:

$$\begin{aligned} \mathbf{F} &= [0 \quad \sigma_{xx} \quad \sigma_{yx} \quad \sigma_{zx} \quad \sigma_{xx}u + \sigma_{xy}v + \sigma_{xz}w - q_x]^T \\ \mathbf{G} &= [0 \quad \sigma_{xy} \quad \sigma_{yy} \quad \sigma_{zy} \quad \sigma_{yx}u + \sigma_{yy}v + \sigma_{yz}w - q_y]^T \\ \mathbf{H} &= [0 \quad \sigma_{xz} \quad \sigma_{yz} \quad \sigma_{zz} \quad \sigma_{zx}u + \sigma_{zy}v + \sigma_{zz}w - q_z]^T \end{aligned} \tag{2.37}$$

The stress tensor σ is

$$\sigma = \mu(\nabla \mathbf{v} + \nabla \mathbf{v}^T) - \frac{2}{3}\mu \mathbf{I}\, \nabla \cdot \mathbf{v}, \tag{2.38}$$

where $\mathbf{v} = \begin{bmatrix} u & v & w \end{bmatrix}^T$ is the velocity vector, $\mathbf{I}$, the identity matrix, and μ is the dynamic viscosity given by the Sutherland law

$$\mu = \frac{1.458 \cdot 10^{-6} T^{3/2}}{T + 110.4} \tag{2.39}$$

The heat flux vector is given by $\mathbf{q} = \kappa \nabla T$, where $\kappa = \frac{\mu c_p}{Pr}$ is the conductivity and Pr is the Prandtl number (which takes the approximate value of $Pr \approx 0.71$ for air).

The fluid is assumed to behave like a perfect gas. Thus, we can use the state equation $p = \rho R_g T$, where $R_g = c_p - c_v$ is the gas constant and c_v and c_p are the specific heats at constant volume and pressure, respectively. Therefore, we can compute the total specific energy as $E = c_v T + \frac{1}{2}\left(u^2 + v^2 + w^2\right)$, and the pressure p in Eq. 2.36 can be obtained from the conservative variables

$$p = (\gamma - 1)\left[\rho E - \frac{1}{2\rho}\left((\rho u)^2 + (\rho v)^2 + (\rho w)^2\right)\right], \tag{2.40}$$

where $\gamma = \frac{c_p}{c_v}$ is the ratio between specific heats.

The gradient of the primitive variables is required to compute the viscous fluxes, and can be obtained differencing in the local element frame by

$$\frac{\partial \phi}{\partial x_i} = \left(\mathbf{J}^{-1}\right)_{ij} \frac{\partial \phi}{\partial \xi_j}, \tag{2.41}$$

where the coordinates are represented by $x_i = x, y, z$ and $\xi_j = \xi, \eta, \zeta$, and

$$\frac{\partial \phi}{\partial \xi_j} = \frac{1}{|J|}\left(\frac{\partial \left(|J|\,\phi\right)}{\partial \xi_j} - \frac{\partial |J|}{\partial \xi_j}\phi\right) \tag{2.42}$$

The treatment of the viscous terms deserves special attention since they involve second derivatives of their polynomial approximation, (generally) incurring in loss of accuracy. The BR2 formulation of Bassi and Rebay [102] was implemented to overcome this issue.

The procedure involves, as a first step, following the flux correction procedure for the discontinuous solution across element interfaces, $\mathbf{U}^h$ (see Equation 2.6). Analogously to the discontinuous fluxes, the addition of a correction function makes $\mathbf{U}^C$ a polynomial of degree $p+1$.

To obtain the corrected fluxes, we need a common solution for the interface. Since diffusion is not directional, we may define such value as the average solution at each side of the interface. For example, for the *left* side of the interface (L) of a one-dimensional element in the computational reference system:

$$\mathbf{U}_L^I = \frac{\mathbf{U}_i(\xi = -1) + \mathbf{U}_{i-1}(\xi = 1)}{2} \tag{2.43}$$

Then, the derivative of the continuous solution in the local reference frame can be obtained in the same manner as the derivative of the corrected fluxes in Equation 2.10.

$$\frac{d\mathbf{U}_{ij}^h}{dx} = \frac{\mathrm{d}\xi}{\mathrm{d}x}\left\{\sum_{k=1}^{p+1}\mathbf{U}_{ik}^h \frac{\mathrm{d}L_k}{\mathrm{d}\xi}(\xi_j) + [\mathbf{U}_L^I - \mathbf{U}_{i,j=1}^h]\frac{\mathrm{d}g_L}{\mathrm{d}\xi}(\xi_j) + [\mathbf{U}_R^I - \mathbf{U}_{i,j=p+1}^h]\frac{\mathrm{d}g_R}{\mathrm{d}\xi}(\xi_j)\right\} = 0, \tag{2.44}$$

The derivatives of the continuous solution can be used to compute the corrected gradients, which are, in turn, used to compute the viscous fluxes. Consequently, such fluxes are of polynomial degree p but, in general, discontinuous.

The last step to complete the algorithm is to make the total fluxes continuous across elements. The discontinuous viscous fluxes are corrected analogously to the discontinuous convective fluxes. However, the interface viscous fluxes are not obtained by an approximate Riemann solver. Instead, a common viscous flux is defined by averaging the discontinuous viscous fluxes at each side of such interface.

2.2 Flux Splitting

Some level of error is unavoidable in the numerical solution of the Navier-Stokes equations. Apart from round-off and truncation errors, significant aliasing errors might be present in our simulations. Such errors arise from the differentiation of the product of two or more variables and are often manifested by an unphysical growth of the energy content of the integration variables at high wavenumbers and a decay at the lower end of the spectrum [103].

Although it might be possible to filter and dissipate the accumulation of energy at the highest wavenumbers, such filtering techniques cannot compensate for the energy loss at the lower modes. Thus, formulations that minimise the need for filtering techniques are of special importance for high-fidelity simulations, where high-order schemes of very low dissipative properties are often employed.

Thus, the baseline high-order scheme can be improved with the so-called skew-symmetric formulations of the convective terms, reducing aliasing errors and increasing the robustness in marginally resolved DNS and LES.

The convective terms in the NS equations (see Section 2.1.3) are of the form

$$\mathcal{C} = \frac{\partial \rho u_j \phi}{\partial x_j}, \tag{2.45}$$

where u_j is the flow velocity in the x_j direction, and ϕ is either 1 for the mass conservation equation, u_i for each of the i momentum conservation equations or E for the total energy equation. Using the chain rule, one may separate the derivative of the triple product into the sum of two or three components, such as:

$$\mathcal{C}^{\rho} = \rho \frac{\partial u_j \phi}{\partial x_j} + u_j \phi \frac{\partial \rho}{\partial x_j}, \tag{2.46}$$

Even though $\mathcal{C}$ and $\mathcal{C}^{\rho}$ are identical, their numerical discretisations might not be equivalent. This is because the product rule does not generally hold at the discrete level. The matter is worse if induced variables, such as the kinetic energy, are compared. However, the (discrete) conservation of the kinetic energy is highly sought after for numerical schemes due to its implications on non-linear stability [104–106].

Coppola et al. [107] introduced the derivation of energy-preserving formulations by firstly defining a generalised energy for any scalar variable, ϕ, that satisfies a balance equation of the form:

$$\frac{\partial \rho \phi}{\partial t} = -\frac{\partial \rho u_j \phi}{\partial x_j} \tag{2.47}$$

Then, the evolution equation of the generalised energy, $\rho\phi^2/2$, is given by

$$\frac{\partial \rho\phi^2/2}{\partial t} = -\left(\phi\frac{\partial \rho u_j \phi}{\partial x_j} + \frac{\phi^2}{2}\frac{\partial \rho u_j}{\partial x_j}\right) = -\frac{\partial \rho u_j \phi^2/2}{\partial x_j}, \tag{2.48}$$

from which Coppola et al. [107] point out that a divergence structure in the right-hand side of Equation 2.47 induces another divergence structure in the evolution of the generalised energy.

We may recover the definition of the kinetic energy by substituting ϕ by u_i. Since the product rule for the spatial derivatives does not generally hold for discrete spatial derivative operators, the divergence structure which was obtained in Eq. 2.48 may not be reproduced by the numerical scheme. Hence, spatial discretisations might produce spurious contributions to the energy balance due to the non-linear terms.

To avoid such an effect of the non-linear terms on the evolution of the generalised energy, we may integrate Eq. 2.48 over all the computational domain. Then, assuming the imposition of homogeneous or periodic boundary conditions, the resulting right-hand side should vanish:

$$\int_\Omega \left(\phi\frac{\partial \rho u_j \phi}{\partial x_j} + \frac{\phi^2}{2}\frac{\partial \rho u_j}{\partial x_j}\right) d\Omega = 0 \tag{2.49}$$

Recalling Equation 2.45, the first term in Equation 2.49 corresponds to the product of the scalar variable in consideration, ϕ, and any of the convective terms in the NS equations, $\mathcal{C}$. The spatial derivative in the second term of Eq. 2.49, which will be referred to as $-\mathcal{M}$ following the notation in Coppola et al. [107], corresponds to the right-hand side of the mass equation, i.e. is equivalent to $-\mathcal{C}$ when $\phi = 1$. Then, Eq. 2.49 can be expressed as

$$\int_\Omega \left(\phi\mathcal{C} - \frac{\phi^2}{2}\mathcal{M}\right) d\Omega = 0 \tag{2.50}$$

In the approach of Kennedy and Gruber [108], the convective terms, $\mathcal{M}$ and $\mathcal{C}$, are expressed as a linear combination of different analytically equivalent forms:

$$\mathcal{M} = \xi\frac{\partial \rho u_j}{\partial x_j} + (1-\xi)\left(\rho\frac{\partial u_j}{\partial x_j} + u_j\frac{\partial \rho}{\partial x_j}\right) \tag{2.51}$$

$$\mathcal{C} = \alpha\mathcal{C}^D + \beta\mathcal{C}^\phi + \gamma\mathcal{C}^u + \delta\mathcal{C}^\rho + \varepsilon\mathcal{C}^L \tag{2.52}$$

$$\begin{aligned}
\mathcal{C}^D &= \tfrac{\partial \rho u_j \phi}{\partial x_j} \\
\mathcal{C}^\phi &= \phi\tfrac{\partial \rho u_j}{\partial x_j} + \rho u_j \tfrac{\partial \phi}{\partial x_j} \\
\mathcal{C}^u &= u_j\tfrac{\partial \rho\phi}{\partial x_j} + \rho\phi\tfrac{\partial u_j}{\partial x_j} \\
\mathcal{C}^\rho &= \rho\tfrac{\partial u_j \phi}{\partial x_j} + u_j\phi\tfrac{\partial \rho}{\partial x_j} \\
\mathcal{C}^L &= \rho u_j\tfrac{\partial \phi}{\partial x_j} + \rho\phi\tfrac{\partial u_j}{\partial x_j} + u_j\phi\tfrac{\partial \rho}{\partial x_j}
\end{aligned} \tag{2.53}$$

Expressions 2.51–2.53 can be introduced in Eq. 2.50. Integrating the resulting expressions, a new system of equations is achieved, leading to a two-parameter family of discretisations that have the property by which non-linear convective terms do not contribute to the global energy balance.

Selecting $\xi = 1/2$ and $\delta = 1/4$, leads to the flux splitting formulation of Kennedy and Gruber [108], which was shown to have the property of being energy preserving by Pirozzoli [109], **and is implemented into the baseline solver**.

Since the analysis of the split forms and the study of non-linear stability is out of the scope of the present work, the interested reader can find the details of different energy-preserving split formulations in [107–109], which feature numerical experiments and quantitative comparisons, as well as in-depth discussions about the properties of each scheme.

2.3 Boundary Conditions

The formulation of the Boundary Conditions (BC) is a fundamental part of any fluid solver and is especially important to achieve statistical convergence in unsteady scale-resolving simulations. Depending on the BC formulation of the baseline solver, the algorithm might require some alterations due to time-inclining. For that reason, the chosen implementation for the boundary conditions is also described in the present chapter.

The accuracy of a computational fluid dynamics solver is very strongly tied to the quality of such implementation. In compressible solvers it is not rare to find non-physical solutions near open boundaries due to perturbations introduced by the boundary conditions formulation.

Such matter is generally worsened for direct numerical simulations and large eddy simulations, where high-order spatial discretisations are commonly used. High-order schemes provide very low dissipation, and the numerical errors introduced at the boundaries propagate through the computational domain instead of quickly decaying as in low-order schemes.

It is not uncommon to locate the boundaries of the computational domain far from the regions of interest. This strategy aims to compensate for such low diffusive properties and dampen the non-physical perturbations before they reach the blades. However, in turbomachinery simulations it is not always possible to carry out such procedure, and then, the spurious noise produced at the boundaries can significantly influence the solution.

Nevertheless, with the goal of reducing such non-physical perturbations, the baseline solver in the present work implements the three-dimensional Navier-Stokes Characteristics Boundary Conditions (NSCBC) [110, 111], but the formulation has been adapted to the data used in ITP Aero for inlets and outlets.

2.3.1 The 3D Navier-Stokes Characteristics Boundary Conditions

In the NSCBC, the Navier-Stokes equations are cast in the reference frame $\begin{pmatrix} x_1 & x_2 & x_3 \end{pmatrix}$, where x_1 is the direction normal to the boundary:

$$\frac{\partial \mathbf{W}}{\partial t} + \frac{\partial \mathbf{f}_1}{\partial x_1} + \frac{\partial \mathbf{f}_2}{\partial x_2} + \frac{\partial \mathbf{f}_3}{\partial x_3} = \frac{\partial \mathbf{F}_1}{\partial x_1} + \frac{\partial \mathbf{F}_2}{\partial x_2} + \frac{\partial \mathbf{F}_3}{\partial x_3}, \tag{2.54}$$

where $\mathbf{W} = \begin{pmatrix} \rho & \rho u_1 & \rho u_2 & \rho u_3 & \rho E \end{pmatrix}^T$ is the vector of conservative variables, and $\mathbf{f}_i$ and $\mathbf{F}_i$ are the inviscid and viscous fluxes in the x_i direction, respectively. To ease the notation, let us group the viscous terms in the right-hand side of Equation 3.50 into a new variable, $\mathbf{D} = \frac{\partial \mathbf{F_1}}{\partial \mathbf{x_1}} + \frac{\partial \mathbf{F_2}}{\partial \mathbf{x_2}} + \frac{\partial \mathbf{F_3}}{\partial \mathbf{x_3}}$.

The NS equations can be expressed as a function of the primitive variables, $\mathbf{W}_p = \begin{pmatrix} \rho & u_1 & u_2 & u_3 & p \end{pmatrix}^T$, pre-multiplying by the inverse of the transformation matrix $\mathbf{P} = \frac{\partial \mathbf{W}}{\partial \mathbf{W}_p}$, since

$$\frac{\partial \mathbf{W}}{\partial t} = \frac{\partial \mathbf{W}}{\partial \mathbf{W}_p}\frac{\partial \mathbf{W}_p}{\partial t} = \mathbf{P}\frac{\partial \mathbf{W}_p}{\partial t} \tag{2.55}$$

The transformation matrix, $\mathbf{P}$, and its inverse, $\mathbf{P}^{-1}$, are:

$$\mathbf{P} = \begin{pmatrix} 1 & 0 & 0 & 0 & 0 \\ u_1 & \rho & 0 & 0 & 0 \\ u_2 & 0 & \rho & 0 & 0 \\ u_3 & 0 & 0 & \rho & 0 \\ \frac{1}{2}(u_1^2+u_2^2+u_3^2) & \rho u_1 & \rho u_2 & \rho u_3 & {}^1\!/_{(\gamma-1)} \end{pmatrix} \tag{2.56}$$

$$\mathbf{P}^{-1} = \begin{pmatrix} 1 & 0 & 0 & 0 & 0 \\ -u_1/\rho & 1/\rho & 0 & 0 & 0 \\ -u_2/\rho & 0 & 1/\rho & 0 & 0 \\ -u_3/\rho & 0 & 0 & 1/\rho & 0 \\ \frac{(\gamma-1)}{2}(u_1^2+u_2^2+u_3^2) & (1-\gamma)\,u_1 & (1-\gamma)\,u_2 & (1-\gamma)\,u_3 & (\gamma-1) \end{pmatrix} \tag{2.57}$$

To recapitulate, the governing equations in terms of the primitive variables and in a reference frame orthogonal to the boundary read

$$\frac{\partial \mathbf{W}_p}{\partial t} + \mathbf{P}^{-1}\frac{\partial \mathbf{f}_1}{\partial x_1} + \mathbf{P}^{-1}\frac{\partial \mathbf{f}_2}{\partial x_2} + \mathbf{P}^{-1}\frac{\partial \mathbf{f}_3}{\partial x_3} = \mathbf{P}^{-1}\mathbf{D} \tag{2.58}$$

The convective terms orthogonal to the boundary, $\frac{\partial \mathbf{f}_i}{\partial x_i}$, can also be expressed as

$$\frac{\partial \mathbf{f}_i}{\partial x_i} = \frac{\partial \mathbf{f}_i}{\partial \mathbf{W}}\frac{\partial \mathbf{W}}{\partial x_i} = \frac{\partial \mathbf{f}_i}{\partial \mathbf{W}}\frac{\partial \mathbf{W}}{\partial \mathbf{W}_p}\frac{\partial \mathbf{W}_p}{\partial x_i} = \frac{\partial \mathbf{f}_i}{\partial \mathbf{W}}\mathbf{P}\frac{\partial \mathbf{W}_p}{\partial x_i}, \tag{2.59}$$

and, therefore, Equation 2.58 can be cast as

$$\frac{\partial \mathbf{W}_p}{\partial t} + \mathbf{P}^{-1}\frac{\partial \mathbf{f}_1}{\partial \mathbf{W}}\mathbf{P}\frac{\partial \mathbf{W}_p}{\partial x_1} + \mathbf{P}^{-1}\frac{\partial \mathbf{f}_2}{\partial \mathbf{W}}\mathbf{P}\frac{\partial \mathbf{W}_p}{\partial x_2} + \mathbf{P}^{-1}\frac{\partial \mathbf{f}_3}{\partial \mathbf{W}}\mathbf{P}\frac{\partial \mathbf{W}_p}{\partial x_3} = \mathbf{P}^{-1}\mathbf{D} \tag{2.60}$$

The characteristic form of the equations can be obtained by diagonalising $\mathbf{P}^{-1}\frac{\partial \mathbf{f}_1}{\partial \mathbf{W}}\mathbf{P}$. The diagonal matrix, $\mathbf{\Lambda} = \mathbf{S}^{-1}\mathbf{P}^{-1}\frac{\partial \mathbf{f}_1}{\partial \mathbf{W}}\mathbf{P}\mathbf{S}$, contains the eigenvalues of $\mathbf{P}^{-1}\frac{\partial \mathbf{f}_1}{\partial \mathbf{W}}\mathbf{P}$, which represent the propagation velocities of each characteristic wave.

$$\mathbf{\Lambda} = \begin{pmatrix} u_1 - a & 0 & 0 & 0 & 0 \\ 0 & u_1 & 0 & 0 & 0 \\ 0 & 0 & u_1 & 0 & 0 \\ 0 & 0 & 0 & u_1 & 0 \\ 0 & 0 & 0 & 0 & u_1 + a \end{pmatrix} \tag{2.61}$$

The transformation matrices $\mathbf{S}$ and $\mathbf{S}^{-1}$ are, respectively,

$$\boldsymbol{S} = \begin{pmatrix} 1/(2a^2) & 1/a^2 & 0 & 0 & 1/(2a^2) \\ -1/(2\rho a) & 0 & 0 & 0 & 1/(2\rho a) \\ 0 & 0 & 1 & 0 & 0 \\ 0 & 0 & 0 & 1 & 0 \\ 1/2 & 0 & 0 & 0 & 1/2 \end{pmatrix} \tag{2.62}$$

$$\boldsymbol{S}^{-1} = \begin{pmatrix} 0 & -\rho a & 0 & 0 & 1 \\ a^2 & 0 & 0 & 0 & -1 \\ 0 & 0 & 1 & 0 & 0 \\ 0 & 0 & 0 & 1 & 0 \\ 0 & \rho a & 0 & 0 & 1 \end{pmatrix} \tag{2.63}$$

This diagonalization leads to

$$\frac{\partial \mathbf{W}_p}{\partial t} + \mathbf{S}\mathbf{\Lambda}\mathbf{S}^{-1}\frac{\partial \mathbf{W}_p}{\partial x_1} - \boldsymbol{\mathcal{T}} = \mathbf{0} \tag{2.64}$$

where $\boldsymbol{\mathcal{T}}$ is the vector of the transverse convective terms and the viscous terms, grouped:

$$\boldsymbol{\mathcal{T}} = -\mathbf{P}^{-1}\frac{\partial \mathbf{f}_2}{\partial \mathbf{W}}\mathbf{P}\frac{\partial \mathbf{W}_p}{\partial x_2} - \mathbf{P}^{-1}\frac{\partial \mathbf{f}_3}{\partial \mathbf{W}}\mathbf{P}\frac{\partial \mathbf{W}_p}{\partial x_3} + \mathbf{P}^{-1}\mathbf{D} = \begin{pmatrix} \mathcal{T}_1 & \mathcal{T}_2 & \mathcal{T}_3 & \mathcal{T}_4 & \mathcal{T}_5 \end{pmatrix}^T \tag{2.65}$$

Finally, we can cast the system of equations 3.54 in characteristic form by pre-multiplying it by $\mathbf{S}^{-1}$,

$$\mathbf{S}^{-1}\frac{\partial \mathbf{W}_p}{\partial t} + \mathbf{S}^{-1}\mathbf{S}\mathbf{\Lambda}\mathbf{S}^{-1}\frac{\partial \mathbf{W}_p}{\partial x_1} - \mathbf{S}^{-1}\boldsymbol{\mathcal{T}} = \mathbf{0}, \tag{2.66}$$

and, since the matrix product $\mathbf{S^{-1}S}$ is equivalent to the unit matrix, we obtain

$$\mathbf{S}^{-1}\frac{\partial \mathbf{W}_p}{\partial t} + \boldsymbol{L} - \boldsymbol{\mathfrak{T}} = \mathbf{0} \tag{2.67}$$

where $\boldsymbol{\mathcal{L}} = \boldsymbol{\Lambda}\mathbf{S}^{-1}\frac{\partial \mathbf{W}_p}{\partial x_1}$ contains the temporal variations of the amplitudes of the characteristic waves:

$$\boldsymbol{\mathcal{L}} = \begin{pmatrix} \mathcal{L}_1 \\ \mathcal{L}_2 \\ \mathcal{L}_3 \\ \mathcal{L}_4 \\ \mathcal{L}_5 \end{pmatrix} = \begin{pmatrix} (u_1 - a)\left(\frac{\partial p}{\partial x_1} - \rho a \frac{\partial u_1}{\partial x_1}\right) \\ u_1\left(a^2\frac{\partial \rho}{\partial x_1} - \frac{\partial p}{\partial x_1}\right) \\ u_1 \frac{\partial u_2}{\partial x_1} \\ u_1 \frac{\partial u_3}{\partial x_1} \\ (u_1 + a)\left(\frac{\partial p}{\partial x_1} + \rho a \frac{\partial u_1}{\partial x_1}\right) \end{pmatrix} \tag{2.68}$$

If we assume x_1 to be aligned with the stream-wise direction, then the amplitude $\mathcal{L}_1$ corresponds to the upstream-travelling acoustic wave, $\mathcal{L}_2$ with the entropy wave, $\mathcal{L}_3$ and $\mathcal{L}_4$ with the vorticity waves and $\mathcal{L}_5$ with the downstream-travelling wave.

The system of equations reads

$$\begin{cases} \left(\frac{\partial p}{\partial t} - \rho a \frac{\partial u_1}{\partial t}\right) + \mathcal{L}_1 - \mathfrak{T}_1 = 0 \\ \left(a^2\frac{\partial \rho}{\partial t} - \frac{\partial p}{\partial t}\right) + \mathcal{L}_2 - \mathfrak{T}_2 = 0 \\ \frac{\partial u_2}{\partial t} + \mathcal{L}_3 - \mathfrak{T}_3 = 0 \\ \frac{\partial u_3}{\partial t} + \mathcal{L}_4 - \mathfrak{T}_4 = 0 \\ \left(\frac{\partial p}{\partial t} + \rho a \frac{\partial u_1}{\partial t}\right) + \mathcal{L}_5 - \mathfrak{T}_5 = 0 \end{cases} \tag{2.69}$$

The viscous and transverse terms (tangential to the boundary) in Eq. 2.67, $\boldsymbol{\mathfrak{T}}$,are related to $\boldsymbol{\mathcal{T}}$ through

$$\boldsymbol{T} = \mathbf{S}^{-1}\boldsymbol{\mathcal{T}} = \begin{pmatrix} \mathfrak{T}_1 \\ \mathfrak{T}_2 \\ \mathfrak{T}_3 \\ \mathfrak{T}_4 \\ \mathfrak{T}_5 \end{pmatrix} = \begin{pmatrix} \mathcal{T}_5 - \rho a \mathcal{T}_2 \\ a^2\mathcal{T}_1 - \mathcal{T}_5 \\ \mathcal{T}_3 \\ \mathcal{T}_4 \\ \mathcal{T}_5 + \rho a \mathcal{T}_2 \end{pmatrix} \tag{2.70}$$

From Eq. 3.54 we can also find the relation between the wave amplitude variations and the primitive variables

$$\frac{\partial \mathbf{W}_p}{\partial t} + \mathbf{S}\boldsymbol{\mathcal{L}} - \boldsymbol{T} = \mathbf{0} \tag{2.71}$$

$$\begin{cases} \frac{\partial \rho}{\partial t} + \frac{1}{a^2}\left[\mathcal{L}_2 + \frac{1}{2}\left(\mathcal{L}_5 + \mathcal{L}_1\right)\right] + \mathcal{L}_1 - \mathcal{T}_1 = 0 \\ \frac{\partial u_1}{\partial t} + \frac{1}{2\rho a}\left(\mathcal{L}_5 - \mathcal{L}_1\right) + \mathcal{L}_2 - \mathcal{T}_2 = 0 \\ \frac{\partial u_2}{\partial t} + \mathcal{L}_3 - \mathcal{T}_3 = 0 \\ \frac{\partial u_3}{\partial t} + \mathcal{L}_4 - \mathcal{T}_4 = 0 \\ \frac{\partial p}{\partial t} + \frac{1}{2}\left(\mathcal{L}_5 + \mathcal{L}_1\right) - \mathcal{T}_5 = 0 \end{cases} \tag{2.72}$$

and between the wave amplitude variations and the conservative variables

$$\mathbf{P}\frac{\partial \mathbf{W}_p}{\partial t} + \mathbf{PS}\boldsymbol{\mathcal{L}} + \frac{\partial \mathbf{f}_2}{\partial x_2} + \frac{\partial \mathbf{f}_3}{\partial x_3} = \frac{\partial \mathbf{F}_1}{\partial x_1} + \frac{\partial \mathbf{F}_2}{\partial x_2} + \frac{\partial \mathbf{F}_3}{\partial x_3} \tag{2.73}$$

The imposition of the appropriate boundary conditions depends on the nature of the boundary. For each type of boundary, there will be some waves that cross inside to outside of the computational domain. In such a case, since the information propagates from inside the domain, their amplitudes can be computed without the need of information from the outside. However, the amplitudes of the waves that travel into the computational domain need to be computed from the values that we wish to enforce on the boundary.

Thus, the implementation of the NSCBCs requires computing the amplitudes of the characteristic waves appropriately, either from Eq. 2.68, or by the derivation of relations that include the temporal evolution of the desired variable at the boundary. For example, to impose the static pressure at the boundary, Eq. 2.72 gives the dependence of the temporal evolution of the static pressure with the amplitudes of the acoustic waves.

Once all amplitudes of the characteristic waves have been computed, the last step calls for re-casting the characteristic equations back in conservative form. Thus, the boundary-conditions-compliant wave amplitudes are transformed into *corrected* fluxes in the normal-to-the-boundary reference system, and then translated into the physical reference system:

$$\left(\frac{\partial \mathbf{f}_1}{\partial x_1} = \mathbf{PS}\boldsymbol{\mathcal{L}}, \frac{\partial \mathbf{f}_2}{\partial x_2}, \frac{\partial \mathbf{f}_3}{\partial x_3}\right) \rightarrow \left(\frac{\partial \mathbf{f}}{\partial x}, \frac{\partial \mathbf{g}}{\partial y}, \frac{\partial \mathbf{h}}{\partial z}\right) \tag{2.74}$$

Once the fluxes of the points at the boundaries are obtained, the temporal integration scheme can finally advance the solution in time.

In the present work, the NSCBCs are used in subsonic inlets, subsonic outlets and adiabatic no-slip walls, and the details of the formulations are included next, for completeness.

2.3.1.1 Subsonic Outflow

At a subsonic outlet, only the amplitude of one characteristic wave is unknown. For the four remaining waves, their amplitudes can be obtained from information within the computational domain. Depending on the direction of the mean flow and the location of the boundary, the incoming wave might be either $\mathcal{L}_1$ or $\mathcal{L}_5$. If the flow is oriented towards positive values of x_1 and the outlet is located at $x_1^{outlet} \geq x_1^{(j}$ for any solution point j, then the only unknown wave is $\mathcal{L}_1$ since $u_1 - a < 0$ for a subsonic outlet. Then, amplitudes $\mathcal{L}_2$ through $\mathcal{L}_5$ are computed from Eq. 2.68.

The physical boundary condition we wish to impose is the static pressure, p_{out}. From Equation 2.72, the temporal evolution of the static pressure in a Locally One-Dimensional

Inviscid (LODI) approach is

$$\frac{\partial p}{\partial t} + \frac{1}{2}\left(\mathcal{L}_5 + \mathcal{L}_1\right) = 0 \tag{2.75}$$

As pointed out in [94, 112, 113], if we obtain $\mathcal{L}_1$ from Eq. 2.75, its dependence with the exiting acoustic wave would necessarily imply that the boundary is reflective. A truly non-reflecting formulation for the incoming wave has to be independent of the outgoing waves.

The proposed formulation for the incoming wave is based on the pressure relaxation condition proposed by Rudy and Strikwerda [114]:

$$\mathcal{L}_1 = \sigma \frac{a\left(1 - M_1^2\right)}{L_x}\left(p - p_{out}\right) \tag{2.76}$$

where L_x is a reference length, M_1 is the mean normal Mach number at the boundary, and σ is a relaxation factor. It is worth noting that, if we followed the LODI approach and set the relaxation parameter to $\sigma = 0$, the boundary would be perfectly non-reflecting. Nevertheless, generally speaking, the mean static pressure would never be set at the desired value p_{out}.

For any non-zero value of σ, perturbations reaching the boundary with $p \neq p_{out}$ lead to some level of reflectivity at the boundary. Such effect is required to force the static pressure to the desired value, p_{out}. It is essential to emphasise this fact since this formulation of boundary conditions is often referred to as "non-reflecting". However, their behaviour and performance have very little to do with actual non-reflecting boundary conditions, such as Giles' 2D single-frequency non-reflecting BCs [115] implemented in the linear solver of the Mu^2s^2T CFD suite, for example.

The physical boundary condition in Eq. 2.76 is completed with the transverse and viscous fluxes, $\mathfrak{T}_1$, following the approaches described in [110, 116, 117]. Such additional terms are modulated by a relaxation coefficient, which, following the approach of Lodato [111], has been chosen to be $(1 - M_1)$.

$$\mathcal{L}_1 = \sigma \frac{a\left(1 - M_1^2\right)}{L_x}\left(p - p_{out}\right) + \left(1 - M_1\right)\left(\mathcal{T}_5 - \rho a \mathcal{T}_2\right) \tag{2.77}$$

Finally, all the components of the vector $\boldsymbol{\mathcal{L}} - \boldsymbol{\mathfrak{T}}$ can be computed. The equations in characteristic form are transformed back into conservative form. Thus, the vector $\boldsymbol{\mathcal{L}} - \boldsymbol{\mathfrak{T}}$ becomes the sum of convective and viscous contributions for the points at the outlet (see Equation 3.50). At this point, such contributions can be cast in the original frame of reference of the problem, coming back from the orthogonal-to-the-outlet frame.

2.3.1.2 Subsonic Inflow

Contrary to the subsonic outlet boundary formulation, subsonic inlets require four quantities to be enforced. This stems from the fact that there are four incoming waves whose amplitudes cannot be computed from information within the computational domain.

Following the same logic as in the subsonic outlet case, if the flow is oriented towards positive values of x_1 and the inlet is located at $x_1^{inlet} \leq x_1^{(j}$ for any solution point j, then the only known wave is $\mathcal{L}_1$, since $u_1 - a < 0$ for a subsonic inlet. Therefore, the solver obtains $\mathcal{L}_1$ using information within the computational domain as

$$\mathcal{L}_1 = (u_1 - a)\left(\frac{\partial p}{\partial x_1} - \rho a \frac{\partial u_1}{\partial x_1}\right) \tag{2.78}$$

A very significant difference with the outlet is that the value that is imposed at the inlet boundary is not a primitive (nor a conservative) variable. The baseline solver follows a common approach in turbomachinery, i.e. imposing total pressure, P_t, total temperature, T_t, swirl angle, $\alpha_r = atan\left({}^{u_\theta}/_{\sqrt{u_x^2+u_r^2}}\right)$, and radial angle, $\alpha_r = atan\left({}^{u_r}/_{u_x}\right)$.

The objective, therefore, is to obtain the amplitudes $\mathcal{L}_2$ through $\mathcal{L}_5$ as a function of the temporal derivatives of the imposed variables (P_t, T_t, α_r and α_s). If the transverse and viscous terms are neglected, Equation 2.72 describes the relationship between the amplitudes in $\boldsymbol{\mathcal{L}}$ and the temporal derivatives of the primitive variables. Since we can write the temporal derivatives of the imposed variables (${}^{\partial P_t}/_{\partial t}$, ${}^{\partial T_t}/_{\partial t}$, ${}^{\partial \alpha_r}/_{\partial t}$, ${}^{\partial \alpha_s}/_{\partial t}$) as functions of the temporal derivatives of the primitive variables (${}^{\partial \rho}/_{\partial t}$, ${}^{\partial u_1}/_{\partial t}$, ${}^{\partial u_2}/_{\partial t}$, ${}^{\partial u_3}/_{\partial t}$, ${}^{\partial p}/_{\partial t}$), we can use Equation 2.72 to obtain the unknown amplitudes as a function of the derivatives of the imposed variables and $\mathcal{L}_1$:

$$\left(\begin{array}{cccc} \mathcal{L}_2 & \mathcal{L}_3 & \mathcal{L}_4 & \mathcal{L}_5 \end{array}\right) = f\left(\begin{array}{cccc} {}^{\partial P_t}/_{\partial t}, & {}^{\partial T_t}/_{\partial t}, & {}^{\partial \alpha_r}/_{\partial t}, & {}^{\partial \alpha_s}/_{\partial t}, \quad \mathcal{L}_1 \end{array}\right) \tag{2.79}$$

Then, the temporal derivatives of the imposed variables can be modelled following the same approach than in subsonic outlets for the static pressure (see Eq. 2.76):

$$\frac{\partial \chi}{\partial t} = -\sigma \frac{a\left(1 - M_1^2\right)}{L_x}\left(\chi - \chi_{in}\right) \tag{2.80}$$

where χ can be either P_t, T_t, α_r or α_s.

2.3.1.3 Adiabatic No-Slip Wall

The formulation of the adiabatic no-slip wall condition, which is used for all surfaces in the viscous simulations of the present work, corresponds to that of Poinsot and Lele [118]. The velocities at the wall are $u_i|_{wall}(t) = 0, \forall t$, where $i = 1, 2, 3$. Therefore, Eq. 2.68

gives $\mathcal{L}_j = 0$, where $j = 2, 3, 4$. Moreover, the temporal evolution of the velocity normal to the wall, $\frac{\partial u_1}{\partial t}$, in Eq. 2.72 shows that $\mathcal{L}_1 = \mathcal{L}_5$.

Then, the amplitude of the wave incoming to the wall (let us suppose it is $\mathcal{L}_5$) can be computed from within the computational domain and its amplitude and the outgoing wave's ($\mathcal{L}_1$ in this example) can be set.

Likewise to the outlet boundary condition, the corrected amplitudes of the characteristic waves and the transverse and viscous terms are introduced in the system of equations 2.69. Then, the system of equations is transformed back into its conservative form and cast in the appropriate frame of reference, providing the corrected value of the fluxes and enabling the time-marching of the solution points at the boundary.

2.4 The Mortar Method for Non-Conformal Grids

The time-inclined method reduces the number of passages required to be present in the computational domains of a rotor/stator simulation. Most commonly, the rotor and stator domains are independently meshed with a grid that is fixed to their respective geometry. Thus, in general, the rotor and stator grids are not conformal at the interface region.

Moreover, since such domains are in relative motion, the relative position between the nodes or cells at each side of the interface changes with every time-step of the time-marching scheme. One may choose to mesh the rotor and stator interfaces with the same grid spacing, $r\Delta\theta$. Then, if elements at each side of the interface are coincident at the start of the simulation, after every iteration of the time-marching scheme the rotor moves a distance equal to the grid spacing, $\Omega r \Delta t = r\Delta\theta$, and new pairs of coincident elements at each side of the interface are obtained.

However, the time-step size Δt is usually very small in scale-resolving simulations ($\Delta t \sim 10^{-7} s$ in the simulations presented in Chapter 5), which would lead to unnecessarily fine grids at the interface, severely increasing the computational cost of the simulations. Additionally, such meshing strategy would not solve the problem for non-conformal domains in time-inclined simulations due to the treatment of the sliding plane interface in such methodology (see Section 3.4).

The nature of the time-inclined method and its intended applications motivate including a brief description of the treatment of non-conformal interfaces. However, it is important to note that the simulations in the present work avoid using both rotor and stator domains, for reasons that are discussed in Section 5.1, and thus avoid using the mortar method. Nevertheless, rotor/stator time-inclined simulations are the next natural step after confirming the suitability of the time-inclined method for retaining the exact blade count in scale-resolving simulations, which is the true objective of the present work.

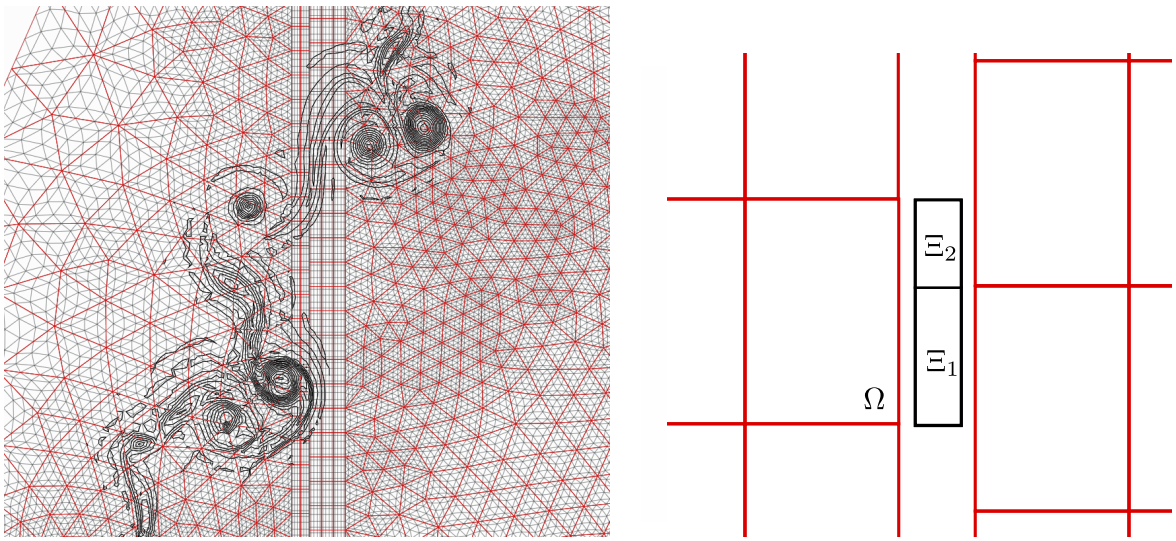

(a) Sliding plane close-up (b) Mortar definition

Figure 2.1: Entropy isolines of vortices crossing the sliding plane in a two-dimensional rotor/stator simulation showing high-order elements in red with their interior points in black (a). Sketch of the definition of mortars Ξ_1 and Ξ_2 from element Ω (b).

2.4.1 Method Description

The mortar method was originally proposed for incompressible flows on fixed grids by Mavriplis [119, 120], and Kopriva proved the conservation property of the method for compressible flows on stationary structured grids [121, 122]. The implementation of the method in the baseline solver is based on its extension for the family of flux reconstruction schemes [123, 124].

The method was also implemented to allow for local refinement, either by dividing particular elements into two or more parts in a sensitive region (h-refinement) or by modifying the polynomial order of such element (p-refinement). Additionally, the method can be used to provide more flexibility or ease the meshing process of complex geometries.

The mortar method can be used to deal with curved, non-uniform interfaces. However, in order to describe the method in the context of the present thesis, let us assume the method is used at the rotor/stator interface region of a linear cascade. Moreover, to simplify the notation, let us assume we are dealing with a two-dimensional case, which results in a one-dimensional sliding interface.

Figure 2.1 (a) corresponds to a two-dimensional rotor/stator simulation. Vortices shed from the rotor are convected downstream, where they cross the sliding plane interface, depicted in the middle section of Fig. 2.1 (a). It can be noticed how the high-order elements from the rotor and stator meshes are non-conformal. The rotor and stator domains have been artificially separated in Figure 2.1 (b) to show how the element faces

at both sides of the sliding plane define a set of mortars, Ξ. In particular, element Ω in Fig. 2.1 (b) gives rise to mortars Ξ_1 and Ξ_2 due to its relative position with the elements of the opposing side of the sliding plane. Since the meshes move with respect to each other, the size and number of mortars vary from time step to time step.

Once the mortars have been defined, they can be discretised similarly to the element faces of the high-order scheme. Thus, the solution within one-dimensional mortars can be represented by a polynomial of degree p using a basis of Lagrange polynomials:

$$\mathbf{U}^{\Xi_i} = \sum_{j=1}^{p+1} \mathbf{U}_j^{\Xi_i} L_j(m), \tag{2.81}$$

where $\mathbf{U}_j^{\Xi_i}$ represents the solution at the j-th solution point of the mortar i, and L_j are the Lagrange polynomials as described in Eq. 2.4.

The mortars are defined by the elements at each side of the sliding plane (let us call them the left-hand, l, and right-hand, r, sides). Then, to compute the solution at the left-hand side of mortar i, denoted by $\mathbf{U}^{\Xi_i,l}$, we project the solution from its adjacent element face at such side of the sliding plane onto the mortar:

$$\int_0^1 \left(\mathbf{U}^{\Xi_i,l}(m) - \mathbf{U}^{\Omega}(\xi)\right) L_j(m) dm = 0, \qquad m = 1, 2, ..., p+1 \tag{2.82}$$

where m is a local coordinate to the one-dimensional mortar Ξ_i, which spans $0 \leq m \leq 1$. Equation 2.82 gives rise to a system which may be expressed in matricial form as

$$\mathbf{U}^{\Xi,l} = \mathbf{M}^{-1}\mathbf{S}^{\Omega\to\Xi}\mathbf{U}^{\Omega} \tag{2.83}$$

Vectors $\mathbf{U}^{\Xi,l}$ and $\mathbf{U}^{\Omega}$ contain the solution at each solution point in a mortar face and its adjacent element face, while the elements of matrices $\mathbf{M}$ and $\mathbf{S}^{\Omega\to\Xi}$ are obtained by

$$M_{i,j} = \int_0^1 L_i(m) L_j(m) dm, \qquad i, j = 1, 2, ..., p+1 \tag{2.84}$$

$$S_{i,j}^{\Omega\to\Xi} = \int_0^1 L_i(\xi(m)) L_j(m) dm, \qquad i, j = 1, 2, ..., p+1 \tag{2.85}$$

The relation between the computational coordinate for the element face, ξ, and the local coordinate for the mortar, m, is given by

$$\xi(m) = o(t) + s(t)m \tag{2.86}$$

where $o(t)$ and $s(t)$ describe the offset and scaling of mortar Ξ with respect to element

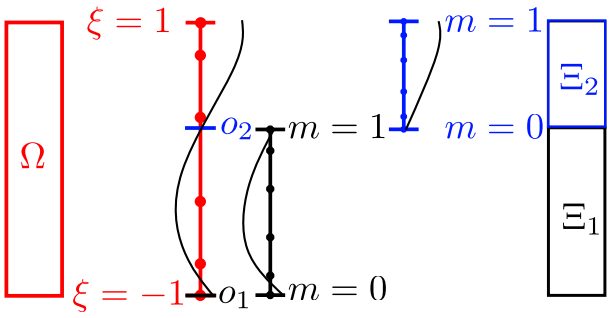

Figure 2.2: Sketch of the interpolation process of the solution from an element face, Ω, to one side of the adjacent mortars, Ξ_1 and Ξ_2.

Ω. This process by which the solution is projected from an element face to the adjacent mortar's side is sketched in Figure 2.2, displaying the local reference systems and the interpolation to the mortar solution points defined therein. Figure 2.2 also displays the offsets of mortars Ξ_1 and Ξ_2, which vary along with the relative sizes of the mortars to the element face, s_1 and s_2, as the rotor and stator meshes move relative to one another. Consequently, the elements of matrix $\mathbf{S}^{\Omega\to\Xi}$, defined in Equation 2.85, are time-dependent.

Conversely, it can be observed that matrix $\mathbf{M}$ is time-independent and does not depend on the mortar size or shape. Therefore, it is computed only once, and it can be used for the whole simulation.

The former process is carried out to obtain the solution at both sides of the mortars, after which, an approximate Riemann solver can be used to compute the common inviscid flux at the mortar elements, $\mathbf{f}^{\Xi}$:

$$\mathbf{f}^{\Xi} = \frac{1}{2}\left(\mathbf{f}_R^{\Xi} + \mathbf{f}_L^{\Xi}\right) - \frac{|\mathbf{\Lambda}|}{2}\left(\mathbf{U}_R^{\Xi} - \mathbf{U}_L^{\Xi}\right), \tag{2.87}$$

where $\mathbf{f}_R^{\Xi} = \mathbf{f}(\mathbf{U}_R^{\Xi})$ and $\mathbf{f}_L^{\Xi} = \mathbf{f}(\mathbf{U}_L^{\Xi})$ are the inviscid fluxes computed with the solution projected at the right and left sides of mortar Ξ, respectively, and$|\mathbf{\Lambda}|$ contains the absolute value of the eigenvalues of $\frac{\partial \mathbf{f}}{\partial \mathbf{U}}$, as defined in Eq. 2.61. The mortar fluxes are then projected back into the element faces imposing:

$$\int_0^{o_2}\left(\mathbf{f}^{\Omega}(\xi) - \mathbf{f}^{\Xi_1}(m)\right)L_j(\xi)d\xi + \int_{o_2}^{1}\left(\mathbf{f}^{\Omega}(\xi) - \mathbf{f}^{\Xi_2}(m)\right)L_j(\xi)d\xi = 0, \qquad m = 1, 2, ..., p+1, \tag{2.88}$$

where we have assumed that element Ω is adjacent only to two mortars, Ξ_1 and Ξ_2, although Eq. 2.88 is easily generalised otherwise. Similarly to Equation 2.82, Equation 2.88 gives rise to the following system of equations:

$$\mathbf{f}^{\Omega} = s_1\mathbf{M}^{-1}\mathbf{S}^{\Xi_1\to\Omega}\mathbf{f}^{\Xi_1} + s_2\mathbf{M}^{-1}\mathbf{S}^{\Xi_2\to\Omega}\mathbf{f}^{\Xi_2} \tag{2.89}$$

where matrices $\mathbf{S}^{\Xi_1\to\Omega}$ and $\mathbf{S}^{\Xi_2\to\Omega}$ are the inverses of $\mathbf{S}^{\Omega\to\Xi_1}$ and $\mathbf{S}^{\Omega\to\Xi_2}$, respectively, which have been computed to originally project the solution onto each mortar (see Eq. 2.82).

It is important to note that, even though matrices $\mathbf{S}^{\Omega\to\Xi}$ are time dependent through $o(t)$ and $s(t)$, for the special case that the rotor and stator interfaces have the same number of uniformly space elements, matrices $\mathbf{S}^{\Omega\to\Xi_1}$ and $\mathbf{S}^{\Omega\to\Xi_2}$ and their inverses, can be computed once per time-step and reused for all the mortars and elements at the interface during such time-step.

The process to compute the viscous fluxes is a bit less direct. Firstly, a common solution is defined in each mortar as the average between the projected solutions in each of its sides, $\mathbf{U}^{\Xi}_R$ and $\mathbf{U}^{\Xi}_L$:

$$\mathbf{U}^{\Xi} = \frac{1}{2}\left(\mathbf{U}^{\Xi}_R + \mathbf{U}^{\Xi}_L\right), \tag{2.90}$$

Then, Equation 2.89 is used substituting the inviscid fluxes, $\mathbf{f}^{\Xi_i}$, with the common solution at each of the mortars that compose any element face Ω. This operation results in the projection of the common solution back into the element faces, which is followed by the computation of its gradients. Then, viscous fluxes can be computed and projected back into the mortars similarly to Eq. 2.83.

Finally, the common viscous fluxes at each mortar may be computed simply by averaging the right and left viscous fluxes, and the result may be added to the common inviscid fluxes and projected to the element faces as in Eq. 2.89.

2.4.2 Algorithm for Rotor/Stator Simulations

An algorithm to deal with the sliding plane interface has been implemented into the baseline solver. This work has been carried out as a first step towards time-inclined simulations of turbomachinery stages. Thus, the sliding plane approach has been verified in two-dimensional rotor/stator simulations of unitary pitch ratio.

In the present thesis, the analysis of the suitability of the time-inclined method for SRSs has been incrementally more complex, reaching the simulation of turbulent flows in 3D linear cascades. The use of sliding planes has been avoided for such simulations. However, time-inclined rotor/stator simulations featuring a sliding plane represent one of the immediate next steps for the further development of the TI method in SRSs. As such, a description of the algorithm and the rationale behind is deemed relevant.

First, let us assume the rotor and stator domains have the same pitch. In an rotor/stator simulation with unequal blade counts this assumption would not be valid but, as will be explained in the next chapter, the time-inclined method bridges the rotor and stator domains such that they have equal sizes in the inclined computational planes.

At the meshing process, a uniform structured grid in the direction of rotation (or translation for linear cascades) is chosen for the sliding boundary in each computational domain. Choosing the same amount of elements to discretise the boundary of each domain does not severely increase the computational cost. In turn, such strategy enables a very efficient treatment of the sliding plane interface that can even compensate for any undesired increase in resolution.

During the start-up of the simulation, and before the first iteration, the solver has access to a set of indices that identify all the element faces located at each side of the sliding plane interface by construction. Such indices are sorted: first, they are sorted depending on the layer they belong to, i.e. the plane $r = cnst$ or $z = cnst$ they belong to; then, for each layer, the indices are sorted from lower to higher azimuthal position of the element face.

To give an example, the sorting process for a two-dimensional rotor/stator simulation with four elements at each side of the sliding plane interface could lead to the following vectors (the element indices within the vectors are arbitrary):

101	28	2	93
5	140	89	6

Next, the algorithm finds the relative position between one element in the stator domain and its neighbouring elements in the rotor domain. The indices in the sorted arrays identify the element, while the data structures of the solver allow to easily gather the coordinates of the solution points at the element faces. Therefore, the azimuthal coordinate of a single point in one of the domains is compared to the azimuthal coordinates of points belonging to the opposite element faces residing in the same layer.

From this operation we obtain two results. Firstly, the pair of element faces to which each element is contiguous is found. This is because, due to the structured and uniform nature of the grid, once we find the correspondence between one element on one side of the sliding plane and the contiguous pair in the opposite side, the sorted arrays provide such information for the rest of element faces. Therefore, a new integer variable can be used to track the correspondence between the stator element face in the first position of the sorted stator vector and its opposing rotor element face. The tracking variable points to the position of such rotor face in the sorted rotor vector. Since each of the stator faces is adjacent to a pair of rotor faces, and since the rotor faces have been sorted, one may choose the tracking value to point to either the lowest or the highest of such indices, as long such definition is maintained for the rest of the simulation.

Following the previous example, if the relative position between the meshes were as depicted in Figure 2.3, the first result of the aforementioned operation would be finding out

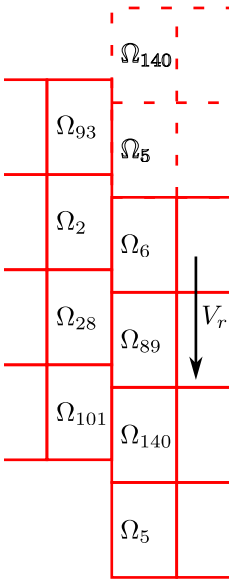

Figure 2.3: Sketch of a rotor/stator interface showing the correspondence between numbered elements at each side.

that element Ω_{101} faces the elements Ω_{140} and Ω_{89} from the opposite domain. By choosing the tracking variable to point to the lowest index among the pair of rotor faces in the sorted rotor vector, and bearing in mind that we are using zero-base numbering from the $C++$ programming language, the value of such variable would be 1.

Then, the algorithm is able to find the correspondence of every element in the stator vector by adding its index in such vector to the tracking variable. The result is used to look into the rotor vector at such a position as well as at the next one. Thus, the stator element at index 1, i.e. element Ω_{28}, is facing the rotor element located adding such index to the tracking variable, 1, and looking into indices 2 and 3 of the rotor vector, which store the values 89 and 6 (by $C++$ numbering standards).

Figure 2.3 also shows how the imposed spatial periodicity in the passages allows establishing the connection between elements that should be paired but are not topologically adjacent at a certain point in time. For example, by virtue of the spatial periodicity conditions, element Ω_{93} should face elements Ω_{140} and Ω_5, which have been replicated with dashed lines in the Figure 2.3. The algorithm takes this into consideration when the result of the tracking operations is greater or equal to the number of elements of the rotor vector, in which case substracts such a number, resulting in the correct correspondence.

The second result is the degree of superposition between two elements, $\theta_s \in (0, 1)$, which we define by the ratio between the surface of the intersection between two opposing element faces and the surface of one of such element faces.

Bearing in mind that both sides of the interface are uniformly meshed and feature the same number of elements, the degree of superposition is easily translated into the offset

for each pair of mortars: $o_i(t) = 0$ and $o_{i+1}(t) = 2\theta_s - 1$.

Moreover, the scaling of every mortar is readily available from the latter result: $s_i = \theta_s$ and $s_{i+1} = 1 - \theta_s$ for each of the two mortars, Ξ_i and Ξ_{i+1}, that are derived from each element (see Figure 2.2).

Therefore, by tracking the temporal evolution of the degree of superposition, which is due to the relative movement of the computational domains, mortar offsets and scalings can also be available throughout the simulation.

In fact, after each iteration, n, the value of θ_s (and the relative position of the meshes) is updated

$$\theta_s^{n+1} = \theta_s^n + \Delta t V_r / \Delta x_e \tag{2.91}$$

where V_r is the rotor speed, Δt is the time-step size, and Δx_e is the size of the elements at the sliding plane interface. At some point, θ_s will reach or surpass 1, which means that the correspondence between element faces at each side of the interfaces has changed. Then, the index tracking which rotor element was facing the first element in the sorted stator elements is incremented by 1, and θ_s is updated by $\theta_s^{n+1} = \theta_s^n + \Delta t V_r / \Delta x_e - 1$. It is worth noting that if the index reaches the last element of the rotor vector, the following updating process should set the index to the first element of such vector, since the passages are periodic.

For the particular case that $\theta_s = 1$, each face in one side of the sliding plane is coincident with another face in the opposite side. At such case, $s_{i+1} = 0$, the meshes become conformal, and the mortar method is only used to provide the face-to-face correspondence.

So far, an efficient sliding plane algorithm for the mortar method has been described. The not-so-severe mesh restriction on the nature of the grid at the interface (uniform and structured) is quite acceptable for 3D rotor/stator simulations of linear cascades, and enables a very efficient treatment of the data structures required for the mortar method. The majority of the workload is located at the start-up of the simulations, and only two small arrays of integers, a floating value θ_s, and an integer are needed to track the element face correspondence and the mortars' offsets and scalings.

Figures 2.4 (a) and 2.4 (b) show the verification process of the implementation of the algorithm in a two-dimensional test case. The subjects of the verification case are two T106 LPT airfoils, one of which was inverted to obtain a rotor/stator configuration of equal pitches. The computational domains are in a state of relative movement at a constant speed, and each side of the sliding plane interface was uniformly meshed with the same number of elements. The results showed no degradation of the solution after several through-flows.

Figure 2.4 (a) shows a snapshot of the static temperature isolines and field in such two-

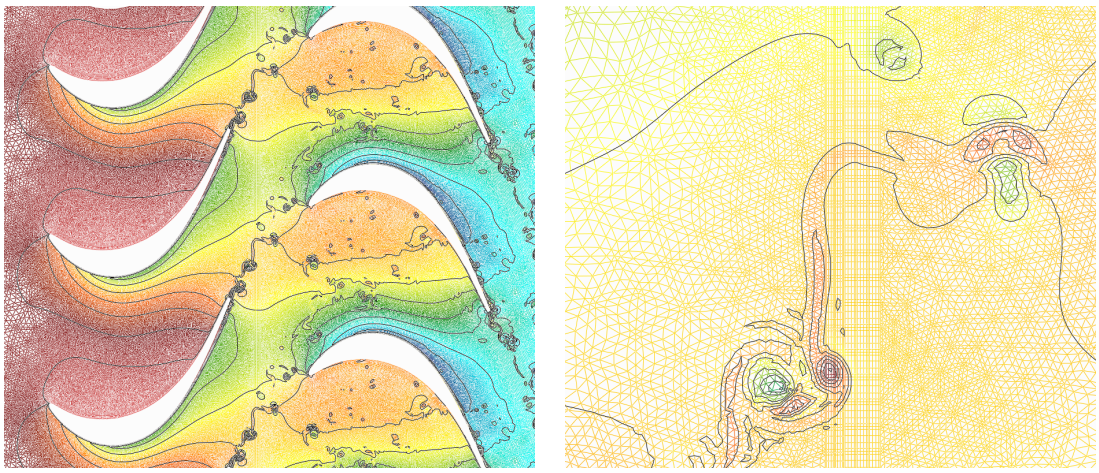

(a) General view (b) Sliding plane close-up

Figure 2.4: Static temperature isolines and field in a two-dimensional rotor/stator simulation of T106 profiles over a 6^{th}-order mesh. General view of the computational domain (a) and close-up of the non-conformal sliding plane interface (b).

dimensional rotor/stator simulation over a 6^{th}-order mesh. The solution has been extended several passages for visualization, since the simulation consisted on a single passage per blade. A close-up of the sliding plane interface can be observed in Figure 2.4 (b), which also shows the static temperature isolines crossing the non-conformal interface with no apparent degradation of the accuracy of the solution. The same conclusions are drawn from a snapshot of the entropy isolines at a different instant in Fig. 2.1 (a), where it can be observed how a vortex has recently crossed the interface without giving rise to noticeable spurious perturbations.

2.5 Temporal Integration

There are several temporal integration schemes implemented in the Mu^2s^2T suit of solvers, including implicit and explicit schemes. An explicit four-stage Runge-Kutta (RK) method was chosen to carry out the high-order simulations in the present thesis.

Implicit methods may offer significant speed-up factors. However, the unsteady nature of the simulations, the required temporal resolution and the memory cost of cases of interest justify the use of an explicit scheme. Additionally, explicit schemes are, in relative terms, computationally inexpensive, easy to understand, and very simple to implement.

The RK method is a family of iterative schemes, and each particular scheme can be identified by its number of stages and three sets of coefficients. For the present work, the classic fourth-order accurate explicit RK scheme (RK4) is used to advance the solution in time.

To introduce the RK4 scheme, first let us write the temporal derivative of the conservative

variables, $\mathbf{U}$, for the solution point j of element i as

$$\frac{d\mathbf{U}_{i,j}}{dt} = \mathbf{R}_{i,j}(\mathbf{U}(\mathbf{x}, t)), \tag{2.92}$$

where $\mathbf{R}_{i,j}$ contains all the inviscid and viscous fluxes, as well as any source terms, in the spatially discretised governing equations evaluated for the solution point j of element i.

The solution at a time $t = t_0 + n\Delta t$ can be written as $\mathbf{U}^n_{i,j}$, where n is the number of iterations and t_0 the time at the start of the time-marching, since the time step size Δt is fixed throughout the simulation.

Therefore, the RK4 scheme, which advances the solution in time ($\mathbf{U}^n_{i,j} \rightarrow \mathbf{U}^{n+1}_{i,j}$), can be written as

$$\mathbf{U}^{n+1}_{i,j} = \mathbf{U}^n_{i,j} + \frac{\triangle t}{6}\left[\mathbf{R}_{i,j}\left(\mathbf{U}^{(1}\right) + 2\mathbf{R}_{i,j}\left(\mathbf{U}^{(2}\right) + 2\mathbf{R}_{i,j}\left(\mathbf{U}^{(3}\right) + \mathbf{R}_{i,j}\left(\mathbf{U}^{(4}\right)\right] \tag{2.93}$$

where the solution at each stage m is denoted as $\mathbf{U}^{(m}$, and is obtained as follows:

$$\begin{aligned}
\mathbf{U}^{(1} &= \mathbf{U}^n \\
\mathbf{U}^{(2} &= \mathbf{U}^n + \tfrac{\triangle t}{2}\mathbf{R}_{i,j}\left(\mathbf{U}^{(1}\right) \\
\mathbf{U}^{(3} &= \mathbf{U}^n + \tfrac{\triangle t}{2}\mathbf{R}_{i,j}\left(\mathbf{U}^{(2}\right) \\
\mathbf{U}^{(4} &= \mathbf{U}^n + \triangle t\mathbf{R}_{i,j}\left(\mathbf{U}^{(3}\right)
\end{aligned} \tag{2.94}$$

It is worth noting that, due to the very small time-step sizes, which are characteristic of explicit high-order scale-resolving simulations, the summation in the right-hand side of Equation 2.93 is performed with the Kahan summation algorithm [125]. This algorithm minimises the potential round-off errors which might be present in such simulations. This problem may severely affect single precision simulations, especially for the long integration times associated to the statistical convergence of (unsteady) rotor/stator simulations.

The effects of neglecting the treatment of round-off errors in single precision simulations with the baseline solver are studied in [94], since such analysis lies outside the scope of the present thesis. Likewise, the interested reader may find the analysis of the numerical properties and stability of the FR schemes implemented in the baseline code in [94].

3 The Time-Inclined Method

Contents

3.1 Time-Inclined Method Formulation 65

3.2 Limitations of the Time-Inclined Method 70

3.3 The Viscous Problem 75

3.4 The Rotor/Stator Problem 79

3.5 The Time-Inclined Method in SRS 82

3.6 Implementation Into a High-Order Solver 85

In 1988, Giles [79] introduced the time-inclined method, which was developed and implemented into the UNSLFO code [88] to carry out unsteady analyses of wake/rotor interaction problems with arbitrary blade counts. Since then, many methodologies have been developed to reduce the computational cost associated to full-annulus simulations, as described in Chapter 1. However, the time-inclined method has several properties that differentiate it from the rest of domain reducing methods and make it worth consideration for scale-resolving simulations.

Firstly, it can be used in time-marching schemes, which are very characteristic of scale-resolving simulations. Secondly, it avoids directly imposing any temporal periodicity condition or approximating the time spectral content of the solution at the boundaries. Such property sets the time-inclined method apart from Fourier based approaches such as the shape correction method or the harmonic balance method, which require the user to pre-define a set of fundamental frequencies. The sum of the fundamental frequencies and their higher harmonics is assumed to approximate the solution, which allows its reconstruction at the periodic boundaries. Avoiding the direct imposition of temporal periodicity is key for the simulation of turbulent flows, where the solution is not only composed of some deterministic periodic signals, but also contains a stochastic component.

In 1996, shortly after the foundational paper of Giles [79], Jung et al. [80] carried out a three-dimensional viscous flow simulation using the time-inclined computational planes.

The method, implemented in a second-order finite volume scheme for structured meshes of hexahedral cells, enabled the simulation of turbomachinery stages of arbitrary pitch ratio in an affordable and efficient manner.

In 2007, Zhou et al. [81] compared the solutions of the time-inclined and the profile transformation approaches in the three-dimensional URANS simulation of the stage of a centrifugal compressor. The results were fairly similar, although the pitch ratio of the stage was very close to unity ($^{P_s}/_{P_r} = 1.0526$), and since the potential errors of both methodologies scale with such ratio, similar solutions could have been expected from both approaches.

Biesinger et al. [82] compared the time-inclined and phase-shift methodologies implemented in ANSYS CFX to a reference, full-annulus simulation of the T106D turbine cascade, deeming the former the superior computational approach. The TI method provided a speed-up factor of 16 times over the full-annulus simulation, while the phase-shift approach was 3 times slower than time-inclining. Some degradation of the convergence rate could have taken place for the phase-shift method, since the number of nodes in such case was twice of those of the TI domain (the dual passage method was employed), but the computational time was three times as large instead of two.

Connell et al. [83] also compared a full-wheel solution to the time-inclined, phase-lagged and profile transformation approaches in the context of RANS simulations of a LPT stage. The stage consisted of 19 rotor and 22 stator blades, and the results showed the time-inclined method leading to a better agreement with the full-annulus solution, while also showing significant savings in computational time.

In spite of its good qualities, the time-inclined method is not free from limitations, being one of the most apparent its range of applicability: solely single stage analyses. In the field of direct or quasi-direct numerical simulations, such a limitation might not pose a serious concern in the short term. Nevertheless, some efforts have been made for time-inclined URANS simulations towards circumventing the problem.

Cornelius et al. [84, 85] investigated an extension of the time-inclined method (in ANSYS CFX) for multi-stage analyses. They performed comparisons between time-inclined, profile transformation and full-annulus RANS simulations. Two sets of simulations were conducted: one set consisted on the front two and a half stages of a compressor, with the focus on evaluating the sensitivity of the methods to the degree of pitch change. The second set, involving a six-stage half scale industrial compressor, was aimed at studying the impact on stall prediction and excitation frequencies. The experimental and computational results from all methodologies agree very well, while the time-inclined predictions of the dominant frequencies stand-out compared to the profile transformation cases. The same approach was used for a 1.5 stage transonic modified compressor of Purdue Uni-

versity, reaching similar conclusions about the high efficiency of the TI method and its predictive capabilities for transient RANS simulations [87].

More recently, Hedge et al. [86] investigated the impact of multi-row interaction on the forced response behaviour of a rotor in a 3.5 stage compressor also using ANSYS CFX implementation of the time-inclined method, which enabled the conservation of an accurate frequency content across multiple domains.

Even though the method was developed more than 30 years ago, the core formulation of the method has not been improved nor thoroughly analysed. Moreover, in contrast to alternative and more popular passage-reducing methods, its use has been very limited. This is evidenced both by the shortage of scientific publications concerning its use and the very small amount of industrial or academic solvers that have implemented it.

For that matter, apart from introducing the time-inclined method and discussing its advantages and limitations, the present chapter includes other theoretical analyses that had not been published by other authors in the past, regarding: the potential sources of error of the method and the reconstruction of the synchronous perturbations captured in a time-inclined simulation. Additionally, since high-order solvers are very popular for scale-resolving simulations, this chapter includes a brief discussion on the impact of implementing the time-inclined method in a high-order baseline solver.

3.1 Time-Inclined Method Formulation

The time-inclined method can be categorised as a domain-reducing technique and has been briefly introduced in Chapter 1. Passage-reducing techniques aim to reduce the size of the computational domain while retaining an accurate representation of the geometry of the problem. As such, the time-inclined method leverages the identicalness of the blade passages that compose the rotors and stators to establish a periodic condition in a computational domain containing a single (or a few) blade passages.

The starting point of the TI method is the idea that, since all the blades in a rotor or stator row are identical, the relative movement between rows allows the formulation of lagged periodic conditions in the boundary of each airfoil passage.

Figure 3.1 shows an illustration of a typical turbine stage. In the stator's frame of reference, the rotor travels upwards with the wheel speed V while, from the rotor's reference frame, the incoming stator wakes travel downwards with such speed.

Since the geometry of the blades in each row is identical, we may derive the lagged periodic

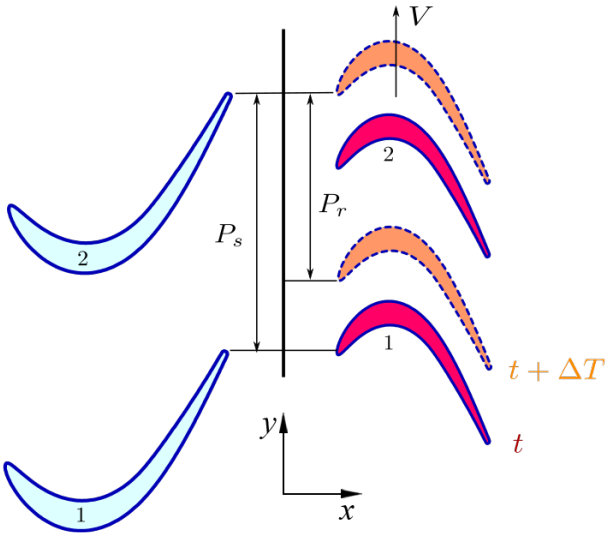

Figure 3.1: Nomenclature and illustration of a stator/rotor problem with unequal pitches.

condition for the rotor

$$\mathbf{U}(x, y, t) = \mathbf{U}(x, y + P_r, t + \Delta T), \tag{3.1}$$

which is called *lagged* because the spatial periodicity of a single passage is achieved at different points in time (t and $t + \Delta T$).

Equation 3.1 takes into consideration that, at instant t, the leading-edge of rotor 1 is in front of the trailing-edge of the stator 1 while the same is not true for rotor 2. The leading edge of rotor 2 is slightly downwards of the stator 2 and, therefore, rotor 1 and rotor 2 are not spatially periodic at the same point in time t due to the presence of the stator.

However, after some time, ΔT, the leading-edge of the rotor 2 faces the trailing-edge of the stator 2 and, thus, it is located in exactly the same relative position to the stator blades as the rotor 1 was at instant t. The time that has elapsed (or the *lag*) between these two situations, sketched in figure 3.1 with different colours, can be computed as

$$\Delta T = (P_s - P_r)/V \tag{3.2}$$

If the rotor and stator had the same number of blades, i.e. equal pitches, the boundary condition would no longer be *lagged*, since $\Delta T = 0$, and we would impose:

$$\mathbf{U}(x, y, t) = \mathbf{U}(x, y + P_r, t) \tag{3.3}$$

Requiring information solely from the current iteration is convenient for time-marching integration schemes, such as those used for scale-resolving simulations, and is the main feature that is sought after by the time-inclined method.

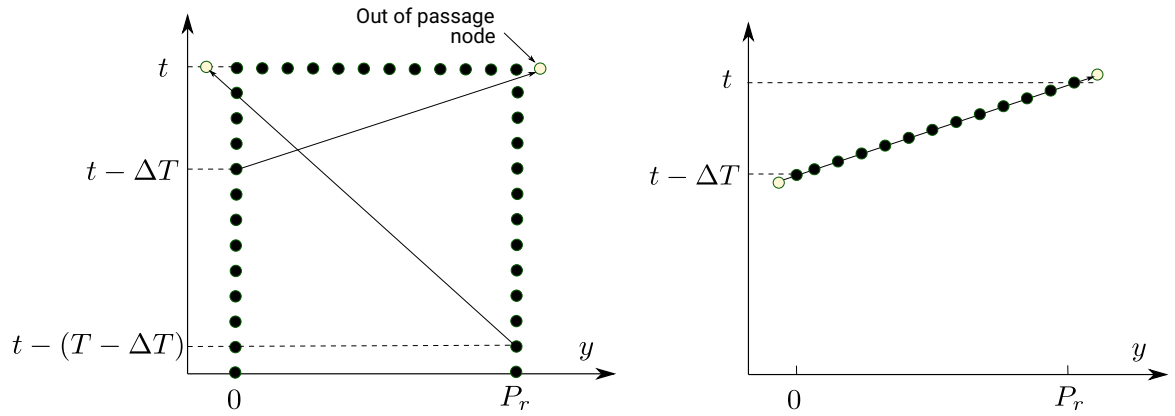

(a) Erdos' method (b) Time-inclined method

Figure 3.2: Representation of the computational domain for a problem of unequal pitches, where the solid circles (●) represent nodes storing the solution. Computational domain for Erdos' method (a) and time-inclined computational plane (b).

The first attempt at addressing rotor/stator interaction problems of arbitrary blade counts from the perspective of computational efficiency is attributed to Erdos et al. [62] in 1997. They followed a single passage approach for each row, and assumed the solution was temporally and spatially periodic. To impose the lagged periodic conditions, they proposed storing the solution in nodes at the periodic boundaries of the domain at earlier times. Thus, for the solution at the upper periodic line, $\mathbf{U}(\mathbf{x} = \mathbf{x}_u, t)$, in a two-dimensional domain such as that of Figure 3.1, the lagged periodic boundary condition would read

$$\mathbf{U}(\mathbf{x} = \mathbf{x}_u, t) = \mathbf{U}(\mathbf{x} = \mathbf{x}_l = \mathbf{x}_u - P_r, t - \Delta T) \tag{3.4}$$

whereas for the lower periodic line, the boundary condition would be imposed as

$$\mathbf{U}_l(\mathbf{x} = \mathbf{x}_l, t) = \mathbf{U}(\mathbf{x} = \mathbf{x}_u = \mathbf{x}_l + P_r, t + \Delta T) = \mathbf{U}(\mathbf{x} = \mathbf{x}_u = \mathbf{x}_l + P_r, t - (T - \Delta T)) \tag{3.5}$$

A representation of Erdos' method is sketched in Figure 3.2 (a) and, as shown in Eq. 3.5, the reference to the future time $t + \Delta T$ is resolved by the assumption that the flow is periodic with period $T = P_r/V$.

As pointed out by Giles [126], this statement probably does not hold in the presence of instabilities such as trailing-edge vortex shedding or compressor rotating stall, whose frequency is unlikely to be a multiple of the blade passing frequency. Moreover, the implementation of this method requires storing the solution at the periodic lines for a whole period (see Fig. 3.2 (a)) and, for common second-order spatial discretisations, it may even require storing also the solution of the neighbouring points of the periodic lines and their neighbours'.

Even if the lack of fulfilment of the temporal periodicity assumption is disregarded, the amount of storage that such method would require for scale-resolving simulations is inadmissible. SRSs are characterised by very small time-step sizes and fine meshes, which would lead to large amounts of data to be stored from many nodes at the periodic lines and from tens of thousands of iterations per blade passing period.

To avoid the flow periodicity assumption and the convergence problems that Erdos' method potentially posed from non-synchronous viscous flow instabilities, Giles proposed the idea of solving the governing equations in what he called *time-inclined computational planes* $(\mathbf{x}', \tau)$. For arbitrary blade count problems, the lagged periodic boundary condition is imposed at the same *inclined* time level in such computational planes, avoiding the necessity for information from the future and the direct imposition of temporal periodicity (see Fig. 3.2 (b)).

This means that any two nodes separated by the rotor blade pitch in the azimuthal coordinate, $|y_2 - y_1| = P_r$, would reside at the same time level τ in the computational planes. Thus, the lagged periodic boundary condition in the physical planes would not appear to be lagged in the inclined planes:

$$\mathbf{U}(x', y', \tau) = \mathbf{U}(x', y' + P_r, \tau) \tag{3.6}$$

To achieve such a result, Giles considered a transformation from the physical coordinates (x, y, z, t) to the computational coordinates (x', y', z', τ). The equations defining the transformation are

$$\begin{aligned} x' &= x \\ y' &= y \\ z' &= z \\ \tau &= t - \lambda y \end{aligned} \tag{3.7}$$

where the inclination parameter, λ, depends on the time lag in the lagged boundary condition, ΔT, and on the pitch of the transformed passage. For the rotor passage, the inclination parameter would be defined as:

$$\lambda = \frac{\Delta T}{P_r} = \frac{P_s - P_r}{V P_r}, \tag{3.8}$$

The transformation in Eq. 3.7 can be regarded as a grid mapping analogous to the one that is performed to map the governing equations from the physical domain to the transformed domain in structured solvers. The main difference is that time is deemed one more dimension and is transformed in the mapping process.

Through such a transformation, a computational time level is no longer fixed to a physical time, but sloped (i.e. **inclined**) in time such that a node located at a coordinate y resides

at the physical time t, while its corresponding periodic node at $y + P_r$ resides at the physical time $t + \Delta T$, as exemplified in Figure 3.2 (b).

Considering the transformation of the Euler equations, we obtain:

$$\frac{\partial \mathbf{Q}}{\partial \tau} + \frac{\partial \mathbf{f}}{\partial x'} + \frac{\partial \mathbf{g}}{\partial y'} + \frac{\partial \mathbf{h}}{\partial z'} = \mathbf{S}, \tag{3.9}$$

where $\mathbf{Q} = (q_1, q_2, q_3, q_4, q_5)^T$ are the new conservation (or *inclined*) variables, defined as $\mathbf{Q} = \mathbf{U} - \lambda \mathbf{g}$. Their relationship with the primitive variables can be written as:

$$\begin{aligned} q_1 &= \rho(1 - \lambda v) \\ q_2 &= q_1 u \\ q_3 &= q_1 v - \lambda p \\ q_4 &= q_1 w \\ q_5 &= \tfrac{1}{2} q_1 (u^2 + v^2 + w^2) + \tfrac{1}{\gamma - 1} p - \lambda \tfrac{\gamma}{\gamma - 1} p v \end{aligned} \tag{3.10}$$

The transformed governing equations in Eq. 3.9, show that the formulation of the fluxes remains unchanged. Therefore, at any iteration n during the execution of the time-inclined method, the values of the conservative variables $\mathbf{U}^n$ must be available to compute the fluxes, $\mathbf{f}^n(\mathbf{U}^n)$, so that the inclined variables can be advanced in time, $\mathbf{Q}^n \rightarrow \mathbf{Q}^{n+1}$.

Thus, obtaining the inverse relationship, $\mathbf{U} = f(\mathbf{Q})$, is the key to complete the time-inclined formulation. For a perfect gas, Giles found a closed algebraic form by eliminating $u = {q_2}/{q_1}$, $v = {(q_3 + \lambda p)}/{q_1}$ and $w = {q_4}/{q_1}$ from the last relation in Eq. 3.10, and arriving to:

$$a p^2 + 2bp + c = 0 \tag{3.11}$$

where

$$\begin{aligned} a &= (\gamma + 1)\lambda^2 \\ b &= -(q_1 - \lambda q_3) \\ c &= (\gamma - 1)(2 q_1 q_5 - (q_2^2 + q_3^2 + q_4^2)) \end{aligned} \tag{3.12}$$

The quadratic equation 3.11 has two solutions:

$$p = \frac{1}{a}\left(-b \pm \sqrt{b^2 - ac}\right) \tag{3.13}$$

However, the negative root is chosen as it yields the correct value for the limit $\lambda \rightarrow 0$, which represents the problem of equal pitches. Once p is obtained, the rest of primitive variables are available:

$$\rho = \frac{q_1}{1 - \lambda v} \quad ; \quad u = \frac{q_2}{q_1} \quad ; \quad v = \frac{q_3 + \lambda p}{q_1} \quad ; \quad w = \frac{q_4}{q_1} \tag{3.14}$$

Finally, we can recover the vector of conservative variables, $\mathbf{U} = \left[\begin{array}{ccccc} \rho & \rho u & \rho v & \rho w & \rho E \end{array} \right]^T$, since $\rho E = \frac{p}{(\gamma-1)} + \frac{1}{2}\left(\rho u^2 + \rho v^2 + \rho w^2\right)$.

3.2 Limitations of the Time-Inclined Method

There are four main concerns regarding the formulation of the time-inclined method for problems of arbitrary blade counts:

- Not any combination of pitch ratio and wheel speed can be used to reduce the problem to a single passage computational (inclined) domain. In other words, there is a limitation on the admissible inclination of the computational planes.
- The discretisation of the inclined equations may noticeably constrain the size of the maximum stable time step of the solver.
- The formulation of the inclined planes is limited to a single lagged periodic boundary condition, i.e. it is not conceived for multiple rows of unequal pitches.
- One of the cornerstones of the method in terms of computational efficiency is the inverse relationship between primitive and the inclined variables, $\mathbf{U} = f(\mathbf{Q})$, which has been obtained considering the governing equations for inviscid flow. However, such a simple algebraic relation does not hold for the inclined Navier-Stokes equations.

The first three concerns are intrinsic to the formulation and are referred to as limitations in the present thesis. Failing to take them in consideration leads to the inability of the method to work. However, the latter, i.e. *the viscous problem*, does not impede the use of the method in an approximate manner. Moreover, its study has been neglected in the literature since the original work of Giles. Thus, a section of the present chapter is dedicated to this topic.

3.2.1 Inclination of the Computational Planes

The first limitation of the method arises from a fundamental limit on the magnitude of the slope of the computational planes, λ. Using expressions 3.12 and 3.14, we can study the conditions under which the determinant of the square root in Eq. 3.13 is greater than zero. Bearing in mind the definition of the speed of sound is $a_0 = \sqrt{\gamma p/\rho}$,we arrive at the following condition for such determinant to be positive:

$$(1 - \lambda v)^2 > (\lambda a_0)^2 \tag{3.15}$$

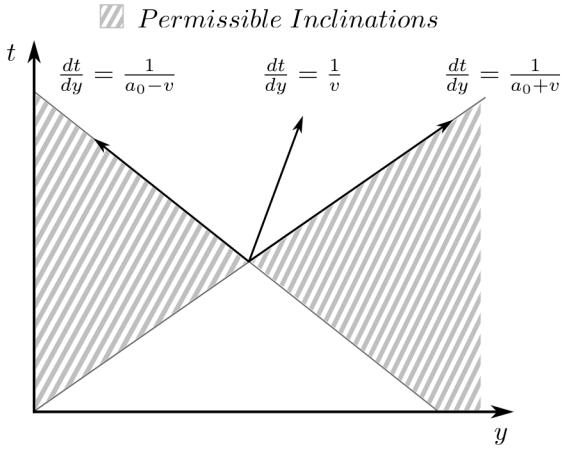

Figure 3.3: Characteristics of the Euler equations and regions of permissible inclination of the computational planes, λ.

If the flow is subsonic in the inclination direction, y, Equation 3.15 can be expressed in terms of the inclination parameter, λ, as

$$-\frac{1}{a_0 - v} < \lambda < \frac{1}{a_0 + v} \tag{3.16}$$

The lower and upper bounds for the slope of the inclined computational planes are coincident with two of the characteristics of the Euler equations. This is clearly a physical limitation of the method: beyond such inclinations, a signal propagating forwards in time in the physical plane would propagate backwards in time in the computational plane, while performing the computation in a forward time-marching scheme. Giles represents the permissible inclinations of the computational planes in a two-dimensional sketch featuring the characteristics of the Euler equations (see Figure 3.3).

The limit on the slope of the computational planes translates, in practice, to a limitation on the combinations of blade counts and wheel speeds which are admissible to perform the transformation of the rotor/stator problem to a one-to-one passage simulation in the time-inclined plane. Substituting the definition of $\lambda = {}^{(P_s - P_r)}/_{(V P_r)}$ in Eq. 3.16 yields the limit for the stator/rotor pitch ratio in terms of the Mach number of the rotor, $M_r = {}^{V}/_{a_0}$, and the Mach number in the inclination direction, $M_y = {}^{v}/_{a_0}$:

$$1 - \frac{M_r}{1 - M_y} < \frac{P_s}{P_r} < 1 + \frac{M_r}{1 + M_y} \tag{3.17}$$

Thus, for a given pitch ratio and rotor speed, Equation 3.17 can be used to obtain the maximum or minimum permissible non-dimensional speed of the flow in the transformed direction, M_y.

Nonetheless, the limitation can be overcome at the cost of including more passages in

the reduced domain. The formulation of the lagged periodic condition may include several rotor or stator passages, leading to a different magnitude of the inclination of the computational planes.

In general, an arbitrary blade count problem may be reduced to a combination of m rotor passages and n stator passages. The pair (m, n) can be chosen so that the ratio m/n approximates the actual pitch ratio P_s/P_r, while still minimising the size of the computational domain. Therefore, as put by Giles [126], the inclination λ makes up the difference between the actual pitch ratio and the chosen computational pitch ratio:

$$\lambda = \frac{\Delta T}{mP_r} = \frac{1}{mP_r}\frac{nP_s - mP_r}{V} = \frac{1}{V}\left(\frac{P_s}{P_r}/\frac{m}{n} - 1\right) \tag{3.18}$$

This problem was encountered by Jung et al. [80] in their simulation of the last stage of a low pressure turbine. The transformation of the stage, consisting of 44 stator blades and 60 rotor blades ($P_s/P_r = 1.364$) and a rotational speed of $12,600$ rpm, led to the violation of the stability condition. The authors found the most economical stable configuration to be two stator and three rotor passages.

It is worth noting that, if the typical LPT configuration is considered to be close to $P_s/P_r \approx 3/2$, then the worst case scenario for time-inclined simulations may entail including a total of five passages in the computational domain. In such case, it is expected the inclination of the computational planes to be minimal.

Requiring such an extensive computational domain contrasts with that of any alternative single-passage (per row) methodology. For example, the shape correction method only requires two passages in a single stage simulation. However, the convergence rate to a quasi-periodic state is generally hindered by such methodology. In contrast, no degradation of the convergence is expected from time-inclining (see Section 4.3 and Biesinger et al. [82]), which may compensate the difference in the size of the domain in terms of computational cost.

The dual-passage technique [127, 128] might be used to accelerate the convergence of the shape correction method at the price of including two passages per row for a total of four passages in the computational domain. Considering the limit case of retaining five passages in the simulation of a typical LPT configuration, the computational cost in terms of mesh size would be reduced by a 20% with respect to using the time-inclined method. Nevertheless, it is important to bear in mind that even if the convergence rate was similar to that achieved by the time-inclined approach, the direct imposition of temporal periodicity in turbulent flows would not be avoided with the shape correction method.

3.2.2 Time-Step Size

Let us consider the numerical solution of the linear wave equation on a periodic one-dimensional domain $x \in [0, L]$,

$$\frac{\partial u}{\partial t} + c\frac{\partial u}{\partial x} = 0, \tag{3.19}$$

where c is the propagation velocity. Assuming we perform the time-inclined transformation to solve it in a smaller computational domain, the transformed equation would read

$$(1 - \lambda c)\frac{\partial u}{\partial \tau} + c\frac{\partial u}{\partial x'} = 0, \tag{3.20}$$

which indicates that the effective propagation velocity of the wave is now $c_{eff} = {}^{c}/_{(1\text{-}\lambda c)}$, since Equation 3.20 can be arranged as:

$$\frac{\partial u}{\partial \tau} + \frac{c}{(1 - \lambda c)}\frac{\partial u}{\partial x'} = 0 \tag{3.21}$$

Bearing in mind that the time-step size stability limit of an explicit scheme is given by $c_{eff}\Delta t/\Delta x < \sigma_I$, where σ_I is a constant of order unity, there is a clear change in the permissible time-step sizes for the physical plane and the time-inclined schemes.

If we consider the numerical solution of the one-dimensional Euler equations in an explicit scheme, the maximum time-step size for subsonic flow is given by

$$\Delta t_{Max} = \sigma_I \Delta x \min\left(\frac{1}{a + u} - \lambda, \frac{1}{a - u} + \lambda\right) \tag{3.22}$$

since the eigenvalues of the linearised problem become $\left(\frac{u_0+a_0}{1-\lambda(u_0+a_0)}, \frac{u_0}{1-\lambda u_0}, \frac{u_0-a_0}{1-\lambda(u_0-a_0)}\right)$.

This limitation has an impact on the achievable speed-up factor of the time-inclined method. It directly translates to a higher amount of iterations needed to simulate a blade passing in the time-inclined scheme than in the baseline solver. However, as the inclination parameter tends to 0, the closer the maximum stable time-step sizes of the time-inclined and baseline solvers get.

In practice, higher inclination parameters may be justified due to large differences between the pitch ratio and its closest integer. In such a case, the savings in computational domain may make up for more stringent limitation of the time-step size. In other cases, such large inclinations may not fulfil the limitation on the slopes of the computational planes, leading to the presence of several passages in the inclined computational domain. As a consequence, the magnitude of λ is usually smaller and so is the time-step size limitation, which compensates for the extra blade passages in the inclined computational domains.

3.2.3 Multi-Stage Analysis

In a multi-stage problem where the blade counts of each row are different, the rotor/stator interfaces of each row must fulfil a different lagged periodic condition. Each pair of such conditions leads to a different inclined computational plane, which means that the governing equations for any row, excluding the first and the last, should be solved simultaneously in two different computational planes. Since this is not taken into consideration in the time-inclined formulation, it leads to the limitation of the time-inclined method to single-stage analyses.

This problem is most concerning for lower-fidelity simulations, where the cost of transient multi-stage simulations can be assumed in an industrial setting. However, for LES or quasi-DNS, three-dimensional simulations of moderately-high Reynolds number flow in a single passage are still very costly, and entail large computational times. The time-inclined limitation to single-stage analyses is not considered to be a serious concern in the short term, although multi-stage simulations may be the obvious next step after achieving the capacity for performing efficient and highly-accurate rotor/stator simulations.

Several authors have carried out multi-stage simulations with the so-called *time transformation* method of ANSYS CFX, which is based on the time-inclined method and commonly used for transient RANS simulations.

For example, transient simulations of the Siemens six stage 1/2 scale compressor test rig ("PCO Rig") on its 100% speed-line were conducted and compared to experimental and steady-state CFD results by Cornelius et al. [84]. The time transformation method was used for such a multi-stage problem. To circumvent the single-stage limitation of the time-inclined formulation, each pair of rotor and stator domains in a single stage were isolated and transformed, and a scaling of the profiles at the interface, i.e. the profile transformation method, was used to connect the solutions at both sides of the interfaces of the stages.

In [85], Cornelius et al. claimed that, in contrast to their previous work, all the interfaces in their time transformation simulations of the same six-stage compressor were modelled by the time transformation approach. Nevertheless, no description of how the limitation is overcome was provided, and it was only indicated that the single-stage method was extended by a blending procedure such that the temporal disturbances were accurately preserved across pitch change interfaces. Moreover, the authors presented frequency spectra for several solution monitors. The time transformation method was able to capture signals from neighbouring and distant rows, but also exhibited lower frequencies not present in the reference solution. Moreover, the amplitudes of the captured signals were, in general, different from those in the reference solution.

3.3 The Viscous Problem

So far, the time-inclined method has been applied to the Euler equations. The methodology has also been shown to be extremely simple, as it only entails one additional step to march in time the inclined variables vector: the recovery of the conservative variables from the inclined variables in order to compute the fluxes. The simplicity of the methodology is directly linked to that of such single step, since it only requires a few algebraic operations per computational node to be performed.

However, the governing equations in the problems of interest are the Navier-Stokes equations, which feature viscous terms. The transformation of such diffusive terms is as straightforward as that of the convective terms, but the resulting formulation of the inclined variables becomes troublesome.

The inclined Navier-Stokes equations are of the form:

$$\frac{\partial}{\partial\tau}\left(\mathbf{U}-\lambda\mathbf{g}+\lambda\mathbf{G}'+\lambda^2\widehat{\mathbf{G}}\right)+\frac{\partial\mathbf{f}}{\partial x'}+\frac{\partial\mathbf{g}}{\partial y'}+\frac{\partial\mathbf{h}}{\partial z'}=\frac{\partial\mathbf{F}'}{\partial x'}+\frac{\partial\mathbf{G}'}{\partial y'}+\frac{\partial\mathbf{H}'}{\partial z'}+\lambda\mathbf{T}+\mathbf{S} \tag{3.23}$$

where vectors $\mathbf{F}', \mathbf{G}'$ and $\mathbf{H}'$ represent the viscous fluxes expressed in terms of the conservative or primitive variables and their gradients in the inclined plane:

$$\begin{aligned}
\mathbf{F}' &= \begin{bmatrix}0 & \sigma_{x'x'} & \sigma_{y'x'} & \sigma_{z'x'} & \sigma_{x'x'}u+\sigma_{x'y'}v+\sigma_{x'z'}w-q'_{x'}\end{bmatrix}^T\\
\mathbf{G}' &= \begin{bmatrix}0 & \sigma_{x'y'} & \sigma_{y'y'} & \sigma_{z'y'} & \sigma_{y'x'}u+\sigma_{y'y'}v+\sigma_{y'z'}w-q'_{y'}\end{bmatrix}^T\\
\mathbf{H}' &= \begin{bmatrix}0 & \sigma_{x'z'} & \sigma_{y'z'} & \sigma_{z'z'} & \sigma_{z'x'}u+\sigma_{z'y'}v+\sigma_{z'z'}w-q'_{z'}\end{bmatrix}^T
\end{aligned} \tag{3.24}$$

The extra terms in 3.23 arise from the transformation of the stress tensor σ and heat flux vector $\mathbf{q}$:

$$\begin{aligned}
\sigma_{xx} &= \mu\left(\tfrac{4}{3}\tfrac{\partial u}{\partial x}-\tfrac{2}{3}\tfrac{\partial v}{\partial y}-\tfrac{2}{3}\tfrac{\partial w}{\partial z}\right)=\mu\left(\tfrac{4}{3}\tfrac{\partial u}{\partial x'}-\tfrac{2}{3}\tfrac{\partial v}{\partial y'}-\tfrac{2}{3}\tfrac{\partial w}{\partial z'}\right)+\tfrac{2}{3}\mu\lambda\tfrac{\partial v}{\partial\tau}=\sigma_{x'x'}+\tfrac{2}{3}\mu\lambda\tfrac{\partial v}{\partial\tau}\\
\sigma_{xy} &= \sigma_{yx}=\mu\left(\tfrac{\partial u}{\partial y}+\tfrac{\partial v}{\partial x}\right)=\mu\left(\tfrac{\partial u}{\partial y'}+\tfrac{\partial v}{\partial x'}\right)-\mu\lambda\tfrac{\partial u}{\partial\tau}=\sigma_{x'y'}-\mu\lambda\tfrac{\partial u}{\partial\tau}\\
\sigma_{xz} &= \sigma_{zx}=\mu\left(\tfrac{\partial u}{\partial z}+\tfrac{\partial w}{\partial x}\right)=\mu\left(\tfrac{\partial u}{\partial z'}+\tfrac{\partial w}{\partial x'}\right)=\sigma_{x'z'}\\
\sigma_{yy} &= \mu\left(-\tfrac{2}{3}\tfrac{\partial u}{\partial x}+\tfrac{4}{3}\tfrac{\partial v}{\partial y}-\tfrac{2}{3}\tfrac{\partial w}{\partial z}\right)=\mu\left(-\tfrac{2}{3}\tfrac{\partial u}{\partial x'}+\tfrac{4}{3}\tfrac{\partial v}{\partial y'}-\tfrac{2}{3}\tfrac{\partial w}{\partial z'}\right)-\tfrac{4}{3}\mu\lambda\tfrac{\partial v}{\partial\tau}=\sigma_{y'y'}-\tfrac{4}{3}\mu\lambda\tfrac{\partial v}{\partial\tau}\\
\sigma_{yz} &= \sigma_{zy}=\mu\left(\tfrac{\partial v}{\partial z}+\tfrac{\partial w}{\partial y}\right)=\mu\left(\tfrac{\partial v}{\partial z'}+\tfrac{\partial w}{\partial y'}\right)-\mu\lambda\tfrac{\partial w}{\partial\tau}=\sigma_{y'z'}-\mu\lambda\tfrac{\partial w}{\partial\tau}\\
\sigma_{zz} &= \mu\left(-\tfrac{2}{3}\tfrac{\partial u}{\partial x}-\tfrac{2}{3}\tfrac{\partial v}{\partial y}+\tfrac{4}{3}\tfrac{\partial w}{\partial z}\right)=\mu\left(-\tfrac{2}{3}\tfrac{\partial u}{\partial x'}-\tfrac{2}{3}\tfrac{\partial v}{\partial y'}+\tfrac{4}{3}\tfrac{\partial w}{\partial z'}\right)+\tfrac{2}{3}\mu\lambda\tfrac{\partial v}{\partial\tau}=\sigma_{z'z'}+\tfrac{2}{3}\mu\lambda\tfrac{\partial v}{\partial\tau}\\
q_x &= \kappa\tfrac{\partial T}{\partial x}=\kappa\tfrac{\partial T}{\partial x'}=q'_{x'}\\
q_y &= \kappa\tfrac{\partial T}{\partial y}=\kappa\tfrac{\partial T}{\partial y'}-\kappa\lambda\tfrac{\partial T}{\partial\tau'}=q'_{y'}-\kappa\lambda\tfrac{\partial T}{\partial\tau}\\
q_z &= \kappa\tfrac{\partial T}{\partial z}=\kappa\tfrac{\partial T}{\partial z'}=q'_{z'}
\end{aligned} \tag{3.25}$$

Expressing the viscous fluxes $\mathbf{G}$ (see Section 2.1.3) in the inclined plane gives rise to $\mathbf{G}'$

and $\lambda\widehat{\mathbf{G}} = \begin{bmatrix} \widehat{G}_1 & \widehat{G}_2 & \widehat{G}_3 & \widehat{G}_4 & \widehat{G}_5 \end{bmatrix}^T$

$$\begin{aligned}
\widehat{G}_1 &= 0 \\
\widehat{G}_2 &= -\mu\tfrac{\partial u}{\partial \tau} \\
\widehat{G}_3 &= -\tfrac{4}{3}\mu\tfrac{\partial v}{\partial \tau} \\
\widehat{G}_4 &= -\mu\tfrac{\partial w}{\partial \tau} \\
\widehat{G}_5 &= u\left(-\mu\tfrac{\partial u}{\partial \tau}\right) + v\left(-\tfrac{4}{3}\mu\tfrac{\partial v}{\partial \tau}\right) + \\
&\quad + w\left(-\mu\tfrac{\partial w}{\partial \tau}\right) + \kappa\tfrac{\partial T}{\partial \tau}
\end{aligned} \tag{3.26}$$

In Eq. 3.23, $\frac{\partial}{\partial \tau}\left(-\lambda\mathbf{g} + \lambda\mathbf{G}' + \lambda^2\widehat{\mathbf{G}}\right)$ arises from the temporal component of the transformation ($\partial/\partial y = \partial/\partial y' - \lambda\partial/\partial \tau$), while the inclined spatial derivatives of the new terms $\widehat{\mathbf{F}}, \widehat{\mathbf{G}}$ and $\widehat{\mathbf{H}}$ are grouped in vector $\mathbf{T} = \begin{bmatrix} T_1 & T_2 & T_3 & T_4 & T_5 \end{bmatrix}^T$:

$$\begin{aligned}
T_1 &= 0 \\
T_2 &= \tfrac{\partial}{\partial x'}\left(\tfrac{2}{3}\mu\tfrac{\partial v}{\partial \tau}\right) + \tfrac{\partial}{\partial y'}\left(-\mu\tfrac{\partial u}{\partial \tau}\right) \\
T_3 &= \tfrac{\partial}{\partial x'}\left(-\mu\tfrac{\partial u}{\partial \tau}\right) + \tfrac{\partial}{\partial y'}\left(-\tfrac{4}{3}\mu\tfrac{\partial v}{\partial \tau}\right) + \tfrac{\partial}{\partial z'}\left(-\mu\tfrac{\partial w}{\partial \tau}\right) \\
T_4 &= \tfrac{\partial}{\partial y'}\left(-\mu\tfrac{\partial w}{\partial \tau}\right) + \tfrac{\partial}{\partial z'}\left(\tfrac{2}{3}\mu\tfrac{\partial v}{\partial \tau}\right) \\
T_5 &= \tfrac{\partial}{\partial x'}\left(u\tfrac{2}{3}\mu\tfrac{\partial v}{\partial \tau} - v\mu\tfrac{\partial u}{\partial \tau}\right) + \tfrac{\partial}{\partial y'}\left(-u\mu\tfrac{\partial u}{\partial \tau} - v\tfrac{4}{3}\mu\tfrac{\partial v}{\partial \tau} - w\mu\tfrac{\partial w}{\partial \tau} + \kappa\tfrac{\partial T}{\partial \tau}\right) + \\
&\quad + \tfrac{\partial}{\partial z'}\left(-v\mu\tfrac{\partial w}{\partial \tau} + w\tfrac{2}{3}\mu\tfrac{\partial v}{\partial \tau}\right)
\end{aligned} \tag{3.27}$$

Then, the transformation of the Navier-Stokes equations no longer leads to a simple relation between the inclined and conservatives variables. Even if the temporal derivatives in $\mathbf{T}$ could be extracted to express it as $\mathbf{T} = \frac{\partial}{\partial \tau}\widetilde{\mathbf{T}}$, the problem of obtaining a closed relation between the new viscous inclined variables, $\mathbf{Q}_{vis}$, and the conservative variables, $\mathbf{U}$, would still be present, since the former would depend of the primitive variables and their gradients:

$$\mathbf{Q}_{vis} = \mathbf{U} - \lambda\mathbf{g} + \lambda\mathbf{G}' + \lambda^2\widehat{\mathbf{G}} - \lambda\widetilde{\mathbf{T}} = f\left(\mathbf{U}, \frac{\partial \mathbf{U}}{\partial x'}, \frac{\partial \mathbf{U}}{\partial y'}, \frac{\partial \mathbf{U}}{\partial z'}\right) \tag{3.28}$$

Moreover, if we assumed the dynamic viscosity μ to be independent from the temperature, T, the energy equation would still include non-linear terms such as $\frac{\partial}{\partial x'}\left(u\frac{2}{3}\mu\lambda\frac{\partial v}{\partial \tau}\right)$, which cannot be expressed as the temporal derivative of a function that only depends of the primitive variables and their gradients.

It can be observed that the expressions for the viscous fluxes in the inclined plane, $\mathbf{F}', \mathbf{G}'$ and $\mathbf{H}'$, remain identical to those of the physical plane. This allows the part of the algorithm in charge of the computation of the standard viscous fluxes to remain unchanged. In this regard, the formulation of the time-inclined method for the Navier-Stokes equations is similar to that of the Euler equations, which required no alterations of the baseline

algorithm to compute the fluxes.

To this day, there have been no new developments to tackle the viscous problem of recovering $\mathbf{U}$ from an appropriate formulation of $\mathbf{Q}_{vis}$. Then, to circumvent it, and as originally proposed by Giles, any term containing temporal derivatives and stemming from a viscous flux is not included in the transformation of the Navier-Stokes equations. By means of such truncation, the transformed NS equations are:

$$\frac{\partial}{\partial\tau}\left(\mathbf{U}-\lambda\mathbf{g}\right)+\frac{\partial\mathbf{f}}{\partial x'}+\frac{\partial\mathbf{g}}{\partial y'}+\frac{\partial\mathbf{h}}{\partial z'}=\frac{\partial\mathbf{F}'}{\partial x'}+\frac{\partial\mathbf{G}'}{\partial y'}+\frac{\partial\mathbf{H}'}{\partial z'}+\mathbf{S}, \tag{3.29}$$

leading to the same conservation variables as in the transformation of the Euler equations, $\mathbf{Q}=\mathbf{U}-\lambda\mathbf{g}$. Thus, the closed algebraic form that can be derived from expressions 3.12 to 3.14 can be used to recover $\mathbf{U}$ from the inclined variables $\mathbf{Q}$.

The incomplete transformation of the viscous terms was instrumental in speeding up the development of a time-inclined formulation in a high-order solver for SRSs. Developing a scheme that retains all the viscous terms in the transformed NS equations may improve the accuracy of the time-inclined method, especially for operating conditions featuring low Reynolds numbers and regions of high local Strouhal numbers, as will be discussed next. Since the neglected terms depend on the temporal derivative of the flow gradients and the second temporal derivative of the primitive variables, a possible approach might be to iteratively converge the equation that links the inclined and conservative variables after each iteration of the baseline solver. Other possible methods could rely on approximating the aforementioned temporal derivatives with information from previous time steps or on modelling the effects of the neglected terms in the regions of the flow where they become relevant. Nevertheless, the truncated approach has been shown to be a valid approximation for the flows of interest [129, 130] and is the chosen methodology for the present work.

3.3.1 Analysis of the Viscous Approximation

The question that remains to be answered is under which circumstances the chosen approach is an acceptable approximation for the Navier-Stokes equations. To that end, let us consider the momentum equation in the TI plane (assuming $\mu = cnst$):

$$(1-\lambda v)\frac{\partial\mathbf{v}}{\partial\tau}+\mathbf{v}\nabla\mathbf{v}=-\frac{1}{\rho}\nabla p-\lambda p_t\mathbf{j}+\nu\,(\underbrace{\nabla^2\mathbf{v}}_{(4)}-2\lambda\underbrace{\frac{\partial^2\mathbf{v}}{\partial\tau\partial y'}}_{(5)}+\lambda^2\underbrace{\frac{\partial^2\mathbf{v}}{\partial\tau^2}}_{(6)}) \tag{3.30}$$

The *unsteady* viscous terms (5) and (6), which are neglected within the framework of the present TI method implementation, can be regarded as error terms since they become

null in the limit $\lambda \to 0$. Comparing the order of magnitude of the term (5) with respect to (4), we arrive at

$$\frac{(5)}{(4)} \sim \frac{\lambda v_c f_c / L_c}{v_c / L_c^2} \sim \lambda f_c L_c = St \tag{3.31}$$

where v_c is the characteristic speed of the problem, f_c the characteristic frequency, and St the Strouhal number of the problem being dealt with. The inclination parameter λ has the units of the inverse of a velocity, and for stability reasons $\tilde{\lambda} = \lambda v_{\text{exit}}$ is at most of the order unity, i.e. $\tilde{\lambda} \sim \mathcal{O}(1)$, being v_{exit} the exit velocity of the cascade.

Analogously, the order of magnitude of the term (6) with respect to the (4) is

$$\frac{(6)}{(4)} \sim \frac{\lambda^2 v_c f_c^2}{v_c / L_c^2} \sim (\lambda f_c L_c)^2 = St^2 \tag{3.32}$$

and therefore, this term is higher or lower than term (5), depending on whether St is greater or less than one.

Inlet region and airfoil passage

Assuming that the Strouhal or reduced frequency of the forcing is $St_f = f_f c / v_{\text{exit}} \sim \mathcal{O}(1)$ where f_f is the frequency of the incoming perturbation, and c the airfoil chord which is typically similar to the airfoil pitch. This effectively means that the decay of the incoming wake due to viscous effects is altered in the TI plane. However, this impact is small for high Reynolds number flows due to the wake decay between the trailing edge of the preceding airfoil and the leading edge, and along the airfoil passage being small since $St_f Re_f \gg 1$. The Rapid Distortion Theory (RDT) [131] of turbulence requires the same condition, which essentially states that vortices pass through the cascade without attenuation nor interaction since the diffusion time is much longer than the residence time in the airfoil. Such assumption has been used successfully in broadband rotor/stator interaction noise simulations [132] [133].

Laminar boundary layers

The characteristic length of a laminar boundary layer (BL) is its thickness, δ, which is much smaller than the characteristic length of the perturbations that has been taken as the airfoil chord. The characteristic velocity in the boundary layer is v_{exit} since this is the origin of the shear in the BL. The characteristic time of the oscillations in the BL is the same as that of the forcing, and hence

$$St_{BL} = \frac{f_f \delta}{v_{\text{exit}}} = St_f \frac{\delta}{c} \sim St_f \frac{1}{Re_c^{1/2}} \tag{3.33}$$

which is small if the Reynolds number is high enough. Thus, the conclusion is that the evolution of an unsteady laminar boundary layer is properly resolved using the TI transformation.

Vortex Shedding

In this case, the characteristic length is the trailing edge thickness, t_{TE}, which is typically similar to the boundary layer thickness, $t_{TE} \sim \delta$. The main difference here, however, is that the frequencies associated with the flow oscillation in the trailing edge are much higher than that of the forcing since

$$St_{TE} = \frac{f_{TE} t_{TE}}{v_{\text{exit}}} \sim \mathcal{O}(1)$$

Therefore, the neglected viscous terms are as important as the retained terms so the approximation is inconsistent. It will be shown in the next chapter that discrepancies between the exact and TI solutions in the mixing process behind a 2D plate can be noticed due to this problem. Nevertheless, it is worth noting that due to the viscous nature of the truncated terms, their relevance is also modulated by the local Reynolds number. Chapter 5, which features 3D simulations of linear cascades of LPT blades, shows that the impact of the truncated terms in the vortex shedding region is minimal and very local. The moderately high Reynolds number of the problem and the quick transition of the vortices to a turbulent wake limit the size of the affected region and the magnitude of the errors.

3.4 The Rotor/Stator Problem

The time-inclined formulation in Section 3.1 describes how to transform the computational domain of a few rotor or stator passages such that they can accommodate the space-time periodicity of the full rotor/stator problem with unequal pitches. The methodology allows to reproduce such a rotor or stator row in a reduced and periodic computational domain, in which the unsteady perturbations from the contiguous row enter the domain through the boundary.

However, to include both the rotor and stator rows in the simulation, each domain must be transformed to the time-inclined computational planes accordingly. Due to their unequal pitches, the lagged periodic boundary condition is different in the rotor and stator (see Fig. 3.1):

$$\mathbf{U}^{rotor}(x, y, t) = \mathbf{U}^{rotor}(x, y + P_r, t + \Delta T), \tag{3.34}$$

$$\mathbf{U}^{stator}(x, y, t) = \mathbf{U}^{stator}(x, y + P_s, t + \Delta T), \tag{3.35}$$

where the time lag is $\Delta T = (P_s - P_r)/V$. Consequently, each row is differently inclined in order to transform its respective lagged periodic condition into a spatial periodicity condition for the reduced computational domains:

$$\lambda^{rotor} = \frac{\Delta T}{P_r} \tag{3.36}$$

$$\lambda^{stator} = \frac{\Delta T}{P_s} \tag{3.37}$$

As usual, the (inclined) equations are marched in the inclined time τ. This is an important detail in rotor/stator simulations: in the time-inclined computational planes, the unequal pitch problem becomes an equal pitch problem, for which the blade passing period is the same[1] when considered from the stator or the rotor frame of reference. However, in the physical planes, the blade passing periods in each of the row's frames of reference are $T_r = {}^{P_s}/_{V}$ and $T_s = {}^{P_r}/_{V}$.

The number of inclined time-steps, n, to fulfil a full period simulation is unique. Therefore, the physical time-step sizes are related by:

$$\frac{n\Delta t_s}{n\Delta t_r} = \frac{T_s}{T_r} = \frac{P_r}{P_s} \tag{3.38}$$

Which indicates that unequal pitches lead to different inclination parameters, and therefore to different time-step sizes in each domain, ${}^{\Delta t_s}/_{\Delta t_r} = {}^{P_r}/_{P_s}$.

Following the example of Giles [88], Figure 3.4 shows a (y, t) diagram of the rotor/stator interface and the inclined computational plane.

The vertical axis, which corresponds to $y = 0$, and the green vertical lines delimit the pitch of the stator. Blue solid lines are tilted due to the rotor moving with constant speed V with respect to the stator domain. It can be observed that both rotor and stator interfaces are uniformly divided into four elements, but due to the differences in pitch, the grid spacings are different: $\Delta y_r \neq \Delta y_s$. Dashed green and blue lines track the azimuthal location of the element interfaces in the physical plane (y, t).

After time-inclining the rotor and stator domains, the computational plane becomes the red solid line. On such a plane, one can see that even though the rotor and stator pitches are different, their boundaries coincide after every $T + \Delta T$ in physical time. Furthermore, even though the rotor and stator grid spacings are different in the physical planes, they become equal in the inclined computational plane (see the triple intersections between

[1]Bear in mind that, in the inclined computational plane, the relative speed of the opposite row is seen altered due to the time-inclination, and that the rotor and stator rows are differently inclined.

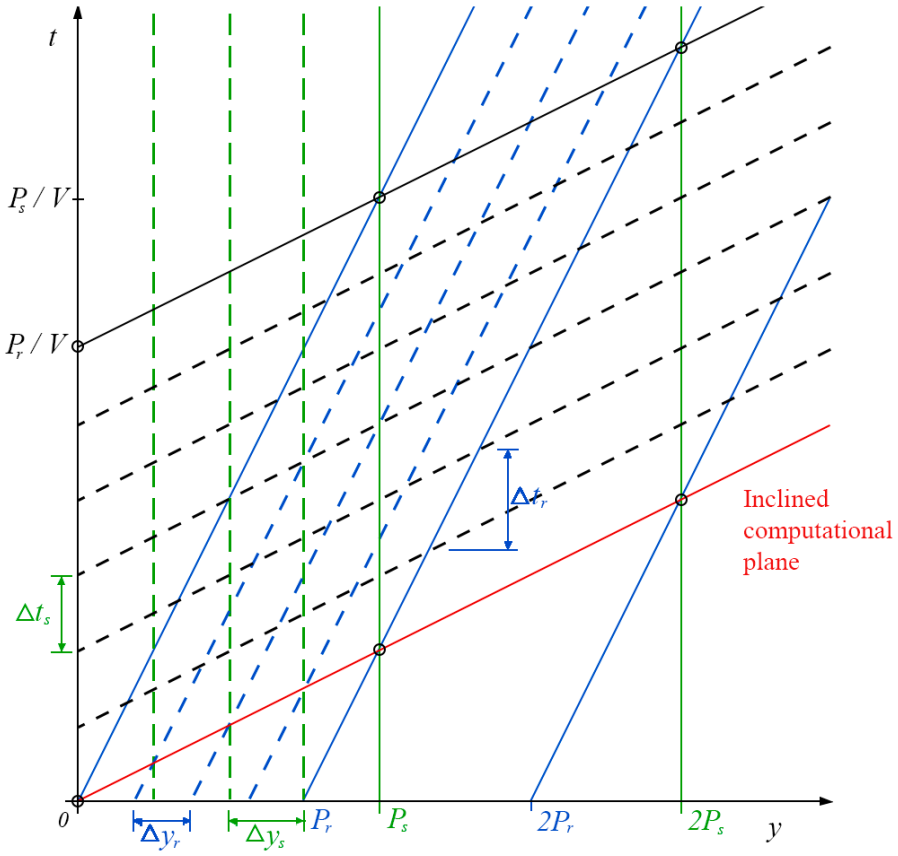

Figure 3.4: Rotor/stator interface diagram.

the green and blue dashed lines and the red solid line in Figure 3.4).

Thus, different inclination parameters ensure that the interfaces of both domains lie in the same inclined computational plane. There, the unequal pitches of the rotor and stator are equal. Moreover, it will be shown next that each domain can reproduce the spectral content of the opposite row, i.e., the spatially periodic components of the solution in the stator also fit in the inclined rotor domain and vice versa.

Therefore, the transference of information between two domains of different sizes is straightforward in the time-inclined computational plane. There the problem is identical to the transference of information in a rotor/stator problem of equal pitches. Consequently, the algorithm to transfer the solution from one row to the other is to scale (either expand or contract) the solution in the transformation direction similarly to the profile transformation method.

The use of the time-inclined method for a rotor (or stator) domain subjected to perturbations from the preceding row is very computationally efficient since, apart from the reduction in the size of the computational domain, only the algebraic operations to transform back the inclined to conservative variables are added to the algorithm. This level of

efficiency is also characteristic of time-inclined rotor/stator simulations due to the simplicity of the scaling procedure that allows transferring the information from one side of the interface plane to the other.

Moreover, if the interface plane boundary in each of the rows is divided into uniformly spaced elements, then the problem becomes even more simple in the time-inclined computational plane: it becomes a rotor/stator problem with equal pitches and uniformly spaced elements of the same size at each side of the interface, as in the former example.

Finally, bearing in mind the methodology described in Section 2.4, the algorithm for such a problem becomes very efficient, with minimal use of computational resources. Therefore, the use of the time-inclined method for rotor/stator simulations can also contribute to the simplification of the treatment of non-conformal interfaces, since it is carried out in the inclined plane, where such interfaces become conformal.

3.5 The Time-Inclined Method in SRS

In rotor/stator scale-resolving simulations, the flow-field may be decomposed in steady, synchronous and non-synchronous signals to which a stochastic component is superimposed. The steady part of the solution, described in a frame of reference fixed to the rotor, contains spatial harmonics which are multiples of the rotor pitch, and takes the form:

$$\mathbf{U}^r(\mathbf{x}) = \sum_m \widehat{\mathbf{U}}^r_m e^{ImN_r\theta}, \tag{3.39}$$

where the angular wave-number $N_r = {}^{2\pi}/_{P_r}$, and P_r is the pitch of the rotor. The time-inclined transformation has no effect on steady perturbations, and therefore they remain unchanged in the inclined computational planes.

Since the frame of reference is relative to the rotor, some of the synchronous unsteady perturbations in the flow-field correspond to travelling waves with the spatial harmonics and passing frequency of the stator:

$$\mathbf{U}^s(\mathbf{x}, t) = \sum_n \widehat{\mathbf{U}}^s_n e^{InN_s(\theta+\Omega t)} \tag{3.40}$$

Such signals are indeed spatial harmonics of the stator and do not fit in a single passage domain of the rotor's pitch. The application of the time-inclined method for the rotor takes into consideration the temporal lag, $\Delta T = \frac{P_s - P_r}{\Omega}$, which is used to compute the appropriate inclination parameter, $\lambda = \frac{\Delta T}{P_r}$. Bearing in mind such definition, the periodic perturbations due to the relative movement of the stator can be expressed in the time-

inclined computational planes as:

$$\mathbf{U}^s(\mathbf{x}',\tau) = \sum_n \widehat{\mathbf{U}}^s_n e^{InN_s(\theta'+\Omega\tau+\Omega\lambda\theta')} = \sum_n \widehat{\mathbf{U}}^s_n e^{InN_s(\theta'+\Omega\tau+\Omega\frac{P_s-P_r}{P_r\Omega}\theta')} = \sum_n \widehat{\mathbf{U}}^s_n e^{InN_s(\Omega\tau+\frac{P_s}{P_r}\theta')} \tag{3.41}$$

Since the whole annulus is composed of either N_s stator passages or N_r rotor blades, it follows that

$$2\pi = P_s N_s = P_r N_r, \tag{3.42}$$

which allows expressing Equation 3.41 as:

$$\mathbf{U}^s(\mathbf{x}',\tau) = \sum_n \widehat{\mathbf{U}}^s_n e^{InN_s\frac{N_r}{N_s}\theta'+InN_s\Omega\tau} = \sum_n \widehat{\mathbf{U}}^s_n e^{In(N_r\theta'+N_s\Omega\tau)} \tag{3.43}$$

Thus, the synchronous stator perturbations, composed of spatial harmonics of the stator pitch (see Eq. 3.40), are transformed into synchronous perturbations with spatial harmonics of the rotor pitch in the inclined computational planes. It is worth noting how the perturbation speed is modified in the inclined computational planes, but the frequency of the perturbations remains unchanged.

Another kind of synchronous perturbations originate from the so-called Tyler-Sofrin (TS) modes which, in the physical plane, take the form:

$$\mathbf{U}^{TS}(\mathbf{x},t) = \sum_{m,n} \widehat{\mathbf{U}}^{TS}_{m,n} e^{I[(nN_s\pm mN_r)\theta+nN_s\Omega t]} \tag{3.44}$$

In the time-inclined planes, however, the TS perturbations are transformed into:

$$\mathbf{U}^{TS}(\mathbf{x}',\tau) = \sum_{m,n} \widehat{\mathbf{U}}^{TS}_{m,n} e^{I\left[(nN_s\pm mN_r)\theta'+nN_s\Omega\tau+nN_s\Omega\frac{P_s-P_r}{P_r\Omega}\theta'\right]} \tag{3.45}$$

which can be simplified into

$$\mathbf{U}^{TS}(\mathbf{x}',\tau) = \sum_{m,n} \widehat{\mathbf{U}}^{TS}_{m,n} e^{I[(n\pm m)N_r\theta'+nN_s\Omega\tau]} \tag{3.46}$$

This result is especially interesting since it indicates that the TS modes of the form $nN_s - mN_r$ with $m = n$, $\mathbf{U}^{TS-}_{m=n}$, are not seen as spatial harmonics of the rotor pitch in the time-inclined computational planes:

$$\mathbf{U}^{TS-}_{m=n}(\tau) = \widehat{\mathbf{U}}^{TS-}_{n,n} e^{InN_s\Omega\tau} \tag{3.47}$$

Such perturbations would rather appear in the inclined computational planes as uniform perturbations, and would be identified by their frequency, $nN_s\Omega$, which is a multiple of

the stator-passing frequency. However, Equation 3.46 shows that they are retained in the time-inclined formulation. Moreover, Eq. 3.46 shows that TS perturbations which are longer than the inclined, **reduced**, computational domain are *coded* into another spatial harmonic of the transformed domain, allowing the time-inclined method to retain them.

For example, Chapter 5 features a rotor/stator problem in which a computational domain of $N_r = 4$ blades are subjected to $N_s = 7$ incoming upstream perturbations. A single passage cannot accommodate the periodicity of the incoming perturbations in the physical plane, since the pitch ratio, 7/4, is not an integer. Nevertheless, the time-inclined method can compensate the difference such that the pitch ratio becomes $8/4 = 2$, and the simulation can be performed in a single passage fitting 2 perturbations. Then, a TS mode stemming from $n = 1$ and $m = -2$ would be of the form:

$$\begin{aligned}\widehat{\mathbf{U}}^{TS}_{-2,1} e^{I[(N_s-2N_r)\theta+N_s\Omega t]} = \widehat{\mathbf{U}}^{TS}_{-2,1} e^{IN_r[(N_s/N_r-2)\theta]+IN_s\Omega t} = \\ = \widehat{\mathbf{U}}^{TS}_{-2,1} e^{IN_r[(7/4-2)\theta]+IN_s\Omega t} = \widehat{\mathbf{U}}^{TS}_{-2,1} e^{I2\pi/P_r[-1/4\theta]+IN_s\Omega t}\end{aligned} \tag{3.48}$$

Such a periodic signal would not fit in a single passage domain (a single pitch, P_r). However, in the inclined computational planes, Equation 3.46 shows how such a mode would be *coded* into a signal of a single passage spatial periodicity, and therefore, it would be present in the single passage solution:

$$\widehat{\mathbf{U}}^{TS}_{-2,1} e^{I[(1-2)N_r\theta'+nN_s\Omega\tau]} = \widehat{\mathbf{U}}^{TS}_{-2,1} e^{I[-N_r\theta'+nN_s\Omega\tau]} = \widehat{\mathbf{U}}^{TS}_{-2,1} e^{I[-2\pi/P_r\theta'+nN_s\Omega\tau]} \tag{3.49}$$

In addition to the steady and synchronous signals, the time-inclined method may also capture non-synchronous perturbations, since it is not directly imposing a certain content of the solution. For example, in the aerodynamic analyses carried out in this work, no significant effect has been appreciated in the frequencies of the vortex shedding mechanisms. Moreover, for the trailing edge shedding phenomenon, it has been speculated that reducing the computational domain to a single passage might lead to clocking in time-inclined simulations, although this has not been thoroughly investigated at this point.

Finally, regarding the stochastic component of turbulent flows in SRSs, time-inclining seems to be suitable for capturing the correct spectra. A detailed analysis of the impact of time-inclining on the turbulent spectra and comparisons to those of physical plane simulations will be shown in Chapters 5 and 6.

One of such analyses consists on comparing the solutions of standard and time-inclined simulations of a canonical turbulent problem: the turbulent boundary layers and flow in a periodic channel. Similarly to the rationale behind choosing the appropriate size of the channel computational domain, the reason why time-inclining seems to accurately capture the correct turbulent spectrum in turbomachinery simulations is because the size of the

passage is large enough so that the fluid structures decorrelate.

3.6 Implementation Into a High-Order Solver

A key feature of the time-inclined method is its simplicity. Since the goal of the present work is to demonstrate its suitability for carrying out SRS, it is worth discussing the impact of its implementation into widespread high-order schemes such as that of the baseline solver presented in Chapter 2.

One of the clear benefits of the method is that, for the inclination of the Euler equations, as well as for the truncated inclined Navier-Stokes equations, the formulation of the fluxes is exactly the same as in the baseline solver. Additionally, the 'direct' [2] increment in computational cost, which pays for the benefit of the reduction of the computational domain to a single or a few passages, consists of recovering the values of the conservative variables after advancing the inclined variables in time. Moreover, that single extra step entails arithmetic operations that only require information of the computational node for which the conservative variables are being computed. Such a property is very advantageous for computational parallelisation, and allows leveraging the fast computing capabilities of GPU architectures.

Thus, the main change to the algorithm of the high-order baseline solver is that inclined variables are marched in time, instead of the conservative ones. After each step of the Runge-Kutta scheme, the transformation back to the conservative variables, $\mathbf{U}_{i,j} = f(\mathbf{Q}_{i,j})$, takes place for every computational node j,of every element i. After such point, the execution takes place as if the time-inclined method was not being used, until the next time-marching step (to the next stage of the RK scheme or to the next iteration) is taken.

3.6.1 Effect on the Boundary Conditions Formulation

The choice of the formulation of the boundary conditions is also an instrumental part of maintaining the alterations to the solver's algorithm to a minimum. Even though the eigenvalues of the equations are modified through the inclination procedure, the form of the fluxes and the nature of the equations are preserved. Such properties can be

[2] Here, when comparing the computational cost to other passage reduction methods, 'direct' cost refers to the amount of extra steps or operations that have to be carried out in the algorithm of the solver. Meanwhile, 'indirectly', the time-inclined method may: show faster convergence to a quasi-periodic state [82, 83], require smaller time-step sizes, require less or multiple times the amount of passages, etc. An actual analysis of the computational cost of the time-inclined method in a practical setting is reported in Chapter 4.

leveraged for certain formulations of the boundary conditions involving the computation of characteristic waves amplitudes, such as the LODI methodology.

The truncated inclined Navier-Stokes equations can be written in an orthogonal-to-the-boundary frame of reference, (x_1' x_2' x_3'), as

$$\frac{\partial \mathbf{Q}}{\partial \tau} + \frac{\partial \mathbf{f}_1}{\partial x_1'} + \frac{\partial \mathbf{f}_2}{\partial x_2'} + \frac{\partial \mathbf{f}_3}{\partial x_3'} = \frac{\partial \mathbf{F}_1}{\partial x_1'} + \frac{\partial \mathbf{F}_2}{\partial x_2'} + \frac{\partial \mathbf{F}_3}{\partial x_3'}, \tag{3.50}$$

where $\mathbf{Q} = \mathbf{W} - \lambda \mathbf{f_2}$ denotes the vector of inclined variables, and $\mathbf{W} = \begin{pmatrix} \rho & \rho u_1 & \rho u_2 & \rho u_3 & \rho E \end{pmatrix}^T$ is the vector of conservative variables in such a reference frame.

Following the same procedure as the one described in Section 2.3.1 for the LODI formulation, we seek the characteristic form of the equations:

$$\mathbf{Q_W P} \frac{\partial \mathbf{W}_p}{\partial \tau} + \frac{\partial \mathbf{f}_1}{\partial \mathbf{W}} \mathbf{P} \frac{\partial \mathbf{W}_p}{\partial x_1} + \frac{\partial \mathbf{f}_2}{\partial \mathbf{W}} \mathbf{P} \frac{\partial \mathbf{W}_p}{\partial x_2} + \frac{\partial \mathbf{f}_3}{\partial \mathbf{W}} \mathbf{P} \frac{\partial \mathbf{W}_p}{\partial x_3} = \mathbf{D} \tag{3.51}$$

where $\mathbf{Q_W} = {}^{\partial \mathbf{Q}}/_{\partial \mathbf{w}}$ is a transformation matrix from conservative to inclined variables, which allows writing the temporal derivative of the inclined variables as:

$$\frac{\partial \mathbf{Q}}{\partial \tau} = \frac{\partial \mathbf{Q}}{\partial \mathbf{W}} \frac{\partial \mathbf{W}}{\partial \mathbf{W}_p} \frac{\partial \mathbf{W}_p}{\partial \tau} = \mathbf{Q_W P} \frac{\partial \mathbf{W}_p}{\partial \tau} \tag{3.52}$$

Then we may pre-multiply Equation 3.51 by $\mathbf{P}^{-1}$, arriving at

$$\mathbf{P}^{-1}\mathbf{Q_W P} \frac{\partial \mathbf{W}_p}{\partial \tau} + \mathbf{P}^{-1} \frac{\partial \mathbf{f}_1}{\partial \mathbf{W}} \mathbf{P} \frac{\partial \mathbf{W}_p}{\partial x_1} + \mathbf{P}^{-1} \frac{\partial \mathbf{f}_2}{\partial \mathbf{W}} \mathbf{P} \frac{\partial \mathbf{W}_p}{\partial x_2} + \mathbf{P}^{-1} \frac{\partial \mathbf{f}_3}{\partial \mathbf{W}} \mathbf{P} \frac{\partial \mathbf{W}_p}{\partial x_3} = \mathbf{P}^{-1}\mathbf{D} \tag{3.53}$$

Similarly to the original LODI formulation, $\mathbf{P}^{-1} \frac{\partial \mathbf{f}_1}{\partial \mathbf{W}} \mathbf{P}$ can be diagonalised to obtain $\mathbf{\Lambda} = \mathbf{S}^{-1}\mathbf{P}^{-1} \frac{\partial \mathbf{f}_1}{\partial \mathbf{W}} \mathbf{P}\mathbf{S}$, leading to

$$\mathbf{P}^{-1}\mathbf{Q_W P} \frac{\partial \mathbf{W}_p}{\partial t} + \mathbf{S}\mathbf{\Lambda}\mathbf{S}^{-1} \frac{\partial \mathbf{W}_p}{\partial x_1} - \boldsymbol{\mathcal{T}} = \mathbf{0} \tag{3.54}$$

where where $\boldsymbol{\mathcal{T}}$ is the vector of the inclined transverse convective terms and the viscous terms in the primitive form of the governing equations, grouped:

$$\boldsymbol{\mathcal{T}} = -\mathbf{P}^{-1} \frac{\partial \mathbf{f}_2}{\partial \mathbf{W}} \mathbf{P} \frac{\partial \mathbf{W}_p}{\partial x_2} - \mathbf{P}^{-1} \frac{\partial \mathbf{f}_3}{\partial \mathbf{W}} \mathbf{P} \frac{\partial \mathbf{W}_p}{\partial x_3} + \mathbf{P}^{-1}\mathbf{D} \tag{3.55}$$

The system of equations 3.54 in characteristic form could be obtained by firstly pre-multiplying by $\mathbf{P}^{-1}\mathbf{Q}_\mathbf{W}^{-1}\mathbf{P}$. After that, the resulting matrix

$$\mathbf{P}^{-1}\mathbf{Q}_\mathbf{W}^{-1}\mathbf{P}\mathbf{S}\mathbf{\Lambda}\mathbf{S}^{-1}, \tag{3.56}$$

should be also diagonalised, obtaining:

$$\widehat{\mathbf{\Lambda}} = \widehat{\mathbf{S}}^{-1}\mathbf{P}^{-1}\mathbf{Q}_{\mathbf{W}}^{-1}\mathbf{P}\mathbf{S}\mathbf{\Lambda}\mathbf{S}^{-1}\widehat{\mathbf{S}} \tag{3.57}$$

The new inclined characteristic equations would be obtained after pre-multiplying the resulting equations by $\widehat{\mathbf{S}}^{-1}$

$$\widehat{\mathbf{S}}^{-1}\frac{\partial \mathbf{W}_p}{\partial \tau} + \widehat{\mathbf{\Lambda}}\widehat{\mathbf{S}}^{-1}\frac{\partial \mathbf{W}_p}{\partial x_1} - \widehat{\mathbf{S}}^{-1}\boldsymbol{\mathcal{T}} = \mathbf{0} \tag{3.58}$$

From Section 2.3.1 we may recall that the objective behind the LODI formulation is to complete the amplitudes of the characteristic waves at the boundaries. Part of such information arrives in the domain from outside, which allows imposing a target value for a desired variable, while other amplitudes can be computed from within the computational domain, since their associated waves travel outwards.

More importantly, once the variations of the amplitudes of the characteristic waves have been appropriately computed, the process described above is run backwards, translating such amplitudes into a set of corrected fluxes. Then, the corrected fluxes can be used to advance the conservation variables in time.

Therefore, one may choose to calculate the amplitudes of the inclined characteristic variables for the information that is travelling outwards, and express the remaining amplitudes as a function of the former, and in terms of the variable to be imposed at the boundary (e.g., a target static pressure at the outlet of the domain). After that, the corrected fluxes of the inclined characteristic equations 3.58 have to be transformed back into the conservation form 3.50.

In other words, after obtaining the corrected values in 3.58 for $\widehat{\mathbf{\Lambda}}\widehat{\mathbf{S}}^{-1}$, one would pre-multiply by $\widehat{\mathbf{S}}$ to obtain the appropriate value of $\mathbf{P}^{-1}\mathbf{Q}_{\mathbf{W}}^{-1}\mathbf{P}\mathbf{S}\mathbf{\Lambda}\mathbf{S}^{-1}$. Next, one would transform the fluxes of the equations in primitive form back to conservation form by pre-multiplying by $\mathbf{P}^{-1}\mathbf{Q}_{\mathbf{W}}\mathbf{P}$. Finally, since

$$\frac{\partial \mathbf{f}_1}{\partial \mathbf{W}} = \mathbf{P}\mathbf{S}\mathbf{\Lambda}\mathbf{S}^{-1}\mathbf{P}^{-1} \tag{3.59}$$

we arrive at the corrected fluxes of the governing equations in conservation form which, in the time-inclined method, involves the inclined variables, $\mathbf{Q}$, instead of $\mathbf{W}$.

Alternatively, instead of obtaining the amplitudes of the inclined characteristic variables, Eq. 3.59 shows that we could have computed the value of the amplitude variations of the physical characteristics, $\mathbf{\Lambda}\mathbf{S}^{-1}$ (see Section 2.3.1). Then, we could simply correct them with the appropriate boundary information, and then transform them back to the corrected fluxes.

This is possible due to the time-inclined method not changing neither the form of the fluxes nor the nature of the governing equations. In fact, the limitation on the slope of the computational domain prevents it, as discussed in Section 3.2.1.

Therefore, it is not necessary to compute the variations of the amplitudes of the inclined characteristic waves, which allows the same baseline algorithm to be used for the execution of the time-inclined simulations, avoids performing multiple operations per computational node and time step, and contributes to the simplicity of the time-inclined methodology.

4 Two-Dimensional Verification of the Time-Inclined Method

Contents

4.1 Flat-Plate Cascades 90

4.2 T106A Low-Pressure Turbine Linear Cascade 110

4.3 Computational Cost Considerations 120

In this chapter, the results of the application of the time-inclined methodology to two-dimensional test cases are presented. The motivation behind such simulations is to address the potential flaws in the implementation and application of the method in simple but representative cases.

Two two-dimensional linear cascades have been chosen as test vehicles, the first consisting of flat plates and the second of T106A [134] airfoils. Several test cases have been conducted to assess the accuracy of the implementation and the approach.

For each cascade, the solution of the Euler equations has been sought after to verify the implementation of the time-inclined method, which should produce exact solutions in inviscid simulations.

Chapter 3 discussed the relevance of the neglected terms in the transformation of the Navier-Stokes equations and is complemented by the results of the viscous simulations shown herein. Similarly to the inviscid verification process, the impact of the viscous approximation is analysed by comparing the solution of the direct periodic domain and the time-inclined simulations for several variables of interest.

The first and second parts of this chapter present and analyse the results for the flat-plate cascade and the T106A linear cascade cases, respectively. Lastly, this chapter discusses the impact of the time-inclined method on the computational cost. The discussion is illustrated by the evolution of an unsteady convergence metric in the viscous simulation of a two-dimensional cascade, which is compared to a reference case.

4.1 Flat-Plate Cascades

4.1.1 Verification of the Time-Inclined Implementation

Two sets of test cases have been produced in order to verify that the implementation of the time-inclined method in the baseline solver is correct. The test cases consist of a two-dimensional cascade located downstream of travelling sinusoidal perturbations. The ratio between the cascade's pitch and the perturbation's wavelength is not unity and, therefore, several pitches must be included in the computational domain to impose periodicity conditions at the boundaries. The aforementioned pitch-ratio and the speed at which the perturbations travel in the azimuthal direction are chosen to allow for a transformation to a single-passage time-inclined domain.

The verification strategy consists of solving the Euler equations for the direct periodic domain (referred to as Multi-Passage, MP, or reference case) and comparing the results to the time-inclined simulation of the transformed problem. It is worth recalling at this point that the transformation of the Euler equations results in a set of inclined variables, $\mathbf{Q} = \mathbf{U} - \lambda \mathbf{g}$, that can be unequivocally related to the conservative variables $\mathbf{U}$. Therefore, the solutions of the multi-passage domain with the baseline solver and the time-inclined simulation should match.

It is important to remark that comparing a single-passage method with the equivalent multi-passage solution in a high-order code can become a daunting task due to the sensitivity of the solution to the details of the numerics. Moreover, the first set of test cases features a cascade of flat plates, a geometry that can accentuate minimal differences between the solutions. Such errors may remain hidden in more realistic configurations, which might not be beneficial for comparing the baseline and time-inclined approaches.

4.1.1.1 Case Description

The verification case consists of a linear cascade of flat plates with zero stagger angle and a pitch-to-chord ratio of $P_s/c = 0.5$. The exit Mach number of the cascade is $M_2 = 0.39$, and the incidence is null. The cascade has a finite thickness t to ease the mesh generation process ($t/c = 1.5\%$).

The plate is considered a stator passing downstream of a row of rotors with pitch P_r. A sinusoidal perturbation of 2.5% of the inlet total pressure is imposed at the inlet section of the computational domain, playing the role of incoming wakes from the preceding rotor row. The ratio between the number of stators, N_s, and rotors, N_r, is $N_s/N_r = 6/15$; therefore, the perturbations do not fit into a single periodic passage.

The total pressure perturbation, which has a dimensionless travelling speed of $M_r = 0.52$, gives rise to a mix of acoustic, vortical, and entropy waves at the inlet of the flat-plate cascade. The combination of the rotor speed M_r, and the number of perturbations gives rise to a high blade-passing reduced frequency $F_{red} = fc/V_{2,is} = 6.43$.

Although it does not concern the (inviscid) verification process, the unusually high value of the reduced frequency was chosen to magnify the errors originating from neglecting viscous terms in the TI transformation. As discussed in Chapter 3, it is important to remark that the time-inclined method cannot be applied to any combination of pitch ratios and rotor speeds. The setup of the present case has been chosen to allow the reduction of the computational domain to a single passage and to achieve a high inclination parameter λ. As the inclination parameter increases, so does the relative magnitude of the errors in the (truncated) time-inclined Navier-Stokes equations. Likewise to selecting a high reduced frequency, a high inclination parameter is sought to magnify the shortcomings of the time-inclined method and ease the analysis. In the present case, the dimensionless parameter of the time-inclined method is $\lambda a_0 = 0.385$, where a_0 is the speed of sound.

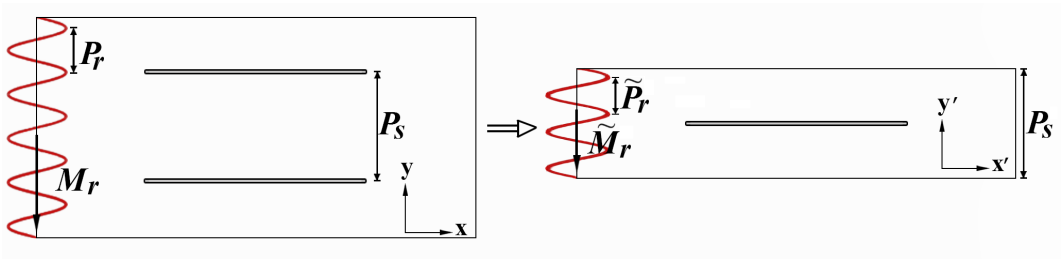

Figure 4.1: Schematic of the flat-plate cascade with inlet perturbations in the physical (left) and time-inclined (right) planes.

A schematic of the case setup is displayed in Figure 4.1. The pitch of the inlet perturbations in the multi-passage domain, P_r, changes to $\widetilde{P_r}$ in order to accommodate 3 sinusoidal perturbations in the time-inclined single-passage domain. As shown in Fig. 4.1 (left), such ratio was 2.5 in the original case, which impeded the imposition of periodicity conditions in a single passage. Due to the transformation, the travelling speed of the perturbations in the inclined plane $\widetilde{M_r}$ also changes. The computational domain of the simulation with direct periodicity (referred to as Multi-Passage simulation of MP) has been chosen to contain 6 plates. In contrast, the time-inclined simulations are performed in a single periodic passage.

The domain is discretized using a grid of 4^{th}-order quadrilateral elements. The equivalent second-order mesh consists of 100 points on the plate and 20 on the leading- and trailing edges. The boundary layer regions are discretized with 4 quad layers (16 computational points in the 4^{th}-order mesh), and the whole mesh totals 13,500 cells per passage. The multi-passage computational domain is constructed by replicating the mesh of a single

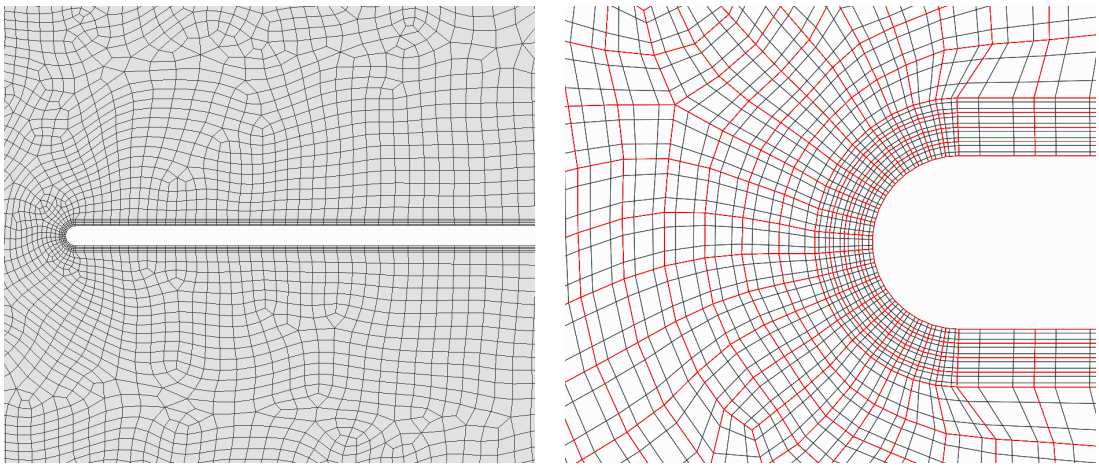

(a) Flat plate mesh (b) Leading edge detail

Figure 4.2: Close-up view of the plate's mesh showing elements without their interior points for the inviscid case (a) and detail of the leading edge mesh with 4^{th} order elements (in red) and interior points (in black) (b).

passage. This procedure eliminates some of the spatial discretization differences between the time-inclined and multi-passage simulations since the mesh per passage is identical. A close-up and detailed view of the plate's mesh can be observed in Figs. 4.2 (a) and (b).

4.1.1.2 Results

The verification process starts with steady-inflow RANS simulations in the second order mesh. The procedure is aimed to speed-up the convergence to a quasi-periodic state and to establish the same starting point in each passage of the multi-passage and time-inclined simulations.

Then, the high-order time-marching code is run until a quasi-periodic state has been reached. The unsteady solutions of these implicit LES are tracked at several locations in the flow field to monitor when such a state is achieved.

From that point onwards, a phase-locked averaging procedure is carried out until a sufficient level of statistical convergence has been obtained. The averaging strategy divides the blade passing period into 48 phases, in which the solution is averaged. In addition to the time-averaged field, the phase averages allow decomposing the solution into the fundamental and higher harmonics of the blade passing frequency, which can then be analysed.

Thus, the static pressure can be expressed as the sum of a mean flow and an unsteady perturbation,

$$p(\mathbf{x},t) = \overline{p}(\mathbf{x}) + p'(\mathbf{x},t) = \overline{p}(\mathbf{x}) + \mathrm{Re}\left(p'_n(\mathbf{x})e^{I2\pi f_n t}\right), \tag{4.1}$$

where p'_n is the n-th complex Fourier coefficient of the pressure. It should be recalled at this point that the comparisons between the physical and inclined plane solutions are straightforward if we compare the modulus of the harmonic content or the time-averaged solution (see Chapter 3).

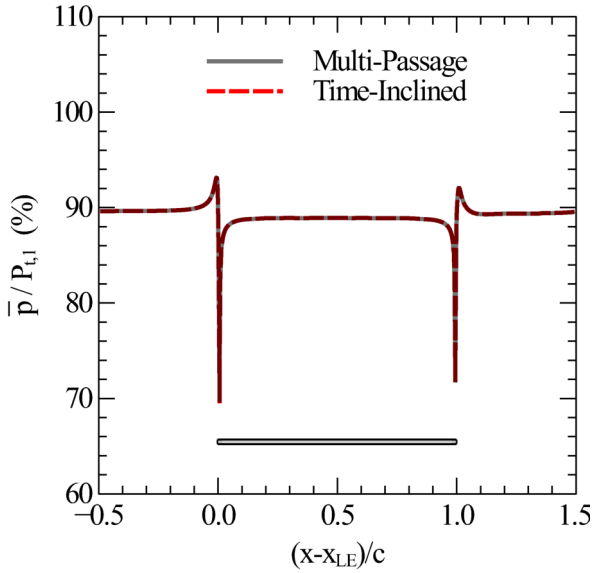

Figure 4.3: Time-averaged static pressure along the passage at $y = y_{plate^+}$, on the plate's top side. The flat plate is included for reference.

The time-averaged solutions of the multi-passage and time-inclined simulations are equal for all variables. To provide an example, Figure 4.3 displays a stream-wise cut at an azimuthal coordinate $y = y_{plate^+}$ corresponding to the upper surface of the flat plate. The reference and inclined solutions are coincident from the inlet to the outlet section, including the plate's surface.

Figure 4.4 compares the normalised modulus (normalised amplitude of the complex unsteady perturbations) of the first harmonic of the static pressure $|p'_1|$ on the lower side[1] of the plate obtained by a multi-passage analysis and the time-inclined method. The degree of agreement between both methodologies is extremely high.

The interaction between the wakes and the flat plates can also be illustrated with the unsteady pressure fields. The field of the modulus of the first harmonic $|p'_1|(x, y)$ is displayed in Figs. 4.5 (a) and (b) for the reference and time-inclined solutions, respectively. Since the time-inclined computational domain consists of a single passage, the solution is artificially extended to several passages for visualisation. Analogously to the time-averaged fields, the fields with the fundamental and higher harmonics obtained in the

[1]Since the geometry of the leading and trailing edges corresponds to a semi-circle, the horizontal coordinate denoting the leftmost part of the plate's surface is $x_0 = x_{LE} + t/2$.

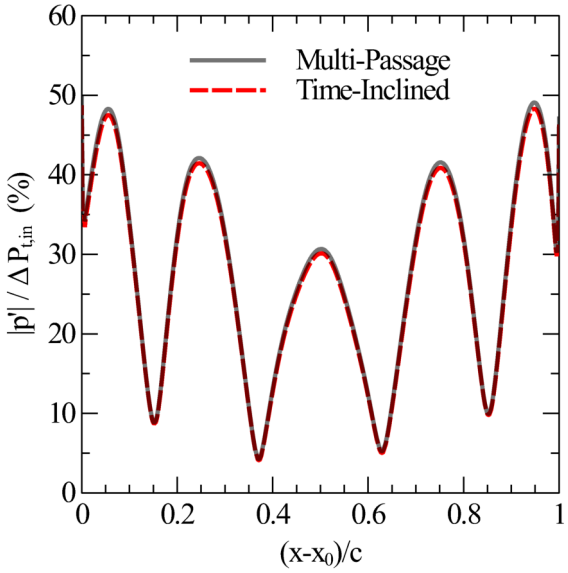

Figure 4.4: Modulus of the first harmonic of the unsteady pressure on the plate's lower surface for the inviscid case.

multi-passage simulation are almost indistinguishable from the time-inclined solutions.

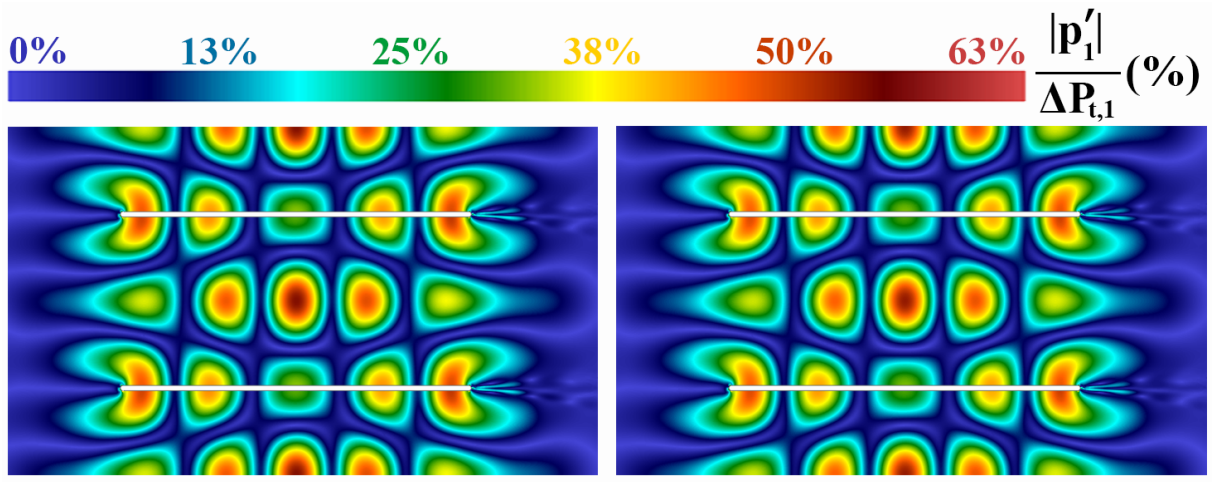

(a) Multi-Passage (b) Time Inclined

Figure 4.5: Modulus of the first harmonic of the unsteady pressure for the multi-passage (left) and time-inclined (right) inviscid simulations.

The second and third harmonics of the unsteady pressure are displayed in 4.6 (a) and (b), respectively. The solutions match almost perfectly for both harmonics, indicating that the solution is converged. The discrepancies shown in Figure 4.6 (b) are very small, especially considering the magnitude of the third harmonic and that the code is run in single precision. The discrepancies, however, can be attributed to several minor differences in the numerics, such as the different numerical dissipation properties between the baseline

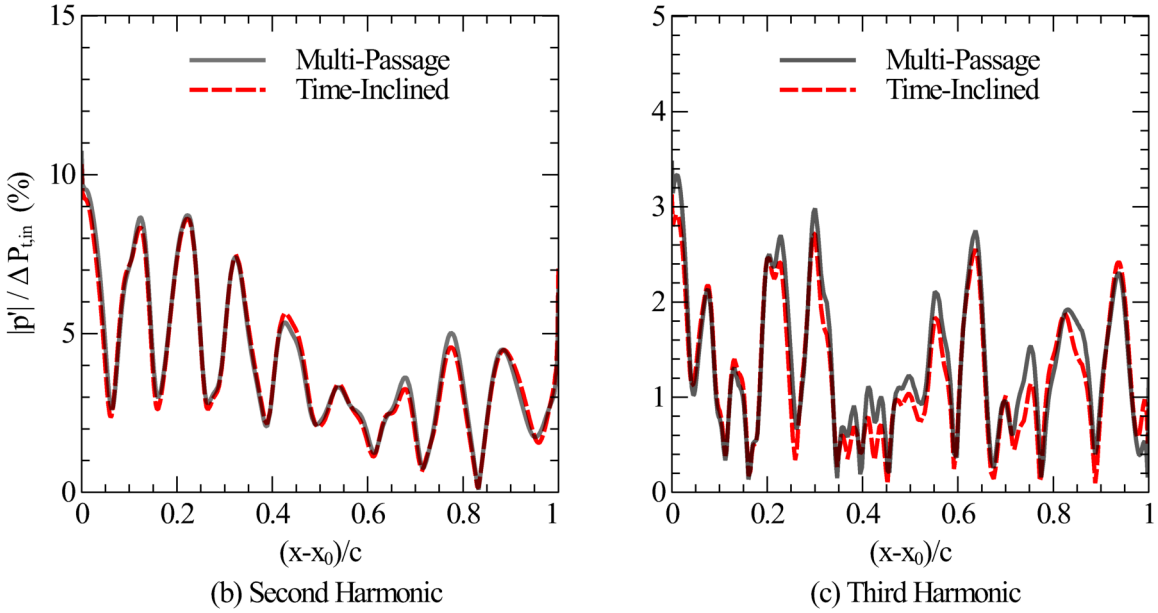

Figure 4.6: Modulus of the second (a) and third (b) harmonics of the unsteady pressure on the plate's lower surface for the inviscid case.

and time-inclined numerical schemes. This is expected since the higher the harmonic, the greater the influence of the numerical errors. Nevertheless, the matching is deemed excellent.

To conclude, the time-averaged solutions obtained with the baseline code and the time-inclined method are essentially equal for all the flow variables. The same can be said for the fundamental and higher harmonics. This is the expected outcome after applying the time-inclined method in inviscid cases, which indicates that the implementation of the method is correct.

4.1.2 Viscous Cases

The relevance of the truncated terms with respect to the viscous terms kept in the transformation has been discussed in Chapter 3. It is established that the local Strouhal number controls the accuracy of the transformation. However, two sets of simulations with different Reynolds numbers have been carried out to verify the analysis due to the viscous origin of the truncated terms.

Three-dimensional scale-resolving simulations are very costly. Moreover, 3D simulations feature significantly more complex physical phenomena than two-dimensional flow. Therefore, in three-dimensional flow, analysing the differences between the baseline and time-inclined simulations and pinpointing the source of such errors becomes more difficult. This

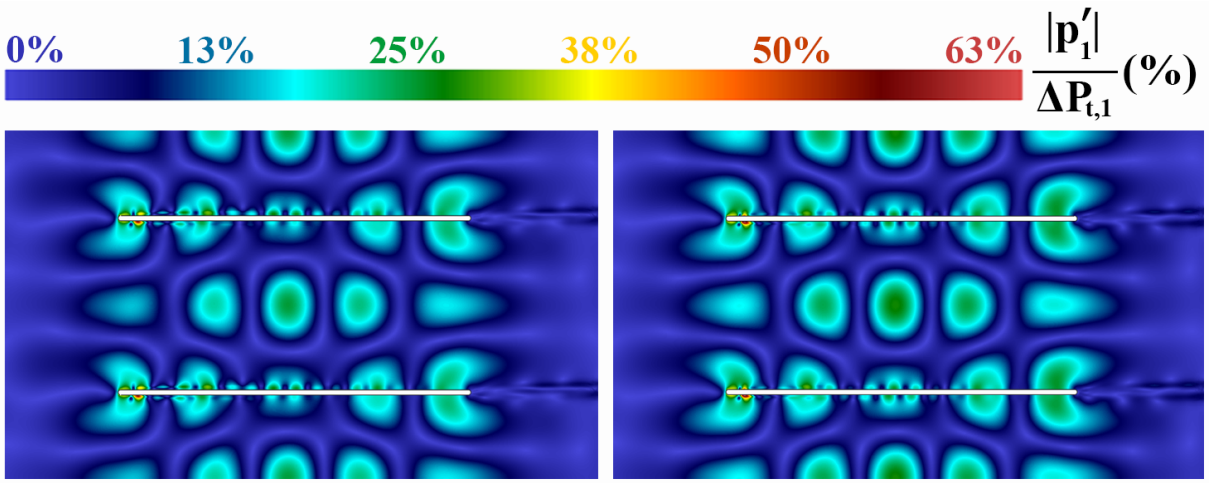

(a) Multi-Passage (b) Time Inclined

Figure 4.7: Modulus of the first harmonic of the unsteady pressure for the multi-passage (a) and time-inclined (b) low-resolution simulations of the cascade of flat plates with $Re_c = 1.1 \times 10^5$.

motivates the present section, in which the results of two-dimensional viscous simulations of the flat-plate cascades are analysed.

High-Reynolds number low-resolution case

The configuration of the inviscid verification cases was computed retaining the viscous terms (see Section 4.1.1.1 for a detailed description). The Reynolds number based on the plate chord of the first set of viscous cases is $Re_c = 1.1 \times 10^5$. The inviscid cases were set up purely for verification purposes. Since the same meshes were used for this set of viscous simulations, the cases were clearly under-resolved. However, the simulations were carried out due to their low computational cost and to gather information about the differences between the baseline and time-inclined numerical schemes on under-resolved scales. Thus, the following set of simulations is referred to as the low-resolution case.

The first observation is that the unsteady pressure fields created due to the interaction of the wake with the plate are different to the inviscid case (see Figures 4.5 and 4.7). The modulus of the unsteady pressure patterns are alike, but it can be observed that, close to the plate, there is a short-wavelength oscillation caused by vortex shedding in the leading-edge region.

The same behaviour can be observed in the first harmonic of the unsteady pressure distribution on the plate as well. The comparison between the full-domain and time-inclined method is displayed in Figure 4.8 (a). It can be noticed that, although the time-inclined and the direct periodic domain curves are alike, the agreement is not as good as in the inviscid case. Nonetheless, the matching is good at the front and rear parts of the plate.

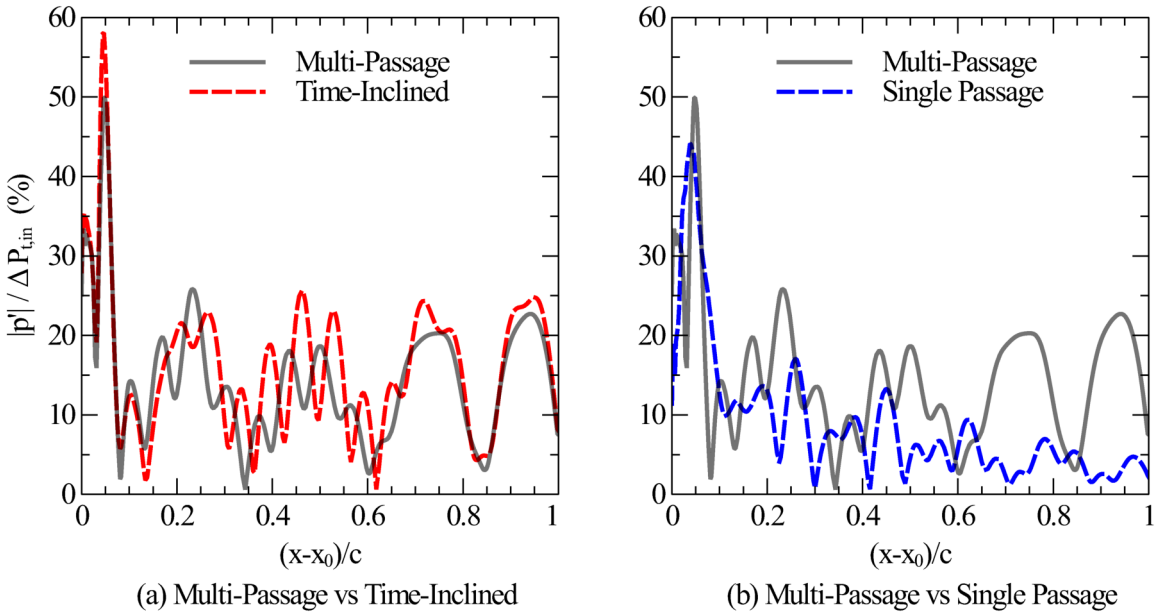

Figure 4.8: Distribution of the 1^{st} harmonic of the unsteady pressure on the flat plate's lower side for the $Re_c = 1.1 \times 10^5$ case. Comparison between the multi-passage solution with the time-inclined method (a) and with the approximate single-passage simulation (b).

A third simulation was conducted to compare to the reference and time-inclined solutions. For such simulation, the common strategy of approximating the pitch ratio to the nearest integer has been followed. The alteration of the pitch ratio allows the problem to be solved in a single passage domain. The rotor speed or, in this case, the speed of the travelling waves, is modified accordingly so that the reduced frequency of the problem remains unaltered. This simulation is referred to as the (approximate) single-passage approach.

Figure 4.8 (b) compares the multi-passage and single-passage methodologies for the first harmonic of the unsteady pressure. The single-passage solution has very little to do with the reference case, showcasing the importance of retaining the exact blade count to achieve accurate predictions of the acoustic field.

Figure 4.9 sketches the physics of the flow past a flat plate subject to incoming disturbances at $Re_c = 1.1 \times 10^5$. Three regions of unsteadiness can be distinguished: Firstly, the plate passage containing wakes, which are essentially undisturbed by the plates. Secondly, the plate unsteady boundary layer. As observed in 4.7, the wall flow is affected by a separation in the leading edge that triggers the convection of small high-frequency vortices along the plate [135]. Finally, the plate trailing edge gives rise to a Karman vortex street that propagates and dissipates downstream.

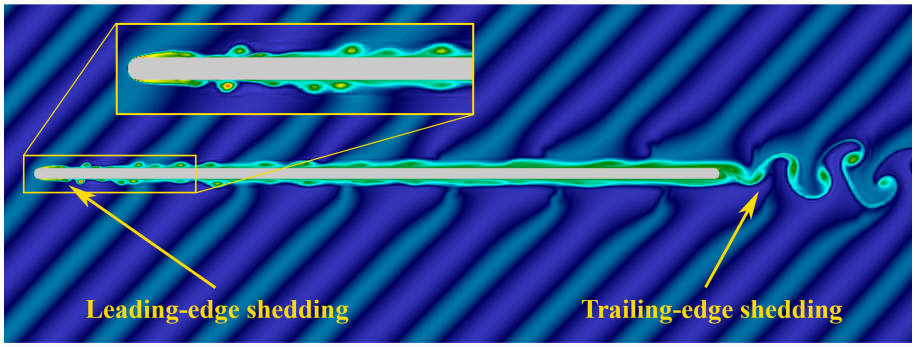

Figure 4.9: Physics of the viscous flow past a cascade of flat plates at high Reynolds numbers sketched by a snapshot of the entropy.

The impact of the TI transformation is different in the three regions. The root cause of the mismatch between the multi-passage and time-inclined solutions in Fig. 4.8 (a) was believed to be the truncation of viscous terms in the transformed Navier-Stokes equations. However, the origin of the differences lies in the lack of sufficient resolution to accurately capture the leading edge shedding, as will be shown next. The problem is exacerbated in this case due to the high-frequency separation in the flat plate leading edge that sheds small vortices convected along the plate through a structured mesh with elements of high aspect ratio.

The frequency of the vortices created by the leading-edge separation is significantly higher than the blade passing frequency exciting the boundary layer. Therefore, since the relative magnitude of the truncated terms scales with the local Strouhal number, the impact of such terms can be significant in a boundary layer affected by the vortex street generated at the leading edge. High-frequency vortices propagating at nearly the free-stream velocity in a viscosity-dominated region is the most challenging case for the TI method.

As seen in Figures 4.7 and 4.8 (a), the vortices mix and dissipate along the plate. This results in a much less disturbed environment in the rear part of the plate and the recovery of the agreement between the reference and time-inclined solutions.

Section 4.2 will show that the impact of the truncated time-inclined transformation on an LPT airfoil is much smaller. The main reason for this different behaviour of the TI on the T106A airfoil is that well-designed LPT airfoils do not present leading-edge separation due to the favourable pressure gradient downstream of the leading edge. Therefore, even without a very fine mesh, a very high level of agreement can be achieved between the multi-passage and time-inclined solutions.

High Reynolds number high-resolution mesh

The goal of the present chapter is not to obtain accurate solutions to the two-dimensional problem, but to compare two solution approaches. The time-inclined results should coincide with those from the baseline solver if the NS equations were properly transformed and if, then, $\mathbf{U}$ was properly computed from $\mathbf{Q}$ (see Section 3.2). Nonetheless, due to the significant under-resolution close to the plate and the presence of the aforementioned leading edge vortex shedding mechanism, the differences between the solutions in Fig. 4.8 (a) cannot be solely attributed to the time-inclined approximate approach for the NS equations.

Thus, a refinement of the viscous mesh was carried out. Through the simulations on finer grids, we intend to discern if the lack of agreement between the solutions is significantly affected by the different dissipative properties of the baseline and time-inclined schemes. Such differences can contribute to the misprediction of the small high-frequency scales of the vortices convected along the plate if they are under-resolved.

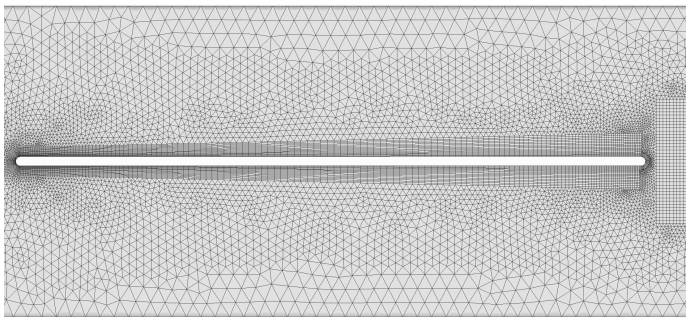

(a) Flat plate mesh

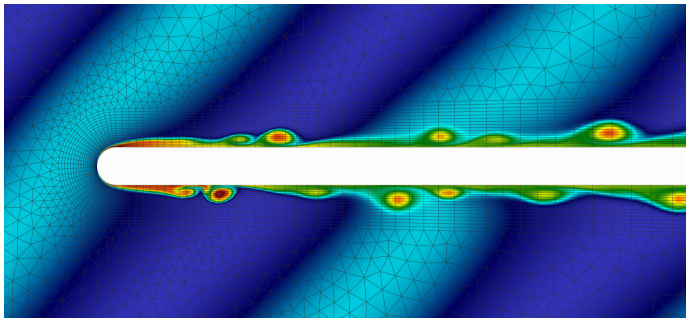

(b) Leading edge detail

Figure 4.10: Flat plate's mesh showing elements without their interior points for the high-resolution case (a) and detail of the leading edge mesh showing the flow separation and vortex shedding (b).

Thus, the higher-resolution mesh consists of 150 fourth-order elements on the plate's surface and 30 on the leading and trailing edges. The boundary layer regions are very finely discretised. They consist of 16 fourth-order quadrilateral elements that span across

the entirety of the boundary layer's thickness close to the trailing edge. The region downstream of the trailing edge has also been finely meshed with a structured quad mesh to capture the mixing process in the wake accurately. The rest of the computational domain has been discretised with triangular elements, and the total hybrid mesh consists of around 32,000 cells per passage. Additionally, to minimise potential sources of error such as the the boundary conditions' reflectivity, the exit section of the computational domain has been relocated further downstream. Figure 4.10 shows a detail of the refined second-order grid representation in the leading edge region over a snapshot of the entropy, highlighting its suitability to simulate the shedding and convection of the vortices.

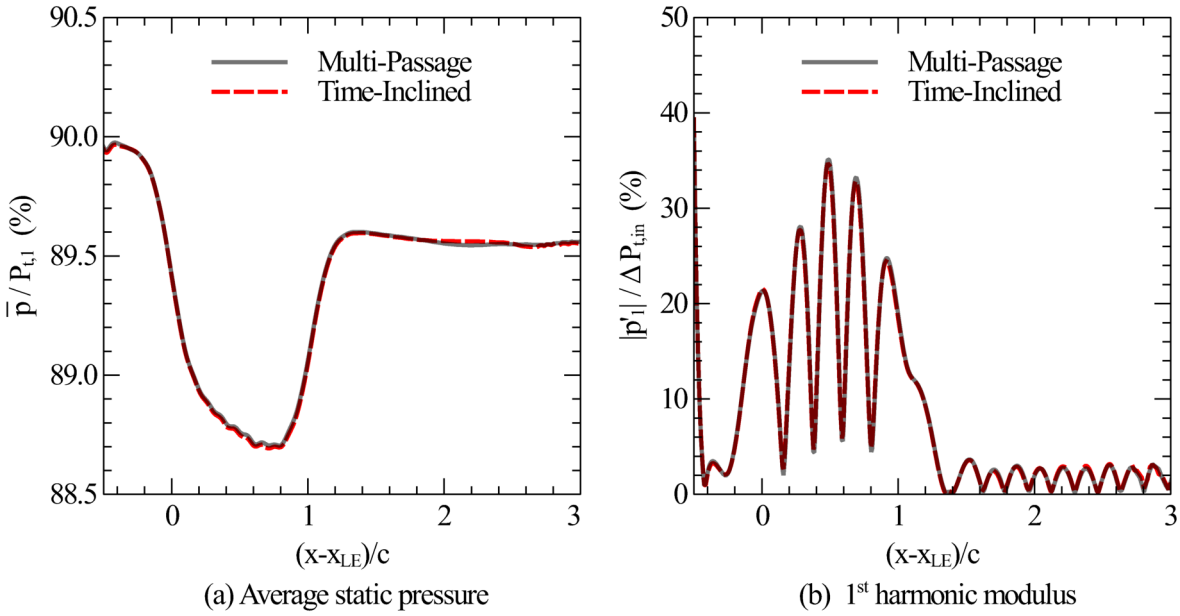

Figure 4.11: Time-averaged (a) and 1^{st} harmonic of the static pressure (b) along the passage mid-line for the $Re_c = 1.1 \times 10^5$ case.

The analysis of the results is divided in three parts, corresponding to the three regions of unsteadiness that have already been distinguished.

Firstly, regarding the plate passage, Figures 4.11 (a) and (b) show the axial evolution of the time-average and $1st$ harmonic static pressure at the passage mid-line, respectively. If we take a look at such sections of the passages in Figures 4.7 (a) or (b), especially in the plate region $0 < (x - x_{LE})/c < 1$, it can be observed how the unsteady pressure field in Fig. 4.11 (b) is very similar to the results obtained in the original mesh. In such part of the flow field the source of the main disturbances is the incoming wakes, for which the level of resolution in the original mesh was sufficient.

Secondly, the improvement achieved with the fine mesh is evidenced in the unsteady boundary layer. Figure 4.12 (a) shows that the level of agreement between the multi-

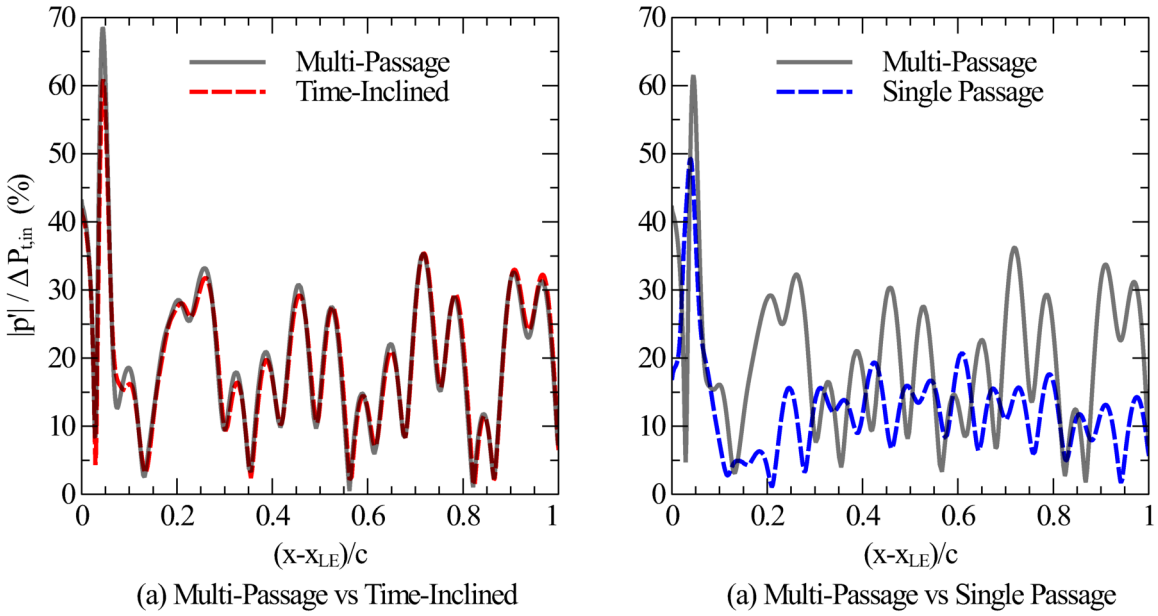

Figure 4.12: Distribution of the 1^{st} harmonic of the unsteady pressure on the flat plate's lower side for the $Re_c = 1.1 \times 10^5$ and fine mesh case. Comparison between the multi-passage solution with the time-inclined method (a) and with the approximate single-passage simulation (b).

passage and time-inclined solutions is excellent in the fine mesh. Small differences can be observed in the magnitude of the local minima and maxima around $(x - x_{LE})/c < 10\%$, but the distribution is very well-captured. These results support the hypothesis about the source of the mismatch in 4.8. The local Strouhal number is higher due to the shedding, which has a higher frequency than the incoming perturbations. However, the Reynolds number of the flow is high enough so that the truncated terms do not dominate over the retained viscous terms, $St_{BL} = St_{shed} Re_c^{-1/2} \approx 0.03$.

The results for the approximate single-passage approach shown in 4.12 (b) evidence the importance of retaining the exact blade count. The unsteady pressure field has nothing to do with the multi-passage approach, and the single-passage methodology cannot reproduce the distribution of the 1^{st} harmonic of the unsteady pressure.

The time-inclined method is also fairly accurate for the higher harmonics. The second harmonic is very well captured (see Figure 4.13 (a)), while the minimal magnitude of the third harmonic is more challenging to match (see Fig. 4.13 (b)). There are significant errors in the separation region for both harmonics, but their effects are very local.

Figure 4.14 displays the velocity profiles across the boundary layer in different axial stations. The time averaged profiles are perfectly matched, while the Root Mean Square (RMS) of the velocity fluctuations shows slight differences. Even for such a high-frequency

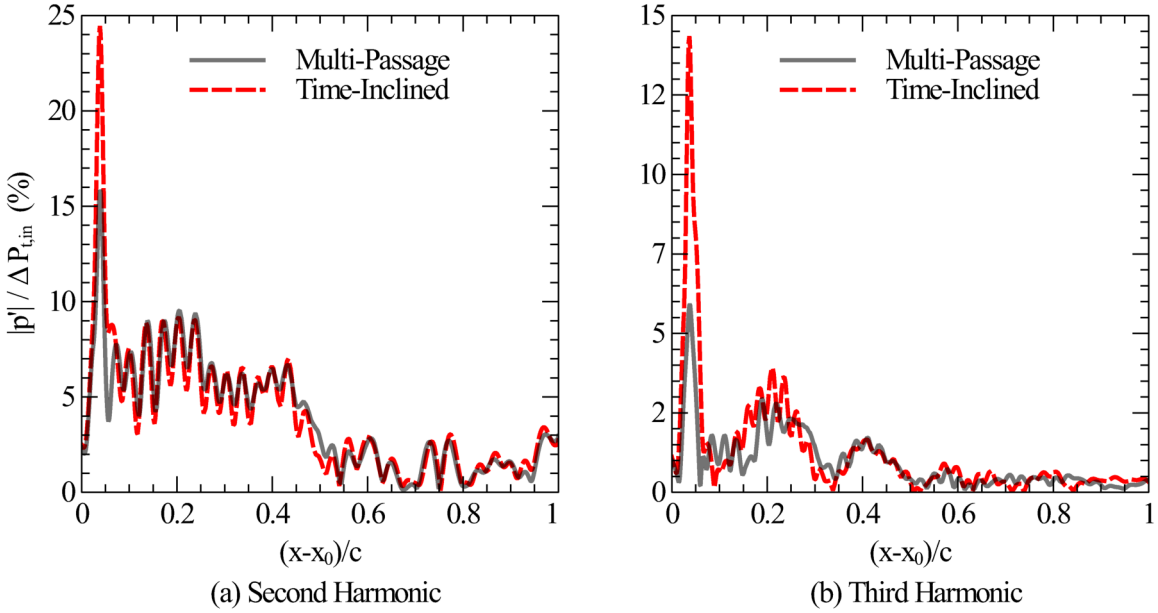

Figure 4.13: Modulus of the second (a) and third (b) harmonic of the unsteady pressure on the plate's lower surface for the $Re_c = 1.1 \times 10^5$ case.

(and high Strouhal number) environment, the flow across the boundary layer is accurately predicted by the time-inclined method, confirming the analysis carried out in Chapter 3.

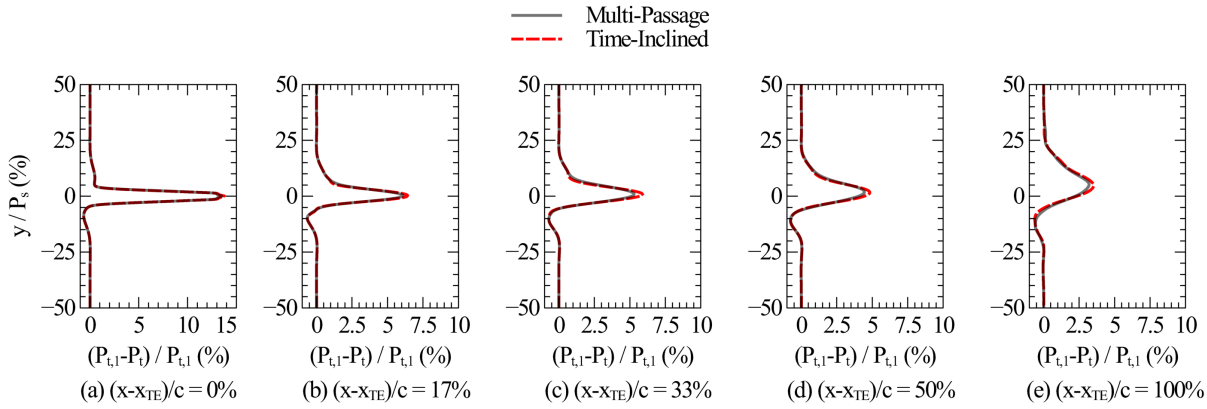

Figure 4.15: Stream-wise evolution of the dimensionless time-averaged total pressure profiles in the flat plate wake at $Re = 1.1 \times 10^5$.

Finally, the third region of high unsteadiness, located in the vortex street downstream of the trailing edge of the plates, is analysed in Figure 4.15. The azimuthal distributions of total pressure are shown in several axial stations. Interestingly, the wake is not symmetric due to the different unsteadiness created by the wake passing in the upper and lower sides of the plate. Although the peak in the defect of total pressure is captured by the time-

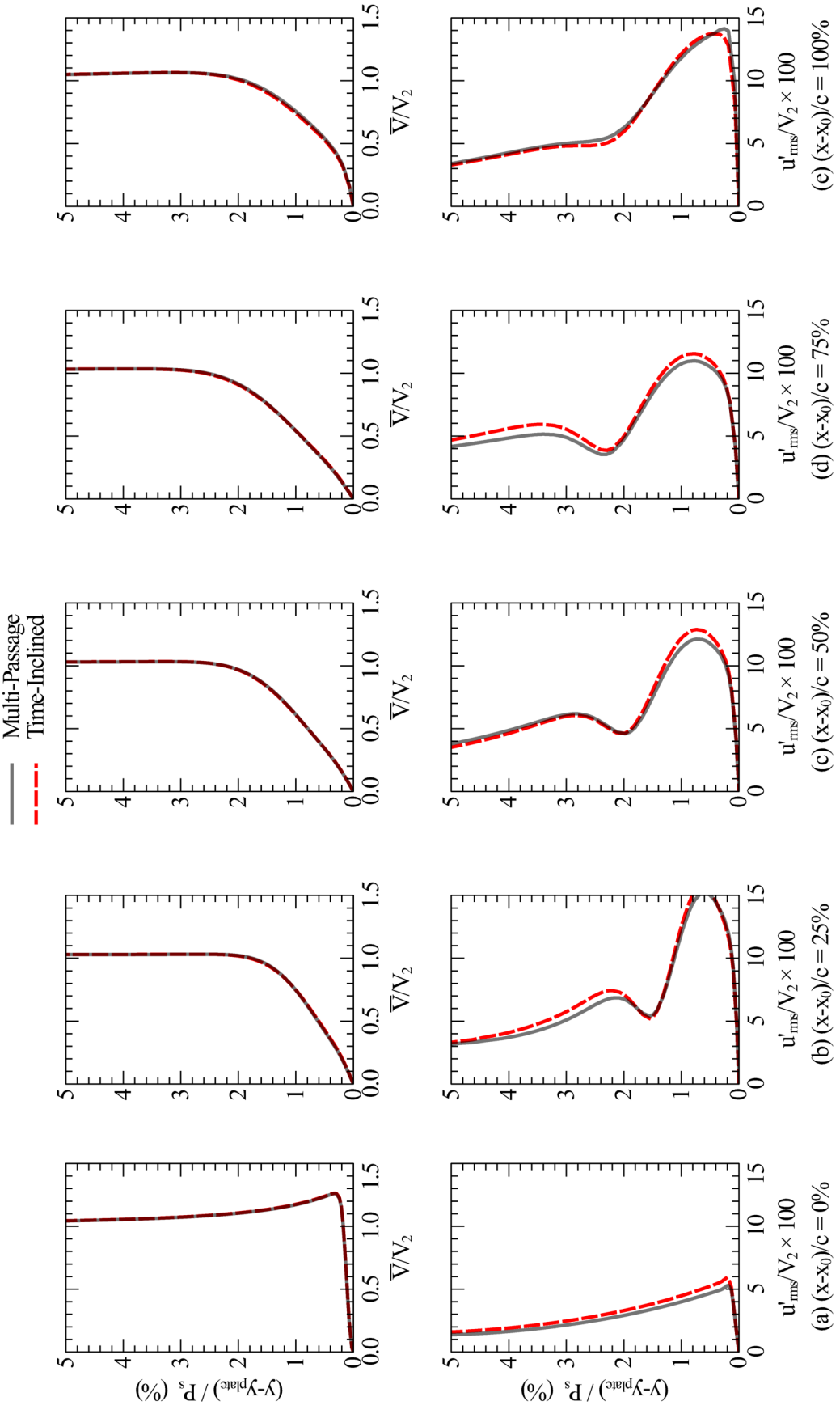

Figure 4.14: Profiles of the time-averaged velocity (top) and root mean squared fluctuations of the unsteady velocity (bottom) at several axial stations of the flat plate boundary layer for the $Re_c = 1.1 \times 10^5$ case.

inclined method at the trailing edge station, the agreement to the reference solution deteriorates further downstream.

The higher frequencies (and Strouhal number) associated with the trailing edge vortex shedding magnify the importance the truncated terms in the transformation. However, the viscous terms have a limited impact for such high Reynolds number flow. This explains how the time-inclined and reference solutions diverge slowly in the present case, which motivates performing lower Reynolds simulations, where the viscous terms are more relevant.

Low-Reynolds number case

The case described in the previous sub-section has been simulated at a much lower Reynolds number ($Re_c = 11,000$). The objective is to elucidate the impact of the approximate transformation of the NS equations in a flow where the relative magnitude of the viscous terms is significantly higher. Since the Reynolds number is lower than in the previous case, the expected relative contribution of the truncated terms is higher.

The fine grid introduced in the present sub-section has also been leveraged to increase the resolution and reduce the uncertainty associated with the different numerics of the baseline and time-inclined schemes.

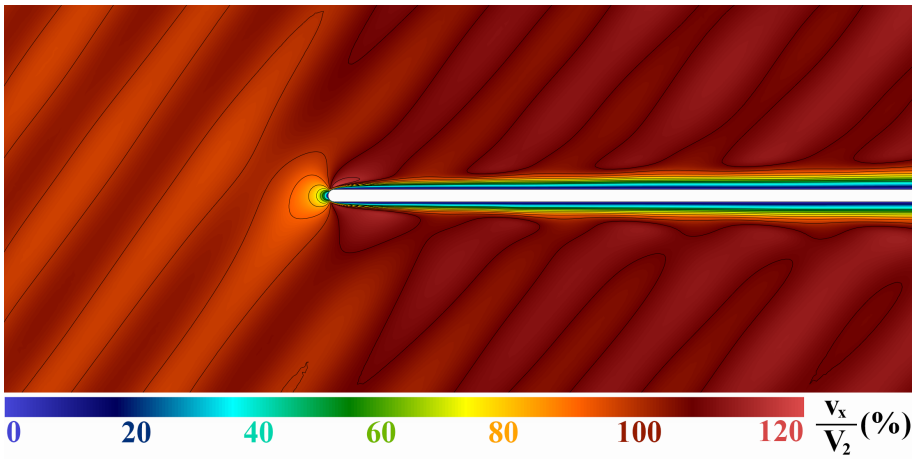

Figure 4.16: Isolines over a snapshot of the stream-wise velocity v_x in the flat-plate passage for a viscous flow of $Re_c = 1.1 \times 10^4$.

Figure 4.16 shows a snapshot of the stream-wise velocity for the low-Reynolds number case. It can be observed that, for $Re_c = 1.1 \times 10^4$, the plates do not feature a leading edge separation. Thus, the high-frequency shedding is suppressed and the Strouhal number in the boundary layer is lower than that of the high-Reynolds number cases.

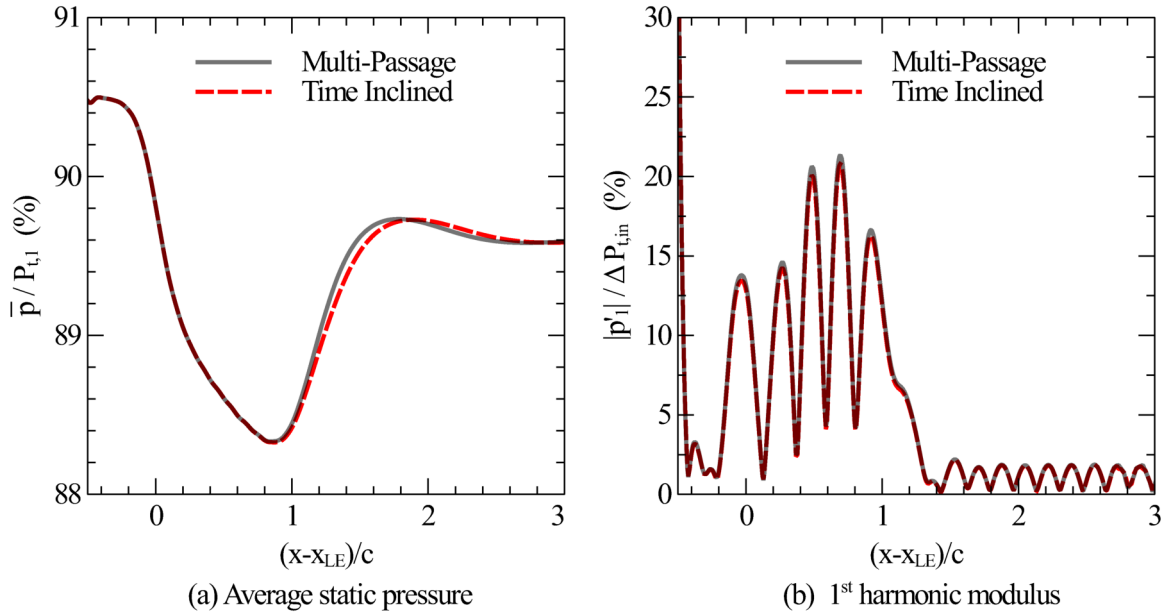

Figure 4.17: Time average (a) and 1^{st} harmonic of the static pressure (b) along the passage mid-line for the $Re_c = 1.1 \times 10^5$ case.

The axial evolution of the time-averaged static pressure at the passage mid-line is shown in Figure 4.17 (a). Although the time-inclined and multi-passage solutions are very close from the inlet to $x = x_{LE}$, the averaged pressure distributions diverge from that point onwards. This effect has to do with the mixing process taking place in the wake. In such a low-Reynolds number flow, the large width of the wake and relative magnitude of the viscous terms have a noticeable impact on the solution at the passage mid-line. The results starkly contrast with those shown in 4.11 (a) for the high-Reynolds number flow. The higher relative magnitude of the viscous terms highlights the differences between the multi-passage and time-inclined approaches in the mixing process, which will be addressed later in this section.

The picture is completely different for the $1st$ harmonic of the unsteady pressure at the passage mid-line in Figure 4.17 (b), which is fairly similar to the higher Reynolds case shown in 4.11 (b). In both cases, the time-inclined matches almost perfectly the reference solution across the computational domain.

Figures 4.18 (a) and (b) show the $1st$ harmonic of the unsteady pressure comparing the multi-passage with the time-inclined and the single-passage approximate pitch ratio approach, respectively. Likewise to the high-Reynolds number case, the truncated terms in the transformation do not dominate over the retained viscous terms. Even if the viscous terms are more relevant in this case, the lack of a leading edge vortex shedding mechanism keeps the relative magnitude of the truncated terms low: $St_{BL} = St_f Re_c^{-1/2} \approx 0.07$. The

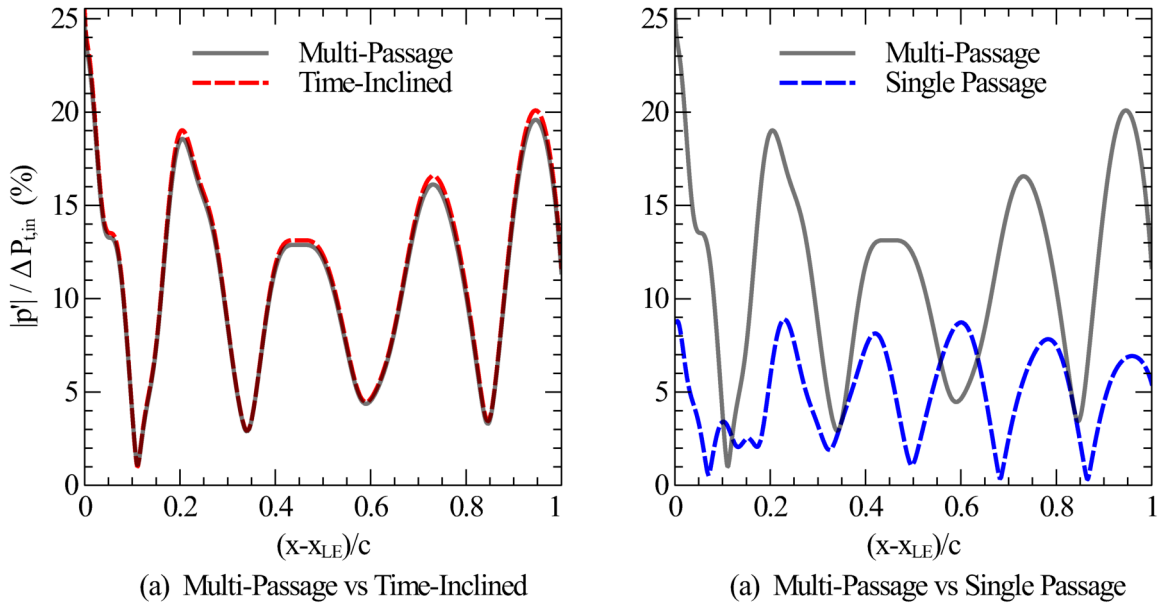

Figure 4.18: Distribution of the 1^{st} harmonic of the unsteady pressure on the flat plate's lower side for the $Re_c = 1.1 \times 10^4$ case. Comparison between the multi-passage solution with the time-inclined method (a) and with the approximate single-passage simulation (b).

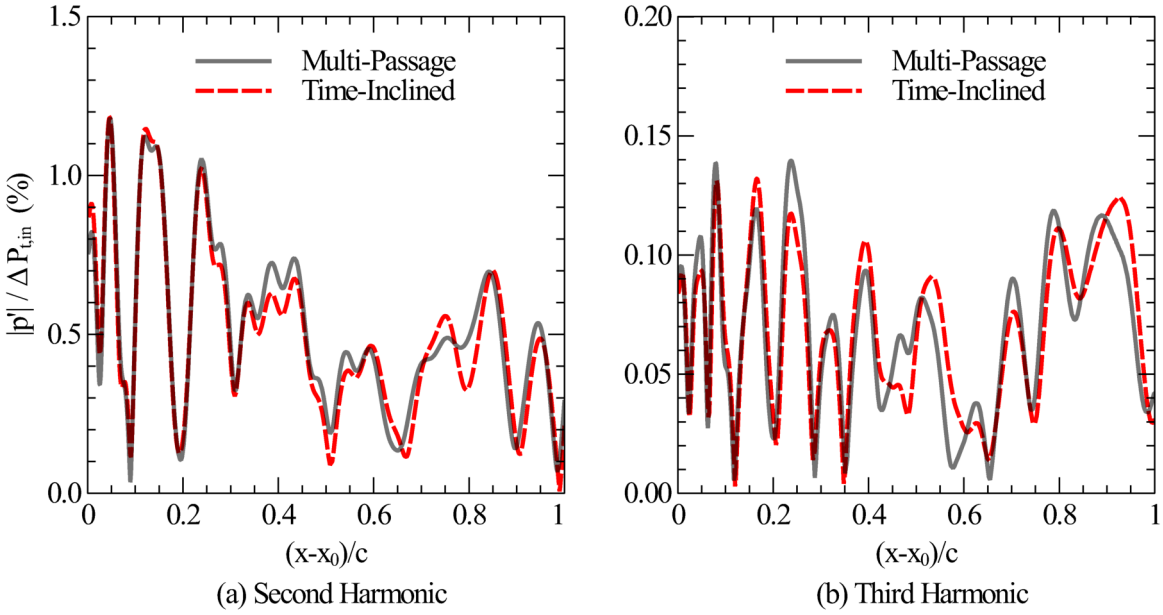

Figure 4.19: Modulus of the second (a) and third (b) harmonics of the unsteady pressure on the plate's lower surface for the $Re_c = 1.1 \times 10^4$ case.

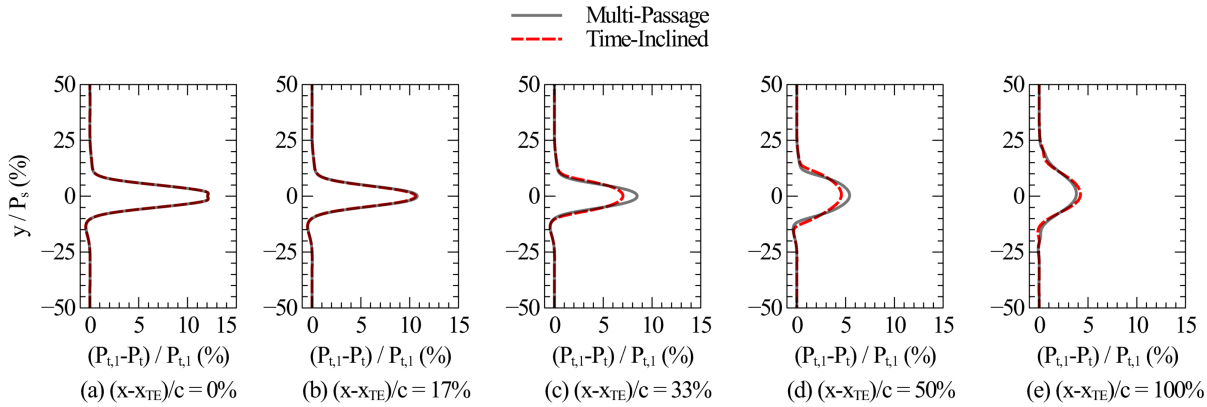

Figure 4.20: Stream-wise evolution of the dimensionless time-averaged total pressure profiles in the flat plate wake at $Re = 1.1 \times 10^4$.

absence of higher levels of unsteadiness, such as the vortex shedding in the leading edge, has no impact on the accuracy of the single-passage methodology to predict the acoustic field. Consequently, the 1^{st} harmonic of the unsteady pressure distributions in 4.18 (b) do not match.

The 2^{nd} and 3^{rd} harmonics of the unsteady pressure are also accurately captured by the time-inclined method, and are shown in Figures 4.19 (a) and (b), respectively. Some differences can be noticed, especially for the third harmonic, but the matching is considered to be excellent since the level of pressure fluctuations is close to single precision accuracy.

Figure 4.20 compares the stream-wise evolution of the time-averaged total pressure profiles downstream of the trailing edge computed using the time-inclined and the multi-passage approaches. The total pressure profiles match perfectly just downstream of the trailing edge ($(x-x_{TE})/c = 0\%$), indicating that up to this point, both approaches yield essentially the same solution. However, the downstream evolution diverges. It can be appreciated at $(x - x_{TE})/c = 33\%$ that the time-inclined solution is less mixed than the reference solution, i.e. the wake is deeper in the former than in the latter. Further downstream, where the wake is more mixed, the matching is recovered.

It is worth remembering at this point that the wake region in a time-inclined simulation is, generally speaking, the most prone to errors. As discussed in Chapter 3, the magnitude of the neglected viscous terms in the time-inclined methodology is of the order of the local Strouhal number. The reduced frequency associated with the trailing edge vortex shedding is fairly constant with the Reynolds number and typically is $St_{TE} \simeq 0.2$. Therefore, for lower Reynolds number flow, the relevance of the viscous terms increases, and the differences between the time-inclined and direct periodic solution become more noticeable.

Figure 4.21 displays a close-up of the two-dimensional wake created downstream of the flat plate by the TI and the MP approaches. One chord downstream of the trailing edge the

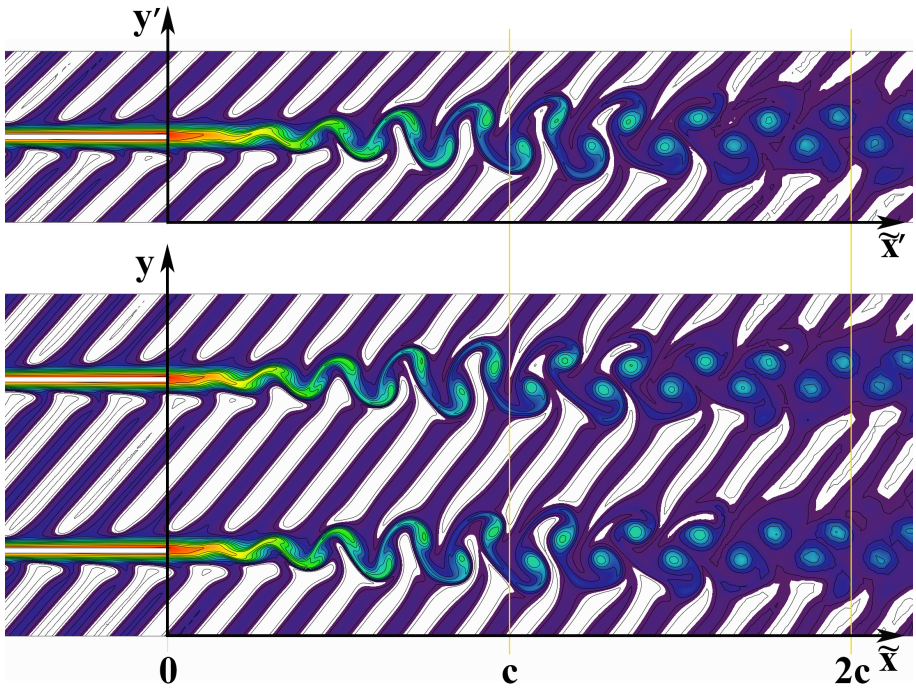

Figure 4.21: Close-up of a snapshot of the entropy isolines for $Re = 1.1 \times 10^4$ in the flat-plates wakes, where $\widetilde{x} = x - x_{TE}$. Top: Time Inclined. Bottom: Multi-Passage

dissipation becomes very effective, and the two solutions begin to diverge. The thickness of the boundary layer and the relative width of the wakes (with respect to the pitch of the cascade) aggravate the impact of the neglected terms in the time-inclined transformation. Such impact can be observed in Fig. 4.17, displaying the differences between the multi-passage and time-inclined average static pressure evolution in the mid-line of the passage. The curves diverge right downstream of the trailing edge; their separation grows for a while and then decreases until the curves converge after more than a 2 chords distance.

Figure 4.22 (top) displays the evolution of the mean velocity profiles along the flat plate computed using the TI method and the equivalent multi-passage domain with direct periodicity. In the first place, it can be noticed that the matching between both approaches is nearly perfect. Except in the leading edge, the remaining time-averaged profiles resemble the classical Blasius profiles at different Re_x. The boundary layer thickness is close to 10% of the pitch at the plate exit, and therefore, some blockage from the BL can be appreciated in the free-stream velocity.

The RMS of the stream-wise velocity fluctuations are made non-dimensional with the isentropic exit velocity, and are displayed in the bottom row of Figure 4.22. All the profiles exhibit extrema inside and outside of the boundary layer that are accurately predicted by the TI method. This result is consistent with the conclusions derived about the validity of the TI method for unsteady laminar boundary layers in Chapter 3.

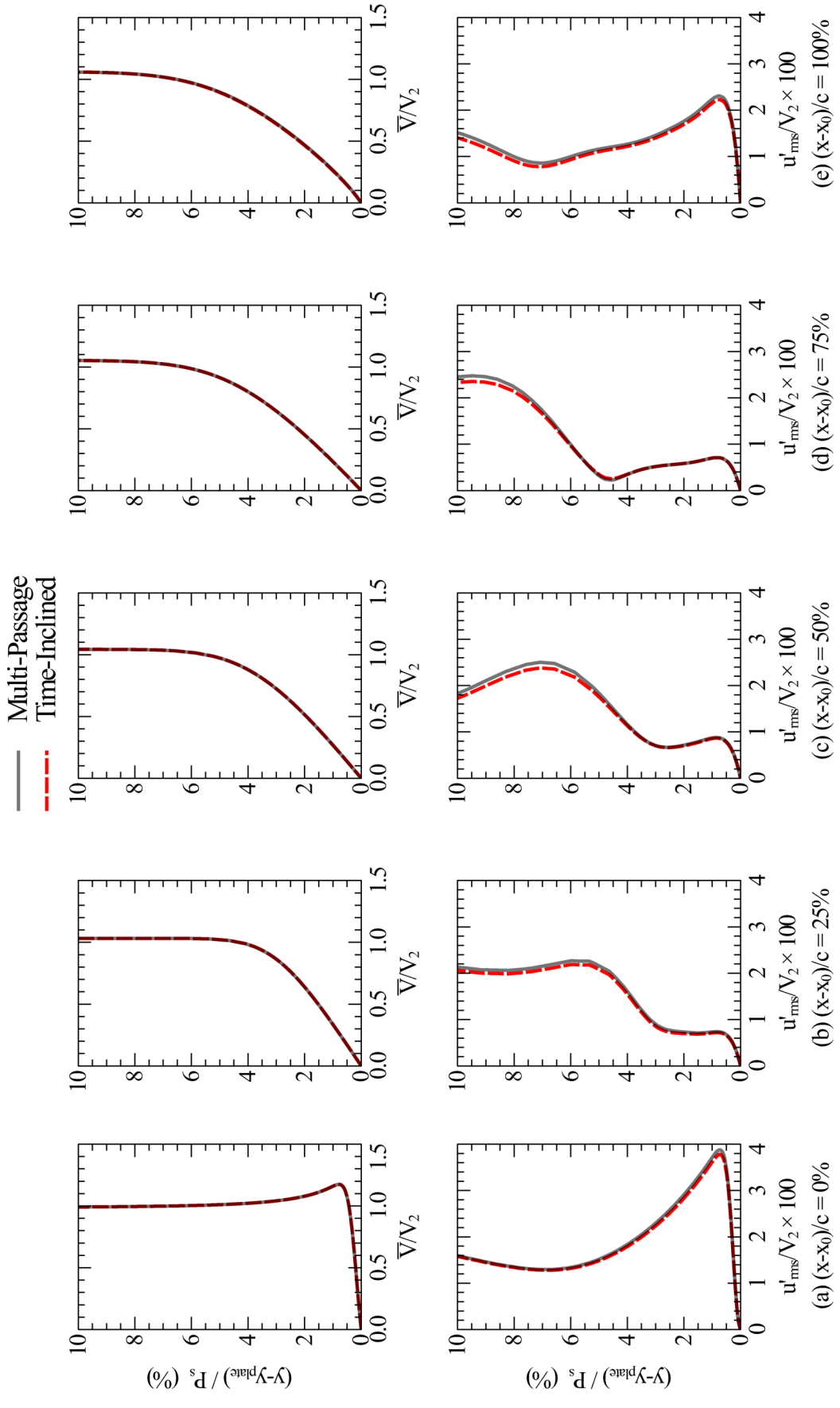

Figure 4.22: Profiles of the time-averaged velocity (top) and root mean squared fluctuations of the unsteady velocity (bottom) at several axial stations of the flat plate boundary layer for the $Re_c = 1.1 \times 10^4$ case.

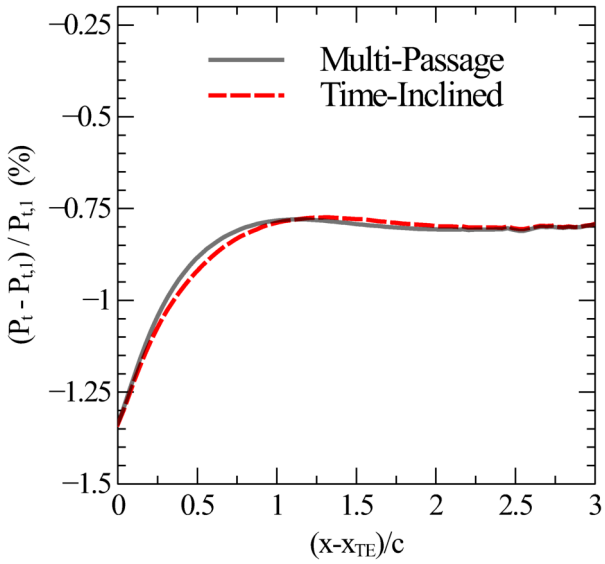

Figure 4.23: Stream-wise evolution of the total pressure loss for the flat-plate cascade at $Re = 1.1 \times 10^4$.

Finally, the stream-wise evolution of the total pressure loss is displayed in Figure 4.23. For that purpose, the total pressure profiles (such as those in Fig. 4.20) are time and pitch-wise averaged. The matching between the time-inclined and multi-passage approaches is good near the trailing edge, diverges downstream and is recovered when the wake is nearly completely mixed.

The impact of the time-inclined approach is to slightly delay mixing, and has become noticeable owing to the low Reynolds number of the present case. However, it is remarkable that even in this extreme case of high-frequency and low Reynolds number that leads to the presence of many wakes in the passage and thick boundary layers, $\delta/c \simeq 10\%$, the TI approach performs so well. Even more so, considering the large magnitude of the transformation parameter λ.

4.2 T106A Low-Pressure Turbine Linear Cascade

4.2.1 Case Description

The T106A airfoil [134] has been chosen to test the time-inclined method in a realistic configuration. The exit isentropic Mach number, $M_{2,is} = 0.39$, the rotor Mach number, $M_r = 0.52$, and the ratio between the rotor and the stator pitch, $P_s/P_r = 15/6$, are the same as in the flat plate cases. Likewise to such cases, a sinusoidal perturbation of 2.5% of the total inlet pressure has been imposed at the inflow. The ratios of pitch to chord

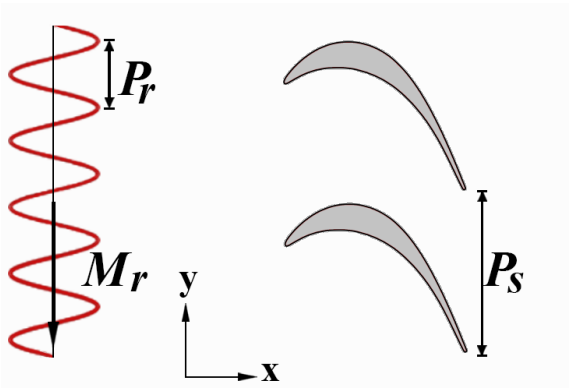

Figure 4.24: Schematic of the T106A cascade with inlet perturbations.

and pitch to axial chord are, respectively, $P_s/c = 0.80$ and $P_s/c_x = 0.93$. A scheme of the case setup is depicted in Figure 4.24.

The computational domain is discretized using a hybrid grid of 4^{th}-order triangles and quads. The equivalent second-order mesh (see Figure 4.25) consists of 150 points on the airfoil and 8 quad layers to account for the boundary layer region, totalling $7,600$ triangular cells and $3,200$ quad cells per passage. As in the flat-plate cascade case, the mesh of each passage of the multi-passage case is identical to the mesh of the passage in the time-inclined case. The discretisation of the 4^{th}-order elements is also the same as in the flat-plate cascade grids, consisting of 16 Degrees Of Freedom (DOF) per quad and 10 DOF per triangle.

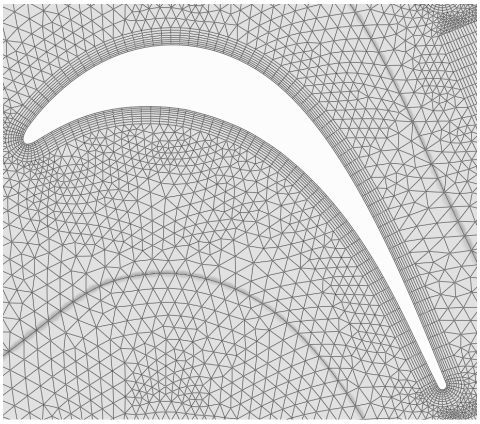

Figure 4.25: Second-order mesh detail of the T106A airfoil.

The focus of this work is to compare the TI and MP approaches, not to achieve the highest level of accuracy or resolution. Nevertheless, a mesh independence analysis has been carried out to minimize grid-induced discretization errors. The procedure involves running the baseline solver in a case with steady boundary conditions on several meshes of different levels of resolution. The flow quantity of interest is the pressure on the airfoil

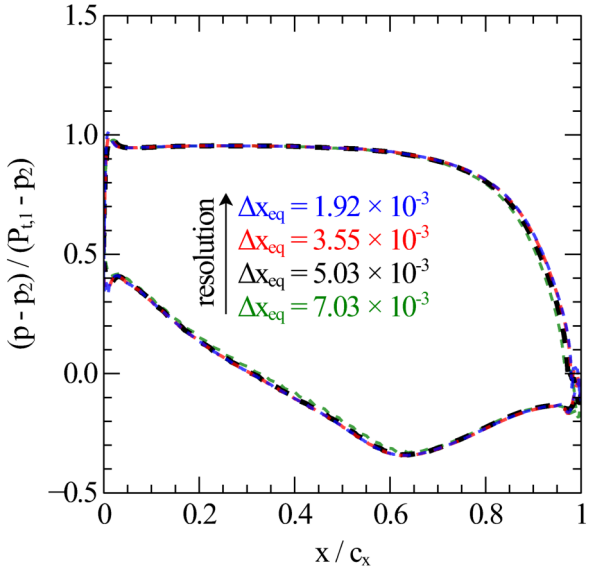

Figure 4.26: Grid sensitivity analysis for the static pressure on the T106A airfoil at $Re_c = 1.1 \times 10^5$.

since such a variable will be later used to compare the time-inclined solutions to the multi-passage approach.

Figure 4.26 displays the pressure coefficient (based on the inlet total pressure and the dynamic pressure at the outlet) on the airfoil under steady inlet conditions for meshes of different number of physical DOF. The unstructured meshes are assigned an equivalent grid spacing defined as $\Delta x_{eq} = 1/\sqrt{\text{DOF}}$.

The chosen mesh resolution, which corresponds to the black dashed line of Fig. 4.26, is more than enough to compare the multi-passage and time-inclined solutions accurately. The achieved level of convergence is deemed suitable for such a task. However, it is worth noting that some slight differences can be seen in the leading and trailing edge regions of the airfoil when comparing the solution with the chosen grid spacing (in black) and simulations of higher resolution (in red or blue).

4.2.2 Verification Results

The inviscid simulation of the T106 airfoil cascade with upstream sinusoidal perturbations has been conducted as part of the verification process of the time-inclined method implementation.

To accentuate the fundamental differences between the TI method and the alternative approach of approximating the pitch ratio in a Single Passage (SP) simulation (see section

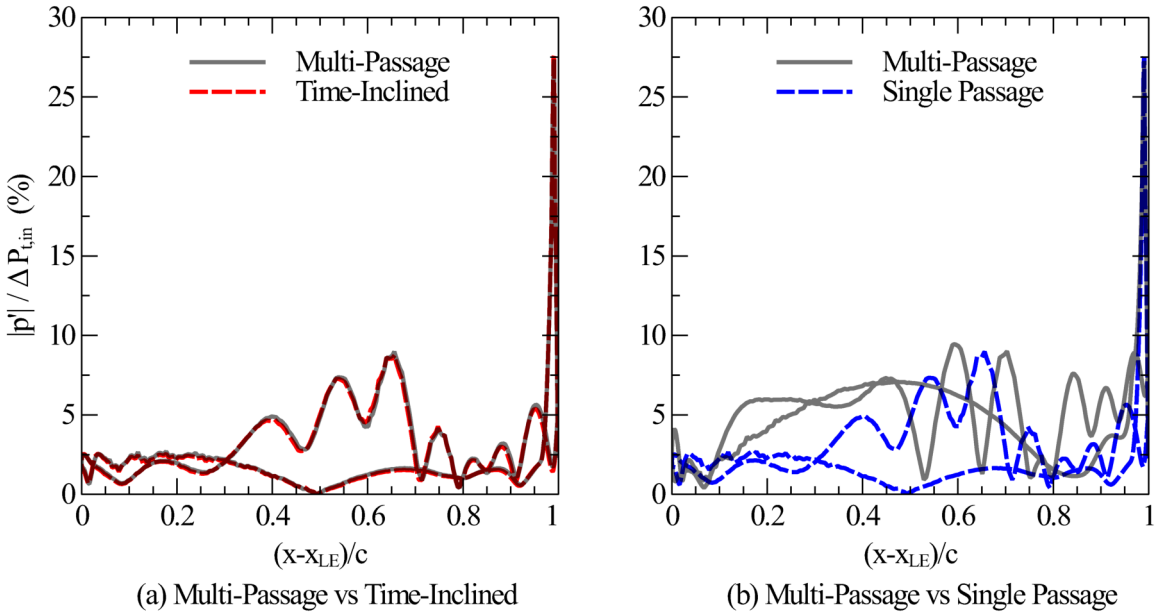

Figure 4.27: First harmonic of the unsteady pressure about an inviscid T106A linear cascade. Comparison of the multi-passage solution to the time-inclined (a) and single-passage (b) methodologies.

4.1.2), Fig. 4.27 compares the modulus of the first harmonic of the unsteady pressure obtained by both methodologies to the solution of the direct periodic simulation.

Figure 4.27 (a) shows that the matching between TI method and the multi-passage solution is very high, but the single passage approximation in Fig. 4.27 (b) cannot capture the fundamental harmonic of the unsteady pressure.

Some disturbances can be seen in the smoothness of all the solutions in Fig. 4.27 near the leading edge region of the airfoil. It is worth noting that the high-order elements of the present simulations were not curved to accommodate the airfoil geometry. Moreover, the numerical scheme of the baseline solver involves a discontinuous solution formulation. Therefore, the inviscid wall boundary conditions can produce small but noticeable errors in regions of high-curvature. Such errors originate in the points shared between two elements since their surface-normal vector is not equal, and the imposition/correction of the velocity field in such a location is inconsistent if the surface components of such field are non-zero.

To give a qualitative idea of the differences in between the three inviscid solutions, Figure 4.28 shows the 1^{st} harmonic of the unsteady pressure for the multi-passage solution (left), the time-inclined method (centre), and the approximate single-passage approach (right). Although it is omitted here for brevity's sake, the high level of agreement between the MP and TI methodologies is achieved for all the variables of interest and is maintained for

higher harmonics. Apparent differences can be found in the single-passage approximation, similarly to the solutions for the flat-plate verification case.

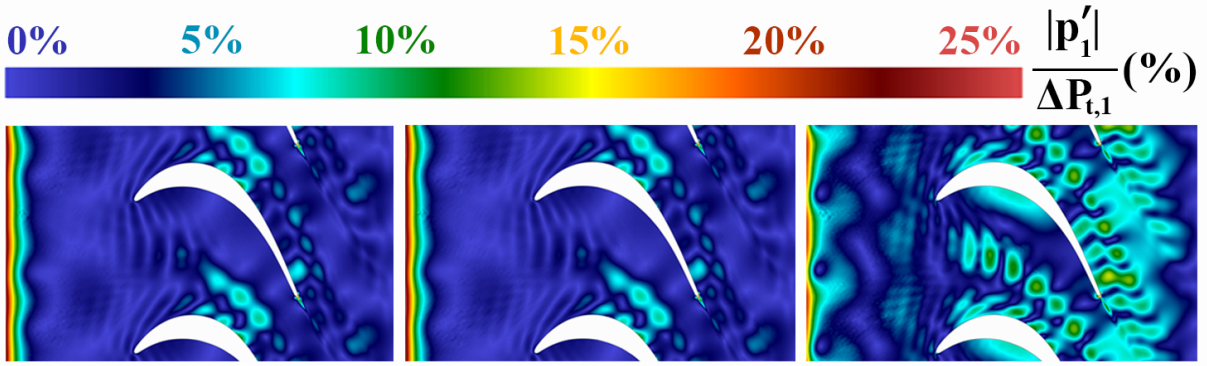

Figure 4.28: Modulus of the first harmonic of the unsteady pressure for the inviscid T106A cascade. Reference (left), time-inclined (centre) and approximate pitch ratio (right) simulations.

To conclude, the results shown so far for the inviscid simulations of the flat-plate cascade and the T106 airfoil cascade indicate that the time-inclined method has been properly implemented in the high-order solver.

4.2.3 Viscous Results

The numerical solution of the Navier-Stokes equations has been carried out for the T106A airfoil cascade to move one step closer to a realistic application of the time-inclined method. The Reynolds number based on the chord and the exit velocity is $Re_c = 1.1 \times 10^5$, and the rest of the simulation parameters have been described in section 4.2.1 but are summarized in 4.1 below for convenience.

$Re_{2,is}$	$M_{2,is}$	F_{red}	P_s/P_r	P_s/c	P_s/c_x	M_r	λa_0
110,000	0.39	4.2	5/2	0.80	0.93	0.52	0.385

Table 4.1: Main parameters of the 2D T106 cascades

Figure 4.29 shows a snapshot of the entropy field to give an overall idea of the unsteady flow field. It can be observed how the incoming wakes propagate undistorted through the inlet uniform field and then are distorted by the mean flow within the passage. A slight separation can be observed in the rear part of the suction side. The separation region is very small due to the high reduced frequency of the incoming wakes ($F_{red} = fc/V_{2,is} = 4.2$) that tend to suppress the steady separation. This phenomenon is qualitatively similar to that described by Bolinches et al. [5] but in a much finer and three-dimensional grid.

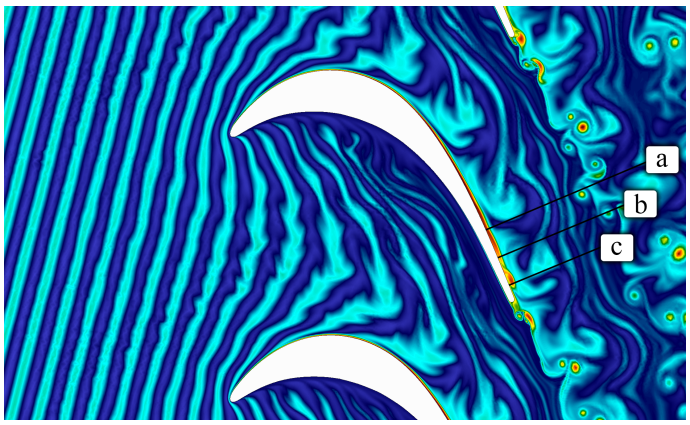

Figure 4.29: Snapshot of the of the entropy field of the T106A airfoil cascade with the location of boundary layer measuring stations **a**, **b** and **c**.

The real part of the first harmonic of the entropy is depicted in Figure 4.30, where it can be seen how the spectrum of the incoming perturbation consists mainly of the fundamental harmonic from the inflow condition. Two vortex shedding mechanisms– taking place at the bubble and the trailing edge– can be identified in Figure 4.29. In Fig. 4.30, it can be seen how the bubble shedding is synchronised to the incoming perturbations.

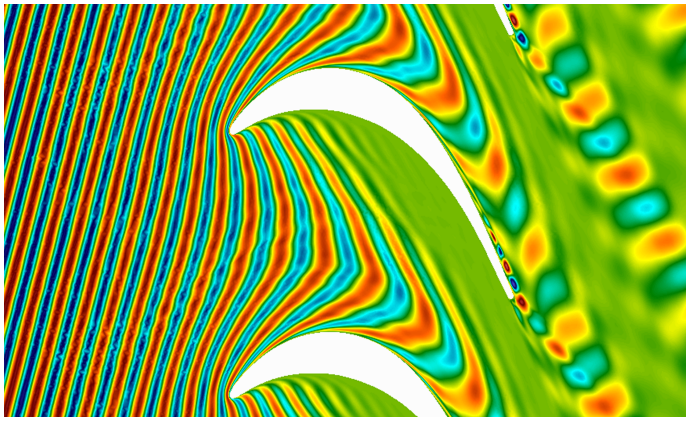

Figure 4.30: Real part of the 1^{st} harmonic of the entropy about the T106A airfoil at $Re_c = 1.1 \times 10^5$.

Figure 4.31 displays the mean isentropic Mach number distribution obtained by a viscous multi-passage analysis (6 passages) and the time-inclined method. It can be noticed that the match between both is nearly perfect. The separation point, located at about 90% of the axial chord, is hardly visible. In addition to the perturbed cases, a steady inflow (solid red line) simulation was carried out. The steady case solution exhibits a longer bubble that reattaches closer to the trailing edge than with unsteady inflow. Moreover, the pressure side is slightly different.

Figure 4.32 shows the distribution of the first harmonic of the unsteady pressure on the airfoil. The highest level of unsteadiness is located in the rear part of the suction side,

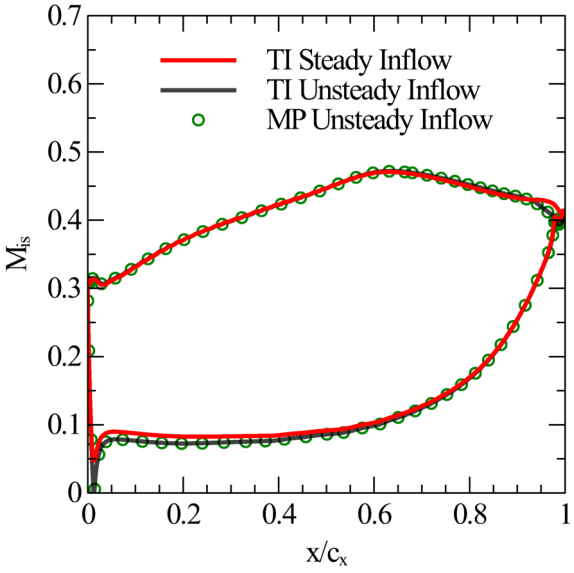

Figure 4.31: Comparison of the mean isentropic Mach number distribution about the T106A cascade between the multi-passage analysis and the time-inclined method.

where a closed and thin recirculating bubble is seen in Fig. 4.31. The shedding of this bubble gives rise to high unsteadiness as can also be observed in Fig. 4.30.

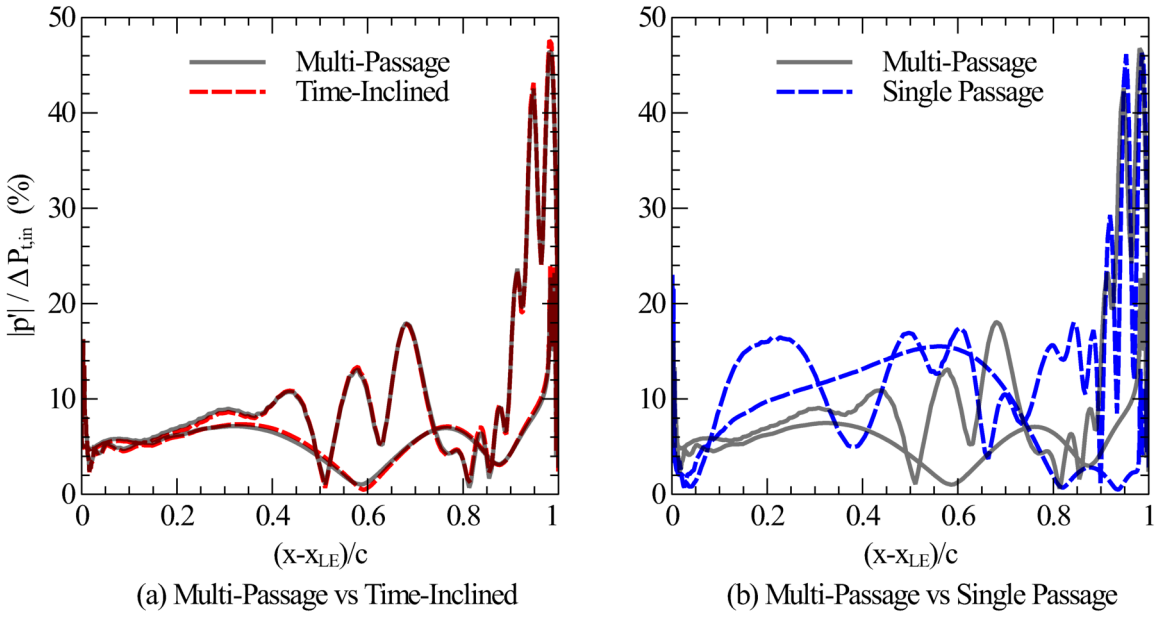

Figure 4.32: First harmonic of the unsteady pressure about the T106A linear cascade. Comparison of the multi-passage solution to the time-inclined (a) and single-passage (b) methodologies.

Figure 4.32 (a) shows a very high level of agreement between the time-inclined approach

and the full-domain simulation. As expected, accurate results cannot be achieved in the single-passage approximate case neither for the viscous (Fig. 4.32 (b)) nor inviscid (Fig. 4.27 (b)) cases, illustrating the importance of retaining the exact blade count to predict the harmonics of the unsteady flow field.

The state of the boundary layer is analysed in three stations on the suction side of the T106A airfoil. The stations *a*, *b* and *c* are located in the bubble region and displayed in 4.29 for reference. Station *a* can be found right after the separation point, at 90% of the axial chord from the leading edge. Station *b* is located in the bubble, at a distance of around 94% of the axial chord. Station *c*, located downstream of the reattachment point, is at 98% c_x.

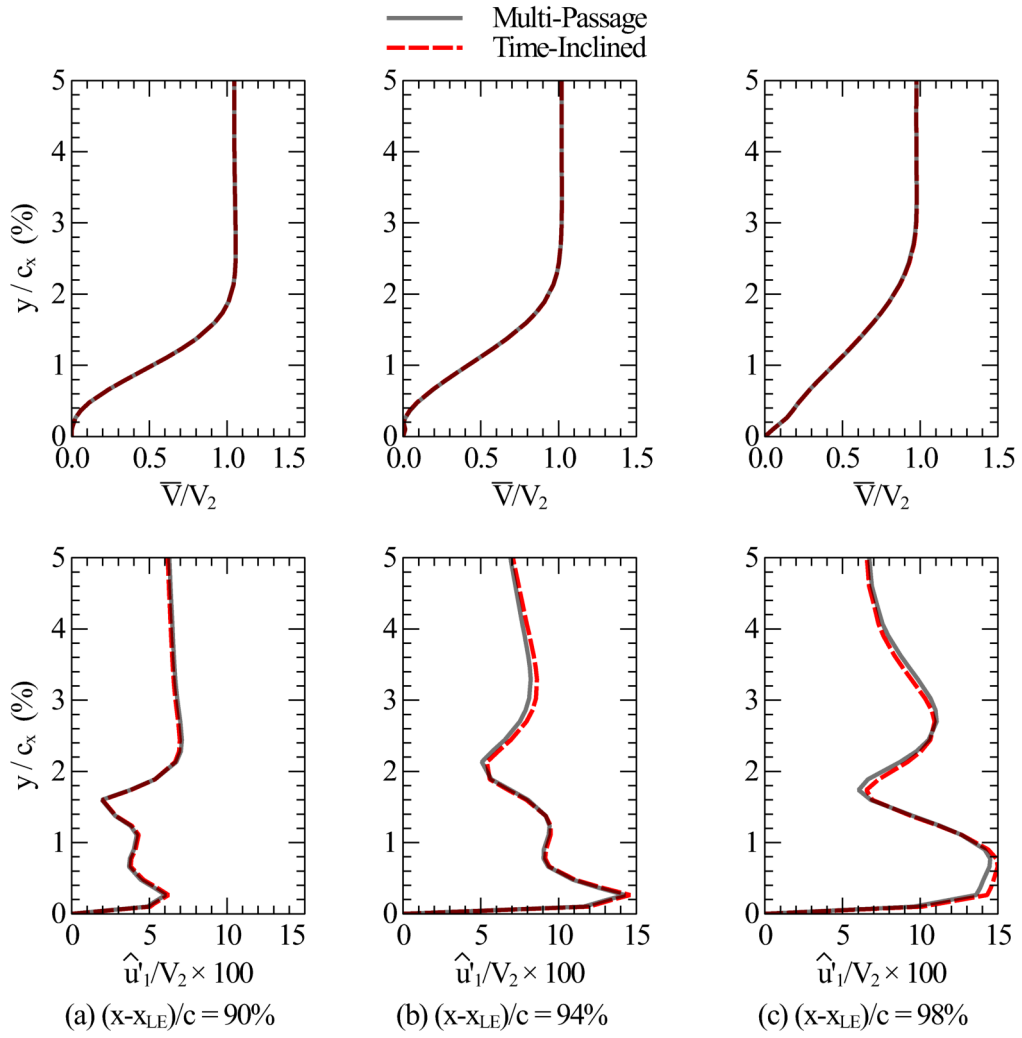

Figure 4.33: Boundary layer profiles of the time-averaged velocity (top) and the first harmonic of the unsteady velocity in the wall-tangential direction (bottom) at the three measuring stations for the T106A cascade.

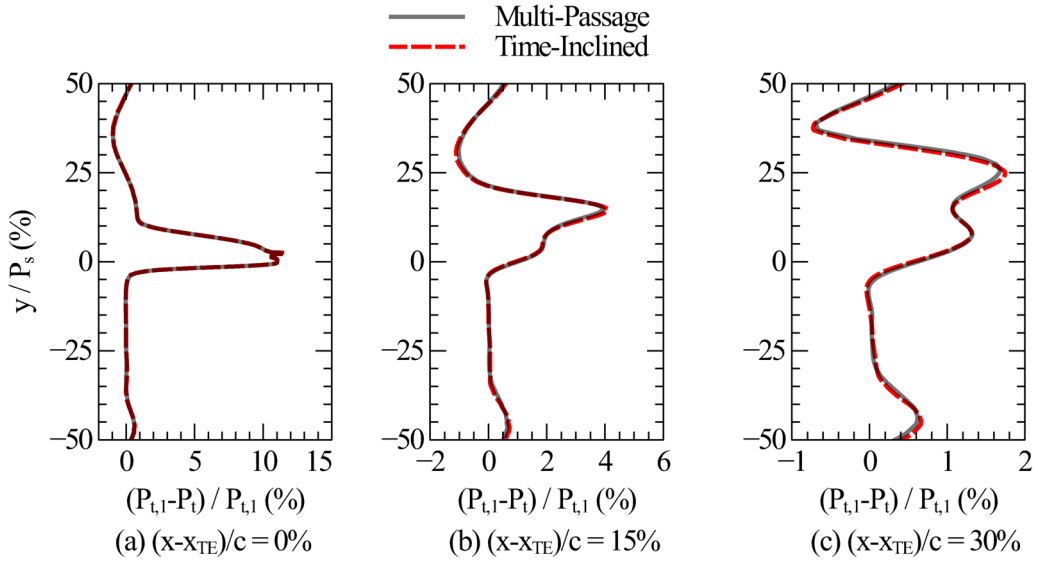

Figure 4.34: Pitch-wise distribution of the time-averaged total pressure in the T106A wake.

The columns of Figure 4.33 show, for each of the three stations, the time-averaged velocity profile across the boundary layer as well as the 1^{st} harmonic of the tangential velocity component. Very high levels of agreement between the multi-passage and time-inclined methodologies are obtained in all the measuring stations, in spite of corresponding to a region of high unsteadiness as shown in Fig. 4.32. Nevertheless, the results are in line with the analysis in Chapter 3: for the boundary layer, the magnitude of the truncated terms in the time-inclined transformation with respect to the retained viscous terms is dictated by the Strouhal number $St_{BL} \sim St_f \frac{1}{Re_c^{1/2}}$, which, in this case, is $St_{BL} \ll 1$.

Figures 4.34 and 4.35 show the axial evolution of the time-averaged total pressure. The pitch-wise distribution of time-averaged total pressure is depicted in Figure 4.34 at three different axial locations, while Fig. 4.35 plots the pitch-wise average from the trailing edge to an axial station 50% c_x downstream. The results are consistent with the wake evolution in the flat-plate cascade at high Reynolds numbers, presenting minimal differences with respect to the multi-passage solution.

The flow angle and velocity distributions are displayed in 4.36 (a) and (b), respectively, at an axial location 30% c_x downstream of the trailing edge and show a very high level of agreement between the multi-passage and time-inclined simulations. Figure 4.36 (c) plots the distribution of Reynolds stress tensor component $\overline{u'v'}$ completing the wake traverse analysis, where some differences can be observed in the azimuthal location of the peak stress $\overline{u'v'}$, while its magnitude is well-captured.

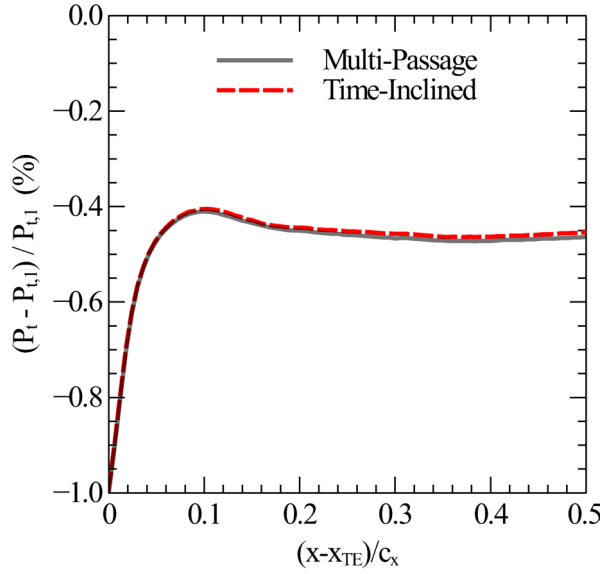

Figure 4.35: Pitch-wise distribution of the time-averaged total pressure in the T106A wake.

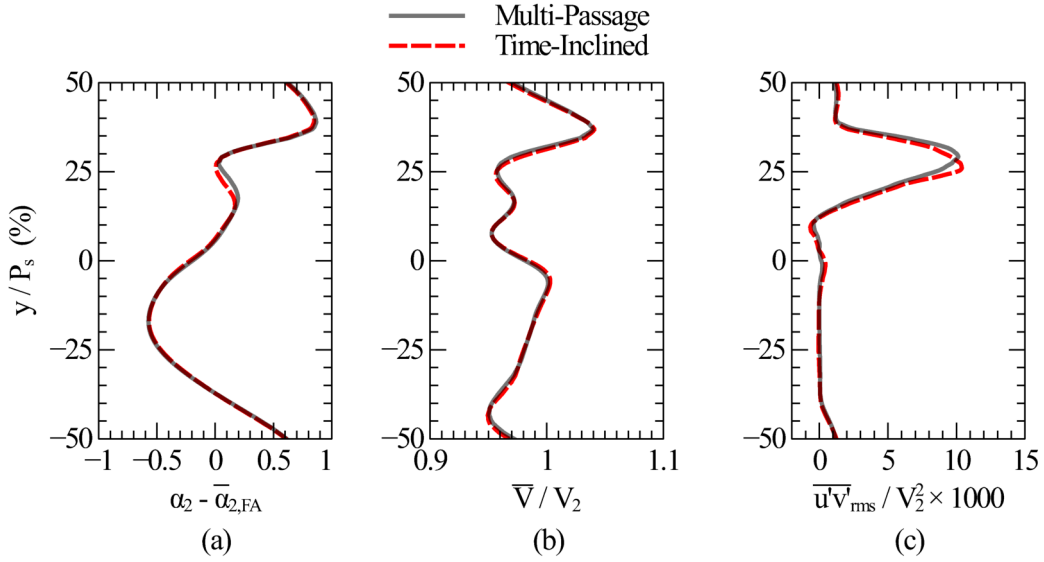

Figure 4.36: Pitch-wise distribution of exit angle (a), velocity (b) and Reynolds stress tensor component $\overline{u'v'}$ (c) on the viscous T106A cascade case at $(x - x_{TE}) / c_x = 30\%$.

4.3 Computational Cost Considerations

The main goal of the time-inclined method is to lower the computational cost of rotor/stator simulations by reducing the size of the computational domain. For unsteady simulations, achieving a periodic or quasi-periodic state can be very tricky.

The convergence problem is further accentuated in scale-resolving simulations. Since meshes are often very fine in order to provide sufficient spatial resolution to the smallest scales, the numerical constrain to the maximum stable time-step size is very stringent. As a consequence, significantly more iterations are usually required to achieve a quasi-periodic state in explicit solvers.

Moreover, low-dissipation schemes, characteristic of the high-order solvers often used for scale-resolving or turbulence-resolving simulations, contribute to the persistence of spurious or non-physical perturbations that must dissipate or leave the computational domain while hindering the convergence rate.

The analysis of the flow requires the statistical convergence of the solution. To that end, several characteristic times (e.g. through-flow times, blade-passing periods, etc.) are simulated after a quasi-periodic state has been reached. Thus, since the time-step size is usually very small, a large portion of the total number of iterations must be dedicated to achieving statistical convergence.

Furthermore, exact, unsteady, non-linear boundary conditions do not exist for such a kind of simulations. Therefore, some level of reflectivity and/or error is expected to be introduced by the boundary condition formulation, which may not be rapidly dissipated by the numerical scheme and can also negatively affect convergence.

Thus, given the difficulties associated with unsteady and scale-resolving simulations, it is essential to understand the impact of the time-inclined method on their computational cost.

Four main factors contribute to the differences in the computational cost of a full-annulus (or multi-passage) and a time-inclined simulation:

Cost per iteration and computational node

The computational cost per time step and point considers the amount of operations involved in the algorithm of the numerical solver to perform a single iteration for one computational point.

The costs of the time-inclined and baseline time-marching methods are essentially the same. The reason is that only one additional operation is required per time-step and

solution point for time-inclining, which consists of transforming back the inclined variables $\boldsymbol{Q}$ to the conservative variables $\boldsymbol{U}$. This operation allows the computation of the fluxes since they are a function of $\boldsymbol{U}$, while the time-marching is performed on $\boldsymbol{Q}$. However, the cost of this algebraic operation is negligible, especially for GPU architectures.

Cost due to time-step size restrictions

The impact of numerical stability constraints on the maximum time-step size depends on the set of equations being solved. As shown in Chapter 3, the time-inclined equations are generally more restrictive of the maximum time step size.

As exemplified by the two-dimensional wave equation, the propagation speed in the inclined equations depends on the inclination parameter λ. Therefore, the restriction of the maximum time-step size is dependent on the magnitude of λ and complicates drawing conclusions about the impact of time-inclining on time-step size.

For instance, the time inclined method may transform a rotor/stator case with a pitch ratio close to 3/2 in a computational domain with exactly 2 stators and 3 rotors. In such a case the inclination parameter should be very small for usual rotor wheel speeds. Therefore, in such a case, the difference between the baseline time-step size and the time-inclined size should be negligible.

On the other hand, the cases that have been presented were chosen to obtain a large inclination parameter and highlight the errors of the neglected terms in the time-inclined transformation. As a result, the restriction to the maximum stable time-step size should be very severe. Nevertheless, in the presented test cases, the time-inclined simulations were carried out with the same time-step size as the multi-passage cases without experiencing any numerical stability problems.

The aforementioned 3/2 rotor/stator case is pretty standard in LPT designs and, since the errors of the viscous time-inclined transformation also scale with the magnitude of λ, both the impact on the computational cost and on the errors in the solution should be even lower than what has been presented herein.

Cost due to computational domain reduction

The time-inclined method allows for reducing the size of the computational domain. The savings in computational cost associated with such a reduction are straightforward.

However, the actual savings may vary depending on the pitch ratio and/or rotor speed since the reduction to a single-passage time-inclined domain is not always guaranteed.

Scale-resolving simulations of full-annulus geometries are, generally speaking, unaffordable. Since blade counts are often selected not to be divisible by each other, the annulus does not contain a reduced periodic sector. Thus, an alternative to the direct periodic approach must be chosen. In such a case, the time-inclined method may allow performing an equivalent reduced domain simulation and the computational cost reduction would not only be meaningful by itself, but also because the alternative blade-count-retaining simulation would be unfeasible in practice.

In the cases presented in this work, the periodicity of the problem required a minimum of two passages in the full domain. Since the transformed cases were reduced to a single passage, the computational cost associated with the domain size was halved. Two-dimensional cases are, nowadays, extremely affordable. For realistic three-dimensional cases, however, the cost reduction is more significant.

Cost due to convergence time to a quasi-periodic state

The most challenging part of quantifying the computational cost reduction obtained by the time-inclined method is the convergence time to a periodic or a statistically converged state. The convergence time of passage-reducing methods is only sometimes well-understood, and small practical details of the implementation often hinder it ([82, 127]). Most rotor/stator simulations do not show a proper unsteady convergence analysis and, if any, it is restricted to monitoring the key engineering figures of merit of the problem.

Figure 4.37 displays the unsteady norm L^2 of the MP analysis with direct periodicity and the TI method[2] for the lower Reynolds flat-plate cascade case, where L^2 is defined as

$$L^2 = \frac{1}{T\,S}\sqrt{\int_S ds \int_{t_0}^{t_0+T} \left\{\frac{p(t) - p(t-T)}{p(t-T)}\right\}^2} \tag{4.2}$$

and S is the plate or airfoil surface. It can be noticed that the convergence rates of both approaches are similar but that they stall at a slightly different level.

It is essential to recall that the final solution is not purely periodic since there are flow instabilities with frequencies different from the fundamental one. If these non-synchronous frequencies dominate, then the chosen unsteady norm says very little about the final converged state.

It can be noticed that the final state is reached in about 100 plate through-flow times, where the residence time is defined as $t_r = c/V_{2,is.}$. The total length of the computational

[2] At the start of the simulations, each passage in the direct periodic domain contains the same RANS solution present in the time-inclined single-passage domain.

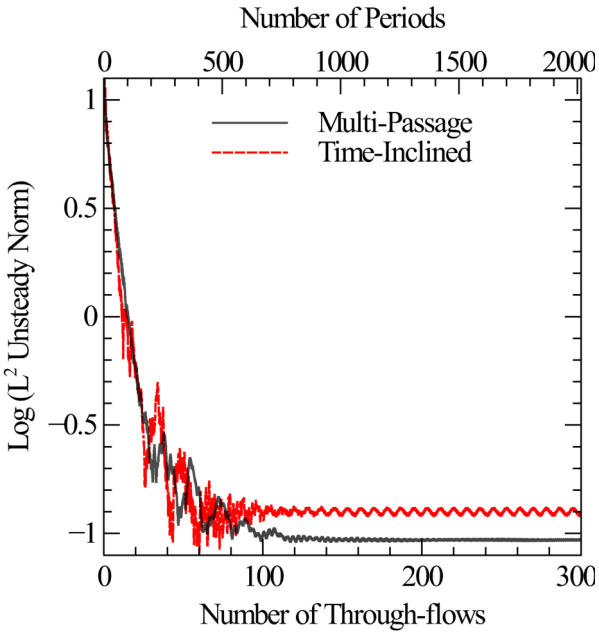

Figure 4.37: Convergence history of a flat plate cascade as a function of the number of inlet perturbation periods and through-flow times ($t_r = c/V_{2,is}$).

domain is $4c$. Since the convergence time is controlled by the total size of the computational domain, it can be stated that the solution converges in about 25 computational domain through-flow times, both in the TI and the multi-passage cases. The main conclusion drawn from Fig. 4.37 is that the TI method does not degrade the convergence rate to the final state.

The physical convergence time of harmonically forced flows depends on the number of periods, $t_{con} \propto f^{-1}$, for low reduced frequency excitations or the number of through-flow times for high reduced frequency excitations, $t_{con} \propto t_r = c/v_c$. The required level of convergence depends on the amplitude of the highest harmonic resolved in the simulation. It can be anticipated that without a high level of convergence, it is impossible to match the third harmonic of the unsteady pressure shown in Figures 4.13 (b) and 4.19 (b), whose amplitude is a small fraction of the inlet total pressure (about $10^{-4}P_{t,1}$). It can be safely stated that the confidence in the level of convergence of the cases shown in this work is high.

If it is assumed that:

1. The convergence rate to the final state of both approaches is the same (see Figure 4.37)
2. Both simulations are run with the same time-step size
3. The same amount of time steps are carried out

4. The added computational time per iteration due to TI is deemed negligible

Then, the cost reduction should be proportional to the decrease in the size of the computational domain.

To provide an example, the low-Reynolds ($Re_c = 10^4$) flat-plate case ran in a single NVIDIA GeForce GTX 1080Ti GPU for 2160 perturbation periods as can be observed in Figure 4.37. It took about 5174 and 9208 minutes using the time-inclined and the multi-passage approaches, respectively, which yields a speed-up factor of around 1.78.

The $Re_c = 10,000$ flat-plate cascade was also run in parallel in multiple GPUs. The MP case consisted of 2 passages and was divided into 12 sub-domains to run on 12 NVIDIA GeForce GTX 1080Ti GPUs. The TI case featured a single passage divided into 6 sub-domains to be ran in 6 GPUs of the same model. The MP and TI cases ran for $1,128$ perturbation periods, which took $1,580$ minutes and $1,409$ minutes, respectively, showing a lack of degradation to the computational time per passage with the time-inclined method.

5 Three-Dimensional Scale-Resolving Simulations

Contents

5.1 Upstream Perturbation Modelling **126**

5.2 Cases Description **129**

5.3 Results **135**

5.4 Summary and Conclusions **153**

In this chapter, three-dimensional simulations of the T106C low-pressure turbine linear cascade with incoming wakes have been conducted to demonstrate the suitability of the time-inclined method for retaining the exact blade count in scale-resolving simulations.

In the previous chapter, the implementation of the TI method was verified and its limitations for the truncated NS equations were analysed in 2D flows. Nevertheless, the features that characterise complex turbomachinery flows are only present in 3D simulations.

Thus, in the present chapter, two sets of three-dimensional simulations are reported. The sets differ in the modelling strategy for the incoming perturbations: firstly, the immersed boundary approach is used to introduce a cascade of moving bars that act as the trailing edges of the preceding row and generate incoming wakes. The second set of simulations introduces wake-like perturbations at the inlet section of the computational domain.

For each of the two modelling approaches, three-way comparisons have been generated. The solution of the direct periodic full domain, spanning several blade passages, is compared to the single-passage time-inclined solution and to a single-passage solution that approximates the pitch ratio to the nearest integer.

The present chapter is organised as follows: first, the different upstream perturbations modelling strategies are discussed. Then, the setup of the three-dimensional turbulence-resolving simulations that have been carried out are described. Next, the results section shows, for all the test cases, the level of agreement between the solutions obtained by the different methodologies comparing several figures of merit. Finally, the chapter is closed with a summary of the results and some concluding remarks.

5.1 Upstream Perturbation Modelling

The TI method transforms the physical plane $(\mathbf{x}, t)$ to the inclined plane $(\mathbf{x}', \tau)$. The transformation is such that periodic signals spanning several passages in the physical plane (like the synchronous unsteady perturbations from the preceding row) are made periodic in fewer passages in the inclined plane.

Since the objective of the present chapter is to evaluate the accuracy of the TI method in SRSs of linear cascades, the methodology involves three-way comparisons between:

1. A reference case –also referred to as direct periodic or Multi-Passage (MP) case– for which the pitch ratio of the perturbations and airfoils is not an integer and, thus, several airfoil passages must be included in the computational domain to impose periodicity conditions.
2. A Time-Inclined (TI) single-passage simulation, which results after transforming the reference problem and retains the exact blade count.
3. A Single-Passage (SP) simulation, which is derived by applying the standard methodology of approximating the pitch ratio of the reference case to the nearest integer, also modifying the perturbation travelling speed to match the reduced frequency of the reference case [5].

Since the computational cost of performing parametric SRSs is very high even for a single passage domain, the most realistic approach of simulating the rotor and stator passages is replaced by modelling the perturbations coming from the preceding rotor row.

Alternatively, another widespread strategy is to introduce moving bars in the computational domain as wake generators [5, 8, 9], which is also a technique used in experimental campaigns [30, 136].

Low-pressure turbine airfoil testing is frequently conducted in low-speed wind tunnels. They are not only more economical than high-speed tests but also ease their instrumentation and enable higher-quality measurements. Unfortunately, low-speed cascade testing is associated with slow bar speeds, which entail the impossibility of performing the TI transformation (see Chapter 3 for details on the limitations of the TI method). Though high-speed experiments are certainly more representative, using moving bars is not exempt from difficulties. In addition to the mechanical constraints of using extremely slender bars, at realistic operating wheel speeds the bars feature shock waves. Such shock waves would not appear at the trailing edges of rotor airfoils and modify the characteristics of the wakes of the bars.

An Immersed Boundary Method (IBM) [137] is commonly used to mitigate some of the adverse effects of the moving bar approach [5, 8], to avoid the stringent mesh size require-

ments of adequately resolving the bars and to circumvent the necessity of a sliding plane to interface the bar and airfoil rows.

With such a perturbation model, strict control over the perturbations that are being injected is lost. The flow field downstream of the bar cascade may differ in the three approaches above which would result in artificial differences between them. At this point, it is worth noting that the dissipation properties of the numerical schemes for the TI method and baseline solver are different, which is relevant since the immersed bars are often notably under-resolved.

Maintaining low levels of uncertainty in the comparisons between the three approaches requires a strict control over the injected upstream perturbations. In rotor/stator simulations, both rows are separately transformed by the TI method. The time-inclined sliding plane naturally accommodates the spatially periodic solution in the inclined rotor passage to the spatially periodic solution in the stator passage. Therefore, the perturbation model chosen for the present chapter as an alternative to the immersed bars approach consists of injecting wake-like perturbations at the inlet section, which takes the role of a rotor/stator interface.

Such a model allows us to accurately transform the perturbations of the physical domain to the inclined plane. Thus, it ensures that the TI case is subjected to the same perturbations as the MP simulation. However, since the perturbations are imposed at the inlet section, the accuracy limitations of the unsteady non-linear Boundary Conditions (BCs) for SRSs gives rise to non-physical reflections at the inlet, which contaminate the solutions.

In SRS, characteristic BC formulations [110, 113] feature a parameter that can be tuned to reduce the unphysical reflections at the boundaries in exchange for a relaxation on the imposition of the desired boundary value. Rigour in comparing the MP and TI approaches requires control over the perturbations imposed at the boundary. Tuning the BC parameters towards a more non-reflecting formulation results in a lack of correspondence between the state of the inlets in the baseline and inclined simulations at any point in time.

A reflective formulation can lead to non-physical perturbations in the flow field, but ensures the fulfilment of the goal of imposing a certain perturbation in the MP case and its accurate time-inclined transformation in the TI simulation. The drawback is that the reflections caused in the original and the transformed set of equations are different. After several tests, for the inlet perturbations cases in the present chapter, such approach has been followed.

It is essential to highlight that state-of-the-art inlet/outlet boundary conditions for turbomachinery flows, such as the ones used here, are not accurate enough for the inlet perturbations problems posed herein.

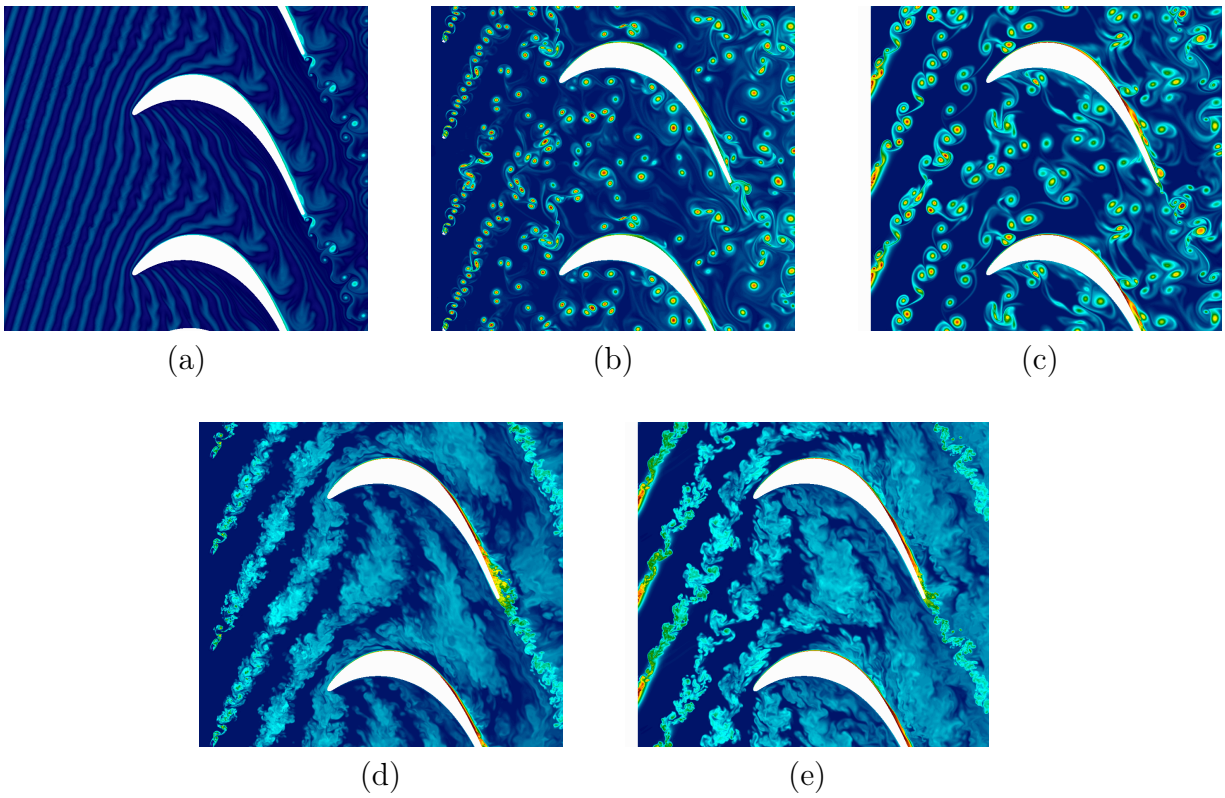

(a) (b) (c)

(d) (e)

Figure 5.1: Snapshot of the unsteady entropy for 2d (top) and 3d (bottom) simulations of the T106 cascade with incoming sinusoidal perturbations (a), immersed boundary bars as wake generators (b) & (d) and wake-like perturbations at the inlet section (c) & (e).

The problem of modelling the perturbations stems from the enormous computational costs of 3D rotor/stator simulations of multiple passages, which are needed as the reference to which TI solutions are compared. Ideally, both rotor and stator rows would be included in the computational domain, potentially avoiding modelling errors. However, such an approach is less widespread at the industry level and entails a high computational cost.

Such cost would be immensely reduced if the comparisons were conducted in 2D flow. However, the physics behind complex 3D flow phenomena such as the breakdown of incoming vortices and their transition to turbulent flow motivate analysing the TI methodology with 3D simulations, which is exemplified in Figs. 5.1 (a) – (e):

Chapter 4 showed the verification of the TI implementation in the baseline code using 2D linear cascades subjected to sinusoidal perturbations (see Fig. 5.1 (a)). Figures 5.1 (b) and (c) correspond to 2D simulations with immersed moving bars and wake-like inlet boundary conditions, respectively. Similarly to 5.1 (a), the perturbations can travel throughout the passage and are found at the outlet section.

In 5.1 (b) and 5.1 (c), the breakdown of incoming vortices takes a much larger characteristic time than in 3D flow. Moreover, the vortices that reach the outlet section gravely

deteriorate the statistical convergence rate. Such perturbations, which would also originate at the trailing edges of a preceding row in 2D, do not resemble a realistic unsteady flow downstream of a rotor row.

Figures 5.1 (d) and (e) correspond to the 3D simulations carried out in the present chapter, which are thoroughly described in the next section. Their two-dimensional counter-parts in figs. 5.1 (b) and (c) show how, in 3D flow, vortex breakdown occurs in a much shorter length and transitions to turbulent flow.

The difficulties described in this section arise from the necessity of performing a SRS of the multi-passage domain. This simulation establishes a reference solution to which the TI method is compared, and has an enormous computational cost due to the required level of resolution, and the number and size of the rotor and stator row passages. Such reference simulation is, in fact, the simulation that would be avoided once demonstrated the suitability of the TI method for retaining the exact blade count in scale-resolving simulations. Furthermore, the computational cost reduction offered by the TI method may allow performing the simulation of the rotor and stator passages, completely avoiding the complications due to perturbation modelling.

5.2 Cases Description

Two sets of three scale-resolving simulations (the reference, the TI, and the modified pitch ratio cases) of a LPT linear cascade with incoming wakes have been carried out. The sets differ in the strategy used to generate such incoming wakes. The first set of simulations uses the IBM with moving bars approach, while the second set injects wake-like perturbations at the inlet section.

As seen in the snapshots of instantaneous entropy in Figs. 5.2 (d) and (e), the incoming wakes from either perturbation models are stretched and deformed in their path through the passages. This can also be appreciated in Figure 5.2 (a), which shows a snapshot of the time-inclined immersed bar case with iso-surfaces of Q-criterion coloured by the Mach number, while the background shows the entropy field. Figures 5.2 (a) and (b) give a qualitative description of the turbulent flow, the convection of wakes through the passages, the turbulent transition of the boundary layer and the ability of the numerical setup to capture all such complex phenomena.

The geometry of the linear cascades corresponds to the T106C cascade tested at the von Karman Institute during the UTAT and TATMo EU projects, for which the pitch-to-chord ratio of the cascade is $P_s/c = 0.95$ and the isentropic Mach number is $M_{2,is} = 0.65$. The Reynolds number based on the chord and isentropic exit velocity is $Re_{2,is} \approx 90,000$.

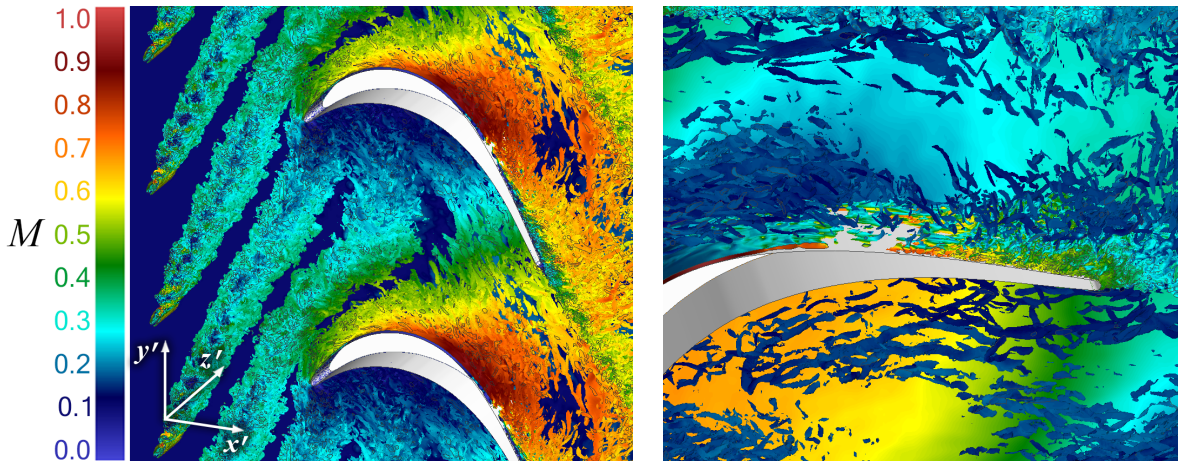

(a) (b)

Figure 5.2: Iso-surfaces of Q-criterion coloured by the Mach number with the entropy field in the background for the time-inclined simulations of the T106 cascade with immersed boundary bars (a). Iso-surfaces of Q-criterion coloured by the entropy with the static pressure field in the background in the aft of the airfoil (b).

The pitch ratio between the upstream perturbations and the cascade is $P_s/P_r = 7/4$ and therefore the reference or Multi-Passage (MP) case consists of four T106 airfoils and seven perturbations. The perturbations travel with a rotor speed u_r such that $M_r = u_r/a_0 = 0.375$, where a_0 is the average speed of sound at the inlet station. The reduced frequency, defined as $f_{red} = fc/v_{2,is}$ is 1.043, and the flow parameter is $\Phi = v_x/u_r = 0.688$.

The TI method allows the reduction of the computational domain to a single passage that contains 2 perturbations, obtaining a non-dimensional transformation parameter $\lambda a_0 = 0.38$.

The computational domains for the multi-passage and time-inclined simulations are displayed in Fig. 5.3. For the inlet perturbations cases, the computational domain is shortened upstream of the cascade to relocate the inlet section to the same axial position as the immersed bars. Such location is depicted with a green line in Fig. 5.3 and corresponds to the axial coordinate $x - x_{LE} = -0.67c_x$, where c_x is the axial chord of the T106 airfoil.

The cascade inflow and exit measuring stations are also shown in Fig. 5.3 in red and blue lines, respectively. The subscript 1 is used in the present chapter to refer to the inflow measuring station, located at $x - x_{LE} = -0.3c_x$, while 2 refers to the exit measuring station, located at $x - x_{TE} = 0.4c_x$.

The time-inclined computational domain in Fig. 5.3 is also used for the approximate single-passage approach, SP, which originates when the pitch of the perturbations P_r is modified to $\widetilde{P}_r$ in order to achieve an integer pitch ratio of $P_s/\widetilde{P}_r = 2$. The perturbation speed $\widetilde{M}_r$ has been likewise modified to retain the reduced frequency of the direct periodic

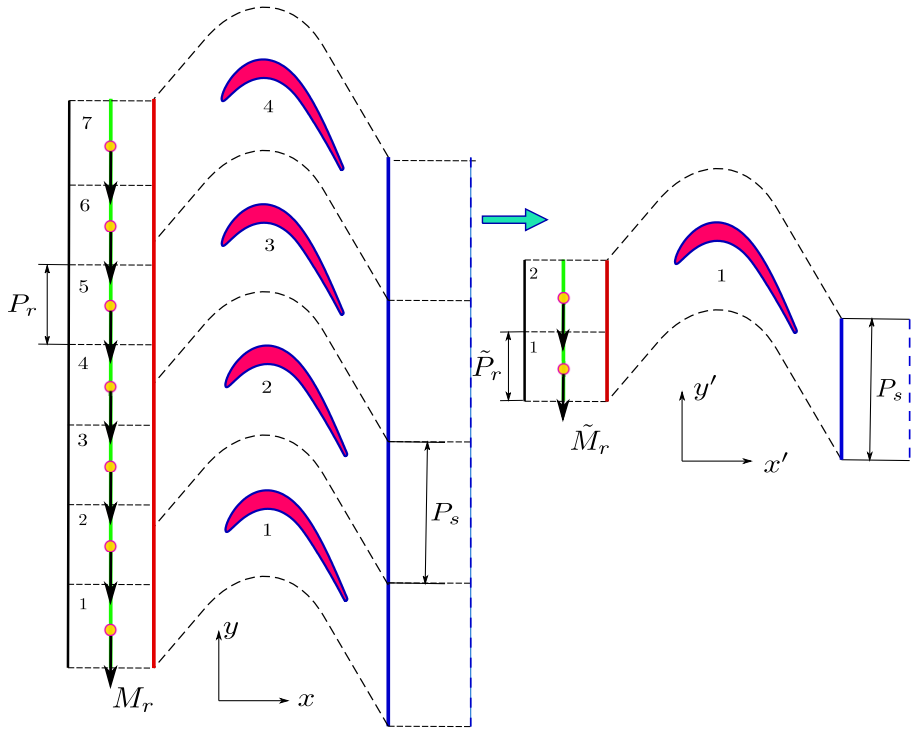

Figure 5.3: Sketch of the MP and TI computational domains with the location of the upstream immersed bar cascade (green), inflow (red) and exit (blue) measuring stations.

case, resulting in an alteration of the flow parameter to $\widetilde{\Phi} = 0.786$.

A summary of the case parameters is displayed in table 5.1.

$Re_{2,is}$	$M_{2,is}$	F_{red}	Φ	P_s/P_r	P_s/c
$90,000$	0.65	1.043	0.688	$7/4$	0.95
P_s/c_x	M_r	λa_0	$P_s/\tilde{P}_r$	$\widetilde{M}_r$	$\widetilde{\Phi}$
1.115	0.375	0.38	2	0.328	0.786

Table 5.1: Main parameters of the simulations.

The first set of simulations features a cascade of moving bars with a diameter-to-airfoil chord ratio of $D_{bar}/c = 2\%$ located $0.67c_x$ upstream of the leading edges of the stator cascade. Figure 5.4 shows a snapshot of the unsteady pressure in the time-inclined simulation with the immersed bar cascade.The snapshot in Fig. 5.4 displays the solution in the inclined plane $(\mathbf{x}', \tau)$. It has been obtained in a single-passage computational domain containing two immersed moving bars per airfoil passage, as shown in Fig. 5.3. Then, the instantaneous solution in the inclined plane was copied to the neighbouring passages for visualization.

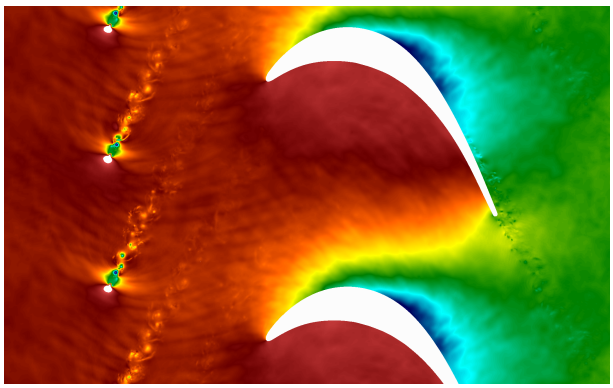

Figure 5.4: Time-inclined snapshot of the unsteady pressure for the case with immersed bars (the computational domain is extended an additional pitch for clarity).

A high disturbance environment is found in Fig. 5.4 due to shock waves in the bar cascade region. As previously discussed, one of the disadvantages of modelling the upstream perturbations with moving bars is that, for realistic wheel speeds, the bars generate shock waves due to the high relative speed perceived by the bars.
Figure 5.5 displays the phase-locked averaged total pressure in the multi-passage domain for the set of simulations with inlet perturbations of total pressure. The wake-passing period is divided into 48 phases to obtain the phase-locked averages, and a temporal and radial average of the unsteady solution is carried out for each phase. The aforementioned lack of accurate non-reflecting boundary conditions and the proximity of the inlet section to the cascade give rise to undesired non-physical perturbations, which can be noticed in the neighbouring elements of the inlet (see Fig. 5.5).

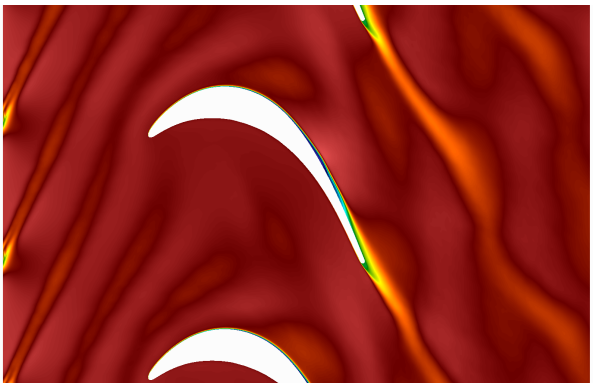

Figure 5.5: Phase-locked average of the total pressure for the multi-passage or reference case with inlet perturbations.

As previously discussed, in a time-inclined rotor/stator simulation the wakes from the preceding rotor, which are spatially periodic in such computational domain, cross the sliding plane interface into the stator domain. The time-inclined sliding plane automatically transforms the rotor spatially periodic signals into spatially periodic signals in the

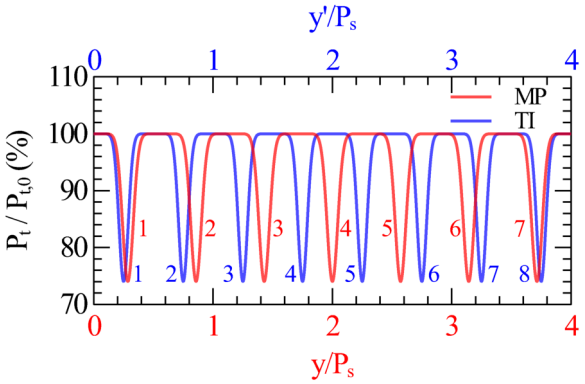

Figure 5.6: Total pressure distributions imposed at the inlet boundary for the multi-passage and time-inclined simulations.

stator domain, which is a consequence of time-inclining each of the domains. The second set of cases seek to retain such property by inclining the total pressure defects imposed at the inlet section, $P_{t,0}(\mathbf{x}, t) \implies P_{t,0}(\mathbf{x'}, \tau)$, as if it was the sliding plane and the preceding wakes were crossing it. Figure 5.6 displays a sketch of the total pressure distribution imposed as a boundary condition for the multi-passage and time-inclined simulations. The time-inclined computational domain only spans a single passage in the pitch-wise direction, $0 \leq y' \leq P_s$. However, the total pressure distribution is extended to show how, in the multi-passage time-inclined plane, $y' \in [0, 4\,P_s]$, there would fit 8 wakes instead of 7. Thus, the time-inclined method achieves an integer pitch ratio of ${}^{P_s}/_{\tilde{P}_r} = 2$, allowing us to reduce the computational domain to a single-passage domain.

The computational multi-passage domain consists of four identically meshed passages to avoid artificial discrepancies due to grid spacing in the comparisons with the single-passage (TI and approximate pitch ratio) simulations. Each passage is discretized into 6^{th} order triangular prisms and hexahedral elements, which are generated after radially extruding the 2D meshes for 50 layers and for a total span of 30% of the axial chord.

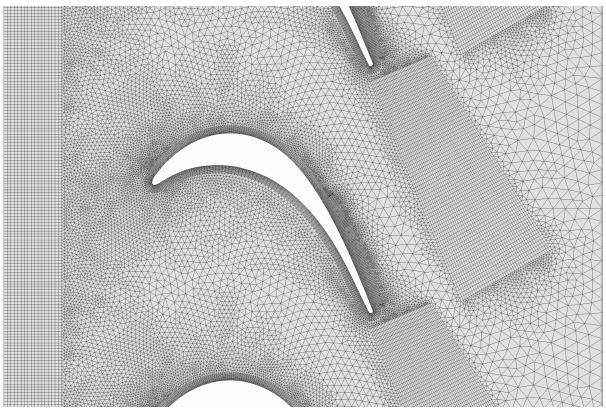

Figure 5.7: General view of the mesh for the case with inlet perturbations.

A general view of the 2^{nd} order mesh (without interior solution points in each element) for the inlet perturbation set of simulations is shown in Fig. 5.7. The inflow region is sufficiently fine to properly capture and propagate the turbulence associated to the incoming wakes (see Fig. 5.2 (e)). The airfoil region is also fine enough for wall-resolved LES applications and a wall-normal spacing $\Delta y^+ < 1$ is ensured for the turbulent region of the boundary layer. The stream-wise and span-wise spacings in such region are $\Delta x^+ \simeq \Delta z^+ < 8$, below the recommended values in [138]. A detailed view of the high-order elements, in red, and their interior points is shown in Fig. 5.8. A structured mesh, located downstream of the trailing edges, ensures accurate simulation of the mixing process in the wake region of the cascade.

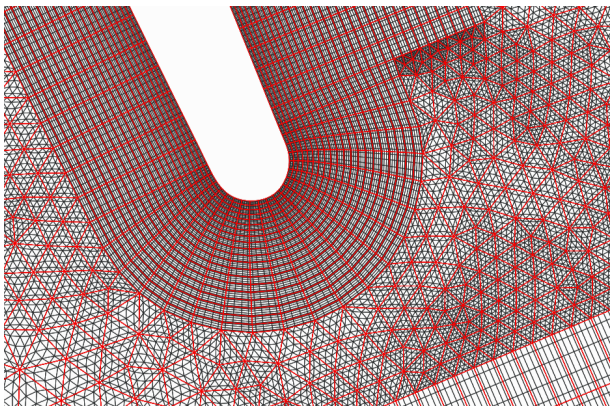

Figure 5.8: Mesh detail of the trailing edge region with 6^{th}order elements (in red) and interior points (in black).

Some of the solution points in the discretization of each element type lie in the element faces, which means that the solution at a point located in a face or a vertex shared by several elements is computed multiple times. For that reason, Table 5.2 displays the number of computational nodes and the number of physical nodes (geometrically unique), in millions, for the single and multi-passage domains.

Case	Comp. Nodes	Phys. Nodes
IBM Bars (4 pass.)	284 (1,136)	156 (624)
Inlet Pert. (4 pass.)	188 (753)	103 (412)

Table 5.2: Number of nodes in the computational domains, in millions.

5.3 Results

The scale-resolving simulations were started from a second-order RANS simulation with a steady inflow. The high-order solver ran for several blade-passing periods until a quasi-periodic state was achieved. Then, the solution was time and radially-averaged for over 50 periods to ensure that convergence was achieved. It is worth remembering at this point that the nomenclature chosen to reference each of the cases in the three-way comparisons below is as follows: the directly periodic or multi-passage domain case is called MP, the time-inclined single-passage simulation is named TI, and the approximate pitch ratio single-passage case is referred to as SP.

Time-Averaged Isentropic Mach Number.

Figure 5.9 (a) shows the averaged isentropic Mach number along the blade surface for the cases with immersed bars. The agreement between the three solutions is very good on the pressure side. Some differences are found in the suction side near the leading edge, especially for the TI case, although the agreement is recovered further downstream. The source of such mismatch is attributed to the differences present in the inflow region of the cascade, which are due to the dissimilar effect of the under-resolved bar cascade on the inflow angle for each case, and which will be discussed in the following section.

A clear improvement is achieved by replacing the bar cascade with inlet perturbations. Figure 5.9 (b) shows a very high degree of agreement between the MP and TI cases. The consequence of injecting inlet perturbations and their appropriate TI transformation is the obtention of the same inflow conditions for both the MP and TI cases. As a result,

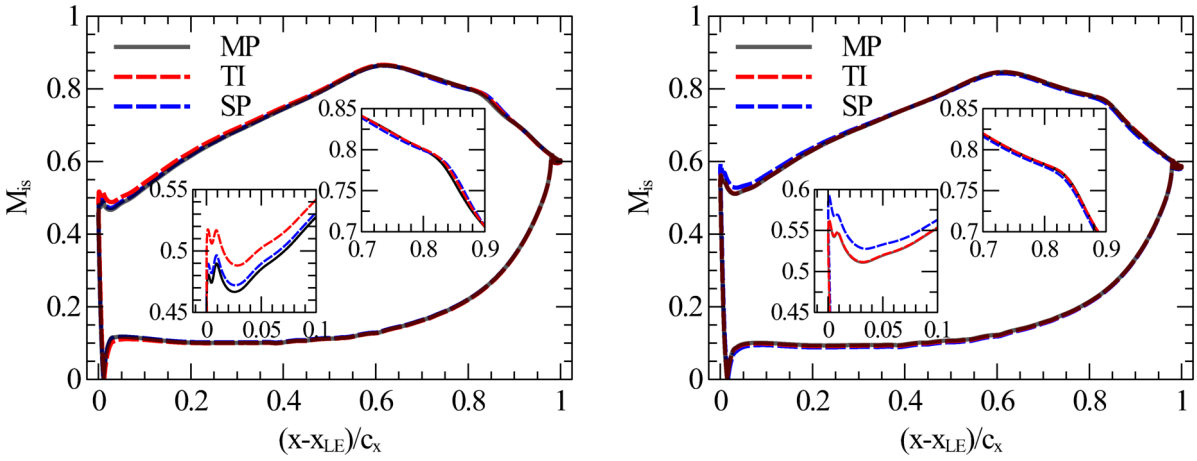

(a) Case with immersed bars (b) Case with inlet perturbations

Figure 5.9: Radially and time-averaged isentropic Mach number distribution along the blade surface for the cases with immersed bars (a) and inlet perturbations (b)

an excellent matching of the MP and TI solutions is achieved.

Since the SP inlet perturbations are obtained by altering the spatial periodicity of the of the MP perturbations, the inflow conditions that are obtained differ from the reference case. Therefore, slight differences in the isentropic Mach number distribution can still be observed. In order to obtain the correct inflow conditions in the SP case, the solution of the MP case has to be *a priori* known. Then, some kind of iterative process, involving modifying the inlet perturbations, should take place to achieve accurate results. Nevertheless, the effects of not retaining the exact blade count may manifest in some other way.

This is important since the problem cannot be circumvented in the SP methodology. Even for rotor/stator simulations, altering the pitch of the rotor can lead to errors. In contrast, a TI methodology that features a sliding plane transforms the incoming wakes correctly, automatically leading to accurate results.

Upstream Time-Averaged Flow Field.

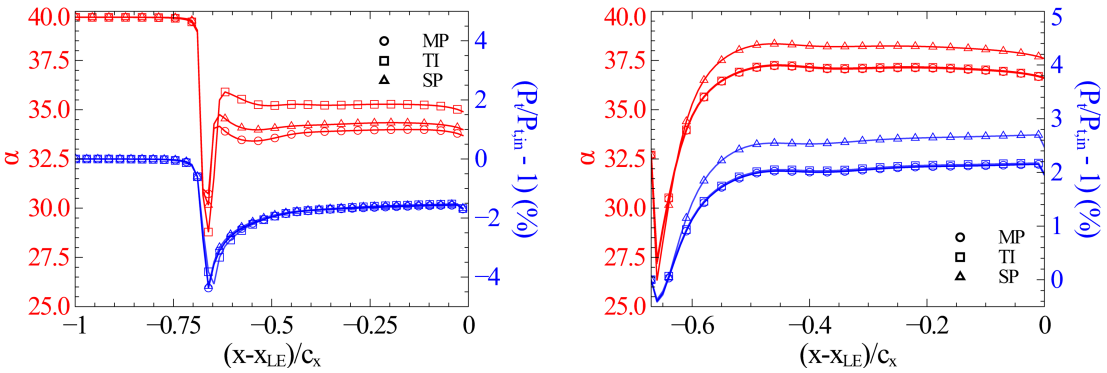

(a) Case with immersed bars (b) Case with inlet perturbations

Figure 5.10: Axial evolution of the pitch-wise and time-averaged inflow angle (in red) and total pressure (in blue) for the cases with immersed bars (a) and inlet perturbations (b)

Figure 5.10 (a) shows the axial evolution of the time and radially-averaged total pressure (in blue) and inflow angle (in red) for the under-resolved immersed bar modelling approach. Even though the total pressure distributions are well-captured, such perturbation model does not accurately reproduce the cascade inlet angle of the MP case neither with the time-inclined method nor when the pitch ratio is approximated. Some of the consequences have already been discussed in Fig. 5.9 (a), and may be avoided in the TI methodology if the bars are appropriately resolved and transformed in a separate row domain. Nevertheless, the total pressure evolution, which is referenced to the total pressure

imposed at the inlet section $P_{t,in}$, is well-captured. Although the treatment of the under-resolved wave-lengths is the same in the MP and SP simulations (both are performed with the baseline numerical scheme), not retaining the exact blade count translates into differences between such solutions downstream of the bar cascade.

It is worth noting that there is a very small lag between the TI and MP or SP axial evolutions of the properties downstream of the bar cascade axial location. In Figure 5.10 (a), a local maximum in the inflow angle of the MP and SP cases is achieved downstream of the immersed bar cascade at $x - x_{LE} \approx -0.63c_x$. For the TI simulation, however, the maximum lags behind and is achieved at $x - x_{LE} \approx -0.62c_x$. Such an effect is attributed to differences in the mixing process due to the neglected terms in the transformation of the NS equations, which are dominant in regions featuring large vortical structures. Such differences were previously documented in the 2D simulations carried out in [129] and are thoroughly described in Chapter 4. However, since large vortical structures rapidly break down to smaller turbulent scales in 3D flow, the impact of the neglected terms is much smaller and more local.

Figure 5.10 (b) shows the results for the cases imposing inlet perturbations, which can be accurately transformed to the time-inclined plane. Using this approach, which emulates the behaviour of a time-inclined rotor/stator interface, very accurate axial evolutions of the inflow angle and total pressure are achieved for the TI case. The angle and total pressure axial evolutions obtained by the SP methodology have little to do with the reference simulation, owing to the approximation of the pitch ratio by the SP approach.

Time-Averaged Skin Friction Coefficient.

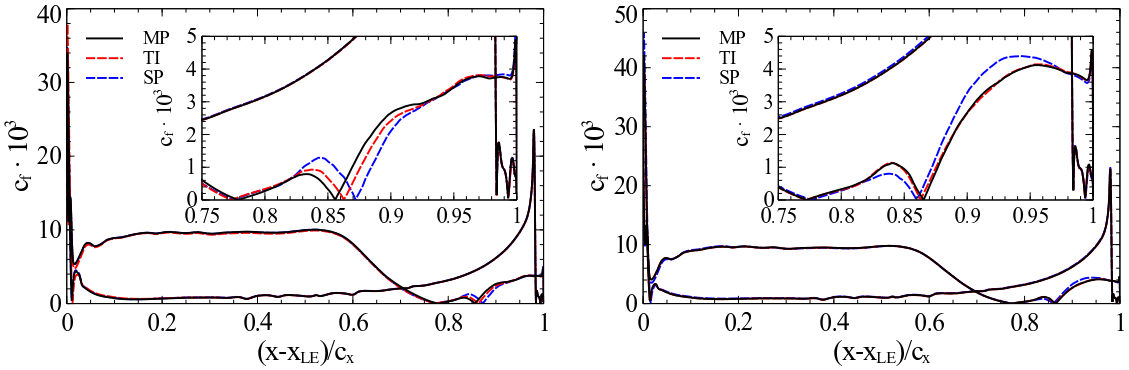

(a) Case with immersed bars (b) Case with inlet perturbations

Figure 5.11: Radially and time-averaged skin friction coefficient along the blade surface for the cases with immersed bars (a) and inlet perturbations (b)

The averaged skin friction coefficient $c_f = \tau_w/(1/2\rho_2 V_2^2)$, where $\tau_w = \mu(\partial u/\partial y)|_{y=0}$, is displayed in Fig. 5.11 (a) for the cases with immersed bars. Overall, good agreement is

found for all the simulations, but the effect of having non-equal flow conditions entering the cascade might have played a significant part in the differences found in the prediction of the size of the bubble. For the immersed bar cases in Fig. 5.11 (a), the differences in the predicted location of the reattachment point are larger between the multi-passage and single-passage cases than between the multi-passage and time-inclined cases. This occurs even though the magnitude of the differences between the multi-passage and time-inclined cascade inlet angles are larger than those between the multi-passage and single-passage simulations (see Fig. 5.10 (a)). It seems, as also evidenced by the cases with inlet perturbations in Figure 5.11 (b), that retaining the exact blade count is more important than accurately capturing the exact inflow conditions. Furthermore, it can partially compensate the errors due to the incorrect inflow angle prediction of the TI simulation. A possible explanation might be that the TI method retains the exact blade count and flow parameter Φ in the physical plane $(\mathbf{x}, t)$, even though in the inclined plane, $(\mathbf{x}', \tau)$, the flow parameter is modified to $\widetilde{\Phi}$ and the pitch ratio ${}^{P_s}/_{P_r}$ to ${}^{P_s}/_{\tilde{P}_r}$. For the single-passage approximation, in addition to the alteration of the pitch ratio, the bar speed is modified to match the reduced frequency of the MP case. Therefore, the resulting flow parameter, $\widetilde{\Phi}$, cannot be matched.

For the inlet perturbations set of cases, in which the MP inflow conditions are accurately captured by the TI method, the MP and TI distributions of skin-friction coefficient in Figure 5.11 (b) are nearly coincident. Meanwhile, the SP approach is hindered by errors in the inflow conditions and the pitch ratio approximation.

Inflow Turbulence.

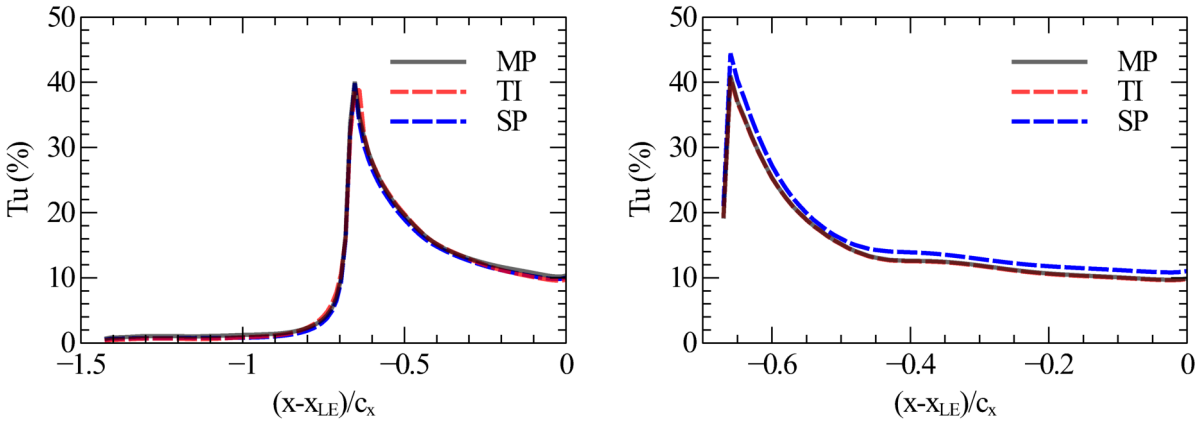

(a) Case with immersed bars (b) Case with inlet perturbations

Figure 5.12: Evolution of the turbulence intensity upstream of the T106 cascade in the cases with immersed bars (a) and with inlet perturbations (b).

Figure 5.12 (a) shows the axial evolution of the turbulence intensity, $Tu = \sqrt{2/3k}/V_2$, where k is the turbulent kinetic energy, for the immersed bars simulations. The turbulence intensity is low at the inlet boundary of the computational domain, but suddenly increases at $(x - x_{LE}) = -0.67c_x$, where the immersed bar cascade is located. From that point, the wakes start to mix and the turbulent intensity decays further downstream.

Overall, the reference axial evolution (MP) is well-captured by the TI and SP approaches, especially far upstream and downstream of the bar cascade. Nonetheless, there is a slight lag in the prediction of the Tu peak for the TI case. Such an effect might be linked to the neglected terms in the time-inclined NS equations. As previously discussed, the biggest challenge for such approximation is dealing with regions that feature vortex shedding mechanisms, such as the region immediately downstream of the bars. Nevertheless, the impact of such lag in the prediction of the Tu peak is very local.

For the cases with inlet perturbations, Figure 5.12 (b) shows how such perturbations quickly break down into a turbulent wake, reaching a Tu peak shortly downstream of the boundary. The appropriate time-inclined transformation of the perturbations allows for a very accurate prediction of the Tu evolution. This result supports the idea that, for the relatively high Reynolds numbers characteristic of the flows of interest, the decay of the integral scale of the wakes between the trailing edge of the preceding row and the leading edge is small. And thus, the impact of the truncated terms in the time-inclined NS equations is also small.

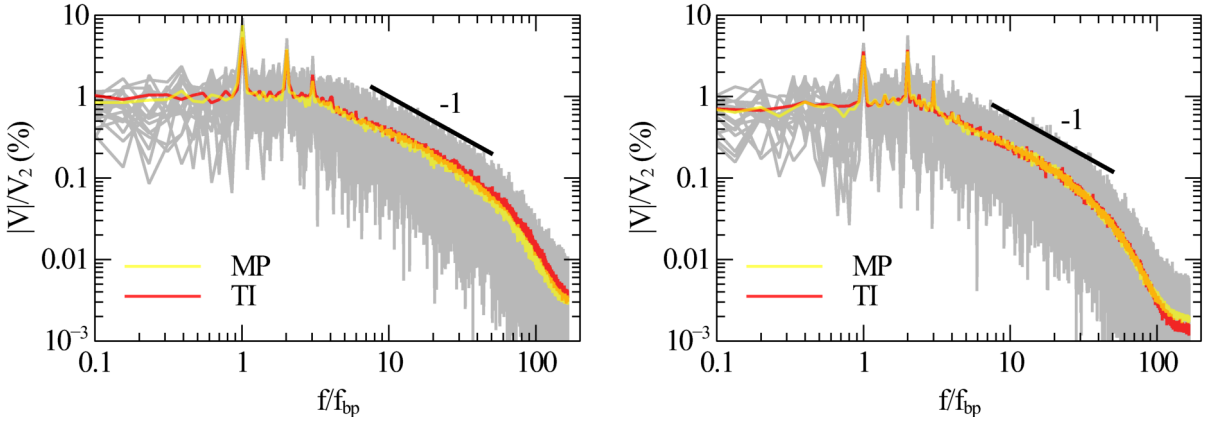

(a) Case with immersed bars

(b) Case with inlet perturbations

Figure 5.13: Comparison between the multi-passage and time-inclined velocity perturbations spectra for the immersed bar (a) and inlet perturbations (b) cases.

The turbulent velocity spectra upstream of the airfoil cascade is displayed in Figures 5.13 (a) and (b) for the immersed bars and inlet perturbations cases, respectively. The temporal evolution of the unsteady velocity is stored at several tracking points to obtain

the spectra. The points are located at an axial station $0.2c_x$ downstream of the bar cascade (or inlet boundary in the inlet perturbations cases) and uniformly distributed in the pitch-wise direction.

The spectra for all the tracking points are displayed in grey, while the red and yellow lines represent the frequency-wise averaged spectra of the TI and MP simulations, respectively. The intersection of such solutions is displayed in orange.

The results for the immersed bars cases in Fig. 5.13 (a) show how the TI method can reproduce the turbulence spectrum downstream of the bars. There are some noticeable differences between the MP and TI spectra in the unsteady velocity at the bar passing frequency, $f/f_{bp} = 1$. The second and third harmonics, as well as the turbulent spectra at higher frequencies, are well captured.
Very similar results have been obtained for the inlet perturbations cases. The spectra are almost coincident for all the resolved scales, as evidenced in orange in Figure 5.13 (b). These results support the claim that the TI methodology does not have a significant impact in the simulation of turbulent flows. Interestingly, since there is no subgrid-scale model in these simulations, the different dissipative properties of the standard and time-inclined schemes are evidenced for the smallest scales in the right-hand side tail of Fig. 5.13 (b), which are solely dissipated by numerical diffusion.

The SP spectra are not shown in Figs. 5.13 (a) and (b) for clarity when comparing the MP and TI approaches. However, they are very similar to the MP and TI results, very slightly favouring the TI method over the SP approach.

Time-Averaged Exit Angle Distribution.

Figure 5.14 displays the pitch-wise exit angle distributions referenced to the average exit angle in the MP simulation. Overall, good agreement is found among the three cases (MP, TI and SP) with the immersed bar modelling strategy in Fig. 5.14 (a). Some differences between the TI and the MP simulations in such cases can be appreciated, especially for $0 < y/P_s < 0.4$. However, the results are better for the TI than the SP simulation, even considering that the inlet angle prediction is better for the latter. Since the inlet total pressure of the TI and SP simulations are very close to the reference MP case, retaining the exact blade count is more important than imposing the inlet angle more accurately.

Figure 5.14 (b) shows the results for the inlet perturbations cases. The TI methodology accurately predicts the exit angle, resulting in almost coincident pitch-wise distributions. Meanwhile, the SP approximation has a slight offset to the MP distribution due to errors in the pitch-wise averaged exit angle.

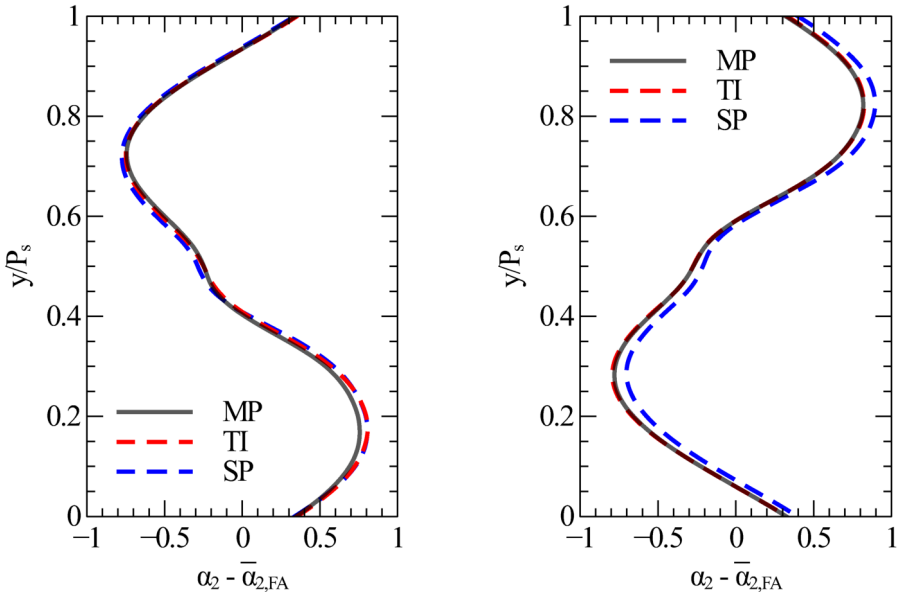

(a) Case with immersed bars (b) Case with inlet perturbations

Figure 5.14: Distribution of the flow angle at the exit station for the cases with immersed bars (a) and inlet perturbations (b) referenced to the averaged exit angle of the respective MP simulation

Cascade Wake Evolution.

Figure 5.15 displays pitch-wise distributions of total pressure at six axial positions from the trailing edge to one axial chord downstream. A good level of agreement with the reference MP solution is achieved for both TI and SP cases in both the immersed bar set of simulations in the top row of Figure 5.15, and the inlet perturbations set, at the bottom. In general, slight improvements are achieved with the TI method.

In Chapter 4, it was shown that, for a moderately low Reynolds number flow, the MP and the TI total pressure distributions diverged downstream of the trailing edge region of the flat plates. The matching was not recovered until some level of mixing had already taken place. Moreover, the axial evolution of the pitch-wise averaged total pressure for the TI simulation lagged the respective MP curve. Such effect, attributed to the aforementioned truncation of some viscous terms of the time-inclined NS equations, is not observed in Fig. 5.15, although a minor effect was detected in Fig. 5.10. The reason behind such results is attributed to the much quicker breakdown of the vortical structures shed at the trailing edges, for which the neglected terms in the TI method dominate over the retained viscous terms, and their transition to turbulent flow in 3D simulations. Therefore, the neglected terms dominate over the retained viscous terms in much smaller regions of the flow field in 3D cases, resulting in more accurate TI simulations. Nevertheless, the Reynolds number of the present cases is one order of magnitude higher, which reduces the impact of the viscous terms.

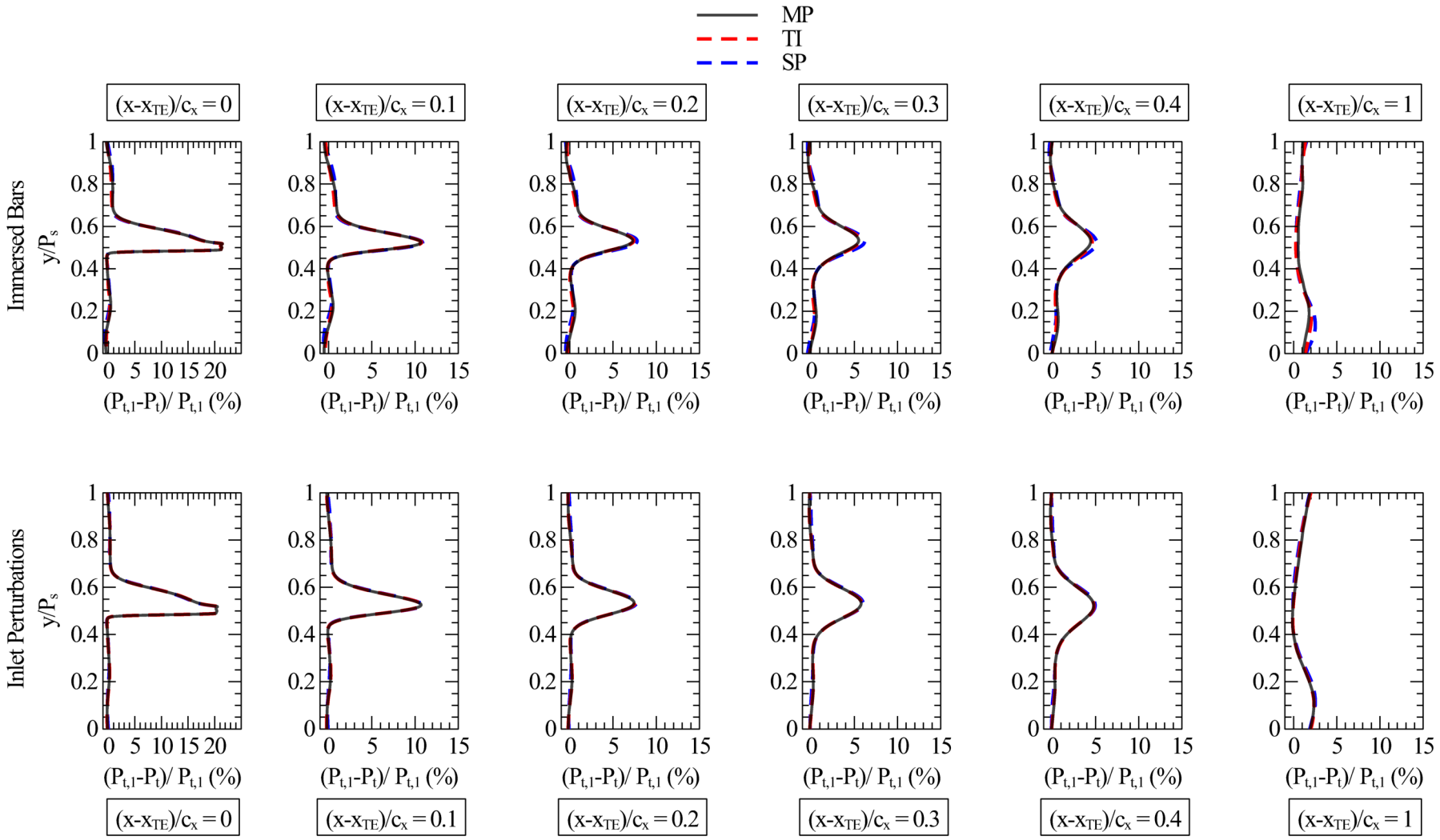

Figure 5.15: Axial evolution of the pitch-wise and time-averaged total pressure distributions for the cases with immersed bars (top) and inlet perturbations (bottom)

Fluctuation Profiles at the Measurement Station.

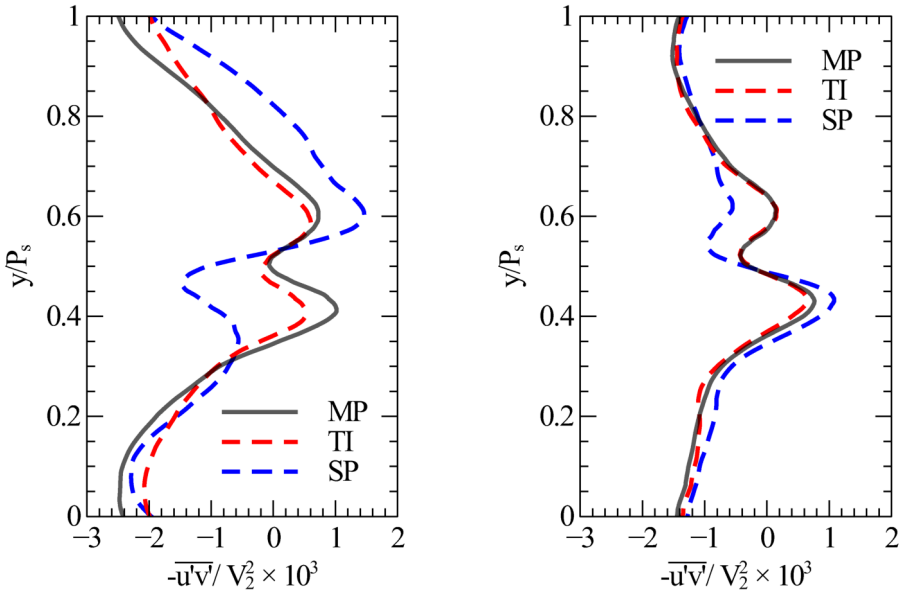

(a) Case with immersed bars (b) Case with inlet perturbations

Figure 5.16: Distribution of $-\overline{u'v'}$ at the exit station for the cases with immersed bars (a) and inlet perturbations (b)

To complement the analysis of the mixing process, Fig. 5.16 shows the pitch-wise distribution of the $-\overline{u'v'}$ component of the Reynolds stress tensor at the exit measurement station. The turbulent mixing in the wake is fairly well-predicted in TI. For the immersed bar case (see Fig. 5.16 (a)), the correct distribution is achieved by the TI methodology, and the deviation with respect to the reference MP solution is most noticeable far from the trailing edge wake region, which also applies to the SP case. However, the SP simulation cannot achieve the correct distribution in the wake region.

The $-\overline{u'v'}$ distributions at the exit station for the inlet perturbations cases are displayed in Fig. 5.16 (b). For such cases, a very high level of agreement is found between the MP and TI distributions. In contrast, the SP methodology features substantial differences with respect to the MP solution in the trailing edge wake region.

Axial Evolution of Cascade Losses.

The time and pitch-wise averaged cascade losses are defined as $\omega = \frac{P_{t1}^{mo} - P_{t2}^{mo}}{P_{t1}^{mo} - p_2}$, where P_t^{mo} is the mixed-out time-averaged total pressure, p is the pitch-wise and time-averaged exit static pressure, and the sub-scripts 1 and 2 indicate the inflow and exit measurement stations, respectively (see Fig. 5.3). Station 1 is located at a distance of $0.37c_x$ downstream of the perturbations and $0.3c_x$ upstream of the leading edges, while station 2 is located $0.4c_x$ downstream of the trailing edges.

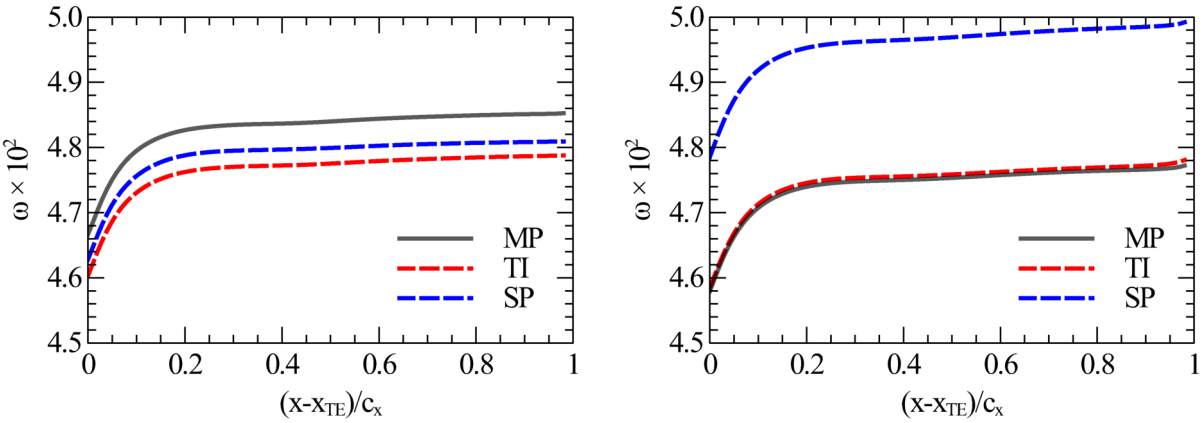

(a) Case with immersed bars (b) Case with inlet perturbations

Figure 5.17: Axial evolution of the cascade losses ω for the cases with immersed bars (a) and inlet perturbations (b).

The axial evolution of the cascade losses for the cases with immersed bars is displayed in Fig. 5.17 (a). The three simulations (MP, TI and SP) predict very similar losses. However, contrary to what has been shown for all the variables of interest so far, the SP approximation results in a slightly better prediction of ω.

It should be recalled at this point that, although the cascade inlet angle of the MP simulation was not matched by either the TI or SP methodologies, the inlet average total pressure was fairly well predicted by both (see Fig. 5.10). This is the result of a compensation of the wake velocity deficits: the SP case has more wakes than the MP case (8 per 4 airfoils instead of 7) but they are weaker (due to the lower bar speed used to match the reduced frequency). This compensation, in addition to the better inlet angle prediction of the SP case, may explain why the losses predicted by the SP methodology are slightly more accurate than the TI method. Nonetheless, owing to the capability of the TI method of retaining the exact blade count, the differences between the TI and SP losses are minimal even though the differences in inlet angle are noticeable.

It is worth noting at this point that the link between Reynolds stresses and mixed-out losses is very weak. Reynolds stress indicates the pace at which the wake is mixed but not of the final mixed-out state. The mixed-out losses depend not on the effective Reynolds number in a first approximation but on the flow field non-uniformity. Figure 5.16 (a) shows how the Reynolds stresses of the SP approach are significantly worse than those of the TI method. However, the mixed-out losses in Fig. 5.17 (a) are better predicted with the SP than the TI method.

For the inlet perturbations set of simulations in Fig. 5.17 (b), the SP methodology did not achieve such accurate results in neither cascade inlet angle nor total pressure upstream of

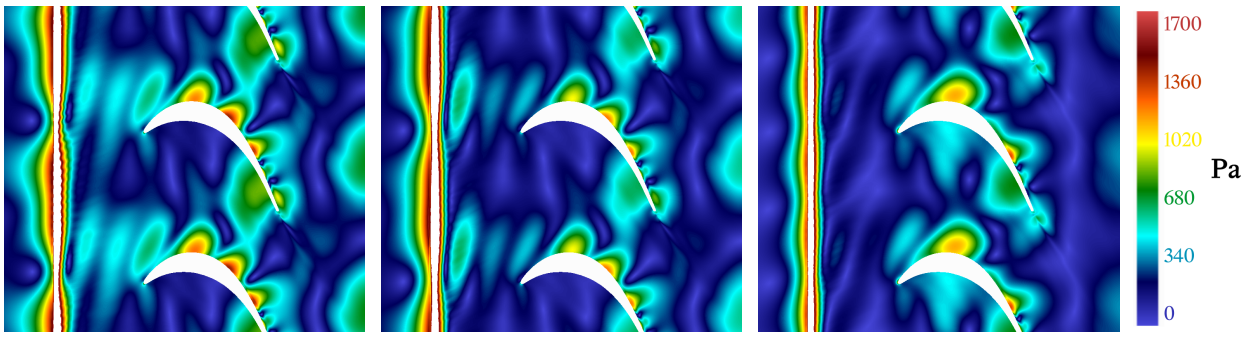

Figure 5.18: Modulus of the first harmonic of the unsteady pressure for the cases with the immersed bars cascade. Multi-passage (a), time-inclined (b) and approximate pitch ratio (c) simulations.

the airfoil cascade when compared to the TI results (see Fig. 5.10). Inlet conditions are automatically matched with the TI methodology in a realistic rotor/stator application case, with an appropriately resolved bar cascade in its separate row domain or imposing wake-like perturbations at the inlet section. For the latter, Fig. 5.17 (b) shows how the TI method matches the multi-passage simulation.

Unsteady Pressure Harmonics.

To close the present section and address a crucial aspect of the TI methodology, the modulus of the first harmonic of the unsteady pressure is shown in Fig. 5.18. One of the advantages of the TI methodology lies in the accurate prediction of the response to the synchronous excitations from the preceding row. The MP solution for the case with immersed bars is shown in Fig. 5.18 (a) and is very close to the TI simulation (b), whereas the SP field in (c) is clearly different. Nonetheless, the MP and TI simulations show discrepancies in the region downstream of the bar cascade, which may be related to the aforementioned differences in the inflow conditions (see Fig. 5.10). Such differences in the flow entering the cascade are smaller in the SP than in the TI case, but retaining the exact blade count is more important to obtain accurate predictions of the acoustic field.

It is worth noting at this point that the single-passage computational domains of the TI and SP simulations were copied to the neighbouring passages in order to generate Figures 5.18 (b) and (c). For the TI approach, the Fourier decomposition of the solution leads to real and imaginary parts that are spatially periodic in the inclined plane $(\mathbf{x}', \tau)$. However, the modulus of each temporal harmonic in the TI solution can be directly compared to the modulus of the same physical MP harmonic, as shown in Fig. 5.18.

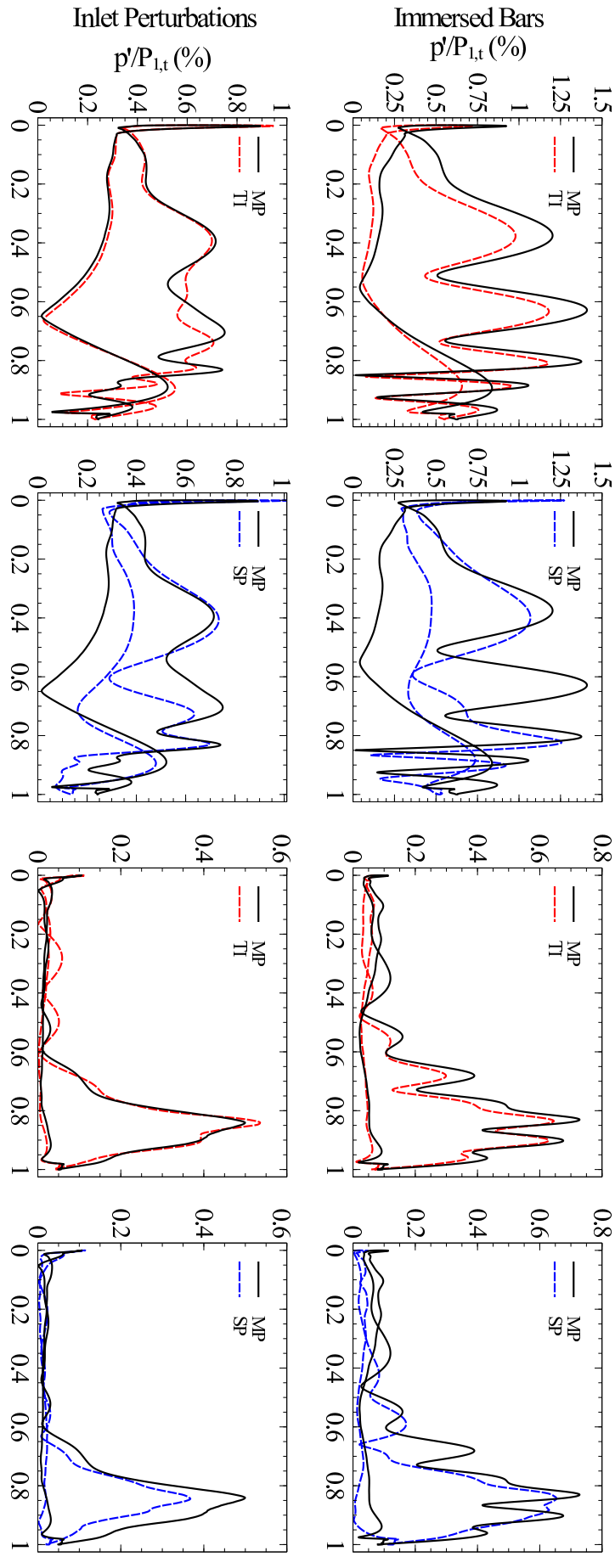

Figure 5.19: First, (a) and (b), and second, (c) and (d), harmonic of the unsteady pressure along the blade surface for the case with immersed bars (top) and with inlet perturbations (bottom).

The modulus of the first and second harmonics of the unsteady pressure on the blade surface are depicted in Fig. 5.19. The curves in the top of Fig. 5.19 correspond to the case with immersed bars. Since, for such case, the TI and SP simulations do not match the angle entering the cascade in the reference case, some differences are found in the leading edge region in the top part of Figs. 5.19 (a) through (d), which show the first ((a) and (b)) and second ((c) and (d)) harmonics of the unsteady pressure. If the offset in such region is disregarded, the shape of the TI curves in Figs. 5.19 (a) and (c) show good agreement with the MP case.

The negative impact of the upstream perturbation modelling is evident for the cases with inlet perturbations shown in the bottom part of Fig. 5.19. In such a set of simulations, even if the reference flow conditions entering the cascade are matched, the high reflectiveness of the inlet boundary conditions leads to the presence of non-physical reflections and oscillations in the flow field. Such reflections can impede fully matching the first harmonic of the MP solution (see bottom part of Fig. 5.19 (a)), especially since some acoustic waves that are cut-on are differently treated and reflected by the TI and MP boundary conditions. Nevertheless, the level of agreement between the MP and TI cases for the first harmonic in the bottom Fig. 5.19 (a) is excellent for most of the suction side and for the whole pressure side.

Remarkably, the shape and level of the first harmonic of the pressure on the blade due to the bars and the prescribed inlet perturbations are different. The differences in the shape, even in the leading edge region, can only be because the prescribed inlet injects a vortical perturbation and a pressure perturbation. Controlling the prescribed perturbations at the inlet leads to a high-level matching in the leading-edge region. The lack of matching of the first harmonic around the bubble region can be attributed to the amplitude of the perturbations in the prescribed inlet case being lower than with bars, and the synchronization of the bubble dynamics with the inlet is weaker than with the bars. However, the agreement between the MP and TI cases at the bubble region for the second harmonic is fairly good in both sets of simulations (see Fig. 5.19 (c)).

It is worth noting that, since the SP cases approximate the pitch ratio, the distributions of unsteady pressure cannot match the reference case (see Figs. 5.19 (b) and (d)). Such limitation showcases how the holistic approach of performing very accurate scale-resolving simulations is hindered if the exact blade count is not retained, which is relevant for the application of SRSs to aeroacoustic problems such as fan noise prediction. It is also relevant to recall that errors in the unsteady pressure on the airfoils can be translated into errors in the far-field acoustic field using Green's functions.

Finally, even when the first harmonic of the unsteady pressure is not fully matched (see Figs. 5.19 (a) and (b)), the TI method can produce accurate predictions of the cascade

losses (see Fig. 5.17), especially for the inlet perturbation case. The same can only be said for the SP methodology with immersed bars, which features a slightly better prediction of the losses than the TI method.

Boundary Layer Analysis.

To conclude the results section, an analysis of the velocity profiles at several axial locations of the Boundary Layer (BL) has been carried out.

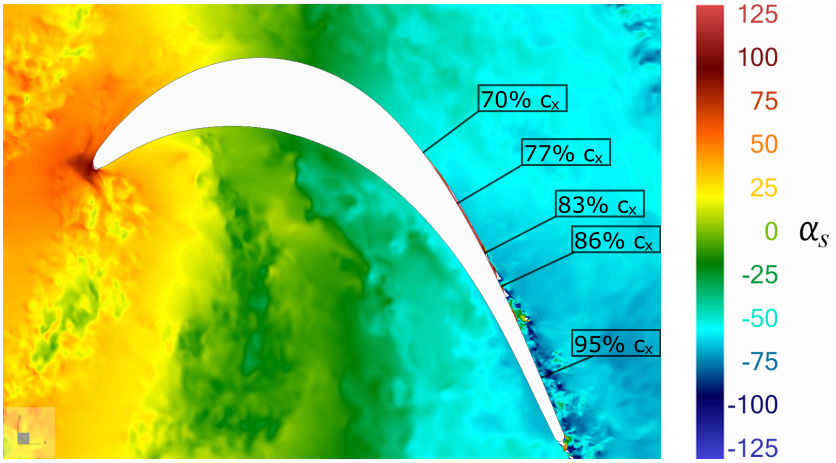

Figure 5.20: Snapshot of the swirl angle, α_s, for the time-inclined case with immersed bars, and location of the measuring stations in the boundary layer.

Figure 5.20 displays the location of such BL measuring stations over a snapshot of the swirl angle, $\alpha_s = atan(V_y/V_x)$, for the TI immersed bars simulation. The station at $x - x_{LE} = 70\%\, c_x$ is located before the separation and the one at $95\%\, c_x$ is downstream of the reattachment point, as can also be observed in Figures 5.11 (a) and (b). It is interesting to note that according to Figure 5.11 (a), for the cases with immersed bars, not all of the remaining stations belong to the separated flow region. For the MP simulation, Figure 5.11 (a) shows how the BL station at $86\%\, c_x$ lies after the reattachment point, whereas the TI and SP simulations predict a longer bubble in the time-averaged solution. This might explain the differences found in the time-averaged velocity profiles at such BL station in Figure 5.21.

The time-averaged velocity profiles are displayed in the top part of Figures 5.21 and 5.22 for the immersed bar and inlet perturbations cases, respectively. In the bottom part of Figures 5.21 and 5.22, the root-mean-square of the turbulent velocity, $u_{rms} = \sqrt{2/3k}$, where k is the turbulent kinetic energy, are shown. Each column corresponds to a BL station.

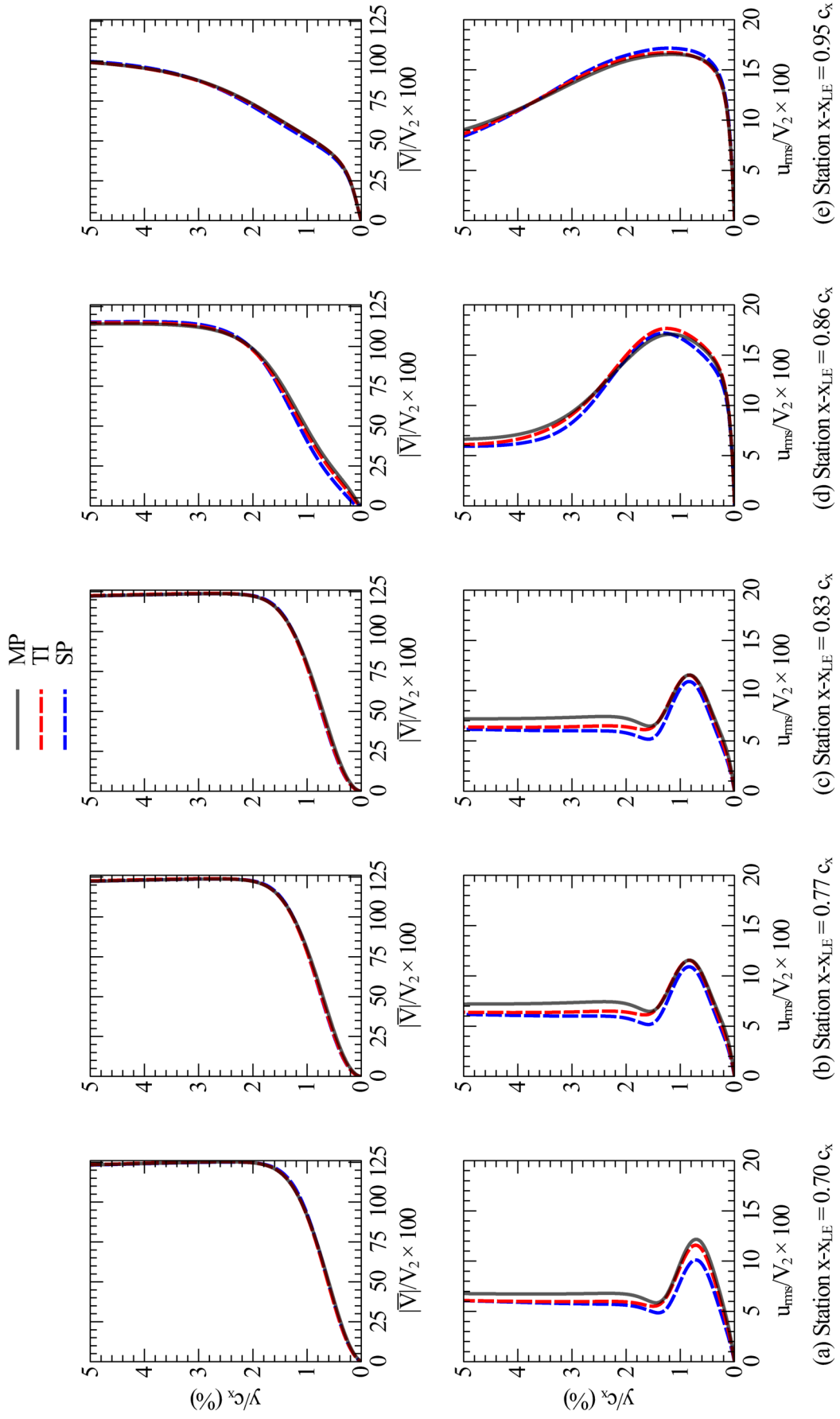

Figure 5.21: Time-averaged velocity modulus profiles (top) and RMS of the velocity fluctuations profiles (bottom) at different stations of the boundary layer for the case with immersed bars.

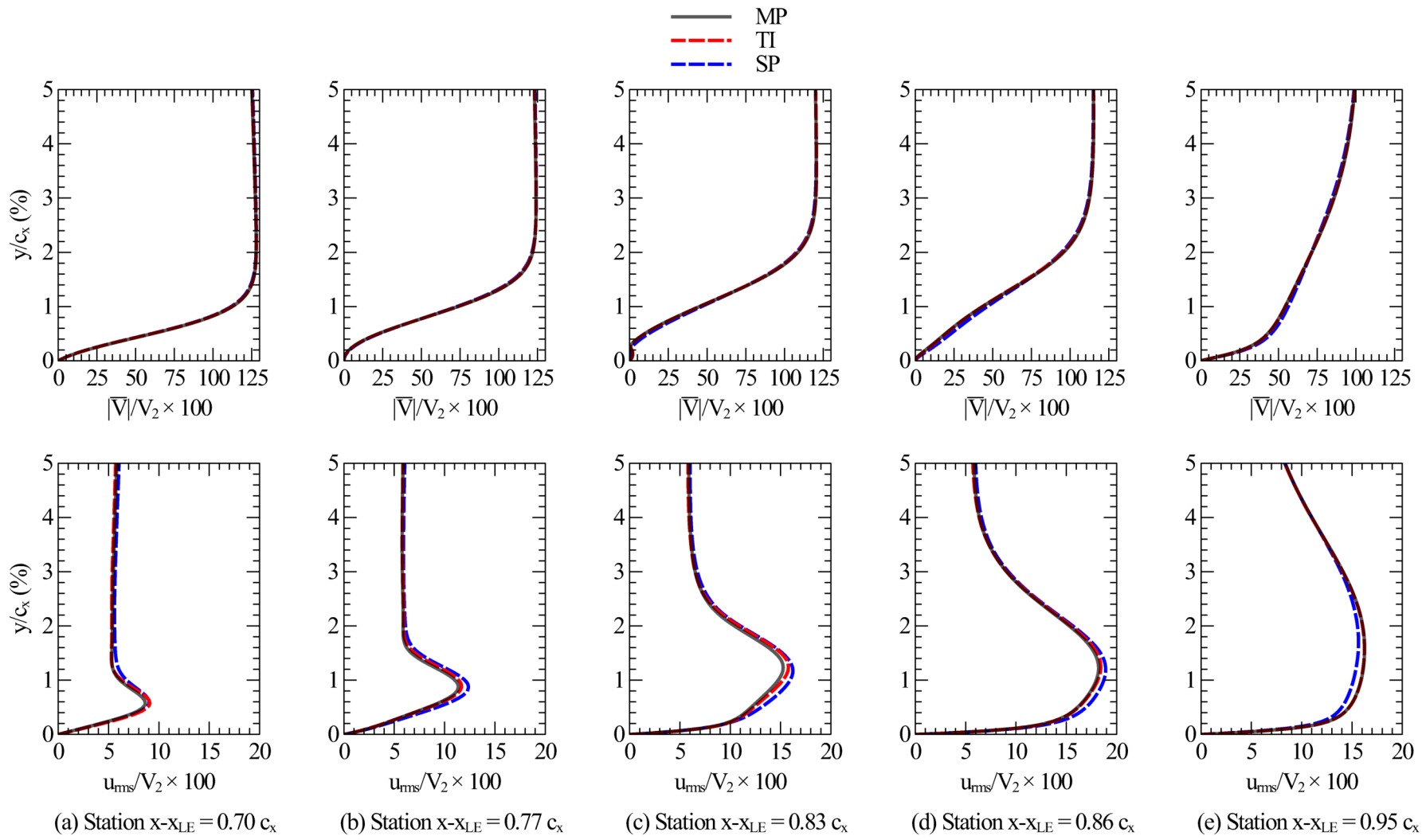

Figure 5.22: Time-averaged velocity modulus profiles (top) and RMS of the velocity fluctuations profiles (bottom) at different stations of the boundary layer for the case with inlet perturbations.

For the time-averaged velocity profiles, very good agreement is found at all BL stations for either the immersed bar cases in Fig. 5.21 and for the inlet perturbations cases in Fig. 5.22. As previously noted, there are some noticeable differences between the MP, TI and SP profiles for the station at $x - x_{LE} = 86\%\, c_x$. The TI simulation is more accurate in the prediction of the size of the bubble and especially in the location of the reattachment point, which is close to such BL station. This may also explain why the TI profile is closer to the MP solution than the SP case for both immersed bars and inlet perturbations cases.

For the velocity perturbations profiles, the TI method systematically outperforms the SP approach, since the latter cannot accurately predict the peak of the turbulent velocity profiles in the bottom parts of Figs. 5.21 and 5.22. However, for the immersed bars perturbation model, the aforementioned errors in the flow field entering the cascade lead to the mismatch of the TI and SP profiles in the exterior part of the BL in the passage.

Thus, the results for the inlet perturbations cases, which match the conditions entering the cascade, show how the TI method has accurately predicted the BL profiles in all the measuring stations (see the bottom part of Fig. 5.22). There are some very slight differences in the peak of the turbulent velocity achieved in the bubble region (station (c) at $x - x_{LE} = 83\%\, c_x$), but the overall agreement to the MP solution is excellent.

Finally, Figure 5.23 shows the profiles of the modulus of the 1^{st} harmonic of the unsteady velocity parallel to the wall, u'_1. The top and bottom parts of Figure 5.23 correspond to the immersed bars and inlet perturbations cases, respectively. Three axial locations on the airfoil suction side, displayed in each column of Figure 5.23, have been selected: before the separation, inside the bubble and downstream of the reattachment point.

For the immersed bar case, the comparisons between the MP and TI profiles of u'_1 (top part of Figure 5.23) are very similar to those between the unsteady velocity profiles (see the bottom part of Fig. 5.21). It can be noted that the matching of the velocity peak is slightly worse.

It is interesting to see how, in spite of the results obtained for the first harmonic of the unsteady pressure in the inlet perturbations cases (see bottom part of Figure 5.19 (a)), the modulus of the velocity of the MP case can be matched by the TI approach in the bubble region (bottom prat of Fig. 5.23).

This result supports the hypothesis that the source of the errors in the unsteady pressure distributions of the TI inlet perturbations simulations are due to the different treatment of the non-physical reflections of acoustic waves that are cut-on, since the unsteady turbulent boundary layer has been accurately predicted.

Therefore, the errors in the unsteady pressure distributions, which were the only significant differences between the MP and TI inlet perturbations simulations, would not be present

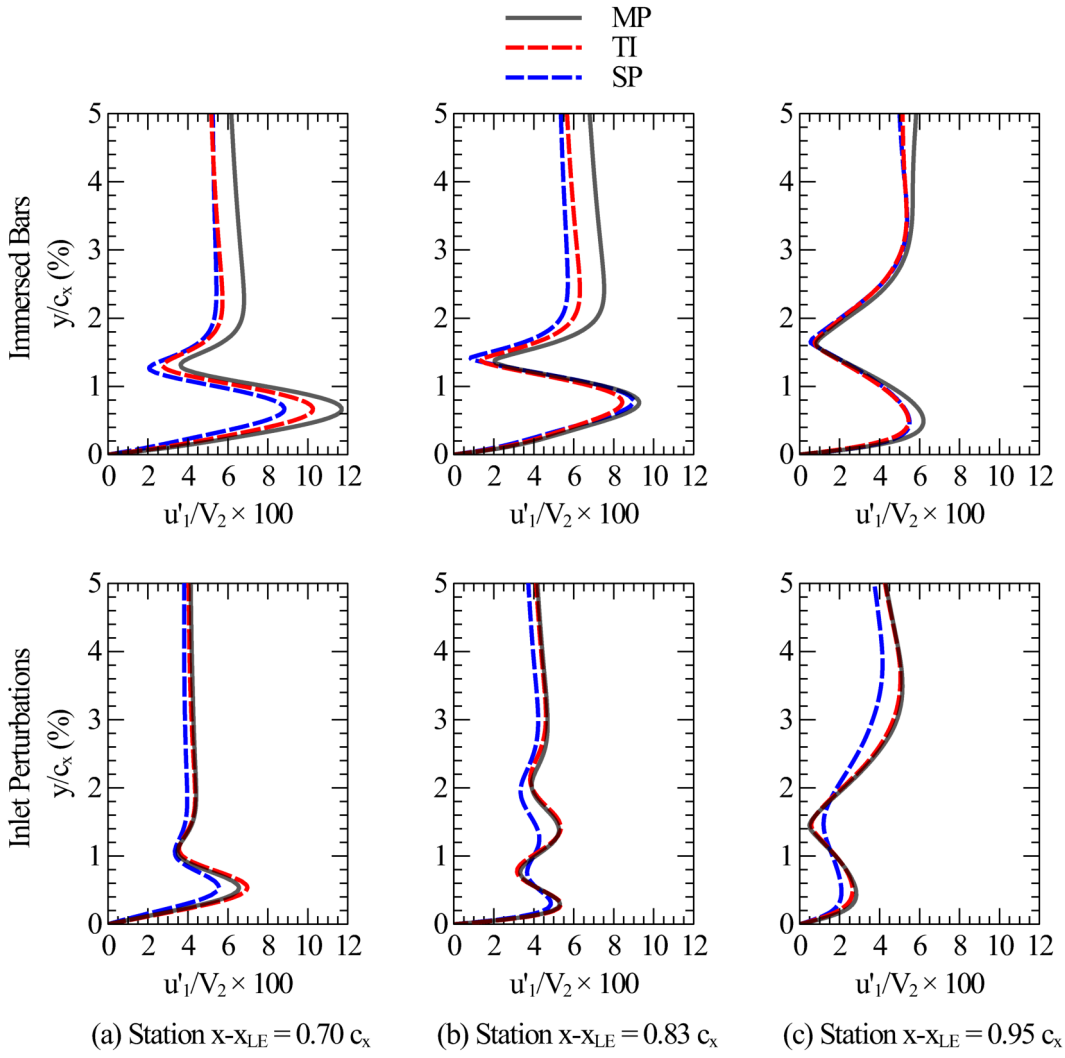

Figure 5.23: Profiles of the modulus of the 1^{st} harmonic of the velocity parallel to the wall at different stations of the boundary layer for the case with immersed bars (top) and with inlet perturbations (bottom).

in a rotor/stator time-inclined simulation. The inlet section in the rotor row could impose steady "non-reflective" BC, and the sliding plane would accurately transform the spatially periodic rotor flow to a spatially periodic flow in the stator domain. Consequently, all variables of interest shown in the present chapter could be accurately predicted by the TI method.

5.4 Summary and Conclusions

Several scale-resolving simulations of the T106C LPT linear cascade with incoming periodic perturbations have been conducted to evaluate the suitability of the time-inclined method for retaining the exact blade count in high-fidelity simulations. The upstream perturbations have been injected following two different modelling strategies: an immersed boundary approach for a cascade of under-resolved moving bars and the imposition of wake-like boundary conditions at the inlet section of the computational domain. Three-way comparisons have been produced between the directly periodic (multi-passage) domain, the time-inclined single-passage domain and the single-passage modified pitch ratio problem.

The results indicate that the time-inclined method is suitable for scale-resolving simulations of turbulent flows to retain the exact blade count. The main problems encountered in the present work are due to the modelling of the perturbations and would not be present in a rotor/stator simulation.

The immersed bar case is the most penalised approach since the bars, included as wake generators, are typically under-resolved. The numerical discretisations of the standard and time-inclined NS equations feature different numerical properties, and their effects are more clearly evidenced in the treatment of under-resolved wave-lengths. Furthermore, the rotor and stator domains would be differently transformed in the time-inclined methodology. Since each domain should be differently transformed, to include the immersed bars –which should be part of the rotor domain– into the transformed stator domain may also be a source of errors.

The flaws in the mixing process that had been identified in the time-inclined two-dimensional cases of the previous chapter are not as impactful in three-dimensional turbomachinery flow. This is due to the accelerated breakdown and transition of the vortical structures, which reduces the size of the regions where the neglected terms in the time-inclined transformation of the NS equations are relevant.

In a rotor/stator simulation, the time-inclined method accurately and automatically captures the flow conditions entering the cascades. This has been exemplified with the inlet

perturbations cases, which show that when such conditions are matched to the multi-passage case, the time-inclined method accurately predicts the aerodynamic performance, outperforming the approximate pitch ratio methodology.

Due to the findings in this detailed study, it is expected that the TI method will outperform the single-passage approximated pitch ratio methodology in a rotor/stator simulation. Moreover, the errors of the TI method scale with the magnitude of the transformation parameter, which in the present work was chosen to be very high. In more realistic applications, unconstrained by the necessity of economically simulating the directly periodic case as a reference solution, the transformation parameter is likely to be much smaller. Moreover, the computational cost reduction of the TI method may allow for the simulation of both the rotor and stator domains, improving the accuracy of the virtual experiments.

6 Turbulent Flow Test Cases

Contents

6.1 Taylor-Green Vortex **155**

6.2 Turbulent Channel Flow **159**

6.3 Closing Remarks **169**

The present Chapter is an extension of the verification process of the time-inclined method for the simulation of transitional and turbulent flows. Chapter 5 addressed such a task by comparing the physical and time-inclined LPT simulations in terms of the magnitude and azimuthal distributions of the turbulent perturbations, as well as the spectra downstream of turbulent wakes. The results showed very high levels of agreement between the physical and time-inclined flow fields in regions of low and high turbulence intensity. Furthermore, the analysis of the turbulent boundary layers that formed on the suction side of LPT airfoils yielded excellent results, showing how the time-inclined method can accurately reproduce both laminar (see Chapter 4) and turbulent boundary layers.

Nevertheless, carrying out simulations of canonical transitional and turbulent problems can shed some light into potential pitfalls of the time-inclined methodology. Low-pressure turbine flows feature complex physical phenomena and their simulation entails dealing with many potential sources of error. Thus, due to the nature of the numerical experiments, it is essential to focus on problems consisting of simple geometries and setups to introduce a minimal level of uncertainty. In the present Chapter, the numerical solutions of the Taylor-Green Vortex (TGV) problem and of the turbulent channel flow problem are reported, which have also been used to validate the baseline solver implementation [93–95].

6.1 Taylor-Green Vortex

The Taylor-Green vortex [139] is a canonical problem which features a transitional flow to anisotropic turbulence, followed by its decay. The case consists of a triple periodic cube $(x, y, z) \in [-\pi L, \pi L]$, in which an analytical vortical structure with zero mean velocity is imposed as the initial condition.

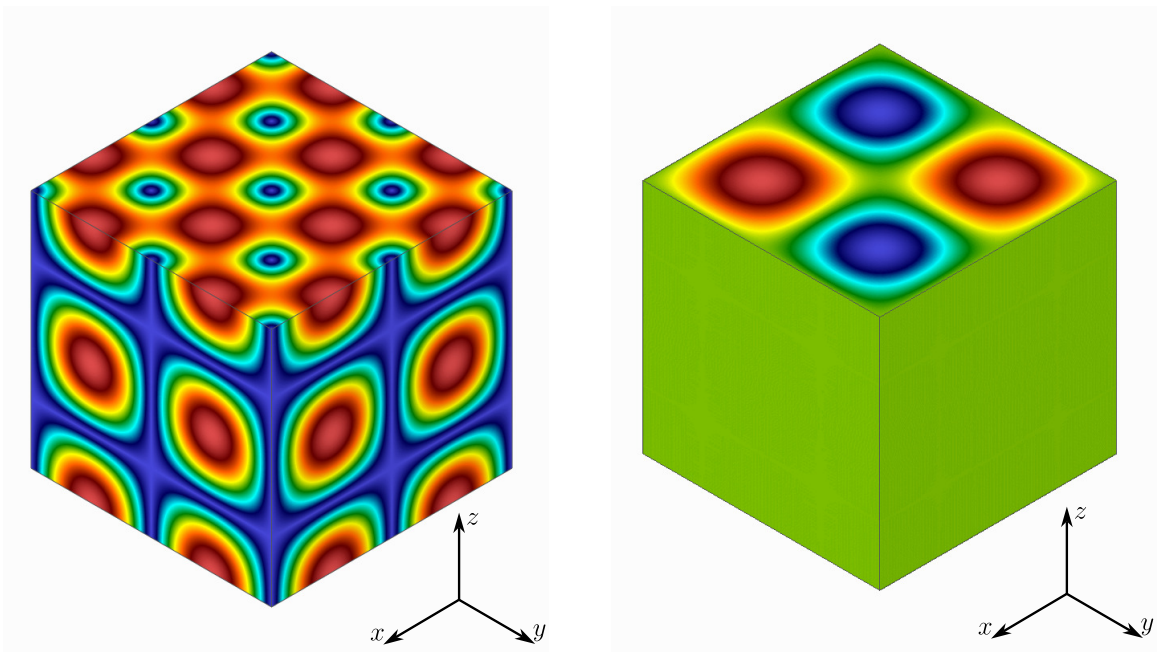

(a) Mach number (b) Vorticity ω_z

Figure 6.1: Initial condition of the Taylor-Green Vortex problem: Mach number field (a) and z-component of the vorticity (b).

The TGV problem is free of the numerical errors often introduced by inlet, outlet and wall boundary conditions, which makes it one of the simplest problems to study the generation of small scales and the decay of turbulence. Thus, it can be used to validate the correct implementation of the diffusive terms in numerical schemes for SRSs.

The initial condition is of the form:

$$\begin{aligned}
\rho &= \tfrac{p}{RT_0} \\
u &= V_0 \sin\left(\tfrac{x}{L}\right) \cos\left(\tfrac{y}{L}\right) \cos\left(\tfrac{z}{L}\right) \\
v &= -V_0 \cos\left(\tfrac{x}{L}\right) \sin\left(\tfrac{y}{L}\right) \cos\left(\tfrac{z}{L}\right) \\
w &= 0 \\
p &= p_0 + \tfrac{\rho_0 V_0^2}{16} \left(\cos\left(\tfrac{2x}{L}\right) + \cos\left(\tfrac{2y}{L}\right)\right) \left(\cos\left(\tfrac{2z}{L}\right) + 2\right) \\
T &= T_0
\end{aligned} \tag{6.1}$$

and represents a group of vortices that, for sufficiently large Reynolds numbers, $Re = \frac{\rho_0 V_0 L}{\mu}$, become unstable and break down into smaller eddies. As smaller scales appear, the viscosity becomes increasingly relevant, dissipating them.

In particular, the Reynolds number for the present simulations has been set to $Re = 1600$. In order not to include compressibility effects, the Mach number has been set to $M = {}^{V_0}/_{a_0} = 0.1$, where the local speed of sound is defined as $a_0 = \sqrt{\gamma R T_0}$. In addition, the bulk viscosity of the fluid is assumed to be zero, $\mu_v = 0$. The computational domain has

been uniformly divided into 6^{th} order elements, 80 along each dimension, for a total of $64,481,201$ physical nodes. Figures 6.1 (a) and (b) show the initial fields of the Mach number and the z-component of the vorticity, respectively, and aid illustrating the form of the vortical structures prior to their transition to turbulence.

Throughout the simulation of the TGV problem, the evolution of the dissipation rate of the kinetic energy is monitored for the baseline and time-inclined solvers. The correct implementation of the diffusive terms for the baseline solver was verified by comparing the results of the TGV problem to DNS and LES from other CFD codes [94].

For the TI simulation, there is no forcing term that can define a time-inclination parameter. Nevertheless, since the faces of the computational domain are periodic, the problem can be arbitrarily transformed as if there was a travelling wave as part of the spectra that would not fit in the computational domain along a certain direction.

Chapter 2 showed that the errors of the truncated inclined Navier-Stokes equations are proportional to the magnitude of the slope of the inclined planes. Since the motivation behind this numerical experiment is to reveal potential pitfalls of the time-inclined method, a significant inclination parameter of $\lambda a_0 \approx 0.397$ has been chosen.

The baseline and time-inclined simulations were run for 40 characteristic times $t_c = {}^{L}/_{V_0}$, tracking the evolution of the total kinetic energy, E_k, defined as:

$$E_k = \frac{1}{\Omega \rho_0} \int_{\Omega} \rho \frac{\mathbf{v} \cdot \mathbf{v}}{2} d\Omega \tag{6.2}$$

where Ω is the volume of the computational domain.

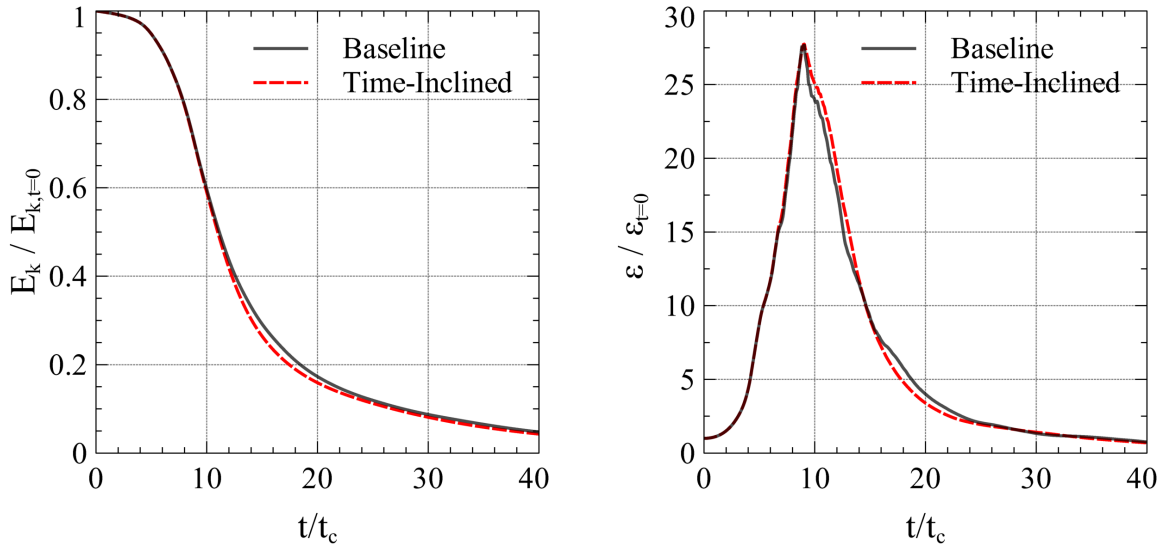

(a) Kinetic Energy (b) Enstrophy

Figure 6.2: Evolution of the total kinetic energy (a) and enstrophy (b) for the baseline and time-inclined simulations of the TGV.

Figure 6.2 (a) shows the evolution of the total kinetic energy obtained with the baseline numerical scheme compared to that obtained with the time-inclined method. For the first 9 characteristic times, both solutions coincide. At such point, the curves diverge and do not converge again until the 25^{th} period. Figure 6.2 (b) displays the enstrophy, ε, which approximates the kinetic energy dissipation rate, since the bulk viscosity of the gas was assumed to be zero and the Mach number of the flow is low enough for the simulation to be in the incompressible regime:

$$-\frac{dE_k}{dt} = 2\frac{\mu}{\rho_0}\varepsilon + \frac{\mu_v}{\rho_0}\frac{1}{\Omega}\int_\Omega (\nabla\cdot\mathbf{v})^2\, d\Omega - \frac{1}{\rho_0\Omega}\int_\Omega p\,(\nabla\cdot\mathbf{v})\, d\Omega \approx 2\frac{\mu}{\rho_0}\varepsilon \tag{6.3}$$

where the enstrophy is

$$\varepsilon = \frac{1}{\Omega}\int_\Omega \rho\frac{\omega\cdot\omega}{2} d\Omega \tag{6.4}$$

and ω is the vorticity.

Thus, the increase in the dissipation rate from the start of the simulation up to $t{\approx}9t_c$ in Figure 6.2 (b) is associated with the process by which the original large vortical structures break down into smaller ones. Taking the baseline solution as a reference, it is clear that such a process is accurately predicted by the time-inclined method. Moreover, the peak in the dissipation rate is well-captured.

However, after the peak, the absence of large dominant structures and the presence of very small scales might explain the divergence between the baseline and time-inclined solutions in Figures 6.2 (a) and (b). The differences in the dissipative properties of both numerical schemes are especially evidenced in such a context of very small vortical structures. As more and more kinetic energy is dissipated and the flow-field becomes uniform, the differences between the schemes become less relevant, and the enstrophy curves of the baseline and time-inclined solvers converge again, which also explains the offset between the kinetic energy curves in Figure 6.2 (a) for $t > 25t_c$.

Figure 6.3 shows the state of the vorticity modulus field in the baseline (left) and time-inclined (right) simulations after 40 characteristic times. At first sight, the spatially periodic structures that were present at the start of the simulation, dividing the computational domain in 8 periodic units, are still preserved after 40 characteristic times in the simulation with the baseline scheme. However, that is not the case for the time-inclined simulation.

As the vortical structures break down, the viscous terms become increasingly relevant. Then, due to the differences between the diffusive properties of the baseline and inclined schemes, it is possible that the asymmetry created by the diffusive terms after transforming the NS equations along a certain *inclined* direction (y in this particular case) has caused the breakdown of the existing spatial periodicity along the x and y directions.

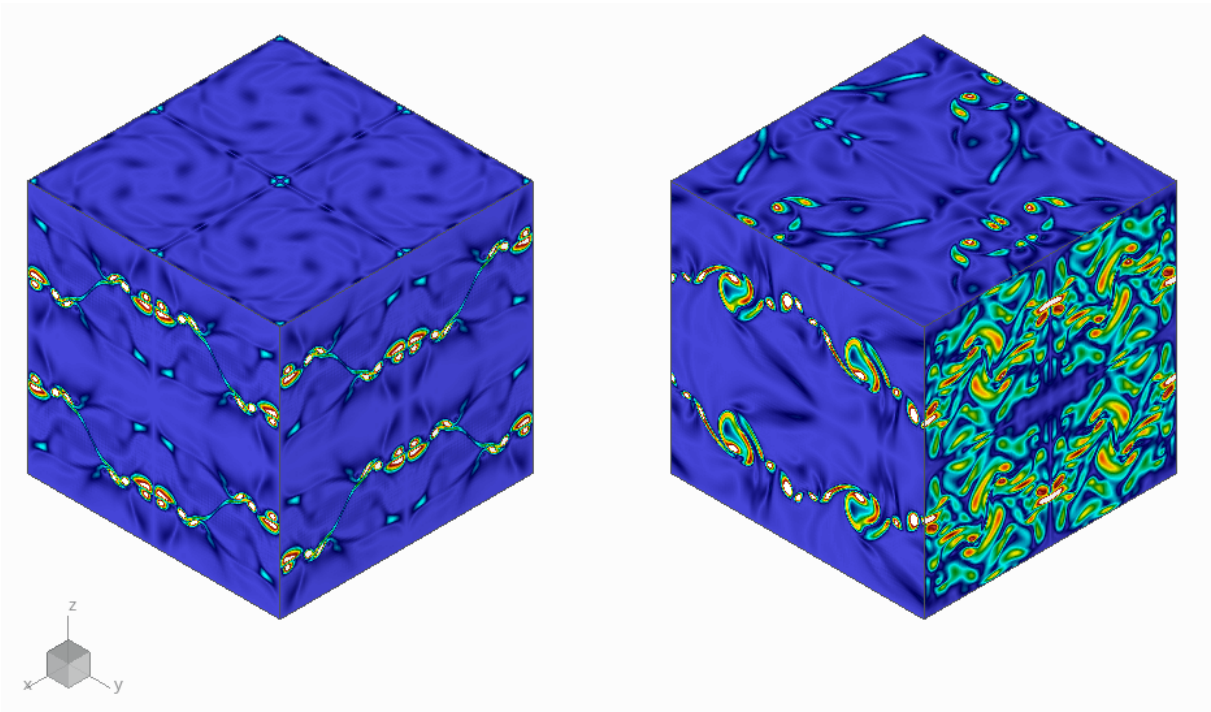

Figure 6.3: Vorticity modulus field in the baseline (left) and time-inclined (right) TGV simulations after 40 characteristic times.

The TGV problem, though in principle far away from that of a turbomachinery stage, has some resemblance with some transitional unbounded flows. The time-inclined method reproduces the enstrophy growth rate of the TGV problem until the peak. This initial phase is controlled by inviscid non-linear mechanisms that the TI method replicates accurately. After the peak, the decay rate of the TI is different from that of the baseline flow since the viscous terms are not adequately transformed. In the latest stages of the process both methods match again. This result is totally equivalent to that described for the mixing process of a wake exchanging the time by the downstream coordinate.

Nevertheless, further developments on the viscous formulation of the time-inclined method may lead to improvements in the predictive capabilities of the method for such kind of transitional processes.

6.2 Turbulent Channel Flow

The fully developed turbulent incompressible flow through a channel has been chosen to evaluate the suitability of the TI method to simulate turbulent boundary layers. Several authors have used such a canonical problem to investigate wall-bounded turbulence [140–143] as well as to validate CFD codes for scale-resolving simulations [94, 95, 144, 145].

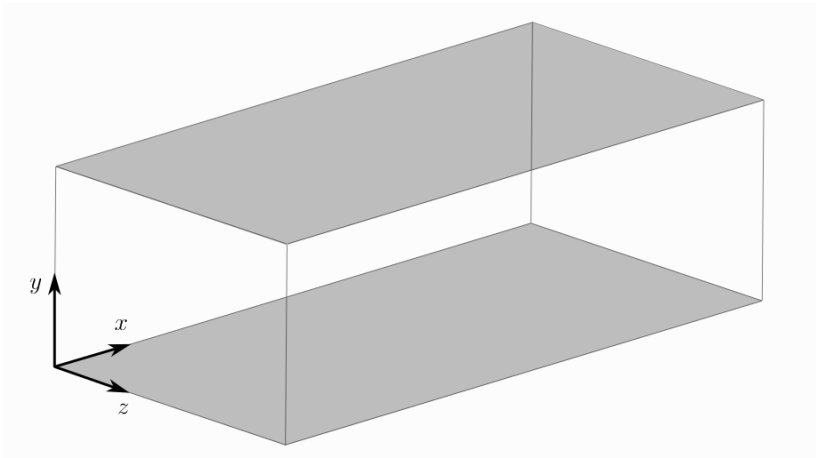

Figure 6.4: Schematic of the turbulent channel computational domain.

The computational domain, depicted in Figure 6.4, consists of a box of dimensions $[0, 2\pi\delta] \times [0, 2\delta] \times [0, \pi\delta]$. The x and z directions are considered to be the stream-wise and span-wise directions, and spatial periodicity conditions are imposed along them. Meanwhile, two parallel planes at $y = 0$ and $y = 2\delta$ represent the lower and upper walls of the channel. Similarly to the TGV setup, there are no inlets or outlets in the problem, which avoids introducing uncertainties due to the choice and implementation of the boundary conditions. Thus, to establish a flow in the channel, a pressure gradient term has been introduced in the stream-wise direction.

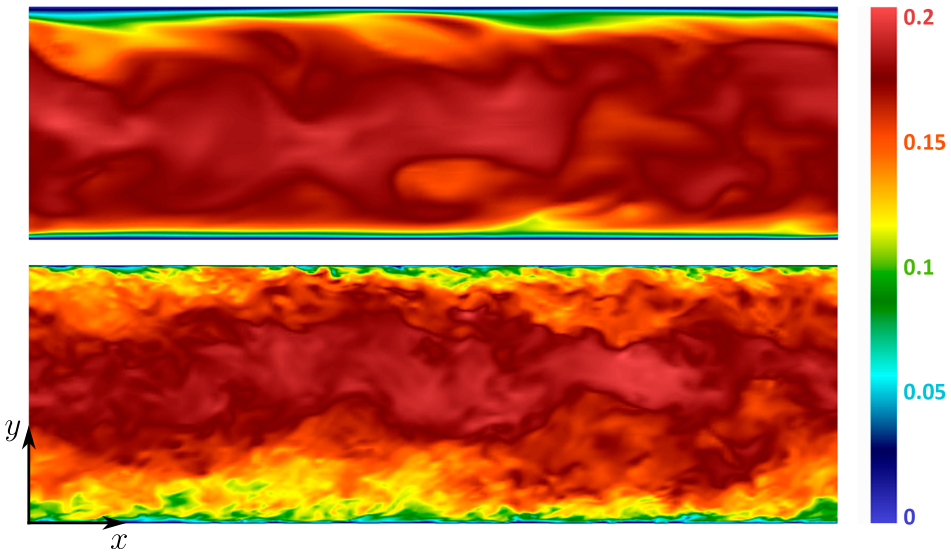

Figure 6.5: Snapshot of the Mach number field for a turbulent channel cases with $Re_\tau = 180$ (top) and $Re_\tau = 870$ (bottom).

After several flow-throughs, the flow in the channel becomes fully turbulent. Then, a temporal and span-wise averaging procedure is carried out until statistical convergence

is reached. A bulk Mach number of 0.2 has been imposed to speed-up the convergence and thus reduce the computational cost of the simulations, while still operating in the incompressible regime.

Figure 6.5 displays snapshots of the Mach number field for the two different problem setups chosen to study the suitability of the TI method. The two cases differ in their respective friction Reynolds numbers, $Re_\tau = 180$ and $Re_\tau = 870$, which is defined as

$$Re_\tau = \frac{\rho u_\tau \delta}{\mu} \tag{6.5}$$

where $u_\tau = \sqrt{\frac{\tau_w}{\rho}}$ is the friction velocity, and $\tau_w = \mu \frac{\partial u}{\partial y}$ the shear stress at the wall. Due to grid spacing restrictions, to maintain a low computational cost of the simulations, low and moderately low values of Re_τ have been chosen. For such friction Reynolds numbers, the aforementioned box dimensions suffice to reproduce one-point statistics of larger boxes [142].

The grid spacing for the wall-normal direction follows the distribution proposed by Ghiasi et al. [145]:

$$\frac{y_n}{L_y} = \frac{1}{2}\left(1 - \frac{tanh\left[C\left(\frac{1}{2} - \frac{n}{N_y}\right)\right]}{tanh\left(\frac{C}{2}\right)}\right), \quad 0 < n < N_y \tag{6.6}$$

where y_n is the y-coordinate of the interface of the n element, N_y the number of elements in the y direction, and C is a parameter to control the clustering of the elements near the wall. In the present numerical experiments, a value of $C = 5.4$ has been chosen following the validation process of the baseline solver in [95]. Additional mesh details can be found in Table 6.1.

Re_τ	N_x	N_y	N_z	y_w^+
180	24	12	12	0.15
870	48	48	48	0.23

Table 6.1: Mesh details for the turbulent channel flow simulations.

6.2.1 Case A: $Re_\tau = 180$

After achieving statistical convergence, the velocity distributions in the y-direction of the channel are time- and span-wise averaged. Figure 6.6 displays the average velocity profile in wall units for the $Re_\tau = 180$ case. The profile corresponding to the simulation with the baseline solver is shown in a solid grey line, whereas symbols are used to plot DNS data from [140].

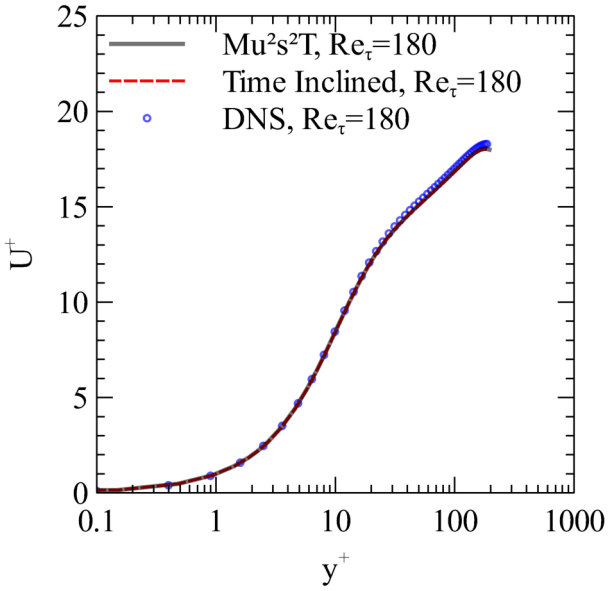

Figure 6.6: Time- and span-wise averaged velocity profile in wall units for the $Re_\tau = 180$ case. Comparison between the baseline and wall-normal time-inclined simulations and DNS in [140].

Similarly to the TGV, time-inclined computational planes are defined along one direction in spite of the lack of a travelling perturbation that needs to fit in the computational domain. However, neither the turbulent channel problem is symmetric, nor the grid spacing is uniform. Thus, differences might appear depending on the direction used to tilt the computational planes. Considering the walls of the channel to represent the blades in a turbomachine, the first approach is to use the wall-normal direction to incline the computational planes. Due to the scaling of the magnitude of the truncated terms in the transformed equations, and to highlight potential errors due to such approximation, a large inclination parameter of $\lambda a_0 \approx 0.397$ has been chosen.

Thus, a red dashed line is used in Figure 6.6 to plot the average velocity profile for a (wall-normal) time-inclined simulation, which matches the baseline solution and is very close to the DNS data.Such high levels of agreement are also found for the profiles of the root-mean-squared velocity fluctuations obtained from the baseline and time-inclined simulations, as depicted in Figures 6.7 (a) through (d). In terms of their comparison to the DNS data in [140], the accuracy achieved is also deemed excellent, while bearing in mind that the resolution in the virtual experiments does not correspond to that of a DNS.

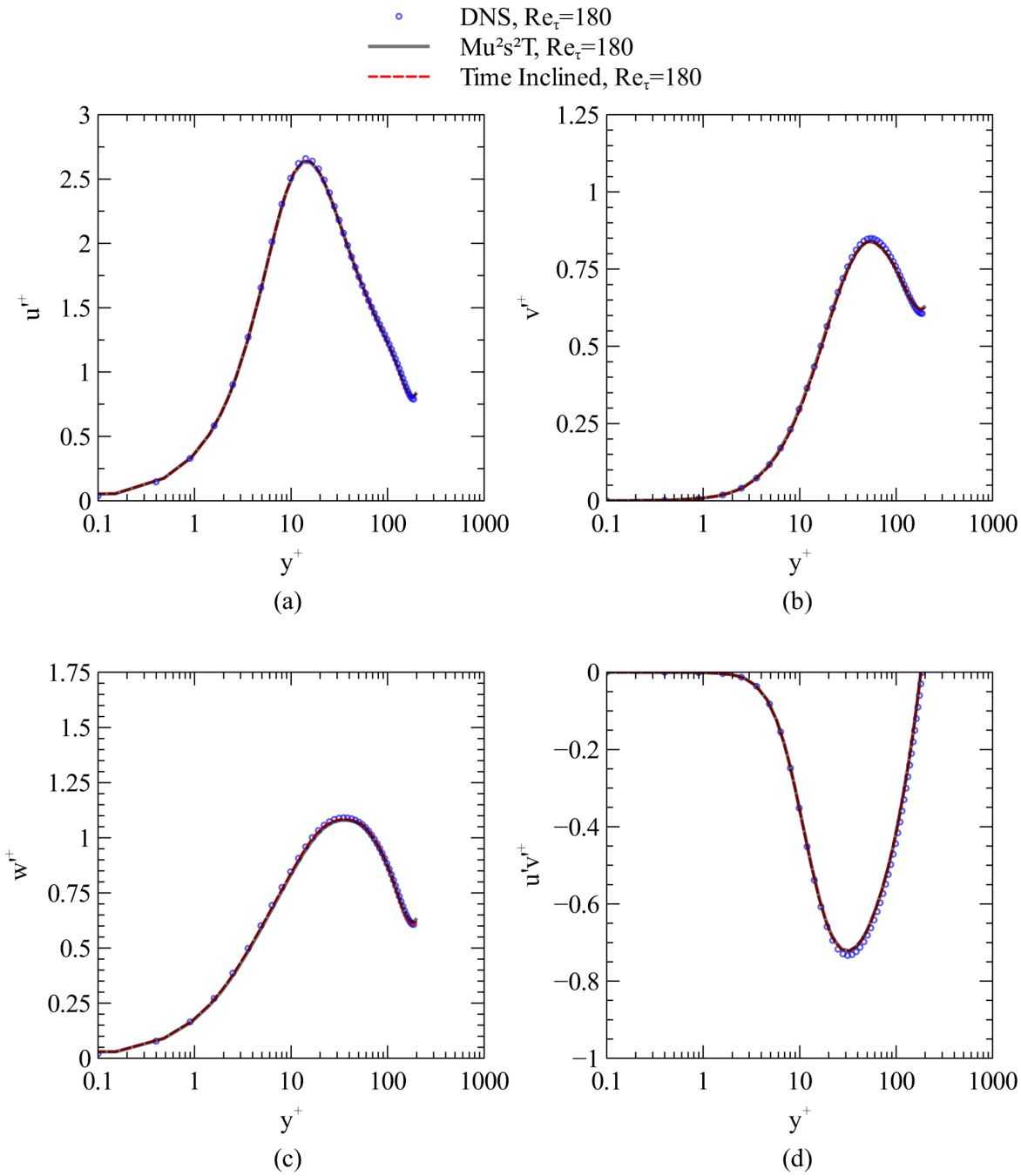

Figure 6.7: Profiles of the root-mean-squared velocity fluctuations in wall units for the $Re_\tau = 180$ case. Comparison between the baseline and wall-normal time-inclined simulations and DNS in [140].

6.2.1.1 Alternative Time-Inclination Directions

To investigate the potential influence of the time-inclination direction in the accuracy of the methodology, two additional time-inclined simulations have been carried out. The only difference with respect to the former lies in the formulation of the time-inclined planes, and subsequent transformation of the Navier-Stokes equations. Thus, the wall-normal direction is substituted as the inclination direction by the stream- and span-wise directions.

The results show no apparent influence on the level of accuracy achieved by the time-inclined methodology. Figures 6.8 (a) and (b) show the average velocity profiles for the x-inclined and z-inclined simulations, respectively, to be identical to those in Figure 6.6. Moreover, Figures 6.9 (a)–(d) and 6.10 (a)–(d) corroborate such hypothesis, showing nearly identical profiles for the velocity fluctuations profiles of the time-inclined simulations.

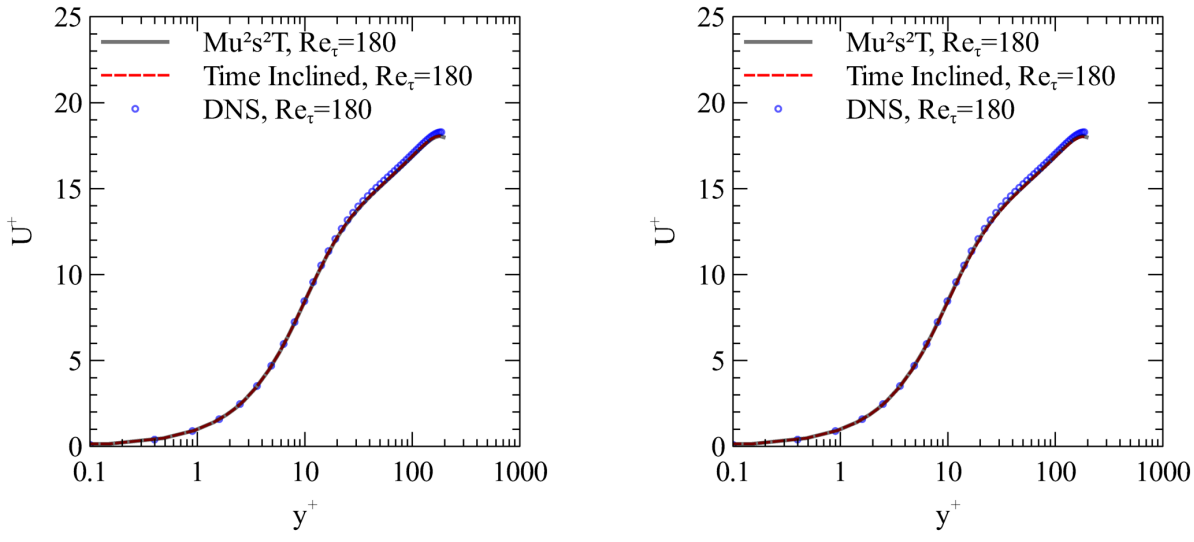

(a) (b)

Figure 6.8: Comparisons of the averaged velocity profiles for the $Re_\tau = 180$ case between the baseline and time-inclined simulations. Results for the x-inclined time-inclined simulation (a) and for the z-inclined time-inclined simulation.

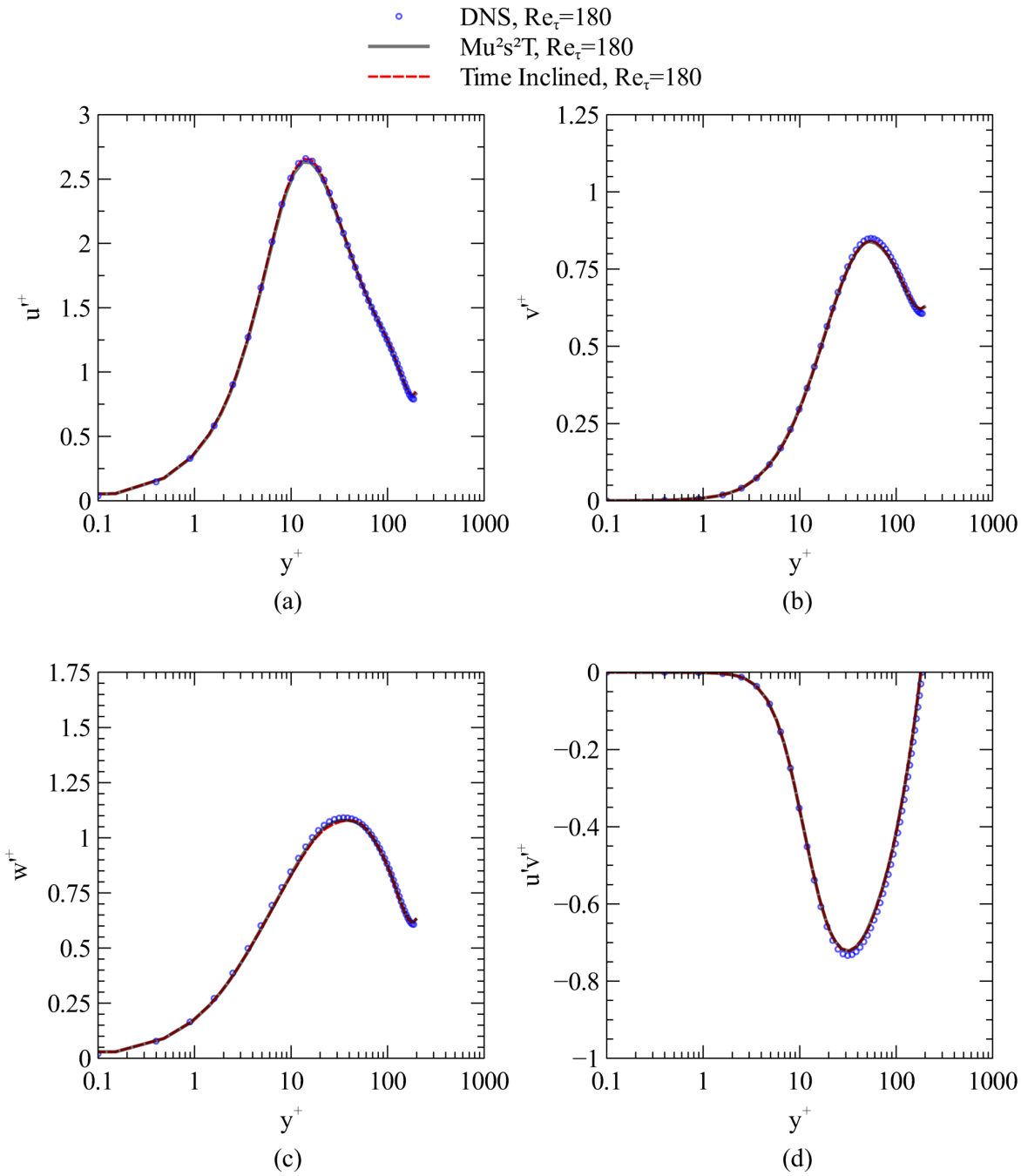

Figure 6.9: Comparisons of the profiles of velocity fluctuations for the $Re_\tau = 180$ case between the baseline and x-inclined time-inclined simulations.

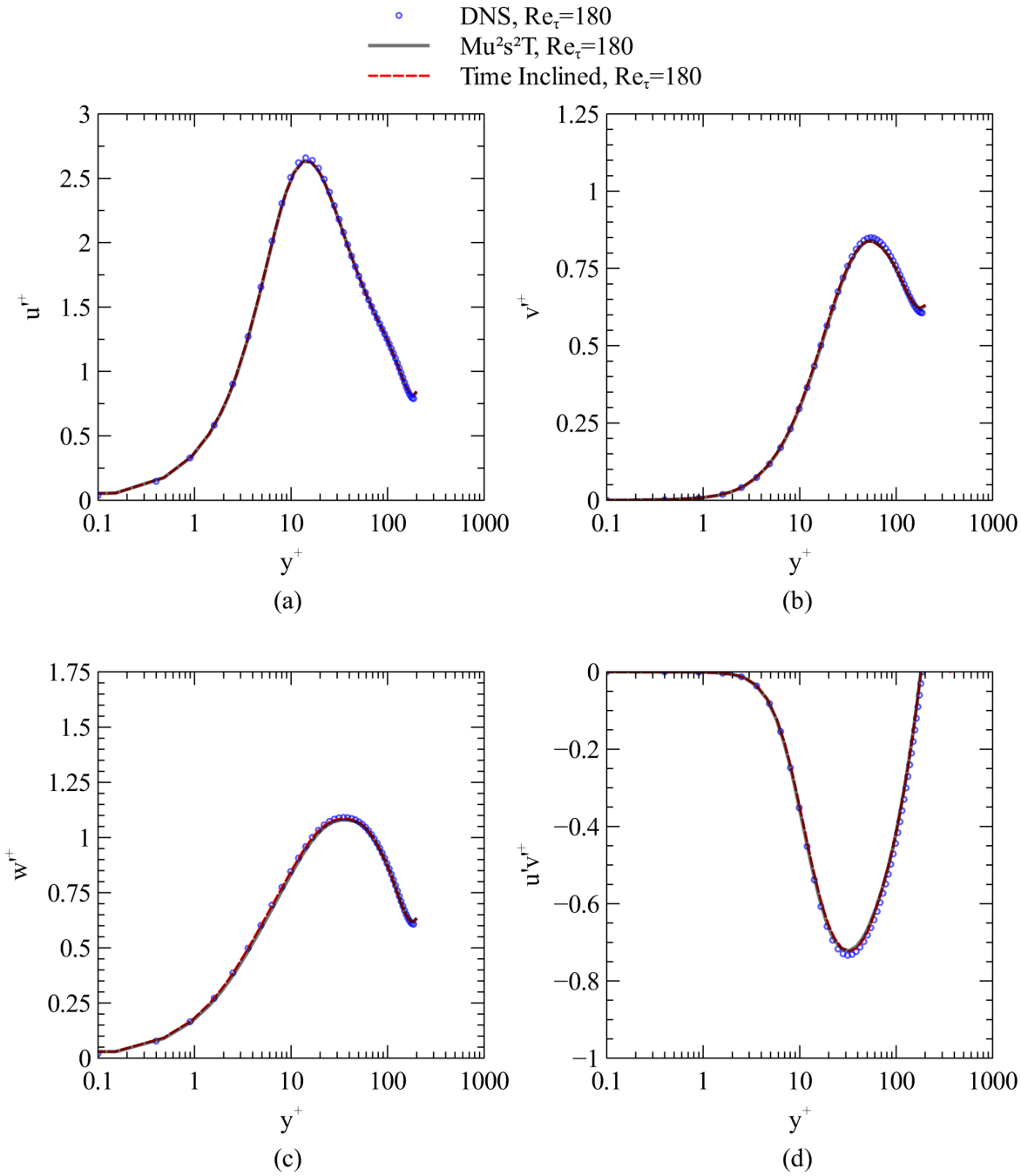

Figure 6.10: Comparisons of the profiles of velocity fluctuations for the $Re_\tau = 180$ case between the baseline and z-inclined time-inclined simulations.

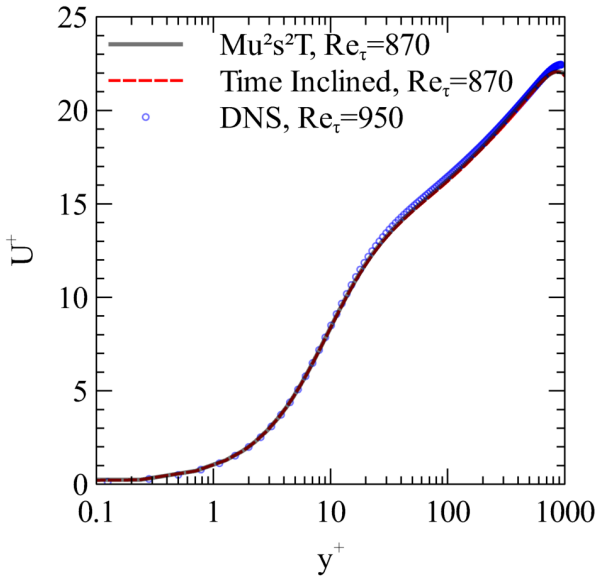

Figure 6.11: Time- and span-wise averaged velocity profile in wall units for the $Re_\tau = 870$ case. Comparison between the baseline and time-inclined simulations and DNS in [146] for a turbulent channel with $Re_\tau = 950$.

6.2.2 Case B: $Re_\tau = 870$

The same methodology of the previous cases has been followed for the $Re_\tau = 870$ simulations. After achieving statistical convergence, the average velocity and RMS profiles of the time-inclined simulation have been compared to those of the baseline code and the DNS data. However, it is important to note that the available data in [146] was for a simulation with $Re_\tau = 950$, which explains the small differences found in Figure 6.11 between the DNS data and the baseline and time-inclined solutions for $y^+ > 20$. Nonetheless, the average velocity profiles obtained with the baseline and time-inclined codes are essentially coincident.

The same conclusions can be drawn from the comparison of the profiles of the velocity fluctuations in Figures 6.12 (a) through (d): the baseline code's and DNS solutions differ slightly, but such a mismatch may be attributed to the differences in Re_τ. This hypothesis is also supported by the results of the validation of the baseline code in [95], which shows a great level of agreement between the code and DNS in simulations with $Re = 950$ and $Re = 2000$.

Even though the baseline and time-inclined fluctuation profiles are very similar, the curves are not as coincident as in the $Re_\tau = 180$ cases. Small differences can be appreciated, especially in the maxima in Figures 6.12 (a)–(c) and the minimum in 6.12 (d), and extend

even to $y^+ \sim 10^3$. Such differences are most noticeable in the curves corresponding to the v' component (Fig. 6.12 (b)), and might be attributed to the lack of sufficient resolution as $y \to \delta$,as the cell sizes overly increase following the law in Eq. 6.6, failing to provide enough resolution.

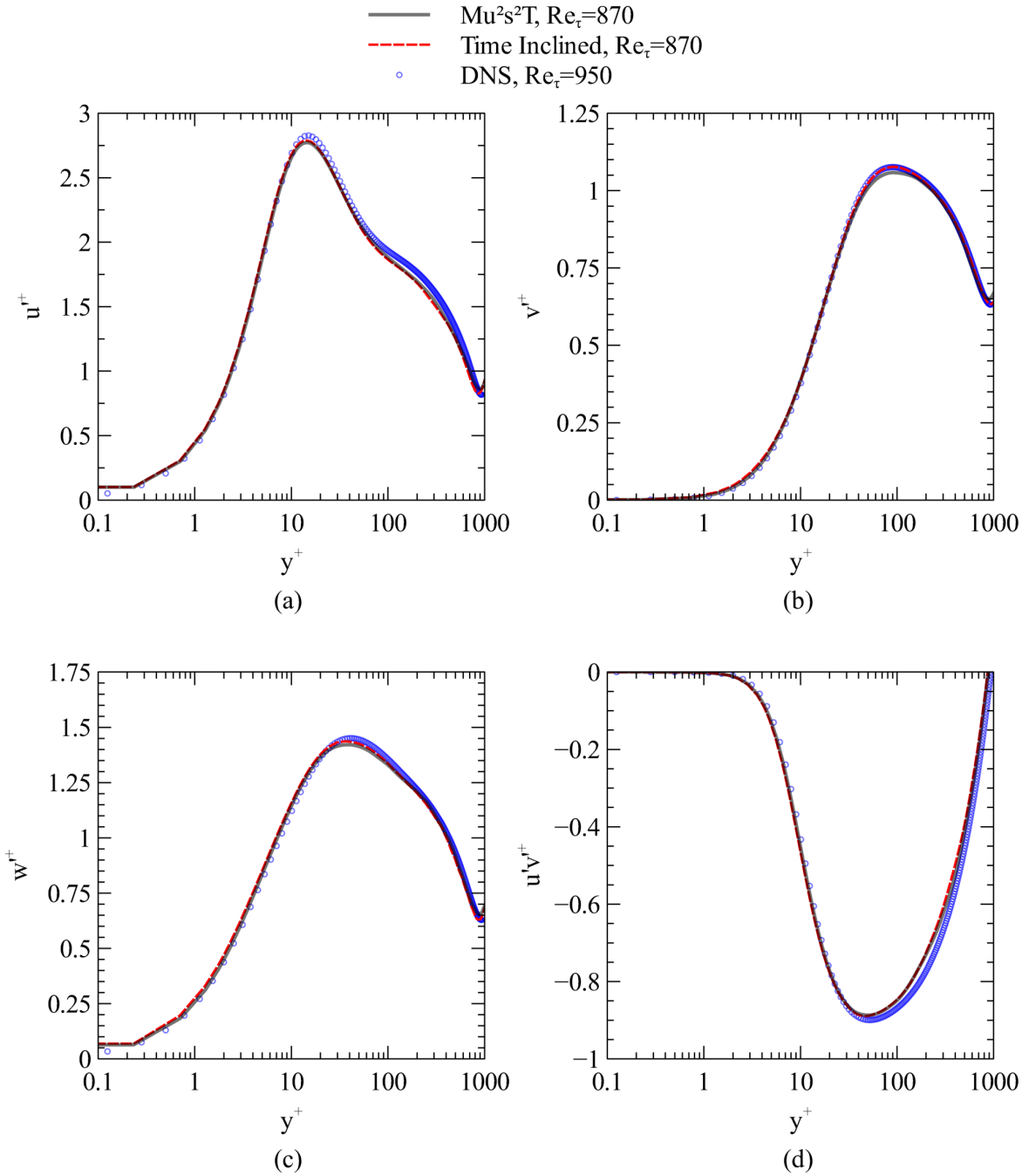

Figure 6.12: Profiles of the root-mean-squared velocity fluctuations in wall units for the $Re_\tau = 870$ case. Comparison between the baseline and time-inclined simulations and DNS in [146] for a turbulent channel with $Re_\tau = 950$.

6.3 Closing Remarks

Several numerical experiments have been carried out to complement the analysis of the suitability of the time-inclined method for transitional and turbulent flows. Even though the TGV and turbulent channel flow problems lack a perturbation to justify the use of the time-inclined method, they can be transformed as if this time shift periodicity were present in the solution.

The results of the comparisons between the baseline and time-inclined approaches show that the latter is appropriate for the simulation of turbulent flows, agreeing with the conclusions drawn in Chapter 5. The main concerns are about the different treatment of the smallest scales by the diffusive terms in the approximate time-inclined implementation with respect to the baseline solver.

In the TGV, such differences not only had an impact on the evolution of the total kinetic energy of the problem, but also on the form of the solution, which lost its original symmetry. The velocity and RMS profiles in the turbulent channel problem were very accurately captured in the $Re_\tau = 180$ case. Such a great level of agreement was not achieved for the $Re_\tau = 870$ case, for which the resolution was insufficient in the central part of the channel.

It is worth noting that the small errors found in these canonical problems are not expected to translate into significant errors in turbomachinery applications of industrial interest. As shown in Chapter 5, the turbulent wakes and boundary layers were accurately predicted. However, it seems that further improvements on the viscous time-inclined methodology may lead to an even better agreement between both approaches, especially in problems or regions with limited resolution.

7 Conclusions

Contents

7.1 Summary and Main Takeaways 171

7.2 Future Work 175

In this final Chapter, a summary of the work that has been carried out and its main takeaways are presented, aiming to provide some conclusions regarding the objectives listed in Chapter 1. The thesis closes with recommendations for future works to further investigate the time-inclined method for high-fidelity turbomachinery applications.

7.1 Summary and Main Takeaways

This work assesses the appropriateness of the time-inclined method for retaining the exact blade count in high-fidelity simulations. Such goal has been divided into several objectives of incremental complexity, which are tackled from **Chapter 3** onwards. **Chapter 1** includes a general view of the problem, and presents the state of the art of domain-reducing (or single-passage) methodologies and high-fidelity simulations of turbulent flows for aerodynamic and aeroacoustic analyses. **Chapter 2** describes the numerical scheme of the high-order baseline solver into which the time-inclined method has been implemented.

Chapter 3 introduces the time-inclined method, which is applied for the transformation of the Euler and Navier-Stokes equations. While the derivation of the correspondence between the time-inclined and conservative variables is straightforward for the Euler equations, the complexity of the inclined Navier-Stokes equations leads to the use of a truncated set of equations. Significant errors may arise from such an approximation and, therefore, one of the main objectives of the thesis (and one of the original contributions from this work) is the evaluation of the impact of such truncated unsteady viscous terms in the transformed equations. The main takeaways from such analysis can be summarised as follows:

The critical parameter controlling the method's accuracy is the local Strouhal number. For the inlet and passage region the decay of incoming wakes is altered in the TI formulation.

However, for moderately high Reynolds numbers, such alterations should be minimal. The basis of this affirmation is the different magnitudes of the diffusion and residence times, a condition upon which the RDT theory also relies to assume that vortices pass through the cascade without attenuation nor interaction.

Conversely, the TI method is expected to produce inaccurate results in the mixing processes downstream of the cascades due to the high frequencies associated with vortex shedding. Nevertheless, the magnitude of such errors is modulated by the Reynolds number. In **Chapter 4** and **Chapter 5** it will be demonstrated that the benefit of retaining the exact blade count in the simulations overcomes the slight differences in the mixing due to this limitation.

Finally, since the frequency of the oscillations in the laminar boundary layers is similar to that of the incoming forcing, the magnitude of the local Strouhal number is $St \sim St_f \frac{1}{Re_c^{1/2}}$, which means that the TI method can reproduce such boundary layers for sufficiently high Re.

Another key part of the work consists of investigating the accurately resolved wavelengths of the problem. **Chapter 3** analyses which scales of the original multi-passage problem are present in the time-inclined simulations. The conclusion is that the synchronous excitations from the relative movement between rotor and stator, including the so-called Tyler-Sofrin modes, are retained but coded into different signals. Moreover, such synchronous signals can be easily recovered, i.e., translated back into the physical plane.

The modus operandi for the test cases of **Chapter 4** and **Chapter 5** consists on performing simulations of linear cascades located downstream of unsteady perturbations. The pitch ratio between the unsteady periodic perturbations and the cascades is not a small integer and, therefore, the imposition of spatial periodicity requires multiple passages in the computational domain, which can be reduced by the time-inclined method to a single passage. Thus, up to three simulations comprise each set of test cases: a multi-passage simulation which includes several passages in order to preserve the spatial periodicity of the problem, a time-inclined simulation which reduces the computational domain into a transformed single-passage simulation, and an approximate problem which alters the pitch ratio so that periodicity is achieved in a single passage called "single-passage approximation".

In **Chapter 4**, the implementation of the time-inclined method into the high-order solver is verified through inviscid simulations of linear cascades, since the multi-passage and the time-inclined solutions match to a extremely high degree. At this point, it is worth recalling that the transformation of the Euler equations is exact and therefore, the solutions obtained with the baseline and time-inclined solver should be almost equal, apart from a relatively small influence of the numerics.

In addition to this result, there are two essential takeaways from **Chapter 4**, which are drawn from the viscous simulations therein:

Firstly, the results from the flat plate cascades at different Reynolds numbers are shown to agree with the theoretical analysis of **Chapter 3**, regarding the impact of the truncated terms in the transformed Navier-Stokes equations. Even in a high reduced frequency perturbation environment, the inlet, passage and laminar boundary layer regions can be accurately captured by the time-inclined method. The analysis of **Chapter 3** explains how the scaling of the truncated terms with respect to the retained diffusive terms allows matching the unsteady pressure perturbations up to the 3^{rd} harmonic (which is close to single precision accuracy) in the passage and boundary layer regions. Moreover, it explains the mispredictions obtained with the TI methodology for the lower Reynolds cases in terms of the total pressure evolution from the trailing edge to the outlet section of the computational domain. Thus, the results also evidence that the mixing processes can be affected due to the relevance of the truncated terms, which are modulated by the Reynolds number of the flow.

The second takeaway from these virtual experiments is that the convergence to a quasi-periodic state is not degraded by means of the time-inclined method. Such a result was obtained from comparisons between the evolution of an unsteady L2 norm in the multi-passage and time-inclined simulations. This is of vital importance: for once, SRS feature very small time-steps, which also contribute to their high computational cost since unsteady simulations require large simulation times to achieve statistical convergence. Moreover, alternative domain-reducing methodologies often require larger times to achieve a quasi-periodic state, which makes the TI method an even stronger candidate for SRS.

One objective of this thesis is to study the suitability of the TI method to perform turbomachinery SRS of problems of industrial relevance. Thus, **Chapter 5** is focused on numerically solving the Navier-Stokes equations for a three-dimensional linear cascade of low-pressure turbine blades subjected to unsteady perturbations. Two different models have been used for such perturbations, emulating the incoming wakes from a preceding row: an immersed boundary approach (i.e. using immersed boundary bars as wake generators) and unsteady wake-like perturbations imposed as inlet boundary conditions.

The aforementioned three-way comparisons between the Multi-Passage, the Time-Inclined and the Single-Passage approximate simulations show how the TI method outperforms the SP standard practice in SRS, accurately predicting the multi-passage solution in most variables of interest. Nevertheless, the results show a dependence on the particular modelling of the incoming perturbations.

The simulations with moving bars as wake generators are the most penalised approach for the TI method. This is because the bars are typically under-resolved, which induces

differences between the MP, TI and SP simulations. For the TI simulation, the differences in the diffusive properties of the baseline and TI schemes lead to different inlet conditions to the blade cascade than the MP case, which makes discerning the sources of the mismatch of the solutions very difficult. For the SP simulation, the number of bars is modified to approximate the pitch ratio to the nearest integer, but their translational speed is also modified so that the reduced frequency of the MP case is matched. The opposing effects of increasing the number of wakes in the domain but decreasing their intensity also unpredictably alter the inlet conditions to the cascade. Nonetheless, the TI method generally outperforms the SP approximation.

Greater levels of accuracy are achieved in the simulations featuring inlet perturbations. The travelling wave perturbations can be analytically transformed into the time-inclined computational plane. Thus, the inlet operates as an inclined sliding plane, translating the physical spatial periodicity and propagation speed into the inclined computational domain of the linear cascade. Therefore, the inlet perturbations case is more representative of an actual rotor/stator time-inclined simulation, and yields the best comparisons between the multi-passage and time-inclined solutions, which are almost coincident for most variables of interest, including: cascade losses, turbulent spectra, laminar and turbulent boundary layer profiles, wake transverse distributions, etc.

Finally, **Chapter 6** demonstrates the suitability of the time-inclined method to accurately reproduce turbulent flow in simple canonical problems. Even though simulations in **Chapter 5** featured turbulent flow, the unsteady simulations of complex physical phenomena characteristic of LPTs entail dealing with many potential sources of error. Thus, carrying out simulations of simpler problems, free of many of such error sources, provides a higher degree of confidence in the analysis of the TI suitability for SRS of turbulent flow.

The main takeaways from such simulations are in line with the conclusions drawn from **Chapter 5**: in the turbulent channel flow problem, the results from the baseline and time-inclined solvers shows very high levels of agreement, even coinciding for the lower Re_τ simulation. The profiles of the average velocity and the turbulent fluctuations essentially agree with DNS data across the channel, from inside of the turbulent boundary layer to the central part of the channel. However, the lack of sufficient resolution in the latter leads to a noticeable mismatch between the TI and baseline solutions in the higher Re_τ simulation, evidencing, once more, the differences in diffusive properties among the baseline and the truncated TI approach.

Such differences are also the cause of the divergence between the predicted kinetic energy evolution curve in the baseline and TI simulations of the TGV when the initial large vortical structures have broken down. The time-inclined method reproduces the growth

rate of the enstrophy in the transitional part of the TGV problem. Such a phase is controlled by inviscid non-linear mechanisms that the TI method replicates accurately. After reaching the enstrophy peak, the absence of large dominant structures and the presence of very small scales makes it very challenging for the approximate TI methodology to capture the actual evolution of the kinetic energy. Nevertheless, as more kinetic energy is dissipated, the differences between the schemes becomes less relevant, and the results of the baseline and TI simulations converge once again.

From the results of this work, the time-inclined method is believed to be a suitable method to retain the exact blade count in turbomachinery scale-resolving simulations. In problems of industrial interest, the TI methodology has been shown to accurately predict the aerodynamic performance while retaining the exact pitch ratio of the problem, and outperforming the standard single-passage methodology in most of the variables of interest.

7.2 Future Work

The present thesis is focused on the verification of the time-inclined method for turbomachinery scale-resolving simulations of arbitrary blade count. The ambitious goal of demonstrating the suitability of the method in ILES or quasi-DNS simulations of industrial relevance has occupied a great part of this research period. Thus, there are several topics that have not been explored, either because they were considered of secondary importance, or because they were considered to be conditionally relevant and depended on the results of the present work. In the present section, some of such topics are described along suggestions to further improve the time-inclined method for SRSs.

The TI verification process has been carried out in steps of incremental complexity. The analysis of the truncated terms in the time-inclined transformation of the Navier-Stokes equations is the culmination of the preliminary analytical work, and was later verified through two-dimensional simulations. However, the formulation of the inclined NS equations remains unchanged since the original work of Giles.

During this research period, several unsuccessful attempts have been taken to either solve this issue or improve the formulation. However, the results from the two-dimensional simulations shown in Chapter 4 indicated that this topic might not be of first-order importance in practice. As demonstrated in Chapter 5, the truncation of the inclined NS equations does not prevent the TI method from obtaining accurate results in problems of industrial relevance. Nonetheless, an accurate formulation of the inclined NS equations would lead to more accurate predictions of the mixing processes, as well as improve the

accuracy of the TI method in regions with small vortical structures and high Strouhal numbers.

A possible approach to this problem could be to firstly advance in time the (complete) inclined NS equations in each iteration of the time-marching scheme, providing a new value for the inclined variables, $\mathbf{Q}^{n+1}$, and then finding a new $\mathbf{U}^{n+1}$ such that the system of equations, $\mathbf{Q}^{n+1} = f(\mathbf{U}^{n+1}, \nabla\mathbf{U}^{n+1}, \partial\mathbf{U}^{n+1}/\partial\tau)$, converges. However, it is important to note that the great level of efficiency achieved by the truncated viscous TI approach is partly due to its restricted impact on the algorithm of the baseline solver. Further improvements on the accuracy cannot be traded for efficiency at a high price, since the former might be negligible in an industrial context (see Chapter 5), while the latter may deter the use of the method altogether.

The next topic of interest for future work concerns the upstream perturbation modelling strategies. As discussed at length in Section 5.1, the present verification process requires ensuring that the reference multi-passage and TI solutions are obtained through the imposition of identical BCs. The results in Chapter 5 showcase the importance of injecting an accurate inclined representation of the physical upstream field in order to obtain very accurate predictions through time-inclining. Such a task might be completely avoided if the incoming wake generators (or the upstream row blade) are included in the simulation in their own separate domain. In such a case, the time-inclined sliding plane formulation accurately transforms the information that crosses the interface.

However, a high-order sliding plane methodology was not implemented and verified for three-dimensional simulations in time. Moreover, such a method would have increased the cost of the multi-passage, time-inclined and single-passage simulations, which were already sufficiently expensive. Nevertheless, after the satisfactory results shown in the present thesis, it would be interesting to pursue the implementation of the time-inclined sliding plane methodology into the high-order baseline solver.

Then, the immersed bar cascade test cases in Chapter 5 could be carried out including the geometry of the bars in a separate domain to the blade cascade, and the results could verify the source of some of the errors reported in such Chapter. Moreover, an inclined sliding plane implementation would enable comparisons between multi-passage and time-inclined SRSs of single stages, for which, to the best of the authors knowledge, there have been no reports in the literature.

Bibliography

[1] Darecki, M., Edelstenne, C., Enders, T., Fernandez, E., Hartman, P., Herteman, J.-P., Kerkloh, M., King, I., Ky, P., Mathieu, M., et al., 2011. Flightpath 2050 - Europes vision for aviation. Tech. rep., European Comission. High-Level Group on Aviation Research.

[2] Federal Aviation Administration (FAA), United States Federal Government, 2021. United states aviation climate action plan. `https://www.faa.gov/sites/faa.gov/files/2021-11/Aviation_Climate_Action_Plan.pdf`. Online; Accessed 29 September 2023.

[3] Wisler, D. C., 1998. "The technical and economic relevance of understanding blade row interaction effects in turbomachinery".

[4] Bolinches-Gisbert, M., Cadrecha-Robles, D., Corral, R., and Gisbert, F., 2020. "Prediction of reynolds number effects on low-pressure turbines using a high-order iles method". *ASME Journal of Turbomachinery,* **142**(3), March, p. 031002. doi:10.1115/1.4045776.

[5] Bolinches-Gisbert, M., Cadrecha-Robles, D., Corral, R., and Gisbert, F., 2021. "Numerical and experimental investigation of the reynolds number and reduced frequency effects on low-pressure turbine airfoils". *ASME Journal of Turbomachinery,* **143**(2), February, p. 021004. doi:10.1115/1.4049612.

[6] Michelassi, V., Wissink, J. G., and Rodi, W., 2003. "Direct numerical simulation, large eddy simulation and unsteady reynolds-averaged navier-stokes simulations of periodic unsteady flow in a low-pressure turbine cascade: A comparison". *Proceedings of the Institution of Mechanical Engineers, Part A: Journal of Power and Energy,* **217**(4), pp. 403–411. doi:10.1243/095765003322315469.

[7] Sandberg, R. D., Michelassi, V., Pichler, R., Chen, L., and Johnstone, R., 2015. "Compressible Direct Numerical Simulation of Low-Pressure Turbines-Part I: Methodology". *Journal of Turbomachinery,* **137**(5), 05, p. 051011. doi:10.1115/1.4028731.

[8] Michelassi, V., Chen, L.-W., Pichler, R., and Sandberg, R. D., 2015. "Compressible Direct Numerical Simulation of Low-Pressure Turbines-Part II: Effect

of Inflow Disturbances". *Journal of Turbomachinery,* **137**(7), 07, p. 071005. doi:10.1115/1.4029126.

[9] Michelassi, V., Chen, L., Pichler, R., Sandberg, R., and Bhaskaran, R., 2016. "High-fidelity simulations of low-pressure turbines: Effect of flow coefficient and reduced frequency on losses". *Journal of Turbomachinery,* **138**, p. 111006.

[10] Pichler, R., Michelassi, V., Sandberg, R., and Ong, J., 2018. "Highly resolved large eddy simulation study of gap size effect on low-pressure turbine stage". *Journal of Turbomachinery,* **140**(2), p. 021003.

[11] Marconcini, M., Pacciani, R., Arnone, A., Michelassi, V., Pichler, R., Zhao, Y., and Sandberg, R., 2018. "Les and rans analysis of the end-wall flow in a linear lpt cascade with variable inlet conditions: Part ii loss generation". In ASME Turbo Expo 2018: Turbomachinery Technical Conference and Exposition, American Society of Mechanical Engineers, pp. V02BT41A024–V02BT41A024.

[12] Tucker, P., 2011. "Computation of unsteady turbomachinery flows: Part 1–progress and challenges". *Progress in Aerospace Sciences,* **47**(7), pp. 522–545. doi:10.1016/j.paerosci.2011.06.004.

[13] Hodson, H. P., and Howell, R. J., 2005. "Bladerow interactions, transition, and high-lift aerofoils in low-pressure turbines". *Annu. Rev. Fluid Mech.,* **37**, pp. 71–98.

[14] Hodson, H. P., and Howell, R. J., 2005. "The role of transition in high-lift low-pressure turbines for aeroengines". *Progress in Aerospace Sciences,* **41**(6), pp. 419–454. doi:https://doi.org/10.1016/j.paerosci.2005.08.001.

[15] Corral, R., and Gisbert, F., 2010. "Prediction of Separation-Induced Transition Using a Correlation-Based Transition Model". Vol. Volume 7: Turbomachinery, Parts A, B, and C of *Turbo Expo: Power for Land, Sea, and Air*, pp. 897–908. doi:10.1115/GT2010-23239.

[16] Hodson, H., and Howell, R., 2001. "High lift low pressure turbines". *Minnowbrooke III Proceedings, NASA/CP–2001,* **210888**, pp. 37–78.

[17] Hodson, H. P., Hynes, T. P., Greitzer, E. M., and Tan, C. S., 2012. "A Physical Interpretation of Stagnation Pressure and Enthalpy Changes in Unsteady Flow". *Journal of Turbomachinery,* **134**(6), 09, p. 060902. doi:10.1115/1.4007208.

[18] Meyer, R. X., 1958. "The effect of wakes on the transient pressure and velocity distributions in turbomachines". *Transactions of the American Society of Mechanical Engineers,* **80**(7), pp. 1544–1551.

[19] Coull, J. D., and Hodson, H. P., 2011. "Unsteady boundary-layer transition in low-pressure turbines". *Journal of Fluid Mechanics,* **681**, pp. 370–410.

[20] Jacobs, R. G., and Durbin, P. A., 1998. "Shear sheltering and the continuous spectrum of the Orr–Sommerfeld equation". *Physics of Fluids,* **10**(8), 08, pp. 2006–2011. doi:10.1063/1.869716.

[21] Wissink, J., 2003. "Dns of separating, low reynolds number flow in a turbine cascade with incoming wakes". *International Journal of Heat and Fluid Flow,* **24**(4), pp. 626–635. doi:10.1016/S0142-727X(03)00056-0. Selected Papers from the Fifth International Conference on Engineering Turbulence Modelling and Measurements.

[22] Halstead, D. E., Wisler, D. C., Okiishi, T. H., Walker, G. J., Hodson, H. P., and Shin, H.-W., 1997. "Boundary Layer Development in Axial Compressors and Turbines: Part 2 of 4–Compressors". *Journal of Turbomachinery,* **119**(3), 07, pp. 426–444. doi:10.1115/1.2841142.

[23] Halstead, D. E., Wisler, D. C., Okiishi, T. H., Walker, G. J., Hodson, H. P., and Shin, H.-W., 1997. "Boundary Layer Development in Axial Compressors and Turbines: Part 3 of 4– LP Turbines". *Journal of Turbomachinery,* **119**(2), 04, pp. 225–237. doi:10.1115/1.2841105.

[24] Halstead, D. E., Wisler, D. C., Okiishi, T. H., Walker, G. J., Hodson, H. P., and Shin, H.-W., 1997. "Boundary Layer Development in Axial Compressors and Turbines: Part 4 of 4–Computations and Analyses". *Journal of Turbomachinery,* **119**(1), 01, pp. 128–139. doi:10.1115/1.2841001.

[25] Bonneau, V., Polacsek, C., Castillon, L., Marty, J., Gervais, Y., and Moreau, S., 2016. "Turbofan broadband noise predictions using a 3-D ZDES rotor blade approach". In 22nd AIAA/CEAS Aeroacoustics Conference, p. 2950. doi:10.2514/6.2016-2950.

[26] Polacsek, C., Daroukh, M., François, B., and Barrier, R., 2020. "Turbofan broadband noise predictions based on a ZDES calculation of a Fan-OGV stage". In Forum Acusticum 2020.

[27] Laskowski, G. M., Kopriva, J., Michelassi, V., Shankaran, S., Paliath, U., Bhaskaran, R., Wang, Q., Talnikar, C., Wang, Z. J., and Jia, F. *Future Directions of High Fidelity CFD for Aerothermal Turbomachinery Analysis and Design.* doi:10.2514/6.2016-3322.

[28] Huynh, H. T., 2007. "A flux reconstruction approach to high-order schemes including discontinuous galerkin methods". In 18th AIAA Computational Fluid Dynamics Conference, p. 4079.

[29] Stadtmüller, P., 2001. "Investigation of wake-induced transition on the lp turbine cascade t106a-eiz". *DFG-Verbundprojekt Fo,* **136**(11).

[30] Stadtmüller, P., and Fottner, L., 2001. "A Test Case for the Numerical Investigation of Wake Passing Effects on a Highly Loaded LP Turbine Cascade Blade". Vol. Volume 1: Aircraft Engine; Marine; Turbomachinery; Microturbines and Small Turbomachinery of *Turbo Expo: Power for Land, Sea, and Air*, p. V001T03A015. doi:10.1115/2001-GT-0311.

[31] Wu, X., and Durbin, P. A., 2001. "Evidence of longitudinal vortices evolved from distorted wakes in a turbine passage". *Journal of Fluid Mechanics,* **446**, pp. 199–228.

[32] Michelassi, V., Wissink, J. G., Fröhlich, J., and Rodi, W., 2003. "Large-eddy simulation of flow around low-pressure turbine blade with incoming wakes". *AIAA Journal,* **41**(11), pp. 2143–2156. doi:10.2514/2.6832.

[33] Cui, J., Rao, V. N., and Tucker, P., 2016. "Numerical investigation of contrasting flow physics in different zones of a high-lift low-pressure turbine blade". *ASME J. Turbomach.,* **138**(1), p. 011003.

[34] Opoka, M. M., Thomas, R. L., and Hodson, H. P., 2008. "Boundary layer transition on the high lift t106a low-pressure turbine blade with an oscillating downstream pressure field". *Journal of Turbomachinery,* **130**, p. 021009.

[35] Lyall, M. E., King, P. I., Sondergaard, R., Clark, J. P., and McQuilling, M. W., 2012. "An investigation of reynolds lapse rate for highly loaded low pressure turbine airfoils with forward and aft loading". *ASME J. Turbomach.,* **134**(5), p. 051035.

[36] Hammer, F., Sandham, N. D., and Sandberg, R. D., 2018. "The influence of different wake profiles on losses in a low pressure turbine cascade". *International Journal of Turbomachinery, Propulsion and Power,* **3**(2), p. 10.

[37] Hultgren, L. S., 2010. "Emerging importance of turbine noise". *Editorial: International Journal of Aeroacoustics.* doi:10.1260/1475-472x.10.1.i.

[38] Moreau, S., 2019. "Turbomachinery noise predictions: Present and future". *Acoustics,* **1**(1), pp. 92–116. doi:10.3390/acoustics1010008.

[39] Peake, N., and Parry, A. B., 2012. "Modern challenges facing turbomachinery aeroacoustics". *Annual Review of Fluid Mechanics,* **44**, pp. 227–248. doi:10.1146/annurev-fluid-120710-101231.

[40] Blázquez Navarro, R. A., 2022. "Efficient turbomachinery broadband noise analysis using linearised navier-stokes solvers and synthetic turbulence models". PhD thesis, Universidad Politécnica de Madrid, Escuela Técnica Superior de Ingeniería Aeronáutica y del Espacio.

[41] Moreau, S., and Roger, M., 2024. "Turbomachinery noise review". *International Journal of Turbomachinery, Propulsion and Power,* **9**(1). doi:10.3390/ijtpp9010011.

[42] Arroyo, C. P., Leonard, T., Sanjosé, M., Moreau, S., and Duchaine, F., 2019. "Large eddy simulation of a scale-model turbofan for fan noise source diagnostic". *Journal of Sound and Vibration,* **445**, pp. 64–76. doi:10.1016/j.jsv.2019.01.005.

[43] Lewis, D., Moreau, S., Jacob, M. C., and Sanjosé, M., 2021. "Acat1 fan stage broadband noise prediction using large-eddy simulation and analytical models". *AIAA Journal*, pp. 1–21. doi:10.2514/1.J060163.

[44] Al-Am, J., Clair, V., Giauque, A., Boudet, J., and Gea-Aguilera, F., 2023. "Direct noise predictions of a 360° full fan stage using LES". In AIAA AVIATION 2023 Forum, American Institute of Aeronautics and Astronautics, pp. AIAA 2023–4295. doi:10.2514/6.2023-4295.

[45] Al-Am, J., Clair, V., Giauque, A., Boudet, J., and Gea-Aguilera, F., 2022. "On the effects of a separation bubble on fan noise". *Journal of Sound and Vibration,* **537**, p. 117180. doi:https://doi.org/10.1016/j.jsv.2022.117180.

[46] Gourdain, N., Burguburu, S., Leboeuf, F., and Michon, G. J., 2010. "Simulation of rotating stall in a whole stage of an axial compressor". *Computers & Fluids,* **39**(9), pp. 1644–1655.

[47] Haug, J. P., and Niehuis, R., 2018. "Full annulus simulations of a transonic axial compressor stage with distorted inflow at transonic and subsonic blade tip speed". *International Journal of Turbomachinery, Propulsion and Power,* **3**(1), p. 7.

[48] He, L., 2010. "Fourier methods for turbomachinery applications". *Progress in Aerospace Sciences,* **46**(8), pp. 329–341.

[49] Corral, R., Escribano, A., Gisbert, F., Serrano, A., and Vasco, C., 2003. "Validation of a linear multigrid accelerated unstructured navier-stokes solver for the computation of turbine blades on hybrid grids". In AIAA Paper 2003-3326, 9th AIAA/CEAS Aeroacoustics Conference.

[50] Corral, R., Gallardo, J. M., and Vasco, C., 2007. "Aeroelastic stability of welded-in-pair low pressure turbine rotor blades: A comparative study using linear methods". *Journal of Turbomachinery,* **129**, January, pp. 72–83.

[51] Fernandez Aparicio, J. R., Serrano, A., and Vázquez, R., 2011. "On the linearity of turbomachinery interaction noise. part i: 2d analysis". In 17th AIAA/CEAS Aeroacoustics Conference (32nd AIAA Aeroacoustics Conference), p. 2951.

[52] Fernandez Aparicio, J. R., Serrano, A., and Vázquez, R. "On the linearity of

turbomachinery interaction noise. part ii: 3d analysis". In 18th AIAA/CEAS Aeroacoustics Conference (33rd AIAA Aeroacoustics Conference), p. 2309.

[53] Serrano, A., and Aparicio, J. R. F., 2016. "Turbine tone noise prediction using a linearized computational fluid dynamics solver: comparison with measurements". *Journal of Turbomachinery,* **138**(6). doi:10.1115/1.4032285.

[54] Ning, W., and He, L., 1998. "Computation of unsteady flows around oscillating blades using linear and nonlinear harmonic euler methods". *Journal of Turbomachinery,* **120**(3), pp. 508–514.

[55] Hall, K. C., Thomas, J. P., and Clark, W. S., 2002. "Computation of unsteady nonlinear flows in cascades using a harmonic balance technique". *AIAA journal,* **40**(5), pp. 879–886.

[56] Rai, M., 1987. "Navier-stokes simulations of rotor-stator interactions using patched and overlaid grids". *Journal of Propulsion and Power,* **5**(5), pp. 387–396. doi:10.2514/3.23003.

[57] Mayorca, M., Andrade, J. D., Vogt, D., Martensson, H., and Fransson, T., 2011. "Effect of scaling of blade row sectors on the prediction of aerodynamic forcing in a highly loaded transonic compressor stage". *ASME Journal of Turbomachinery,* **133**(2), p. 021013. doi:10.1115/1.4000579.

[58] Denton, J., 1992. "The calculation of three-dimensional viscous flow through multistage turbomachine". *ASME Journal of Turbomachinery,* **114**(1), pp. 18–26.

[59] Gourdain, N., Burguburu, S., Leboeuf, F., and Miton, H., 2006. "Numerical simulation of rotating stall in a subsonic compressor". *Aerospace Science and Technology,* **10**(1), pp. 9–18.

[60] Connell, S., Hutchinson, B., Galpin, P., R, C., and Godin, P., 2012. "The efficient computation of transient flow in turbine blade rows using transformation method". In ASME Turbo Expo 2012 Proceedings, pp. 2631–2640.

[61] Gout, C., Dombard, J., Odier, N., Duchaine, F., Gicquel, L., and Papadogiannis, D., 2021. "Revisiting profile transformation for mono channel turbomachinery large eddy simulations". In ASME Turbo Expo 2021, ASME, ed., no. GT2021:59293.

[62] Erdos, J., Alzner, E., and McNally, W., 1977. "Numerical solution of periodic transonic flow through a fan stage". *AIAA Journal,* **15(11)**, pp. 1559–1568.

[63] He, L., 1990. "An euler solution for unsteady flows around oscillating blades". *ASME Journal of Turbomachinery,* **12**, pp. 714–722.

[64] He, L., 1992. "Method of simulating unsteady turbomachinery flows with multiple perturbations". *AIAA journal,* **30**(11), pp. 2730–2735.

[65] Burgos, M., and Corral, R., 2000. "Comparison and validation of phase-shifted boundary conditions". In 9th International Symposium on Unsteady Aerodynamics, Aeroacoustics and Aeroelasticity of Turbomachines, pp. 296–309.

[66] Dewhurst, S., and He, L., 2000. "Unsteady flow calculations through turbomachinery stages using single passage domain with shape correction method". In 9th International Symposium on Unsteady Aerodynamics, Aeroacoustics and Aeroelasticity of Turbomachines.

[67] Gerolymos, G. A., Michon, G. J., and Neubauer, J., 2002. "Analysis and application of chorochronic periodicity in turbomachinery rotor/stator interaction computations". *AIAA Journal of Propulsion and Power,* **18**(6), pp. 1139–1152. doi:10.2514/2.6065.

[68] Li, H., and He, L., 2005. "Toward intra-row gap optimization for one and half stage transonic compressor". *ASME Journal of Turbomachinery,* **127**(7), July, pp. 589–598. doi:10.1115/1.1928934.

[69] Connell, S., Braaten, M., Zori, L., Steed, R., and ang G. Cox, B. H., 2011. "A comparison of advanced numerical techniques to model transient flow in turbomachinery blade row". In ASME Turbo Expo 2011 Proceedings, pp. GT2011–45820.

[70] Corral, R., Romera, D., and Montiel, M., 2024. "Block Spectral Method Analysis for Turbomachinery Applications". *Journal of Turbomachinery*, 04, pp. 1–26. doi:10.1115/1.4065411.

[71] He, L., 2006. "Fourier modeling of steady and unsteady nonaxisymmetrical flows". *Journal of propulsion and power,* **22**(1), pp. 197–201.

[72] He, L., 2011. "Efficient computational model for nonaxisymmetric flow and heat transfer in rotating cavity". *Journal of Turbomachinery,* **133**(2), p. 021018.

[73] He, L., 2011. "Block-spectral approach to film-cooling modeling". *Journal of turbomachinery,* **134**(2), 06. doi:10.1115/1.4003073. 021018.

[74] He, L., 2013. "Block-spectral mapping for multi-scale solution". *Journal of Computational Physics,* **250**, pp. 13–26.

[75] He, L., 2013. "Fourier spectral modelling for multi-scale aero-thermal analysis". *International Journal of computational fluid dynamics,* **27**(2), pp. 118–129.

[76] Romera, D., and Corral, R., 2020. "Efficient passage-spectral method for unsteady flows under stall conditions". *ASME Journal of Turbomachinery,* **142**(12), December, p. 121007. doi:10.1115/1.4047934.

[77] Romera, D., and Corral, R., 2021. "Nonlinear stability analysis of a generic fan with

distorted inflow using passage-spectral method". *ASME Journal of Turbomachinery,* **143**(6), June, p. 061001. doi:10.1115/1.4050144.

[78] Tyler, J. M., and Sofrin, T. G., 1962. Axial flow compressor noise studies. Tech. rep., SAE Technical Paper.

[79] Giles, M. B., 1988. "Calculation of unsteady wake/rotor interaction". *Journal of Propulsion and Power,* **4**(4), pp. 356–362.

[80] Jung, A. R., Mayer, J. F., and Stetter, H., 1996. "Simulation of 3d-unsteady stator/rotor interaction in turbomachinery stages of arbitrary pitch ratio". Vol. Volume 1: Turbomachinery of *Turbo Expo: Power for Land, Sea, and Air*, p. V001T01A025. doi:10.1115/96-GT-069.

[81] Zhou, L., Xi, G., and Cai, Y. H., 2007. "Unsteady numerical simulation in a centrifugal compressor using the time-inclined operator". *Proceedings of the Institution of Mechanical Engineers, Part G: Journal of Aerospace Engineering,* **221**(5), pp. 795–804. doi:10.1243/09544100JAERO194.

[82] Biesinger, T., Cornelius, C., Rube, C., Braune, A., Campregher, R., Godin, P. G., Schmid, G., and Zori, L., 2010. "Unsteady cfd methods in a commercial solver for turbomachinery applications". In ASME Turbo Expo 2010, ASME, ed., Vol. 7, pp. 2441–2452. doi:10.1115/GT2010-22762.

[83] Connell, S., Hutchinson, B., Galpin, P., Campregher, R., and Godi, P., 2012. "The efficient computation of transient flow in turbine blade rows using transformation methods". In ASME Turbo Expo 2012, ASME, ed., Vol. 8: Tuurbomachinery, pp. 2631–2640. doi:10.1115/GT2012-69019.

[84] Cornelius, C., Biesinger, T., Galpin, P., and Braune, A., 2013. "Experimental and Computational Analysis of a Multistage Axial Compressor Including Stall Prediction by Steady and Transient CFD Methods". Vol. Volume 6C: Turbomachinery of *Turbo Expo: Power for Land, Sea, and Air*, p. V06CT42A016. doi:10.1115/GT2013-94639.

[85] Cornelius, C., Biesinger, T., Zori, L., Campregher, R., Galpin, P., and Braune, A., 2014. "Efficient time resolved multistage cfd analysis applied to axial compressors". In ASME Turbo Expo 2014, ASME, ed., Vol. 2D: Turbomachinery, p. V02DT44A035. doi:10.1115/GT2014-26846.

[86] Hegde, S., Kielb, R., Zori, L., and Campregher, R., 2020. "Impact of Multi-Row Aerodynamic Interaction on the Forced Response Behaviour of an Embedded Compressor Rotor". Vol. Volume 2E: Turbomachinery of *Turbo Expo: Power for Land, Sea, and Air*, p. V02ET41A012. doi:10.1115/GT2020-14482.

[87] Zori, L., Galpin, P., Campregher, R., and Morales, J., 2017. "Time-transformation simulation of a 1.5 stage transonic compressor". *ASME Journal of Turbomachinery,* **139**(7), July, p. 4035450. doi:10.1115/1.4035450.

[88] Giles, M., 1988. Unsflo: A numerical method for unsteady inviscid flow in turbomachinery. Tech. rep., Cambridge, Mass.: Gas Turbine Laboratory, Massachusetts Institute of Technology.

[89] Giles, M. B., 1990. "Stator/rotor interaction in a transonic turbine". *Journal of Propulsion and Power,* **6**(5), pp. 621–627.

[90] Vincent, P., Castonguay, P., and Jameson, A., 2011. "Insights from von neumann analysis of high-order flux reconstruction schemes". *Journal of Computational Physics,* **230**(22), pp. 8134–8154. doi:10.1016/j.jcp.2011.07.013.

[91] Moura, R., Sherwin, S., and Peiró, J., 2015. "Linear dispersion–diffusion analysis and its application to under-resolved turbulence simulations using discontinuous galerkin spectral/hp methods". *Journal of Computational Physics,* **298**, pp. 695–710.

[92] Corral, R., Gisbert, F., and Pueblas, J., 2017. "Execution of a parallel edge-based Navier–Stokes solver on commodity graphics processor units". *International Journal of Computational Fluid Dynamics,* **31**(2), pp. 93–108. doi:10.1080/10618562.2017.1294686.

[93] Gisbert, F., Bolinches-Gisbert, M., Pueblas, J., and Corral, R., 2018. "Efficient implementation of flux reconstruction schemes for the simulation of compressible viscous flows on graphics processing unigs". In Tenth International Conference on Computational Fluid Dynamics (ICCFD10), no. ICCFD10-307.

[94] Bolinches i Gisbert, M., 2020. "Development of a high-order method for the prediction of low-pressure turbine losses using quasi-direct numerical simulations". PhD thesis, Universidad Politécnica de Madrid, Escuela Técnica Superior de Ingeniería Aeronáutica y del Espacio.

[95] Gisbert, F., Sotillo, A., and Pueblas, J., 2022. "Efficient implementation of a high-order compressible navier-stokes equations solver running on graphics processing units". *8th European Congress on Computational Methods in Applied Sciences and Engineering.* doi:10.23967/eccomas.2022.105.

[96] Vincent, P. E., Castonguay, P., and Jameson, A., 2011. "A new class of high-order energy stable flux reconstruction schemes". *Journal of Scientific Computing,* **47**(1), pp. 50–72. doi:10.1007/s10915-010-9420-z.

[97] Wang, Z., and Gao, H., 2009. "A unifying lifting collocation penalty formulation

including the discontinuous galerkin, spectral volume/difference methods for conservation laws on mixed grids". *Journal of Computational Physics,* **228**(21), pp. 8161–8186.

[98] Roe, P., 1981. "Approximate riemman solvers, parameters, vectors and difference schemes". *Journal of Computational Physics,* **43**, pp. 357–372.

[99] Warburton, T., 2006. "An explicit construction of interpolation nodes on the simplex". *Journal of Engineering Mathematics,* **56**(3), pp. 247–262. doi:10.1007/s10665-006-9086-6.

[100] Hesthaven, J. S., and Warburton, T., 2007. *Nodal discontinuous Galerkin methods: algorithms, analysis, and applications.* Springer Science & Business Media.

[101] Chan, J., and Warburton, T., 2015. "A comparison of high order interpolation nodes for the pyramid". *SIAM Journal on Scientific Computing,* **37**(5), pp. A2151–A2170. doi:10.1137/141000105.

[102] Bassi, F., and Rebay, S., 1997. "A high-order accurate discontinuous finite element method for the numerical solution of the compressible navier–stokes equations". *Journal of Computational Physics,* **131**(2), pp. 267–279. doi:https://doi.org/10.1006/jcph.1996.5572.

[103] Boyd, J., Marilyn, T., and Eliot, P., 2000. *Chebyshev and Fourier Spectral Methods.* 10.

[104] Kravchenko, A., and Moin, P., 1997. "On the effect of numerical errors in large eddy simulations of turbulent flows". *Journal of Computational Physics,* **131**(2), pp. 310–322. doi:https://doi.org/10.1006/jcph.1996.5597.

[105] Verstappen, R., and Veldman, A., 2003. "Symmetry–preserving discretization of turbulent flow". *Journal of Computational Physics,* **187**(1), pp. 343–368. doi:https://doi.org/10.1016/S0021-9991(03)00126-8.

[106] Capuano, F., Coppola, G., Balarac, G., and de Luca, L., 2015. "Energy preserving turbulent simulations at a reduced computational cost". *Journal of Computational Physics,* **298**, pp. 480–494. doi:https://doi.org/10.1016/j.jcp.2015.06.011.

[107] Coppola, G., Capuano, F., Pirozzoli, S., and de Luca, L., 2019. "Numerically stable formulations of convective terms for turbulent compressible flows". *Journal of Computational Physics,* **382**, pp. 86–104. doi:https://doi.org/10.1016/j.jcp.2019.01.007.

[108] Kennedy, C. A., and Gruber, A., 2008. "Reduced aliasing formulations of the convective terms within the navier–stokes equations for a compressible fluid". *Journal of Computational Physics,* **227**(3), pp. 1676–1700. doi:https://doi.org/10.1016/j.jcp.2007.09.020.

[109] Pirozzoli, S., 2010. "Generalized conservative approximations of split convective derivative operators". *Journal of Computational Physics,* **229**(19), pp. 7180–7190. doi:https://doi.org/10.1016/j.jcp.2010.06.006.

[110] Lodato, G., Domingo, P., and Vervisch, L., 2008. "Three-dimensional boundary conditions for direct and large-eddy simulation of compressible viscous flows". *Journal of Computational Physics,* **227**(10), pp. 5105–5143. doi:https://doi.org/10.1016/j.jcp.2008.01.038.

[111] Lodato, G., 2008. "Tridimensional Boundary Conditions for Direct and Large-Eddy Simulation of Turbulent Flows. Sub-Grid Scale Modeling for Near-Wall Region Turbulence". Theses, INSA de Rouen, Dec.

[112] Guezénnec, N., and Poinsot, T., 2009. "Acoustically nonreflecting and reflecting boundary conditions for vortcity injection in compressible solvers". *AIAA Journal,* **47**(7), pp. 1709–1722. doi:10.2514/1.41749.

[113] Odier, N., Poinsot, T., Duchaine, F., Gicquel, L., and Moreau, S., 2019. "Inlet and outlet characteristics boundary conditions for large eddy simulations of turbomachinery". In ASME Turbo Expo 2019: Turbomachinery Technical Conference and Exposition, American Society of Mechanical Engineers Digital Collection.

[114] Rudy, D. H., and Strikwerda, J. C., 1980. "A nonreflecting outflow boundary condition for subsonic navier-stokes calculations". *Journal of Computational Physics,* **36**(1), pp. 55–70. doi:https://doi.org/10.1016/0021-9991(80)90174-6.

[115] Giles, M., 1988. Non-reflecting boundary conditions for the Euler equations. Tech. rep., Computational Fluid Dynamics Laboratory, Department of Aeronautics and Astronautics, Massachusetts Institute of Technology.

[116] C. S. Yoo, Y. Wang, A. T., and Im, H. G., 2005. "Characteristic boundary conditions for direct simulations of turbulent counterflow flames". *Combustion Theory and Modelling,* **9**(4), pp. 617–646. doi:10.1080/13647830500307378.

[117] Yoo, C. S., and Im, H. G., 2007. "Characteristic boundary conditions for simulations of compressible reacting flows with multi–dimensional, viscous and reaction effects". *Combustion Theory and Modelling,* **11**(2), pp. 259–286. doi:10.1080/13647830600898995.

[118] Poinsot, T. J., and Lele, S. K., 1992. "Boundary conditions for direct simulations of compressible viscous flows". *Journal of computational physics,* **101**(1), pp. 104–129.

[119] Mavriplis, C., 1989. "Nonconforming discretizations and a posteriori error estimators for adaptive spectral element techniques". PhD thesis, Massachusetts Institute of Technology.

[120] Maday, Y., Mavriplis, C., and Patera, A. T., 1988. "Nonconforming mortar element methods: Application to spectral discretizations".

[121] Kopriva, D. A., and Kolias, J. H., 1996. "A conservative staggered-grid chebyshev multidomain method for compressible flows". *Journal of computational physics,* **125**(1), pp. 244–261.

[122] Kopriva, D. A., 1998. "A staggered-grid multidomain spectral method for the compressible navier–stokes equations". *Journal of computational physics,* **143**(1), pp. 125–158.

[123] Zhang, B., and Liang, C. C., 2015. "A simple, efficient, high-order accurate sliding-mesh interface approach to the spectral difference method on coupled rotating and stationary domains". *Journal of Computational Physics,* **295**, 04, p. 160. doi:10.1016/j.jcp.2015.04.006.

[124] Zhang, B., Qiu, Z., and Liang, C., 2018. "A flux reconstruction method with nonuniform sliding-mesh interfaces for simulating rotating flows". In 2018 AIAA Aerospace Sciences Meeting, p. 1094.

[125] Kahan, W., 1965. "Pracniques: Further remarks on reducing truncation errors". *Commun. ACM,* **Vol. 8**(No. 1), Jan, p. 40. doi:10.1145/363707.363723.

[126] Giles, M., 1991. Unsflo: A numerical method for the calculation of unsteady flow in turbomachinery. Tech. rep., Cambridge, Mass.: Gas Turbine Laboratory, Massachusetts Institute of Technology.

[127] Giovannini, M., Marconcini, M., Arnone, A., and Bertini, F., 2013. "Evaluation of unsteady cfd models applied to the analysis of a transonic hp turbine stage". In Proceedings of the 10 th European Conference on Turbomachinery Fluid dynamics & Thermodynamics, no. .ETC2013-132.

[128] Lobo, B., Zori, L., Galpin, P., and Holmes, W., 2016. "Efficient modeling strategy of an axial compressor fan-stage under inlet distortion". In ASME Turbo Expo 2016, ASME, ed., Vol. 2A Turbomachinery, p. V02AT37A039. doi:10.1115/GT2016-57467.

[129] Montiel, M., and Corral, R., 2023. "Time-inclined method for high-fidelity rotor/stator simulations". *Aerospace,* **10**(5). doi:10.3390/aerospace10050475.

[130] Montiel, M., and Corral, R., 2024. "Scale–Resolving Simulations of Turbulent Flow Retaining The Exact Blade Count With the Time–Inclined Method". Vol. Volume 12C: Turbomachinery – Design Methods and CFD Modeling for Turbomachinery; Ducts, Noise, and Component Interactions of *Turbo Expo: Power for Land, Sea, and Air*, p. V12CT32A025. doi:10.1115/GT2024-125689.

[131] Batchelor, G., and Proudman, I., 1954. "The effect of rapid distortion of a fluid in turbulent motion". *The Quarterly Journal of Mechanics and Applied Mathematics,* **7**(1), pp. 83–103. doi:10.1093/qjmam/7.1.83.

[132] Blázquez-Navarro, R., and Corral, R., 2023. "Validation of Broadband Noise Prediction Methodology Based on Linearised Navier-Stokes Analyses". *Journal of Turbomachinery*, 04, pp. 1–25. doi:10.1115/1.4062398.

[133] Blázquez-Navarro, R., and Corral, R., 2021. "Prediction of fan acoustic blockage on fan/outlet guide vane broadband interaction noise using frequency domain linearised Navier–Stokes solvers". *Journal of Sound and Vibration,* **500**, p. 116033. doi:10.1016/j.jsv.2021.116033.

[134] Hoheisel, H., Kiock, R., Lichtfuss, H., and Fottner, L., 1987. "Influence of free-stream turbulence and blade pressure gradient on bondary layer and loss behavior of turbine cascades". *ASME J. Turbomach.,* **109**(2), April, pp. 210–219. doi:10.1115/1.3262087.

[135] Lin, N., Reed, H., and Saric, W., 1992. *Instability, Transition, and Turbulence.* ICASE NASA LaRC Series. Springer, New York, NY, ch. Effect of Leading-Edge Geometry on Boundary-Layer Receptivity to Freestream Sound, pp. 421–440. doi:10.1007/978-1-4612-2956-8_42.

[136] Kirik, I., and Niehuis, R., 2015. "Comparing the effect of unsteady wakes on parallel and divergent endwalls in a lp turbine cascade (t106a-eiz and t106d-eiz)". In Proceedings of the 11th International Gas Turbine Congress, Tokyo, Japan, pp. 15–20.

[137] Goldstein, D., Handler, R., and Sirovich, L., 1993. "Modeling a no-slip flow boundary with an external force field". *Journal of computational physics,* **105**(2), pp. 354–366.

[138] Hallbäck, M., Henningson, D., Johansson, A., and Alfredsson, P., 2013. *Turbulence and Transition Modelling: Lecture Notes from the ERCOFTAC/IUTAM Summerschool Held in Stockholm, 12–20 June, 1995*, Vol. 2. Springer Science & Business Media.

[139] Carton de Wiart, C., Hillewaert, K., Duponcheel, M., and Winckelmans, G., 2014. "Assessment of a discontinuous galerkin method for the simulation of vortical flows at high reynolds number". *International Journal for Numerical Methods in Fluids,* **74**(7), pp. 469–493. doi:https://doi.org/10.1002/fld.3859.

[140] del Álamo, J. C., and Jiménez, J., 2003. "Spectra of the very large anisotropic scales in turbulent channels". *Physics of Fluids,* **15**(6), 06, pp. L41–L44. doi:10.1063/1.1570830.

[141] Hoyas, S., and Jiménez, J., 2006. "Scaling of the velocity fluctuations in turbulent channels up to $Re_\tau = 2003$". *Physics of Fluids,* **18**(1), 01, p. 011702. doi:10.1063/1.2162185.

[142] Lozano-Duran, A., and Jiménez, J., 2014. "Effect of the computational domain on direct simulations of turbulent channels up to $re_\tau = 4200$". *Physics of Fluids (1994-present),* **26**, 01, pp. –. doi:10.1063/1.4862918.

[143] Lee, M., and Moser, R. D., 2015. "Direct numerical simulation of turbulent channel flow up to $re_\tau \approx 5200$". *Journal of Fluid Mechanics,* **774**, pp. 395–415.

[144] Carton de Wiart, C., and Murman, S. M., 2017. "Assessment of wall–modeled les strategies within a discontinuous-galerkin spectral–element framework". In 55th AIAA Aerospace Sciences Meeting, p. 1223.

[145] Ghiasi, Z., Li, D., Komperda, J., and Mashayek, F., 2018. "Near–wall resolution requirement for direct numerical simulation of turbulent flow using multidomain chebyshev grid". *International Journal of Heat and Mass Transfer,* **126**, pp. 746–760. doi:10.1016/j.ijheatmasstransfer.2018.05.114.

[146] del Álamo, J. C., Zandonade, P., and Moser, R., 2004. "Scaling of the energy spectra of turbulent channels". *Journal of Fluid Mechanics,* **500**, 04, pp. 135 – 144. doi:10.1017/S002211200300733X.